University College London
Department of Electronic & Electrical Engineering
DOCTOR OF PHILOSOPHY THESIS

Advancing nanofabrication processes for the generation of multifunctional surfaces

Doctoral thesis of:

Sophia Katharine Laney

Primary Supervisor:
Prof. Ioannis Papakonstantinou

Secondary Supervisors:
Prof. Manish K. Tiwari
Prof. Ivan P. Parkin

I, Sophia K. Laney, confirm that the work presented in this thesis is my own. Where information has been derived from other sources, I confirm that this has been indicated in the work.

Abstract

Ubiquitous in the natural world, micro- and/or nano-structured surfaces can afford simultaneous control over a range of interfacial properties; providing an attractive solution for where the accumulation of fluids (fog/rain/oil) and bacteria, and the mismanaged interaction of photons, can impede the safety or efficiency of the surface. Although surfaces found in nature provide a wealth of inspiration, replicating the structures synthetically persists to be a challenge, particularly so when striving for scalability and simplicity to encourage industrial/commercial uptake. Furthermore, the fabrication challenges become amplified when aiming for sub-wavelength structures; often necessary to unlock or enhance additional functionality. In this thesis, I present novel fabrication routes based on lithography and reactive ion etching (RIE) to achieve a range of ordered structures at the nano-scale in glass and silicon, and further replicate the resultant structures into polymers. I explore scalable masking techniques including block copolymer (BCP) lithography, laser interference lithography (LIL) and nanoimprint lithography (NIL), to achieve a series of pitches from 50 – 600 nm. By coupling the masking with novel combinations of etching chemistries, and taking advantage of the etch resistivity of different materials, I fabricate high aspect ratio nanostructures through simplified processes and demonstrate their ability to target applications in wettability, photonics and anti-bacterial action. Specifically, for silicon and glass nanocones, I focus on their anti-fogging, superhydrophobic, anti-reflective and anti-bacterial properties. I also investigate the impact of the nanostructure morphology on a sub-class of water-repellent surfaces, namely, slippery liquid infused porous surfaces, and their ability to retain lubricant under dynamic conditions; continuing on the theme of smart nanostructure design and simplified fabrication to pave a route to multifunctional surfaces. It is anticipated that the surfaces and their properties will find use as car windscreens, coatings for solar panels, high-rise glass facades, and high-touch surfaces to name a few.

Impact Statement

Climate change, healthcare, and a depletion of natural resources are listed as some of the most pressing global issues by the United Nations.[1] Fuelled by over population and over consumption, we are approaching an era where breathing in air could trigger 6.6 million premature deaths a year,[2] over half the global population could suffer water droughts whilst the demand for water is set to increase by 50%,[3,4] and where common infections could kill again (antimicrobial resistance; AMR).[5,6]

Efforts to curb these events have led to a myriad of different approaches; each contributing in their own way to the problems at large. Interfaces, for instance are often a breeding ground for inefficiencies, adhesion and growth of undesirable matter, or are just passive participants in a situation where they could otherwise play an active role. Altering the surface properties to act symbiotically in such seemingly distinct application spaces to target bacterial killing without inducing AMR,[7] to harvest water,[8] or to prevent reflections on solar panels[9] can be achieved through nanotechnology and material engineering; providing a wealth of solutions to solve problems related to basic needs, but also advanced wants.

However challenges remain when it comes to their fabrication; be it expensive equipment, multi-step processes or a lack of reproducibility. Such drawbacks are often the downfall of these high-performance materials, as they lack the financial appeal necessary for industrial up-take. New processes which achieve/advance such functionalities through nanostructuring, with a focus on simplicity, scalability, and precision, are therefore in high demand. The work presented in this thesis offers a contribution towards overcoming some of these hurdles. I present three novel fabrication routes to create an expansive library of well-controlled and scalable nanostructures, and showcase their multiple functionalities.

Firstly, I present a breakthrough two-step fabrication method to generate high-aspect ratio, nanocone arrays in glass with exceptional precision via Regenerative Secondary Mask Lithography (RSML). By harnessing the remarkable ability of nanocones to interact with photons, liquids and biological systems, impact-resistant superhydrophobicity, omnidirectional antireflectivity, and crucially, the first demonstrated antibacterial properties on a glass surface towards *S. aureus* is achieved, paving the way for a new range of high-value glass products.

By taking advantage of RSML, I present a route to achieve highly-engineered silicon nanocones with controlled height/angles/shape. The nanocones presented not only offer excellent superhydrophobicity and broadband antireflectivity, but are also shown to display remarkable antifogging abilities, and provide a fundamental understanding into the antifogging mechanism of geometries of nanocones.

Finally, I demonstrate Spacer Defined Intrinsic Multiple Patterning (SDIMP), a technique to generate 2D and 3D periodic nanoarrays in silicon and glass with unprecedented precision through independent dimension control and structural complexity. To showcase the diversity, structural fine-tuning and broad applicability of SDIMP, the nanotube arrays are exploited to induce a performance enhancement in two intentionally unrelated areas; photonics and wettability, through ultra-high broadband absorption and liquid infused (slippery) surfaces.

These fabrication pathways can be used for both fundamental research, and future commercialisation owing to their control, simplicity and scalability.

Acknowledgements

I would first like to thank my supervisor Prof. Ioannis Papakonstantinou, who has provided me with unrelenting support, mentorship, and above all, encouragement. Since the first day of my PhD, he has invested time instilling the skills needed to be a good researcher; from being methodical but at the same time creative, to asking the right questions. This however, requires a strong understanding of the fundamentals, and I will always fondly remember the time he spent going through the Droplets book with me (I am certain however, his memories of these sessions incite more wearisome emotions!). In addition to the time spent in the lab discussing various results, his constructive criticism and input into the publications has advanced them to another level. From my perspective, it is rare to find a supervisor who gives as much time to his students as Ioannis, and I will be forever grateful for his guidance and knowledgeable insight, and thankful for his good sense of humour; as this has made Photonic Innovations Lab an extremely fun place to be.

I would also like to thank my secondary supervisors Prof. Manish Tiwari, and Prof. Ivan Parkin. Manish’s vast knowledge in interfacial phenomena and nanoengineering has made him the first person I turn to with any questions on the wettability of surfaces. And even with his extremely busy schedule, he has always been willing to set aside the time to talk through the problems and inspire the next steps. Ivan’s wide ranging expertise in chemistry and materials has been incredibly useful, and has often nudged me onto the right track. Coming from a chemistry background myself, I have enjoyed our weekly meetings which have tended to take a more chemical as opposed to an engineering spin, and I have appreciated his cautionary tales, all of which have influenced my lab practice; particularly when handling the more hazardous materials such as hydrofluoric acid! Both Manish and Ivan have provided invaluable advice and input for each publication, for which I am extremely grateful.

Throughout my doctoral studies I was assisted by a number of people, and I will acknowledge each of their input at the beginning of each chapter when describing methods they developed, characterisation they performed, or samples they made. The people referred to are:

- Ioannis Papakonstantinou (IP)

- Manish K. Tiwari (MKT)
- Ivan P. Parkin (IPP)
- Martyna Michalska (MM)
- Tao Li (TL)
- Mark Portnoi (MP)
- Francisco Ramirez (FR)
- David Quéré (DQ)
- Pierre Lecointre (PL)
- Junho OH (JO)

I would like to specially thank Tao Li who shared his expertise in lithography and etching, and his ideas for fabrication routes. This enabled me to find my feet much sooner than I otherwise would have, and allowed me to join projects that had already made great progress. I would also like to thank Martyna Michalska, who has been an amazing colleague, mentor, and friend, and someone from whom I have learnt a great deal. Her passion for science and pursuit for excellence has influenced my approach both within and outside of research. In addition to Tao and Martyna, I would also like to thank all my other fellow Pi-Lab group members: Mark, Christian, Radhika, Guru, Francisco, Usama, Alessandro, Zhijie and Lingxi. Thank you for the insightful conversations, and for joining me for after work drinks.

Beyond the group, I would like to thank the members of office 1111, for the coffee, camaraderie, and laughter. The office has been host to plenty of unforgettable memories; including competitions, games, and late night dinners to fuel paper writing. I also want to give thanks to the funding bodies that have supported my research, such as the EPSRC, and Lloyds register foundation (International Consortium of Nanotechnology (ICON)).

Outside the world of research, I would like to thank all my friends for providing non-science related distractions, without which I would not have been able to finish a PhD. Finally, I would like to thank my boyfriend Fergal who has heard more about nanocones than he ever could have anticipated, and my family: my parents, step-parents, brother, grandparents, and extended family – whose continued love and support have made it all possible.

List of Publications

Publications directly related to the work described in this thesis:

1. Sophia K. Laney,[‡] Tao Li,[‡] Martyna Michalska,[‡] Francisco Ramirez, Mark Portnoi, Junho Oh, Manish K. Tiwari, Iain G. Thayne, Ivan P. Parkin, and Ioannis Papakonstantinou. Spacer Defined Intrinsic Multiple Patterning, **ACS Nano**, 2020, 14, 12091-12100
2. Pierre Lecointre, Sophia K. Laney, Martyna Michalska, Tao Li, Alexandre Tanguy, Ioannis Papakonstantinou and David Quéré. Unique and robust dew repelllency of nanocones, **Nature Communications**, 2021, 12, 3458
3. Sophia K. Laney,[‡] Tao Li,[‡] Martyna Michalska,[‡] Francisco Ramirez, Mark Portnoi, Junho Oh, Manish K. Tiwari, Iain G. Thayne, Ivan P. Parkin, and Ioannis Papakonstantinou. Delayed Lubricant Depletion of Slippery Liquid Infused Porous Surfaces Using Precision Nanostructures, **Langmuir**, 2021, 37, 33, 10071-10078
4. Martyna Michalska,[‡] Sophia K. Laney,[‡] Tao Li,[‡] Mark Portnoi, Nicola Mordan, Elaine Allan, Manish K. Tiwari, Ivan P. Parkin and Ioannis Papakonstantinou. Bioinspired Multifunctional Glass Surfaces through Regenerative Secondary Mask Lithography, **Advanced Materials**, 2021, 2102175
5. Martyna Michalska,[‡] Sophia K. Laney,[‡] Tao Li,[‡] Manish K. Tiwari, Ivan P. Parkin and Ioannis Papakonstantinou. A route to engineered high aspect-ratio silicon nanostructures through regenerative secondary mask lithography, 2021 (in preparation)

Some of the figures and text in this thesis appear verbatim in the papers listed above. Where necessary, permission has been sought and granted from the publisher.

Publications co-authored during this PhD, but not directly related to the work described in this thesis:

1. Johannes Schläefer, Christian Sol, Tao Li, Delphine Malarde, Mark Portnoi, Thomas J. Macdonald, Sophia K. Laney, Michael J. Powell, Isıl Top, Ivan P. Parkin, and Ioannis Papakonstantinou. Thermochromic VO2 - SiO2 nanocomposite smart window coatings with narrow phase transition hysteresis and transition gradient width. **Solar Energy Materials and Solar Cells**, 2019, 109944

Contents

Abstract 4

Impact Statement 5

Acknowledgements 7

List of Publications 9

Contents 10

List of Tables 13

List of Figures 13

List of Supplementary Figures (Appendix) 15

List of Abbreviations 16

INTRODUCTION: MULTIFUNCTIONALITY 17

- 1.1 Motivation 18
  - 1.1.1 The problem 20
- 1.2 Lessons from nature 20
- 1.3 The Physics of Wetting 21
  - 1.2.1 Flat surfaces 21
  - 1.2.2 Rough surfaces 23
  - 1.2.3 Achieving superhydrophobicity 26
- 1.4 Photon management 33
  - 1.4.1 Antireflectivity 33
- 1.5 Bactericidal action 35
- 1.6 Fabrication requirements 38
- 1.7 Thesis outline 38

LITERATURE REVIEW: PRECISE NANOPATTERNING 39

- 2.1 Introduction 40
- 2.2 Nanolithography 40
  - 2.2.1 Colloidal lithography 42
  - 2.2.2 Nanoimprint lithography 43
  - 2.2.3 Block copolymer lithography 44
  - 2.2.4 Laser Interference Lithography 49

2.2.5 Summary 50
2.3 Pattern transfer: high-resolution etching 51
2.3.1 Glass etching 53
2.3.2 Silicon etching 56
2.3.3 Summary 58
REGENERATIVE SECONDARY MASK LITHOGRAPHY FOR MULTIFUNCTIONAL GLASS NANOCONES 59
3.1 Abstract 60
3.2 Introduction 60
3.3 Results and Discussion 62
3.3.1 Two-Step Fabrication – Regenerative Soft Mask Lithography (RSML) 62
3.3.2 Application of Nanostructure Arrays 82
3.4 Conclusions 96
3.5 Methods 97
TUNEABLE SILICON NANOSTRUCTURING FOR MULTIFUNCTIONAL NANOSTRUCTURES, AND HIGHLY EFFICIENT ANTIFOGGING NANOCONES 102
4.1 Fabrication 103
4.1.1 Abstract 103
4.1.2 Introduction 103
4.1.3 Results And Discussion 105
4.1.4 Conclusions 114
4.1.5 Methods 114
4.2 Antifogging 116
4.2.2 Introduction 116
4.2.3 Results and discussion 117
4.2.4 Conclusion 130
4.2.5 Methods 131
SPACER DEFINED INTRINSIC MULTIPLE PATTERNING FOR COMPLEX NANOARRYS WITH MULTIFUNCTIONAL SURFACE PROPERTIES 135
5.1 Fabrication 136
5.1.1 Abstract 136
5.1.2 Introduction 136
5.1.3 Results And Discussion 139

5.1.4 Applications – broadband antireflection ... 153
5.1.5 Conclusion ... 157
5.1.6 Methods ... 158
5.2 Slippery Liquid Infused Porous Surfaces ... 164
5.2.1 Abstract ... 164
5.2.2 Introduction ... 164
5.2.3 Results And Discussion ... 167
5.2.4 Conclusion ... 175
5.2.5 Methods ... 176
CONCLUSIONS AND OUTLOOK ... 179
6.1 Conclusions ... 179
6.2 Future Outlook ... 181
6.3 Summary of contributions ... 183
Bibliography ... 184
Appendix ... 206

List of Tables

Table 1 | Characteristics of the nanotextured materials for antifogging. 119
Table 2 | Nanotube dimensions (SDIMP) 161
Table 3 | Nanotube fabrication: (i) etching times and (ii) deposition thicknesses 162
Table 4 | Nanotube etching conditions – Oxford RIE 162
Table 5 | Nanotube etching conditions – ICP STS 162
Table 6 | Iterative SDDP structure fabrication 163
Table 7 | Dimensions of the nanostructures for SLIPS. 168
Table 8 | Etching times and deposition thickness for SLIPS nanostructure generation 178
Table 9 | Oxford RIE etching conditions for SiO_2 mask etching of SLIPS nanostructures 178
Table 10 | STS etching conditions for Si etching of SLIPS nanostructures 178
Table 11 | Interfacial energy values 178

List of Figures

Figure 1 | Droplet spreading. 22
Figure 2 | Wenzel and Cassie Baxter 24
Figure 3 | Contact angle as a function of roughness 26
Figure 4 | Contact angle as a function of solid fraction 26
Figure 5 | Snapshots of a water droplet impacting a superhydrophobic surface 27
Figure 6 | The effect of array dimensions (height, pitch) on impalement scenarios 28
Figure 7 | Critical pressure as a function of pitch for two penetration depths 29
Figure 8 | Cicada with nanostructured wing. 30
Figure 9 | Wetting configurations for a SLIPS surface. 32
Figure 10 | Refractive index profiles at the interface glass/air interface 35
Figure 11 | SEM images of E. coli on a black silicon surface 36
Figure 12 | A model of bacterial infiltration into the nanostructure 37
Figure 13 | Key nano-lithographic techniques 41
Figure 14 | Colloidal lithography using polystyrene nanospheres 42
Figure 15 | The three common nanoimprinting techniques 44
Figure 16 | Phase diagram of an AB diblock copolymer 46
Figure 17 | The two variants of block copolymer lithography 48
Figure 18 | Lloyd’s interferometer 50
Figure 19 | Etch characterisation and sources of plasma 52
Figure 20 | Nanostructures generated through mask-less etching. 53
Figure 21 | SEM images of BCP-generated masks and resulting glass nanostructures 55
Figure 22 | Bosch silicon etching 56
Figure 23 | SEM images of Si nanostructures generated by etching BCP masks 58
Figure 24 | RSML - Two-step fabrication process of glass nanopillars 63
Figure 25 | Characterization of BCP patterns 65
Figure 26 | BCP mask after breakthrough etch 1 (Step 2.1) 66

Figure 27 | A schematic of glass etching chemistry 67
Figure 28 | Manipulation of etching/deposition gas composition for anisotropy control 69
Figure 29 | Exemplary structures obtained by Pseudo-Bosch process 70
Figure 30 | Secondary mask evolution and structure tapering when $\boldsymbol{RD \gg RS}$ 72
Figure 31 | The glass etching rates when varying argon flow. 73
Figure 32 | Effect of secondary mask tuning 74
Figure 33 | Exemplary glass nanopillars 75
Figure 34 | Glass nanopillars templated from BCP P400 76
Figure 35 | Fabrication process of glass nanopillars templated from BCP P400 77
Figure 36 | Control experiment 77
Figure 37 | RSML applicability 79
Figure 38 | The effect of an RSML-mediated etch on nanostructure diameter, using a photoresist mask 80
Figure 39 | Tape-peel test 82
Figure 40 | Double-sided glass processing 84
Figure 41 | Optical properties 85
Figure 42 | The effect of sharpening on the sample wettability 86
Figure 43 | Rebound characterization of a water droplet 87
Figure 44 | Wettability characterisation. 88
Figure 45 | Capillary pressure versus penetration percentage 90
Figure 46 | Schematic of S. aureus adhered to the surface 91
Figure 47 | Effect of geometry of nanopillars on the interactions with S. aureus 94
Figure 48 | Antibacterial properties of glass nanostructures 95
Figure 49 | Schematics of the four key process steps to generate a range of tailored Si nanostructures. 106
Figure 50 | Tuning of the SiO2 hard mask height and shape 108
Figure 51 | Tuning of nanostructure profile and aspect ratio 110
Figure 52 | Tuning of truncation and re-entrant profile 111
Figure 53 | Method scalability, optical properties, and wetting characteristics 113
Figure 54 | Families of samples 118
Figure 55 | Direct visualization of droplets condensing on nanotexture 120
Figure 56 | Breath figures on pillars A and the homothetic family H 126
Figure 57 | Antifogging ability of nanocones. 127
Figure 58 | Schematics highlighting the differences between SDIMP and SDDP/D-SDDP 138
Figure 59 | Nanotube fabrication process and tuning of the pitch and height 140
Figure 60 | Corresponding SEM images to the fabrication scheme 142
Figure 61 | Corresponding SEM images to the fabrication of nanotubes in glass and polymer imprints 143
Figure 62 | SEM images of nanotubes generated at two different pitches. 145
Figure 63 | Fine-tuning the nanotube dimensions during one SDIMP iteration 147
Figure 64 | Investigation into the effect of coil power, platen power and time 148
Figure 65 | Tuning the transfer of the crown structure to the nanotube 149
Figure 66 | Exemplary complex structures by two SDIMP iterations 151

Figure 67 | Further nanostructures generated through two SDIMP iterations 153
Figure 68 | Antireflective study of silicon nanotube arrays 155
Figure 69 | Optical properties of the tapered nanotube with a top crown at oblique angle of incidence. 157
Figure 70 | SLIPS nanostructures.. 170
Figure 71 | Water contact angles of SLIPS samples and the shear tolerance test....................... 171
Figure 72 | Water droplet shedding test; set-up an results 172
Figure 73 | Water droplet shedding test; weighing 175

List of Supplementary Figures (Appendix)

Figure S 1| ESEM images of water condensing on samples and plots of the corresponding contact angles of condensing microdroplets.. 206
Figure S 2 | Contact angle of condensing microdroplets on nanostructures.. 207
Figure S 3 | Antifogging model parameters 207
Figure S 4 | Sinking depth *z* for a drop of radius *r* in a Cassie state on an array of hydrophobic cones.. 208
Figure S 5 | SEM images and breath figures of the nanocones E0 with pitch *p* = 110 nm and reduced height *h* = 101 nm.. 208
Figure S 6 | Phase diagram of antifogging on sharp nanocones.. 209
Figure S 7 | Breath figures on the truncated family T (samples T1-T2-T3-T4) 210
Figure S 8 | Absolute number of drops on sample H1 (red dots) and A (blue dots) as a function of time. 210
Figure S 9 | Global jumping rate N_g as a function of time *t* for all samples H and E. 211
Figure S 10 | Comparison of Sample A nanopillars and sample E4 nanocones. 213
Figure S 11 | SEM images of convex nanocones E2’ and the corresponding jumping rate.. 213

List of Abbreviations

- **AFM** – Atomic Force Microscopy
- **ALD** – Atomic Layer Deposition
- **AMR** – Antimicrobial Resistance
- **AR** – Aspect Ratio
- **ARC** – Antireflective Coating
- **BCP** – Block Copolymer
- **CAH** – Contact Angle Hysteresis
- **CCP** – Capacitively Coupled Plasma
- **CD** – Creep Deformation
- **CLSM** – Confocal Laser Scanning Microscopy
- **DBR** – Distributed Bragg Reflector
- **DRIE** – Deep Reactive Ion Etching
- **DS** – Double Sided
- **EBL** – Electron Beam Lithography
- **ED** – Elastic Deformation
- **ESEM** – Environmental Scanning Electron Microscopy
- **FDTD** – Finite Difference Time Domain
- **FFT** – Fast Fourier Transform
- **FIB** – Focus Ion Beam
- **ICP** – Inductively Coupled Plasma
- **IPS** – Intermediate Polymer Stamp
- **LIL** – Laser Interference Lithography
- **NIL** – Nanoimprint Lithography
- **NIR** – Near Infrared
- **PECVD** – Plasma Enhanced Chemical Vapour Deposition
- **PR** – Photoresist
- **PS** – Polystyrene
- **PUA** – Polyurethane Acrylate
- **RCA** – Receding Contact Angle
- **RF** – Radio Frequency
- **RIE** – Reactive Ion Etching
- **RSML** – Regenerative Secondary Mask Lithography
- **SDDP** – Spacer Defined Double Patterning
- **SDIMP** – Spacer Defined Intrinsic Multiple Patterning
- **SEM** – Scanning Electron Microscope
- **SERS** – Surface Enhanced Raman Scattering
- **SLIPS** – Slipper Liquid Infused Porous Surfaces
- **STU** – Simultaneous Thermal and UV
- **SVA** – Solvent Vapour Annealing

1

INTRODUCTION: MULTIFUNCTIONALITY

In this chapter, I first present the range of multifunctional surfaces found in nature, and discuss their remarkable properties and the mechanisms at play. I delve into greater detail in the mechanism behind water repellence; one of the more prominent surface characteristics in this thesis, as well as antireflectivity and antimicrobial action. Later, focussing on ordered nanostructure arrays, I introduce the fabrication requirements to synthetically achieve multifunctionality.

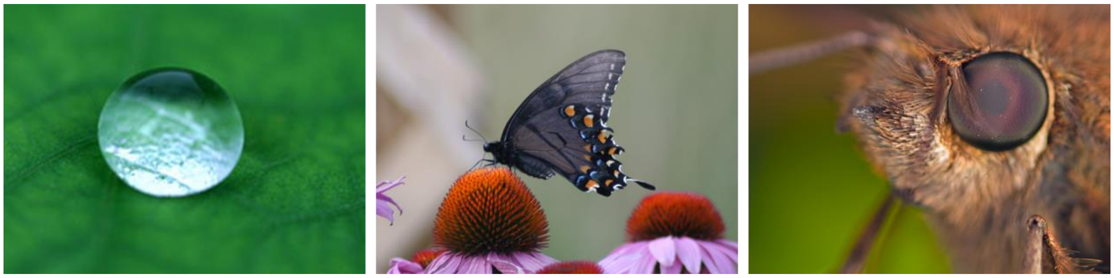

Natural surfaces of multifunctional character: lotus leaf,[10] *wings of a butterfly,*[11] *compound eye of a moth.*[12]

1.1 Motivation

Nanostructured surfaces are those which have nanoscale protrusions or intrusions on their surface, and as a consequence, are observed to have properties that significantly depart from their bulk material counterparts. With the size of the nanofeatures commensurate with those of biomolecules,[13,14] microdroplets,[15,16] and certain wavelengths of light,[17,18] these surfaces interact in a unique manner, providing a means to access and manipulate new entities of interest. It is therefore unsurprising that the field of nanomaterials science has attracted the attention of scientists worldwide, with research groups continuing in their pursuit to implement nanotechnology's miniature answers to address the World's biggest problems.

The unwanted adhesion of water to surfaces, which may seem a trivial problem, can in fact cause a multitude of issues. Fogging for instance, occurs when water vapour condenses onto a surface forming micro-droplets with dimensions on the order of the visible wavelengths of light. This results in blurred vision and a loss of optical transparency or specular reflectance,[19] and whilst this can merely be a nuisance, it can also have severe safety implications; reducing visibility whilst driving, impairing vision when wearing safety goggles, and reducing the field of vision for laparoscopic surgery.[20–22] Routes developed to combat fogging fall into two categories: active or passive. Active approaches invoke changes in the environmental conditions (humidity, temperature, air flow) to prevent the phenomena of condensation from occurring. Such systems have been successfully implemented in buildings and vehicles, however the cost to the environment is large; with cooling and heating of electric vehicles using heating, ventilation and air conditioning (HVAC) systems accounting for a 40% reduction in driving range, for instance.[23] With the huge concerns brought by global warming, attention therefore turns to passive solutions. These exploit the surface wetting properties to either repel the microdroplets from the surface (superhydrophobic) or encourage them to spread and form a uniform film (superhydrophilic). Such passive solutions require surface structuring on the nano- or micro-scale, and if engineered cleverly, can also be utilised for additional functionalities. For instance, converting the problem of fogging into a solution for water harvesting.[8] Or delaying ice formation; overcoming a major hazard for aircraft, powerlines and roads.[24]

Reducing surface reflectivity is also a key area of interest. Achieving higher transparency or a greater absorbance is crucial for enhancing the performance of optical devices over a wide range of wavelengths. Strategies aimed at abating climate change have driven the adoption of solar photovoltaics as a sustainable, renewable and environmentally friendly alternative to fossil fuels. [25] Silicon, as one of the second most abundant materials on the earth's crust, is the most popular material for solar cell manufacture, accounting for 95% of the total market share in 2020.[26] However, Si photovoltaics are limited to a theoretical maximum efficiency of 29%[27,28] and furthermore the refractive index of silicon results in over 30% of light being reflected rather than absorbed. A well-designed solar cell therefore needs to be optically thick to ensure high-absorbance, however to avoid losses when collecting the photo excited electron-hole pairs, it must be electronically thin. This conundrum can be resolved through nanostructuring the surface of the Si to induce a much greater absorbance of light and thus allowing for the thickness of the substrate to be reduced.[29] Nanostructuring is not the only route to increase absorbance as antireflective layers can also achieve the same effect,[30,31] nonetheless to be able to maintain these optical properties in various environments, the surface must remain free from pollutants (dust, bird-droppings, water-stains); a factor that is often over-looked but detrimental to the performance with a degradation in the efficiency of ~19% after one month of dust collection.[32] Therefore multifunctional surfaces that can manage photons and pollutants under different environmental conditions are key for the long-term viability of Si photovoltaics.

One of the World's greatest challenges currently lies in the uncontrolled accumulation of microorganisms (bacteria, viruses). Historically, this problem has been addressed through the use of antimicrobials (antibiotics, antivirals, and antifungals). However, with the emergence and spread of drug resistant pathogens, our ability to treat common infections is being severely threatened. In 2020, the World Health Organisation (WHO) named antimicrobial resistance (AMR) one of 'the top 10 global public health threats facing humanity'.[5] A review commissioned by the UK government in 2014 estimated that by the year 2050, AMR could cause up to 10 million deaths per year.[6] Alternative solutions to antimicrobials have therefore been actively explored, and once more, nature revealed the answer; with the discovery in 2012 that nanopatterns present on the wings of the cicada act to mechanically kill bacterial cells upon contact.[7] Such an approach, which does not rely on chemical agents is not only safer and more sustainable, but crucially should not induce AMR. The field is still in its infancy with optimum topographies and materials yet to be determined, likely due to the difficulty in the manufacture of systematically varied nanostructures; but holds great promise for surfaces within hospital environments, food processing units and for high-touch surfaces to name a few.

1.1.1 The problem

Surfaces that are capable of targeting these different areas of interest simultaneously present many advantages, with each functionality acting symbiotically to boost the overall performance. This being said, challenges remain when it comes to their fabrication; be it expensive equipment, multi-step processes or a lack of reproducibility. Such drawbacks are often the downfall of these high-performance materials, as they lack the financial appeal necessary for industrial up-take. New processes which achieve, and even advance the aforementioned functionalities through nanostructuring, with a focus on simplicity, scalability, and precision, are therefore in high demand.

1.2 Lessons from nature

Through billions of years of evolution, nature has arrived at extraordinary materials solutions to ensure survival. Plants, insects, aquatic, and land animals have developed intricate surface patterns invisible to the naked eye, on the micro- and nano-metre scale to serve a range of different purposes. Examples include the lotus leaf, and its ability to repel water; ensuring it remains clean, dry, and free of bacterial colonies and fungal spores, and thus has adapted to living in polluted waters.[33] In a similar vein, the eyes of a mosquito are also observed to repel water, however unlike the lotus leaf, they are capable of resisting micro-droplet formation on their surface; allowing the mosquito to maintain clear vision in humid conditions.[34] Whilst humans have admired these properties for centuries and hypothesised their origin, it is only with the advent of the electron microscope that the structures responsible were identified.[35] Since then studies across multiple species of plants, insects and animals revealed the vast diversity in topographic features; often of high complexity or with subtle geometric features, maximising the performance with minimal resources.[36]

Mimicking these structures to obtain advanced functional materials has since become a rapidly evolving field, and it holds promise to tackle unwanted interactions at interfaces which can impede the safety or efficiency of devices. For instance, ice accumulation on the wings of aircraft[37] or the proliferation of bacteria on hospital surfaces.[38] However, in order to implement the design principles laid out by nature, and even advance properties beyond those observed in the natural world, it is necessary to understand the fundamental interaction mechanism of the surface patterns with liquids, light and living organisms.

1.3 The Physics of Wetting

The phenomenon of wetting refers to the study of how a liquid deposited on a solid substrate spreads out.[39] It is an occurrence that can be observed in everyday life from drying your hair to watching raindrops race each other as they slide down a car window, and yet this seemingly mundane phenomenon is complex, and understanding how to tame it is of high-importance.

Liquids are observed to form a range of shapes when in contact with a solid surface or another liquid; from a perfect sphere to a film. Within a liquid phase, charge polarisation of the molecules induces neighbours to align, generating a cohesive force. In the bulk liquid, molecules benefit from interactions with all neighbours, and are thus in a favourable state. Moving to the interface however it is a different story; these molecules are in an unfavourable state with fewer cohesive interactions, and thus exhibit stronger attractive forces on their nearest neighbours on and below the surface. In turn, this creates a net inward force causing molecules on the surface to contract and minimise the liquid-air interface. The energetic cost per surface area is known as the surface tension, γ. Dependent on the nature of the liquid, γ ranges from ~20 mN/m for oils, to ~72 mN/m for water; the highest surface tension value for a liquid, save for mercury (~500 mN/m). As water molecules interact through hydrogen bonds, the loss in cohesion energy for a water molecule at the interface gives rise to a higher surface tension value.

1.2.1 Flat surfaces

The degree of wetting is determined by a force balance between the adhesive and cohesive forces, and when a liquid is in contact with a flat solid, the surface energies at the solid-liquid γ_{SL}, solid-vapour γ_{SV}, and liquid-vapour γ_{LV} interface govern its shape.

Whether a liquid fully wets or partially wets a surface is dictated by the spreading parameter *S*, which, using the aforementioned surface energies, measures the difference between the surface energy of the substrate when dry and when wet.

$$S = \gamma_{SV} - (\gamma_{SL} + \gamma_{LV}) \qquad \textit{Eq. 1}$$

A positive value of S indicates that the solid lowers its energy by being wetted, and thus total wetting occurs (Figure 1a). This occurs for solids of high surface energy such as glass (with no pollutants present). It is also observed with liquids of low surface tension such as alkanes or silicone oils. In contrast, when S is negative, only partial wetting occurs, and the droplet forms a spherical cap with a contact angle θ_E (Figure 1b).

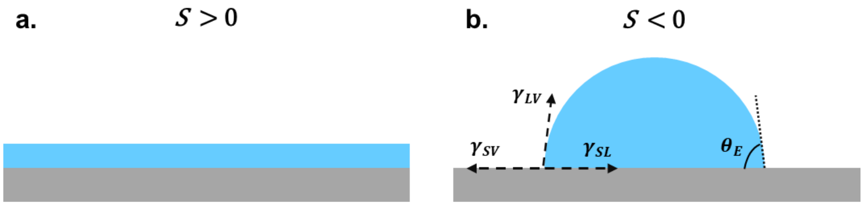

Figure 1 | a. For the case where S is positive, the liquid fully wets the surface. **b.** For the case where S is negative, the liquid partially wets the surface, forming a cap with a contact angle $\boldsymbol{\theta_E}$.

In 1805, Thomas Young derived the relation between the surface energies and the contact angle.[40] Each interface wishes to minimise the corresponding surface area thus draws the contact line, and so balancing the surface tension (on the horizontal) yields the following relation:

$$\gamma_{LV} cos\, \theta_E = \gamma_{SV} - \gamma_{SL} \qquad \textit{Eq. 2}$$

For flat surfaces, θ_E can span from 0 to 120°, with hydrophilic and hydrophobic surfaces delineated by a θ_E of 90°.

So far it has been assumed that solid surfaces exhibit perfect smoothness, rigidity and chemical homogeneity, however this is very rarely the case in the real world. Defects cause pinning of the contact line and consequently the liquid will exhibit different contact angles dependent on the location of the surface. The contact angle of a static droplet deposited onto a surface will lie within the range of two extremes: the advancing θ_{adv} and the receding θ_{rec} angle. The contact angle hysteresis (CAH) is the difference between these (CAH = $\theta_{adv} - \theta_{rec}$). These angles can be measured one of two ways: (i) slowly dispensing a droplet onto a flat surface and measuring the angle as the volume increases and contact line advances, and similarly for the receding as liquid is withdrawn and the contact line begins to recede; (ii) placing a droplet on an inclined surface and tilting it until the moment when the droplet begins to move, these maximum and minimum angles are considered as the advancing and receding respectively.

1.2.2 Rough surfaces

As mentioned, surfaces in reality are not atomically smooth and instead exhibit some level of roughness. As the roughness of a surface is increased however, different regimes of wetting are observed, and contact angles greater than 120° can be attained. Two theories, described by Wenzel in 1936 and Cassie & Baxter in 1944 depict the different configurations of wetting on rough surfaces.[41,42]

1.2.2.1 Wenzel model

Wenzel realised that the nature of a material (if hydrophilic or hydrophobic) is enhanced by the presence of textures. The rationale being, that roughness increases the surface area, so for a hydrophilic material ($\theta_E < 90°$), the liquid will spread more and thus there will be a favourable increase in the solid/liquid contact. Conversely for a hydrophobic material ($\theta_E > 90°$), the liquid will develop a much larger contact with the solid which is unfavourable, unless the contact angle changes.

Wenzel's model assumes that the liquid follows the grooves of the solid surface (Figure 2a) with the contact angle changing locally from one point to another (given by Young's equation (θ_E)). To calculate the apparent contact angle (θ_w) we can consider a small displacement dx in the contact line. The change in surface energy, dE, associated with the displacement can be written as:

$$dE = r(\gamma_{SL} - \gamma_{SV})dx + \gamma_{LV}\, dx\, \cos\theta_w \qquad \textit{Eq. 3}$$

Where r is the roughness factor, which is defined as the ratio of the true surface area over the apparent surface area. At equilibrium ($dE = 0$) when $r > 1$, we obtain Wenzel's relation:

$$\cos\theta_w = r\, cos\, \theta_E \qquad \textit{Eq. 4}$$

Due to the surface roughness, $r > 1$ always, therefore $|\cos\theta_w| > |\cos\theta_E|$. As a result of this relationship, when $\theta_E < 90°$, $\theta_w < \theta_E$ thus resulting in increased hydrophilicity in the Wenzel regime, compared to the ideal. Furthermore, when $\theta_E > 90°$, $\theta_w > \theta_E$, which results in increased hydrophobicity in the Wenzel regime, compared to the ideal.

In this regime, the high contact between the solid and liquid means droplets tend to adhere to the surface compared with a similar flat surface. As a result, droplets in the Wenzel regime display high contact angle hysteresis.

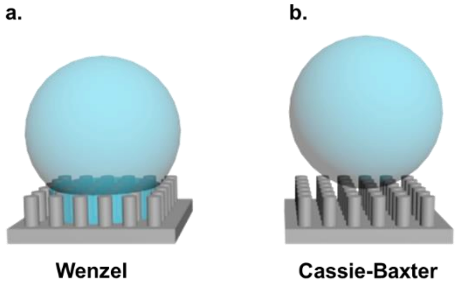

Figure 2 | Schematics of the two wetting configurations on rough surfaces. **a.** The Wenzel model in which the liquid impregnates into the surface texture. **b.** The Cassie-Baxter model in which the droplet sits above the surface texture on a composite solid/air interface.

1.2.2.2 Cassie-Baxter model

The same line of reasoning can be applied to the case with a planar but chemically heterogeneous surface. Here, the droplet sits above the surface structures forming air pockets beneath (Figure 2b). The surface is then assumed to be composed of two species of fractional coverage $\emptyset_1$ and $\emptyset_2$, forming their own contact angles θ_1 and θ_2 respectively, with textures much smaller than the size of the drop. The energy variation associated with moving the contact line by amount *dx*, is:

$$dE = \emptyset_1(\gamma_{SL} - \gamma_{SV})_1 dx + \emptyset_2(\gamma_{SL} - \gamma_{SV})_2 dx + \gamma_{LV}\, dx\, cos\theta^* \qquad Eq.\ 5$$

Again, at equilibrium (when *dE* = 0), together with Young's equation, we obtain the Cassie-Baxter relation:

$$cos\ \theta_{CB} = \emptyset_1 cos\ \theta_1 + \emptyset_2 cos\ \theta_2 \qquad Eq.\ 6$$

As the liquid is assumed to be sitting on a solid-air composite surface, the air sections can be considered to be perfectly non-wetting, thus $\theta_2 = 180$ and so Eq. 6 then becomes:

$$cos\ \theta_{CB} = \emptyset_s(cos\ \theta_E + 1) - 1 \qquad Eq.\ 7$$

Where $\emptyset_s$ is the fractional area of the solid surface with a contact angle of θ_E on the flat solid surface, calculated through:

$$\emptyset_s = \frac{2\pi r^2}{p^2\sqrt{3}} \qquad \textit{Eq. 8}$$

where r = radius of curvature of the tip, p = pitch.

In contrast to the Wenzel regime, droplets display a low contact angle hysteresis due to the reduced liquid-solid contact.

1.2.2.3 Wenzel or Cassie-Baxter?

Having described the two mechanisms which promote hydrophobicity, how does one know which particular mechanism is at play? The fundamental experiment by Johnson and Dettre in 1964 nicely uncovers the two distinct behaviours operating on a wax surface of different roughness (Figure 3). [43] Successive heat treatments enabled them to lower the roughness, however as accurate analysis of the roughness was not performed, the data is qualitative only. Nonetheless it shows clearly the influence of surface roughness on the advancing and receding contact angles. At low r, the advancing angle was observed to increase whilst the receding angle decreases; consistent with Wenzel's model in that, if at zero r the contact angle is < 90°, then increasing r serves to decrease the contact angle (i.e. amplifying the hydrophilicity). However, after reaching a certain threshold of r, both angles jump, and further increases lead to higher receding angles. This transition can then be interpreted as the sudden formation of air pockets (Cassie state). This suggests that at a certain roughness, the energetic cost of creating air pockets is lower than that required to wet the solid.

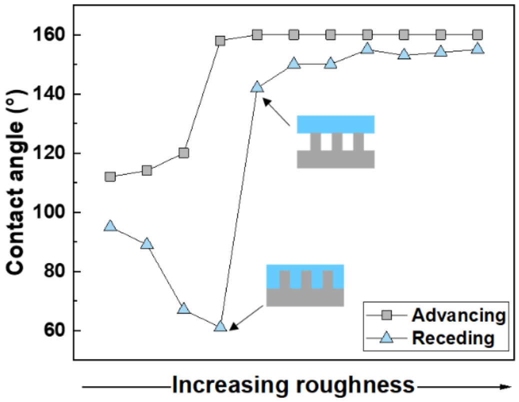

Figure 3 | Advancing and receding contact angles of water drops placed on a wax surface of increasing roughness. Reproduced from experimental data in ref [43].

1.2.3 Achieving superhydrophobicity

Surfaces on which water droplets assume a near spherical shape, and exhibit contact angles greater than 150° are deemed to be superhydrophobic. As mentioned, these surfaces can induce the Wenzel wetting regime; exhibiting characteristically high contact angle hysteresis > 10°. Or alternatively, and most commonly, surfaces induce Cassie-Baxter behaviour with hysteresis < 10°. [44] In order to render a surface superhydrophobic, a combination of surface roughness and a low surface energy is typically required. [45] This can be achieved through either roughening a hydrophobic material, or roughening a hydrophilic material and then applying a low surface energy coating.

To impose a change on the apparent contact angle of a droplet in the Cassie-Baxter regime, there are two parameters that can be tuned according to (Eq. 7): the solid fraction f_s and Young's angle θ_E. Figure 4 explores the relationship of solid fraction on the apparent contact angle for an inherently hydrophilic ($\theta_E = 20°$) and hydrophobic ($\theta_E = 120°$) material. It can be observed that firstly, low solid fractions are crucial for achieving superhydrophobic behaviour and secondly, at these low solid fractions, the difference between the apparent contact angles of the two materials, and hence the contribution of the surface energy, decreases. Thus highlighting the importance of surface structuring.

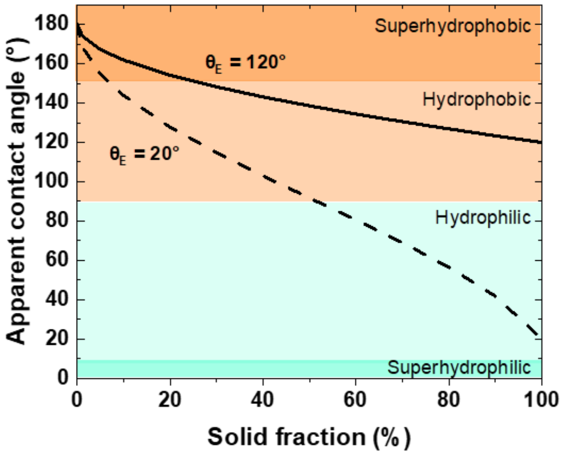

Figure 4 | The relationship between the apparent contact angle and the solid fraction for an ideal Cassie-Baxter state at two values for the Young's contact angle θ_E. The superhydrophobic

(>150°) and hydrophobic (90 – 150°) regions are shaded in deep and light orange respectively, meanwhile the hydrophilic (10 – 90°) and superhydrophilic (<10°) regions are shaded in light and deep turquoise respectively.

Used in this way, the solid fraction and surface energy provide an accurate indication of the water repellence of static droplets. However, for surfaces exposed to real-world conditions where the size of droplets and speed of impact vary, the geometry, spacing and dimensions of the texture play an important role.

1.2.3.1 Repelling raindrops

Raindrops are typically on the order of millimetres (mm) and are thus significantly larger than the size of the surface textures. Owing to the low adhesion of water to the surface, raindrops impacting the surface are able to bounce off. Figure 5 shows a series of snapshots taken as a millimetric water droplet impacts, spreads, recoils and rebounds off the surface.

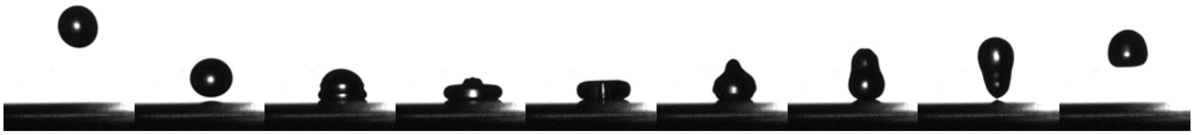

Figure 5 | Snapshots of a water droplet impacting a superhydrophobic surface.

However, the ability of the droplet to rebound off the surface depends on the impact velocity. Too low a velocity, and the kinetic energy ($\rho r^3 V^2$ where ρ is the density, r is the radius of the drop, and V is the velocity) will not overcome the stored surface energy ($\gamma r^2 \Delta cos\theta$ where γ is the surface tension and $\Delta cos\theta$ is the hysteresis).[46] The minimum velocity typically corresponds to release heights of a few mm. This battle between the kinetic and surface energy also dictates that at fixed velocity, the radius of the droplet will influence whether it rebounds or sticks; with lower a radius resulting in the latter.

Turning to higher velocity impacts, the ability of the structures to resist penetration of the meniscus becomes challenging, and at a critical impact velocity the pressure becomes large enough for the interface to curve and touch the base of the structures; transitioning into a Wenzel state (Figure 6a). Here, the dimensions of the structures play a key role. For structures of low h and high p (Figure 6a), the impalement scenario becomes that of a touch down; as the drop pressure increases so does the curvature of the interface. In turn, the height which separates the liquid interface and the base is diminished, and the wetting state transitions into the Wenzel. In this case, the contact angle θ may be lower than the advancing contact angle. By increasing the height of the structures (Figure 6b), at the same interfacial curvature, the 'touch down' scenario does not occur, and instead the critical impalement pressure is induced through a sliding scenario. If the curvature of the interface exceeds the advancing contact angle, the contact line will spontaneously slide downwards. Similarly for structures with a low *p* (Figure 6c), this sliding scenario also occurs, however a far greater interfacial curvature is required in order to exceed the advancing contact angle.

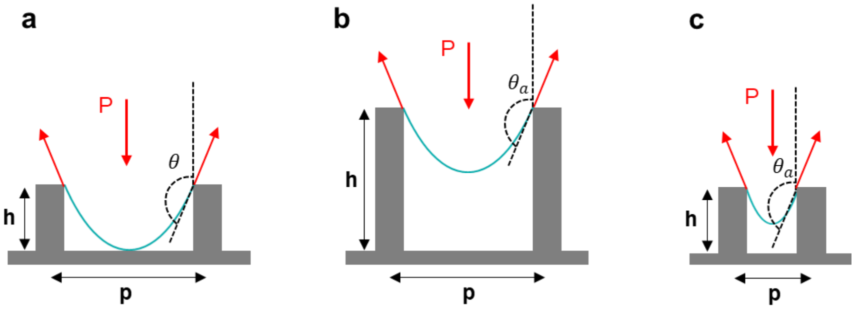

Figure 6 | The effect of array dimensions (height, pitch) on impalement scenarios. **a,** for structures with a low *h* and large *p* the pressure generated by an impacting droplet causes the liquid interface to curve and reach the base resulting in a 'touch-down'. **b,** for structures of greater *h* and equivalent *p*, the additional height protects from the 'touch-down' scenario, and the contact line only advances downwards after the advancing contact angle has been exceeded. **c,** for structures with a reduced *p*, contact line advancing also only occurs once the advancing contact angle has been exceeded, however this requires a greater curvature of the liquid interface.

Transitioning the nanostructure morphology from a nanopillar to a tapered nanocone, the pressure required to force the contact line further down the structures increases with the penetration depth *z* owing to the increase in radius and thus contact area. To estimate the critical pressure required to force the meniscus inside tapered cone, the capillary and hydrostatic forces are balanced to obtain:[47]

$$P_c = \frac{4\pi\gamma r \cos(\theta-\alpha)}{\sqrt{3}p^2-2\pi r^2} \qquad \textit{Eq. 9}$$

Where r is the radius of the structure, θ is the advancing angle on the corresponding smooth surfaces, α is the cone angle, and γ is the interfacial tension of water (7.2 x 10^{-2} N m^{-1}). Plotting the critical pressure as a function of pitch (Figure 7) for nanocones of equal aspect ratio (h/p) reveals that those of reduced pitch require a far greater pressure for the meniscus to penetrate into the structure. Owing to the tapered profile, the critical pressure increases as the meniscus moves further down the nanocones as seen in Figure 7 going from a *z* of 10% to a *z* of 50%.

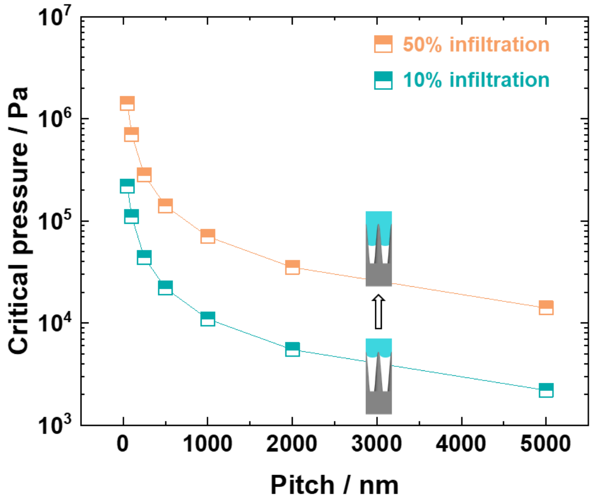

Figure 7 | Critical pressure plotted as a function of pitch for two penetration depths: 10% (blue) and 50% (orange).

As briefly mentioned earlier, the transition from the Cassie to Wenzel state is not just induced by high speed impacts, the radius of the droplet also alters the propensity to transition. This therefore concerns the ability of superhydrophobic structures to repel fog or work under humid conditions which we now discuss.

1.2.3.2 Antifogging behaviour

Condensation is the process upon which there is a change in the physical state of water from a gas phase into a liquid phase. This phase change occurs when hot air comes into contact with a cold surface which consequently cools the air. This cooled air holds more water vapour than is allowed by equilibrium and thus water spontaneously transfers from a vapour to a liquid. Condensation is initiated by the nucleation of water molecules; forming molecular clusters which grow as more molecules condense. This becomes a problem for many reasons pertaining to reduced optical transparency. Controlling fogging through passive means relies on tuning the wetting characteristics of the surface and two distinct strategies can be employed: encouraging wetting ($\theta_{adv} < 10°$) so that a thin uniform film is formed, or discouraging wetting ($\theta_{adv} > 150°$) so that nucleating droplets are repelled from the surface. Whilst the former is considerably easier to achieve[48] with a wealth of literature,[49,50] the latter may be necessary for when formation of a liquid film is detrimental (integration with electronics, or phase-change heat transfer[51]).

Studies into fog-repelling surfaces are much fewer in number, likely due to their more challenging fabrication and more complex anti-fogging mechanism. On lotus leaf structures and some micrometric structures – where structural features are of comparable size to the nucleating droplets – it has been observed that water nucleation often begins within the cavities of the structuring, and thus, as the nuclei grow and coalesce, a Wenzel state is formed; which destroys the water repellent properties.[52,53] However, this is not a problem that plagues all superhydrophobic surfaces; in 2009 Boreyko and Chen discovered that on nanostructured or hierarchical superhydrophobic surfaces, a new phenomenon occurs, whereby neighbouring condensed droplets coalesce and jump from the surface.[54] Subsequently a number of other studies have shown that scaling down the texture size proves effective.[55,56] In particular, nanocones, which are found on the wing of the cicada (Figure 8), have been shown to dispel fog with extremely high efficiency (>90%).[16]

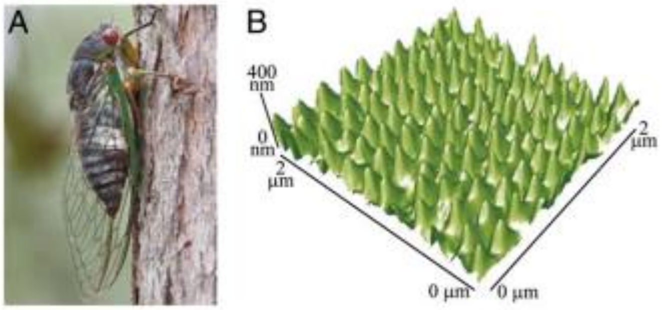

Figure 8 | a, Photograph of the cicada resting on a branch. **b,** An AFM image of the nanostructures present on the wing of the cicada. Image reproduced from K. M. Wisdom *et al.*, PNAS, 2013, 110, (20) 7992-7997 with permission. [57]

So far it has been assumed that this spectacular property originates from the combination of texture scale (sub-micrometre), shape (conical) and density (dense array). Experiments by Mouterde *et al.* compared two surfaces: (i) one comprising silicon pillars with a pitch of 52 nm and height 88 nm; (ii) the other comprising silicon nanocones with the same pitch, and a height of 115 nm.[16] The study showed that the surface with nanopillars exhibited a very low antifogging ability (~ 0.2%), whilst the nanocones exhibited much greater antifogging ability (~90%). The significant difference in performance was hypothesised to be due to the nanocones maintaining a Cassie state; with the tapered landscape preventing droplets from being pinned within the texture, unlike the nanopillars which have straight walls. However systematic experiments to verify this hypothesis are lacking, but will be discussed in the later chapters.

1.2.3.3 Slippery Liquid Infused Porous Surfaces

The self-cleaning phenomenon of superhydrophobic surfaces has been widely studied and achieved in a range of different materials. These lotus leaf-inspired structures, as discussed earlier, provide excellent self-cleaning performance under many different environmental conditions. However, for certain applications where oil-repellence is required, or physical damage to the surface is expected, superhydrophobic surfaces face several limitations.

Therefore, since their introduction in 2011, there has been an upsurge of interest in pitcher plant-inspired surfaces, known as Slippery Liquid Infused Porous Surfaces (SLIPS).[58] This family of non-wettable surfaces which comprise a thin lubricating layer trapped within surface roughness, resides at the forefront of the literature, having consistently been shown to succeed where their gas-cushioned counterparts fail; in repelling organic liquids or complex mixtures with low surface tension, sustaining no damage under physical stress, and an ability to self-heal.[59,60] Prized for their anti-adhesive nature, SLIPS bestow interfacial properties that are highly desired across a broad range of applications including anti-icing,[61,62] drag-reducing properties,[63] heat transfer,[64] anti-fouling coatings in the marine[65] and medical sectors,[66,67] non-stick packaging,[68] and droplet manipulation.[69]

To achieve liquid repellence, SLIPS essentially exploit the immiscibility of lubricants with other liquids. A low surface energy lubricant is infused into the surface structure, and the lubricant forms the interface with the immiscible working liquids (e.g., water, ethanol), as opposed to the solid surface, thus resulting in very low contact angle hysteresis (minimal adhesion). In order to attain these properties, three criteria need to be met: (i) the solid substrate must have a higher affinity for the lubricant over the droplet, (ii) the lubricant and the working fluid must be immiscible, (iii) the lubricant must wick into, spread and stably adhere within the structure.[58,70] The prime source of failure for SLIPS lies in this third criterion and the poor ability of the structure to retain the lubricant leading to drainage of the lubricant layer causing contact line pining of the working fluid on the exposed solid structures.[71,72]

Whether or not a solid will be preferentially wetted by Liquid A (immiscible liquid to be repelled) or Liquid B (lubricant), can be predicted experimentally by comparing the total interfacial energy of the individual wetting configurations (Figure 9).[58] Here, there are three possible configurations; configuration A refers to the state where the structured solid is completely wetted by Liquid A; configurations 1 and 2 refer to the states where the structured solids are completely wetted by Liquid B with (1) and without (2) Liquid A present.

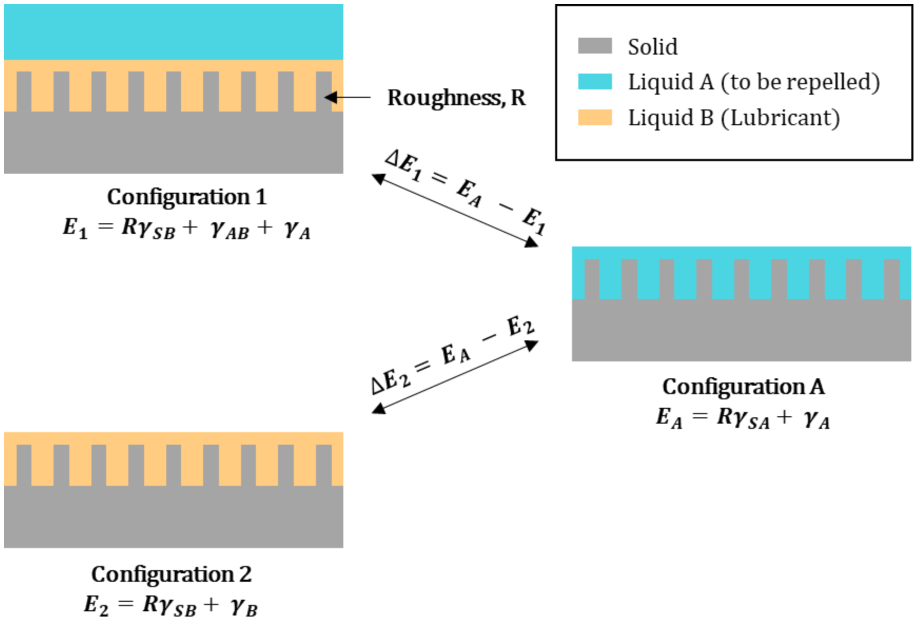
Solid
Liquid A (to be repelled)
Liquid B (Lubricant)
Roughness, R
Configuration 1
$E_1 = R\gamma_{SB} + \gamma_{AB} + \gamma_A$
$\Delta E_1 = E_A - E_1$
$\Delta E_2 = E_A - E_2$
Configuration A
$E_A = R\gamma_{SA} + \gamma_A$
Configuration 2
$E_2 = R\gamma_{SB} + \gamma_B$

Figure 9 | Wetting configurations for a SLIPS surface. Configuration A refers to the state where the structured solid is completely wetted by Liquid A. Configurations 1 and 2 refer to the states where the structured solids are completely wetted by Liquid B with (1) and without (2) Liquid A present. E_1, E_2, and E_A represent the total interfacial energies per unit area of the corresponding wetting configurations. γ_{AB}, γ_{SA}, γ_{SB}, γ_A, and γ_B represent the surface energies of the respective interfaces. R represents the surface roughness.

It is therefore necessary to find the conditions under which configuration A is always the higher energy state than 1 and 2. Taking the example of configuration 1, for this to be true, we have $E_A - E_1 > 0$, which further expands to:

$$R(\gamma_{SA} - \gamma_{SB}) - \gamma_{AB} > 0 \qquad \text{[Eq. 10]}$$

To reduce this to measurable quantities, we can use Young's equation to obtain

$$R[(\gamma_S - \gamma_A cos\theta_A) - (\gamma_S - \gamma_B cos\theta_B)] - \gamma_{AB} > 0 \qquad \text{[Eq. 11]}$$

which can be simplified to:

$$\Delta E_1 = R(\gamma_B cos\theta_B - \gamma_A cos\theta_A) \ - \gamma_{AB} > 0 \qquad \text{[Eq. 12]}$$

The same approach is taken for ΔE_2 to obtain:

$$\Delta E_2 = R(\gamma_B cos\theta_B - \ \gamma_A cos\theta_A) - \gamma_A - \gamma_B \ \ > 0 \qquad \text{[Eq. 13]}$$

where θ_B and θ_A are the Young's contact angles of the lubricant and water on the solid surface.

Satisfying both [Eq. 12] and [Eq. 13], will ensure the formation of a theoretically stable lubricant film. Exploiting the physical interaction between the lubricant and the structure is therefore, crucial for its retention, and will be explored in a later chapter.

1.4 Photon management

Photon management properties such as transparency and haze (for non-absorbing materials), and antireflectivity/absorption (for non-transparent materials) are important for increasing the amount of light going into or coming out of the device. For displays and touch screens, high transmittance and low haze are required for clarity of text and images. Meanwhile for solar cells, increasing the absorption of light within the absorption wavelength band boosts the efficiency of such devices.

1.4.1 Antireflectivity

Reflections occur at flat interfaces between two materials with differing refractive indices n_1 and n_2. The reflectance R at the interface is defined as the fraction of incident power that is reflected. At normal incidence, the reflectance for a surface in contact with air (n_{air} = 1) is represented by the following Fresnel equation:

$$R = \frac{(n_1 - 1)^2}{(n_1 + 1)^2} \qquad \textit{Eq. 14}$$

For glass with n_{glass} = 1.46, the contrast in the refractive index between glass and air (Figure 10a) gives rise to R = 3.5%. For high index-contrasting materials such as Si ($n_{silicon}$ = 3.44) the flat-interface reflectance can be considerably higher (R = 30.2%).

Antireflective coatings (ARCs) have been developed to reduce reflectance and increase transmittance, and are based around three concepts: single-layer interference, multi-layer interference and a graded refractive index. Single layer ARCs (Figure 10b) typically comprise a homogenous layer with a thickness equal to a quarter of the wavelength of light, and with a refractive index of $\sqrt{\boldsymbol{n_s}}$ (where $\boldsymbol{n_s}$ = refractive index of substrate). As light hits the surface, the two interfaces produce two reflected waves, and destructive interference occurs when these two waves are out of phase. However these coatings are specific to a certain wavelength, angle and polarisation of light.[73] Furthermore, for glass substrates, finding a material which has a refractive index $\sqrt{\boldsymbol{n_{glass}}}$ = 1.22 is challenging. Therefore, the performance is often compromised, as magnesium fluoride is the most commonly employed material with $\boldsymbol{n_{MgF2}}$ = 1.38. Multi-layer interference films (Figure 10c), otherwise known as Distributed Bragg Reflectors (DBRs) operate *via* the same principle, however they comprise of alternating layers of high and low refractive index materials to provide greater broadband antireflection.[74] Similarly each layer has to be of a certain refractive index and thickness in order to achieve the destructive interference as light waves are reflected from each interface.

An alternative approach to antireflectivity, which does not rely on finding suitable materials with specifically tuned refractive indices or ensuring precise control over the thickness of each layer, is inspired by ‘moth eyes’ and based on micro- and/or nano-structuring the surface. Depending on the scale of the structures, different mechanisms operate.[75] If the structures are larger than the wavelength of light, the light is reflected and scattered, leading to reduced transmission (for glass) or increased absorption (for silicon). If the structural dimensions are of the same scale as the wavelength of light, the light gets trapped within the gaps and undergoes multiple internal reflections; with incident radiation being transmitted or absorbed and thus leading to low levels of reflections. However, if the structures are of dimensions much smaller than the wavelength of light (nanoscale) the light tends to bend progressively, having the effect of a gradient refractive index (Figure 10d). Such surfaces exhibit broadband, omnidirectional and polarisation insensitive antireflectivity; outperforming that of layered films.

In a controlled laboratory environment, all the aforementioned ARCs may satisfy the reflectance requirements for an application, however upon contamination or fogging, light waves scattering and reflecting off these contaminants can significantly deteriorate the performance. Thus, the multifunctionality provided by nanostructuring ensures performance longevity through the ability to self-clean and rid the surface from contaminants.[76]

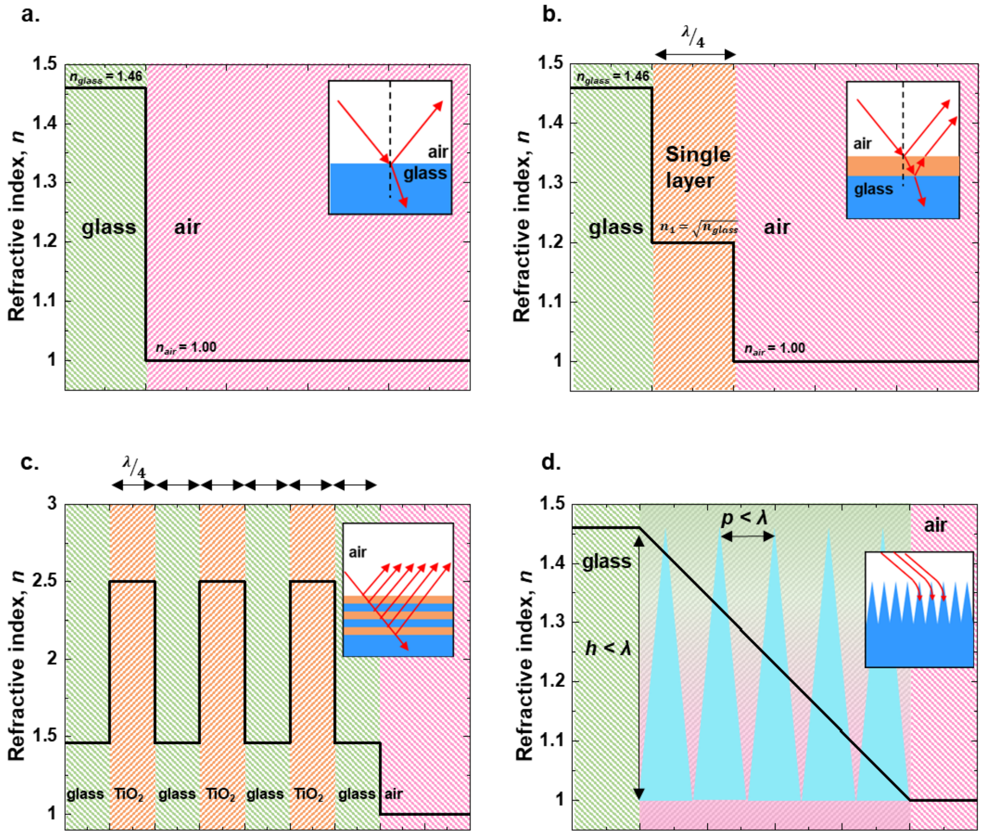

Figure 10 | Representation of the refractive index profiles at the interface glass/air interface with and without antireflective coatings. Insets schematically demonstrate the propagation of light. **a,** Step-discontinuity in refractive index that occurs at the bare glass/air interface with n_{glass} = 1.46 and n_{air} = 1.00. **b,** Glass/air interface with a single layer film of $\boldsymbol{n_1 = \sqrt{n_{glass}}}$ and thickness $\boldsymbol{\lambda/4}$. **c,** Distributed Bragg reflector consisting of multiple layers of alternating materials (SiO_2 and TiO_2) with varying refractive index. **d,** Glass surface structured with nanocones (blue) with dimensions (height *h* and pitch p) smaller than the wavelengths of visible light. The nanocones create a graded refractive index profile with air.

1.5 Bactericidal action

Strategies to prevent microbial colonisation on surfaces have never been more important. Typically, eradicating microbes has been achieved through the use of chemical agents, but with their continued misuse, microbes are evolving to survive such treatments. As such, antimicrobial resistance (AMR) heralds a serious global health epidemic, and unlike the COVID-19 pandemic, the perpetrators are well-known; for example methicillin-resistant *Staphylococcus aureus* (MRSA) which is responsible for the vast majority of hospital-acquired infections.[77,78] This resistance has been heightened by MRSA’s propensity to form bio-films; here, bacteria grow in very high densities making it harder for antibiotics to penetrate the matrix of bacteria, whilst simultaneously enabling horizontal gene transfer of antibiotic resistant genes.[79] As a consequence, infections caused by *S. aureus* bio-films are very challenging to treat.[80] Its formation on medical implants is of particular concern, and with the increasing number of implants fitted in hospitals each year, it is heading in a dangerous trajectory.[81]

Nature, with its limited resources, has developed its own smart way of dealing with microbial colonisation. This was revealed recently while investigating the adhesion of *Pseudomonas aeruginosa* on the wings of a species of cicada.[7] Here, it was found that the surface of the wing was deadly to the bacterial cells, and upon inspection *via* electron microscopy, it was discovered that nanopillars present on the surface of the wing were penetrating the cells, causing cell lysis within minutes of contact. As the action is purely mechanical and non-selective, these surfaces have the potential to overcome multidrug-resistant bacteria.[79] Since this discovery, synthetic analogues have been made in materials ranging from silicon (Figure 11)[14,82,83] to titanium.[79] However, the exact mechanisms of bacteria cell death and optimal topographies are still poorly understood; likely owing to the lack of systematic studies capable of isolating and quantifying the effect of the many variables involved.[84]

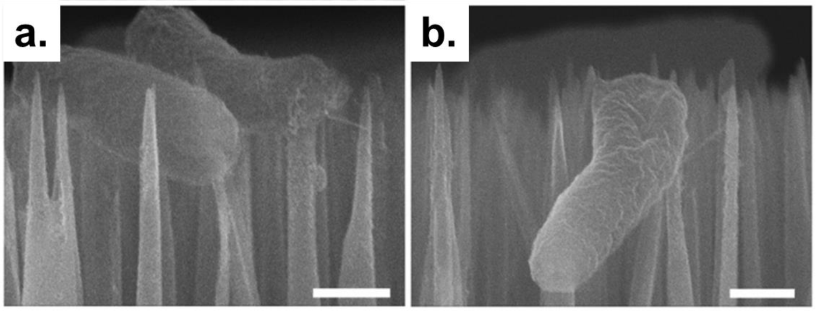

Figure 11 | SEM images (titled at 90°) of *E. coli* on a black silicon surface with sharp nanopillars, at different stages of interaction. **a,** The *E. coli* is pierced by the sharp nanopillar leading to; **b,** cytoplasm leakage and cell rupture. The *E. coli* have a diameter of 0.5-1 µm and length 1.7-2.5 µm, and the nanopillars have a length of 3.6 µm. Scale bars = 500 nm. Adapted with permission from reference [14].

These variables include pillar spacing,[85] height,[82] tip angle,[86] geometry,[14] and material/elasticity.[82,87] Predicting the antibacterial properties through variation of these parameters and cellular features (rigidity/motility)[88] is highly complex. The non-trivial simulations have led to models which propose often opposite design criteria, with ambiguity concerning pitch but general agreement on the merits of sharper tips.[89] One such model by Liu *et al.*, treats the interfacial energy as the driving force promoting bacteria to migrate into the nanostructure, and investigates the effect of pillar dimensions on bacterial rupture.[90] The outcome of the interactions between nanopillars (d = 30 nm and p = 300-60 nm), and a bacillus bacteria cell (l = 2 µm and d = 0.5 µm) is seen in Figure 12.[90] It can be deduced that, for a bacteria of this size, as the pitch increases there is a transition from ‘no deformation’ to ‘elastic deformation’ and then to ‘creep deformation’; as a result of a greater pressure being applied on the cell by a few nanopillars, as opposed to distributing the pressure over many nanopillars. Furthermore, there is a dependence on the height; insufficient height will allow the cells to gradually deform (creep deform) to the base of the nanopillars and remain there unruptured.

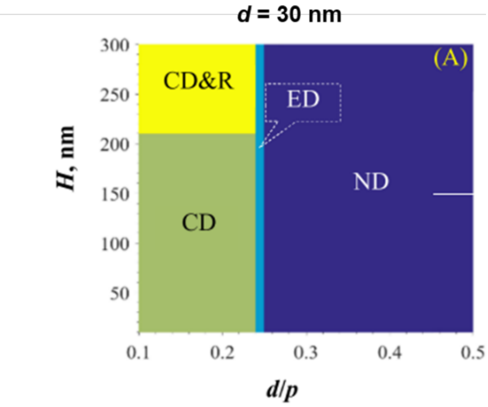

Figure 12 | Calculations based on the interfacial energy gradient as the driving force for bacterial migration into the nanostructure, highlighting the influence of nanopillar parameters on cell deformation. Abbreviations: ND = no deformation; ED = elastic deformation; CD = creep deformation; CD&R = creep deformation & rupture. Bacterial cell length = 2µm, diameter = 0.5 µm. Adapted with permission from T. Liu, Q. Cui, Q. Wu, Mechanism Study of Bacteria Killed on Nanostructures, J. Phys. Chem. B, 2019, 123, 8690. *Copyright © 2019, American Chemical Society*.[90]

However, it is important to note that bacterium of smaller size require a lower pitch to ensure that they do not settle within the spacing between nanopillars. Fabricating nanostructures of reduced pitch to target smaller bacteria (e.g. *S. aureus*), particularly in transparent materials, remains a relatively untouched area of research; but one which could have a significant impact on controlling microbial accumulation on displays, and hospital equipment for instance.

1.6 Fabrication requirements

Nanostructures capable of achieving special wettability, photon management and antibacterial activity are not trivial to fabricate. One class of nanostructures capable of repelling water at the millimetric[91] and micrometric[16] scale, achieving very low reflectivity[92] and inducing bacterial cell lysis,[14] is the nanocone. These structures have been successfully fabricated in the past and have proven to deliver high-performance functionalities, however routes to their fabrication remain limited; with either scalable techniques but poor control, or high control but costly and time-consuming processes, as will be discussed in the subsequent chapters. By taking advantage of controlled processing, more complex structures can then be realised which can lead to more exotic surface phenomena.

1.7 Thesis outline

Having introduced the key surface functionalities and their importance for industrial and commercial application, the following chapter will discuss the current fabrication techniques through which these structures are achieved. The literature review begins by investigating different lithographic methods to generate polymeric etch masks; highlighting the limitations in resolution, throughput and cost. Keeping in mind the different lithographic processes, the second half of the literature review focusses on the process of transferring the polymeric etch-pattern into the underlying layers of two industrially useful materials: silicon and glass. It is during this process that the issue of multi-step/complex processes arises, particularly when it comes to high-resolution and high-aspect ratio etching, and therefore the current strategies to mitigate this are discussed. The subsequent chapters are adapted from published (or nearly published) work, and concentrate on distinct pattern transfer methods into silicon or glass to generate a specific nanostructure, and showcase the functionality of the surfaces produced. The work carried out for these published chapters has been a collaborative effort, and I have many parties to thank for their incredible work and knowledgeable insight.

2

LITERATURE REVIEW: PRECISE NANOPATTERNING

In the first half of this chapter, I review different lithographic techniques reported in the literature for the generation of polymeric etch-masks; highlighting their limitations in terms of mask dimensions, process cost, complexity and reproducibility. In the second half, I review the processes currently used to transfer the pattern of the etch-mask into the underlying silicon or glass substrate; placing emphasis on simplicity, control and reproducibility.

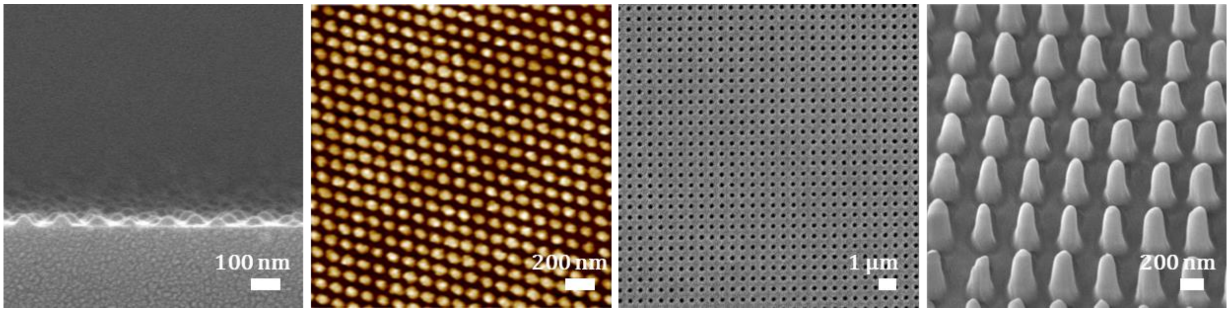

Nanopillars and nanoholes of varying pitch generated through block copolymer lithography (left), laser interference lithography (centre left, centre right), and nanoimprint lithography (right).

2.1 Introduction

Nanofabrication techniques can be categorised many different ways: through the tools used, the resolution attainable, or based on whether the nanostructure construction has been from the bottom-up or top-down. It is worth noting however, that nanofabrication schemes are often a combination of several different processes. As this thesis focusses on precise/controlled nanostructuring, the fabrication schemes comprise two key steps, and therefore the literature review will be split into: (i) lithographic techniques to generate an etch mask, and (ii) pattern transfer processes, to obtain ordered, precise nanostructures for surface multifunctionality.

The lithographic process dictates the pitch and morphology of the pattern, whilst the transfer process dictates the aspect ratio and structural complexity. During the pattern transfer into the underlying substrate, each material presents its own set of challenges owing to differences in etch resistivity, and therefore the latter section is separated into glass and silicon etching. Particular attention is paid to nanopillar/nanocones; as these structures provide broad multifunctionality.

Throughout the literature review and subsequent fabrication chapters, there are a number of common themes, and certain criteria to meet in terms of nanostructure characteristics (high resolution, high aspect ratio, controlled shape) to ensure multifunctionality, as well as consideration for the ease of processing (scalability, simplicity, versatility, cost).

2.2 Nanolithography

Lithography is the process used to create a (typically polymeric) pattern on top of a substrate. The ability to structure polymeric materials has accelerated over the past several decades, culminating in a vast palette of different techniques (Figure 13) with different resolutions, costs and throughputs. This makes it difficult to summarise their limitations and qualities as the field is constantly changing, and boundaries are constantly being challenged. However, there are overarching qualities and limitations when focussing on the requirements for surface multifunctionality.

Mask photolithography has been a crucial technique within the microelectronics industry, and occurs when a mask, which has a pattern of transparent and opaque areas, is transferred to a photosensitive layer through irradiation.[93] The resolution of mask lithography is however limited by the diffraction of light, and also requires expensive equipment and costly masks; thus for multifunctional surfaces, where patterns are typically uncomplicated periodic arrays, photolithography has several limitations. Electron beam (EBL) and Focussed Ion beam (FIB) lithography are also considered conventional techniques, and can reach greater resolution than photolithography. The two operate in a similar way; for EBL, a focussed beam of electrons gets scanned across the surface which is covered in an electron sensitive material, to draw custom shapes. Whereas for FIB, it is a focussed beam of ions. FIB also has the ability to locally mill or deposit material, and as the ions are heavier than photons or electrons, and have a smaller wavelength, the resolution of the pattern is greater than that produced by EBL. Nonetheless, these techniques are notoriously costly and low-throughput, and are hence not suitable for large-scale production.

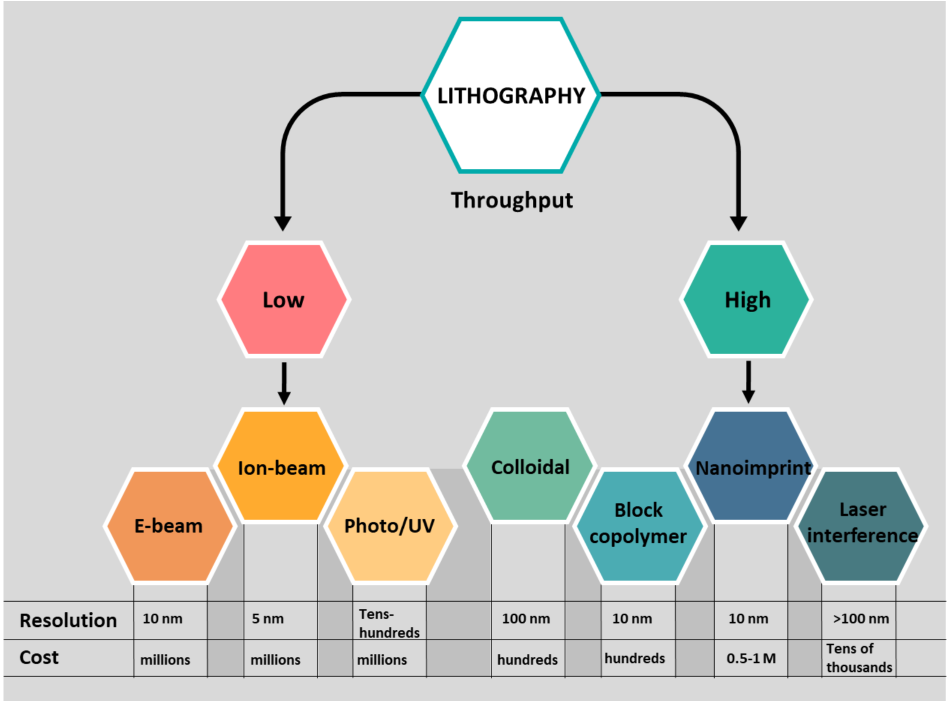

	E-beam	Ion-beam	Photo/UV	Colloidal	Block copolymer	Nanoimprint	Laser interference
Resolution	10 nm	5 nm	Tens-hundreds	100 nm	10 nm	10 nm	>100 nm
Cost	millions	millions	millions	hundreds	hundreds	0.5-1 M	Tens of thousands

Figure 13 | Schematic showing the key nano-lithographic techniques, delineated by the method throughput. Pattern resolution and approximate cost of equipment is listed below.

For many surfaces which do not require customised, computer aided design (CAD) patterning, alternative techniques offering greater throughput at lower costs have been gaining in popularity, for instance colloidal, nanoimprint, block copolymer and laser interference lithography. Particularly for multifunctional surfaces, these techniques provide access to a range of different pitches and morphologies, and can be applied on cm-m^2 length scales.

2.2.1 Colloidal lithography

Synthesising monodisperse colloidal particles can easily be achieved through wet chemistry means such as emulsion polymerisation and sol-gel synthesis.[94] Polystyrene (PS) and silica (SiO_2) are the most commonly synthesised nanoparticles, and owing to the monodispersity in size and shape, they can readily self-assemble into long-range ordered 2D and 3D arrays with hexagonal packing. There are a whole host of routes through which to obtain these colloidal crystals; vertical deposition,[95] dip-coating,[96] and spin-coating,[97] to name a few. Once assembled, the resultant films display a characteristic iridescence (Figure 14b) which arises from the Bragg reflection of light by the periodic structures.

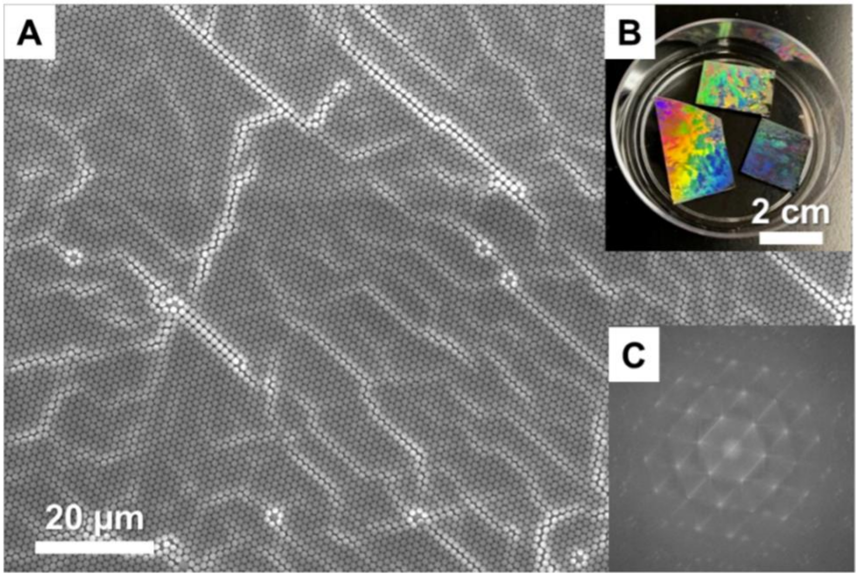

Figure 14 | Colloidal lithography using polystyrene nanospheres. **a,** SEM image of close-packed 1μm polystyrene nanospheres. **b,** Photograph of the Si wafers covered by the monolayer of PS nanospheres. **c,** Fast Fourier Transform (FFT) image of the SEM image. Reprinted with permission from X. Xu, Q. Yang, N. Wattanatorn, *et al*., Multiple-Patterning Nanosphere Lithography for Fabricating Periodic Three-Dimensional Hierarchical Nanostructures, ACS Nano, 2017, 11, 10384-10391 *Copyright © 2017, American Chemical Society.* [98]

The pitch of the nanostructures is controlled by the diameter of the nanospheres. For larger nanoparticles (> 200 nm), the films display good uniformity with large crystal domains (few cracks). And whilst there have been demonstrations of nanoparticles with diameters of 130 nm,[99] for sub-100 nm pitch, controlling the domain sizes of colloidal crystals, the orientation and pattern order is challenging, and requires more sophisticated techniques such as template assisted self-assembly to ensure long-range order.[100,101] This has been highlighted as one of the key weaknesses of colloidal lithography, when compared to other lithographic techniques,[102] alongside the high density of defects.[103]

Owing to the reduced pitch and high uniformity required for some targeted surface functionalities, colloidal lithography was not pursued as a etch-mask generating technique.

2.2.2 Nanoimprint lithography

Thermal embossing, in one form or another, has been around since the early Mesopotamian civilizations, however it was not until 1995 that this technique was adapted to nanometre length-scale patterns by Chou *et al.*, when they successfully demonstrated the replication of sub-25 nm vias and trenches with a depth of 100 nm.[104,105] Unlike other lithographic techniques, nanoimprint lithography (NIL) operates through mechanical deformation; using heat and pressure to induce a pattern transfer from a rigid mould to a thermoplastic polymer film. As the process is not reliant on light diffraction, NIL can achieve very high-resolution patterns; as low as 10 nm.[104,106] This resolution, combined with the simplicity, low-cost and high-throughput, make NIL a very attractive alternative to conventional techniques.

Since this resurgence of interest in imprinting technologies in 1995, many different types of NIL systems have since been developed. Thermoplastic NIL (T-NIL), the original technique developed by Chou *et al.*, remains very popular and operates by spin-coating a layer of imprint resist onto a substrate, and bringing into contact a mould with a predefined topological pattern (Figure 15a). By applying a certain pressure and heating the resist to above the glass transition temperature, the mould is pressed into the softening film. Once cooled, the mould is separated, and the inverse pattern is left on the substrate.

A variation on the original is UV-NIL (Figure 15b), which involves imprinting a transparent mould onto a layer of photo-sensitive polymer and curing using UV light to induce cross-linking and hardening. The imprint mechanism is very similar to T-NIL, however does offer several advantages in that it can be conducted at room temperature and thereby eliminates any problems resulting from thermal expansion variations between the mould, substrate and resist. [107,108]

A further advance in imprinting technology has been brought about by the Obducat system which enables Simultaneous Thermal and UV (STU) curing (Figure 15c). This is not the only difference however, as Obducat also employ their proprietary Intermediate Polymer Stamp (IPS). This enables the same pattern (as opposed to the inverse) to be replicated into photoresist, and increases the lifespan of the master stamp by preventing rigid-mould to rigid-substrate imprinting. Unlike other flexible polymer films which suffer from local deformations and consequently resolution issues, IPS has been proven to imprint 17 nm features.[109] During the pattern transfer from the IPS, the UV curable thermoplastic pre-polymer resist is heated at a constant temperature to soften and infiltrate the IPS pattern. UV exposure crosslinks and solidifies the resist, thereby negating the need to cool down prior to mould lifting.

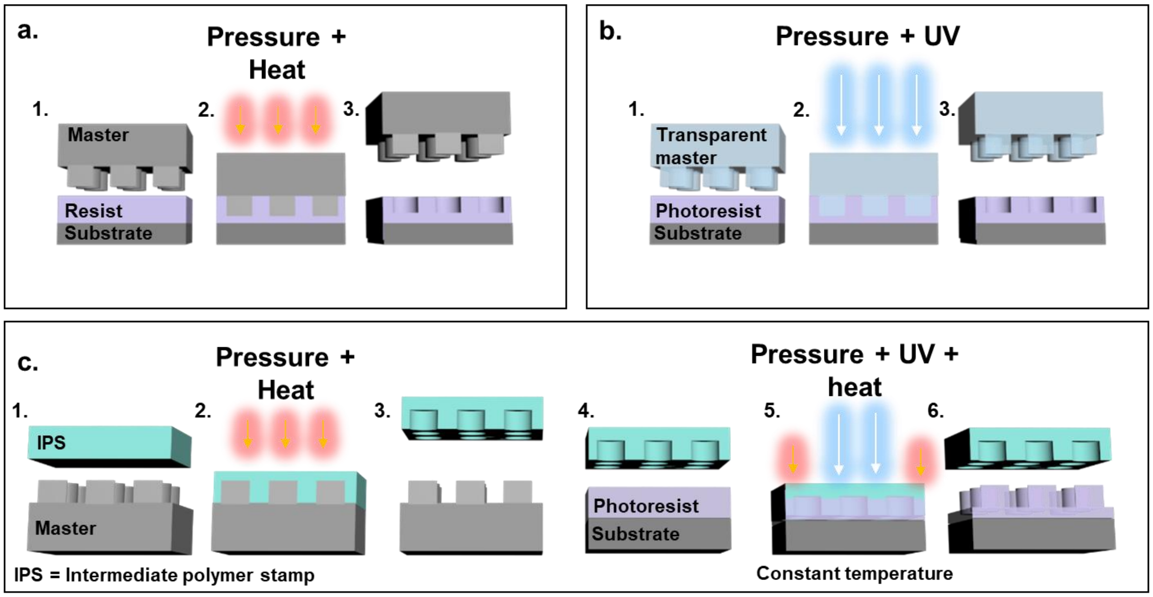
a.
Pressure + Heat
1.
Master
Resist
Substrate
2.
3.
b.
Pressure + UV
1.
Transparent master
Photoresist
Substrate
2.
3.
c.
Pressure + Heat
1.
IPS
Master
2.
3.
4.
Photoresist
Substrate
Pressure + UV + heat
5.
6.
IPS = Intermediate polymer stamp
Constant temperature

Figure 15 | The three common nanoimprinting techniques. **a,** Thermal NIL (T-NIL); **b,** UV-NIL; **c,** Simultaneous Thermal and UV NIL (STU-NIL)

One of the key advantages of NIL, is the ability to up-scale. Whilst laboratory research is conducted using plate-to-plate systems, increasing the throughput can be achieved using roll-to-plate[110] or roll-to-roll systems,[111,112] making NIL a highly promising solution for industrial-scale nanomanufacturing.

2.2.3 Block copolymer lithography

Block copolymers (BCPs) also offer an attractive patterning route for the generation of etch masks owing to their ability to phase separate and self-assemble into micelles; forming regular patterns at dimensions from sub-10 nm up to hundreds of nanometres. [113] They can be controlled to form a range of different morphologies (spherical, cylinders, lamellae etc.), therefore making it a tuneable, high-resolution technique to generate etch masks, that is also scalable and cost-effective. [114]

Self-assembly is defined as a process in which components in a disordered system form an organised structure because of specific, localized interactions among the components. The self-assembly process is governed, predominantly, by the underlying thermodynamics of the system and can take place either in the bulk phase, thin films, or in solution.

Bulk self-assembly

In the bulk phase and in thin films, BCPs micro phase separate due to the inherent immiscibility of the different polymer segments resulting in morphologies with domain sizes of around 10-100 nm.[115] The phase behaviour of bulk BCPs is dictated by three experimentally controllable factors: the degree of polymerisation N, the composition (monomer volume fraction of the minority block f), and the Flory-Huggins interaction parameter χ_{AB}.[113]

The Flory-Huggins interaction parameter describes the free energy cost per monomer of contacts between A and B monomers and is defined as:

$$\chi_{\mathrm{AB}} = (z/K_{\mathrm{B}}T)[\varepsilon_{\mathrm{AB}} - 0.5(\varepsilon_{\mathrm{AA}} + \varepsilon_{\mathrm{BB}})] \qquad \textit{Eq. 15}$$

Where Z is the number of nearest neighbour monomers to a copolymer configuration cell, K_BT is the thermal energy and ε is the interaction energy per monomer. Positive χ_{AB} indicates a net repulsion between species A and B whereas a negative χ_{AB} indicates a free energy drive towards mixing.[116]

χ_{AB} multiplied by N represents the interaction per chain and gives an indication of how compatible the two blocks are and whether they will microphase separate. $\chi_{AB}N$ is often plotted as a function of f to produce a phase diagram, an example of which is shown in Figure 16. This demonstrates how the segregation strength and volume fraction influences the most thermodynamically stable morphology. The phase behaviour of BCPs in the bulk is well understood both theoretically and experimentally.[117–119]

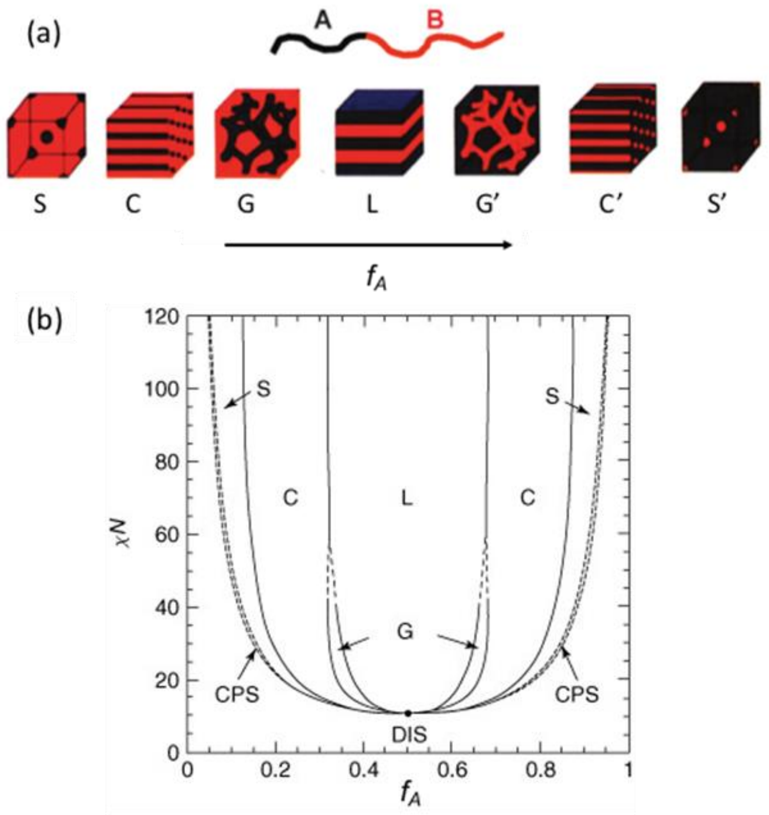

Figure 16 | a, Equilibrium morphologies of AB diblock copolymers in bulk, where S and S' = body-centred cubic spheres, C and C' = hexagonally packed cylinders, G and G' = bicontinuous gyroids and L = lamellae. **b,** Theoretical phase space diagram of AB diblocks predicted by self-consistent mean field theory which depends on the volume fraction f of the blocks and the segregation parameter χN where χ is the Flory-Huggins parameter and N is the degree of polymerisation. CPS and CPS' = closely packed spheres. Reproduced from F. Bates, G. Fredrickson, Physics Today, 1999, 52 (2), pp. 32 with the permission of the American Institute of Physics.[116]

Solution phase self-assembly

The introduction of solvents increases the level of complexity for BCP self-assembly. For example, in a solvent–non-solvent mixture, six χ parameters are involved; namely χ_{AB}, χ_{AS}, χ_{AN}, χ_{BS}, χ_{BN}, χ_{SN} where S represents the good solvent for both blocks and N denotes the non-solvent (selective solvent) for one of the blocks. Thus, when the BCPs are in a solvent–non-solvent mixture, they can self-assemble into core-shell nanostructures (micelles). The formation of micelles requires the presence of two opposing forces, i.e. an attractive force between the insoluble blocks, which leads to the aggregation, and a repulsive force between the soluble corona blocks that prevents unlimited growth of the micelle into a distinct macroscopic phase.

The three key thermodynamic contributions that govern micelle morphology are: (i) the extent of stretching of the core-forming blocks, (ii) the interfacial tension between the insoluble micelle core and the solvent, andc(iii) the repulsive interactions between coronal chains.[120] Therefore adjusting factors that affect these contributions, such as BCP composition (block ratio, block length, block chemistry), BCP concentration and the ratio of common solvent to non-solvent allows control over micelle morphology. However, additional factors such as low molecular weight, partial crystallinity or the addition of surfactants or core-soluble additives may direct the self-assembly process to the formation of unexpected or more complex morphologies.

2.2.3.1 Conventional BCP lithography

In a typical BCP lithography process, the self-assembly into distinct domains occurs after the BCP has been deposited onto the surface as a thin film. As such, to ensure the domains orient and align correctly, a non-preferential layer (neutral surface for both blocks) first needs to be deposited (Figure 17a; step 2). [121,122] Subsequently, the BCP thin film is cast atop this layer, however as a result of the rapid and local phase-separation, the as-cast film is often kinetically trapped in a non-equilibrium disordered state. To adopt the highly regular structures expected, the mobility of the polymer chains needs to be increased to allow for reorganisation. In some systems, simple thermal annealing is sufficient, whereby the film is heated to above the glass transition temperature (Tg) of both blocks. However, for higher molecular weight systems, solvent-vapour annealing (SVA) is necessary. During SVA, the film is exposed to the vapour of one or more solvents at a temperature below the Tg of both blocks to form a swollen and mobile film which, upon solvent evaporation, reorganises into the equilibrium or metastable nanodomains. [123] The repeatability of SVA can be limited, especially if the desired morphology is a metastable state as the reorganisation can be drastically affected by factors such as swelling rates and swelling ratios. [124] Having obtained a BCP thin film with distinct and ordered domains, one block is selectively etched to expose the regions of the underlying substrate to be removed. Commonly used BCPs include poly(styrene-*block*-methyl methacrylate) and poly(styrene-*block*-dimethylsiloxane).

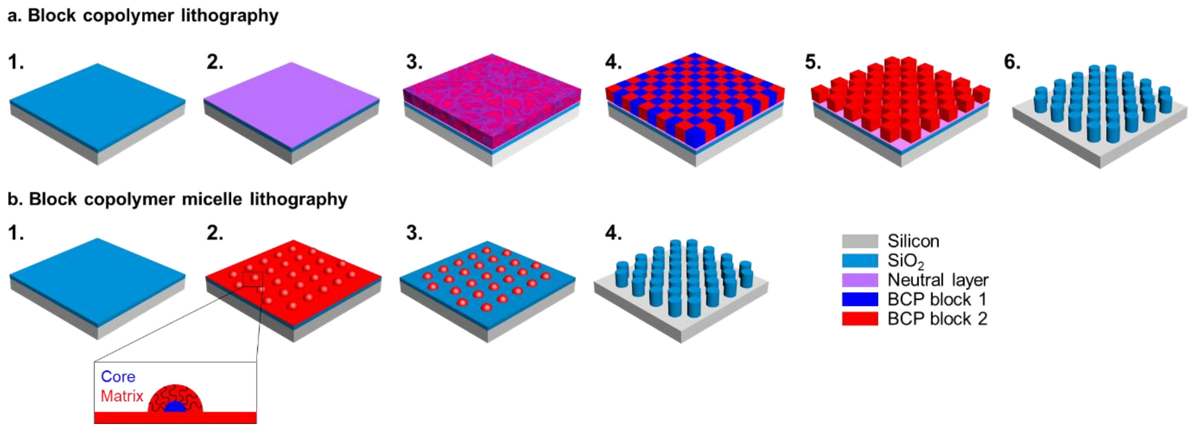

Figure 17 | The two variants of block copolymer lithography**. a,** Conventional block copolymer lithography proceeds with the deposition of a neutral surface layer (2); followed by spin coating a disordered BCP film (3); annealing of the BCP film to create an ordered surface pattern with perpendicular domains (4); selective removal of one BCP domain (5); pattern transfer (6). **b,** Block copolymer micelle lithography proceeds by spin coating pre-assembled spherical micelles onto the substrate (2); breakthrough etch to remove the matrix (3); pattern transfer (4).

2.2.3.2 BCP micelle lithography

In contrast to the conventional route, BCP micelle lithography (Figure 17b) makes use of solution-phase pre-assembled micelles.[125–127] For the case of poly(styrene-*block*-2-vinylpyridine) (PS-*b*-P2VP) – the most commonly used BCP – once dissolved in a solvent that is highly selective for the PS block (e.g. toluene, xylene), the polymer chains begin to self-assemble into spherical micelles. The micelles comprise a P2VP core and PS coronal matrix, and upon spin-coating onto the untreated substrate, form hexagonally packed micellar bumps. The process occurs within seconds, under ambient conditions and does not require the aforementioned pre-processing or post-processing steps.[128,129]

Demonstrations of using BCP micelle lithography for the generation of multifunctional surfaces have yielded impressive results, with wafer-scale uniform films possessing sub-50 nm features.[127] This simplified approach therefore constitutes a powerful tool for etch mask generation, and enables the mask dimensions to be tuned by simply varying the molecular weight of the polymer. Nonetheless, the small height of the micellar bumps presents an issue for the pattern transfer; and this will be discussed in detail in the proceeding chapters.

2.2.4 Laser Interference Lithography

Laser interference lithography (LIL) has become a powerful technique in nano-/micro-fabrication. It provides high-resolution periodic nanoarrays with excellent precision, uniformity and reproducibility; similar to EBL/FIB but for a fraction of the processing time and at significantly reduced expense, whilst also allowing for much larger-area patterning.

Interference lithography (IL) is a mask-less technique, relying instead on the interference between two or more coherent beams of radiation to create spatially periodic regions of high and low intensity light. These regions are recorded within a photosensitive layer before being developed and transferred to a specific substrate through a variety of well-established physical or chemical processes.[130] The technique therefore requires the beam to be split so that upon recombination of the beams, the interference pattern is produced. There are two classes of interferometers, delineated by the way in which the beam is separated; amplitude-division and wavefront interferometers. The first involves using partial reflection or refraction to split the amplitude of one coherent beam into two or more waves, which take different paths and then coincide at a desired location to create an interference pattern. [131–133] The second involves dividing the input wavefront, originating from a common source, by using mirrors, bi prisms or lenses.

Lloyd’s mirror interferometry is one such wavefront technique, requiring only one mirror and one beam; popular for laboratory settings. For larger exposure areas, dual beam systems are required.[134] The set-up for a one-mirror system is shown in Figure 18 and comprises a laser with a long coherent Gaussian beam, a lens, a pinhole and a mirror. The mirror is attached perpendicular to the sample to create a second beam. The mirror and sample stage are placed on a rotating table, allowing for easy variation in the period of the interference pattern. The lens and pinhole serve the purpose of creating a diverging beam; necessary to allow both the sample and the mirror to be illuminated whilst ensuring the effects of the Gaussian intensity profile are reduced.[135] Additionally by locating the beam far from the sample, only a small part of the Gaussian intensity profile falls on the samples thus maximising the uniformity; but at the expense of energy loss.

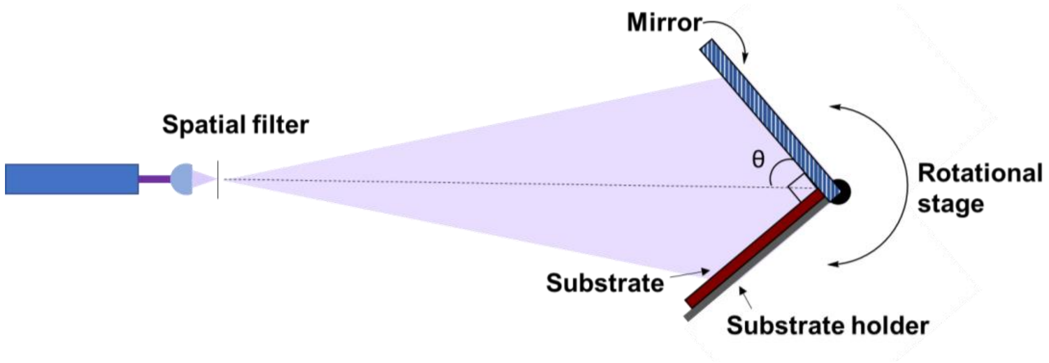

Figure 18 | Experimental set up for a Lloyd's interferometer with one mirror which is attached perpendicular to the substrate, both of which are on a rotational stage.

Using a one mirror system, gratings can be formed with a pitch determined by the wavelength λ of the laser, the angle of intersection θ between mirror and sample and stage orientation with respect to direction of laser beam, according to:[136]

$$P = \frac{\lambda}{2\sin\theta} \qquad \textit{Eq. 16}$$

Higher resolution patterns can be achieved through either increasing the mirror angle, or using a laser with a smaller wavelength; EUV radiation (10 – 124 nm) for instance, can produce higher-density interference patterns with sub-22 nm pitch.[137] Furthermore, rotation of the sample by 90° or 60° mid-way through the illumination can result in square-packed or hexagonally packed nanoholes or nanopillars; whilst more complex interference patterns can be achieved with increased numbers of beams.[138] Through a combination of illumination and development time, the diameter of the photoresist features can be tuned.

Despite the many merits of LIL, few examples exist in the literature of using LIL to generate etch masks for multifunctional surfaces; perhaps due to the added complexity involved in achieving lower pitches. However, square-packed nanocones of 200 nm pitch have been successfully attained through the use of LIL.[17]

2.2.5 Summary

Whilst each nanolithographic technique presents its own advantages, for multifunctional surfaces where uncomplicated periodic arrays are required with a high degree of uniformity, reproducibility and ease of scalability, only a few techniques offer these qualities. BCP micelle lithography and LIL enable access to pitches across the full range of interest (50 – 600 nm), whilst NIL provides a means to reproducibly replicate the masters produced from these processes, and progress into industrial-scale manufacture. Therefore, these are the techniques which are employed throughout the thesis, in combination with novel etching schemes.

The next half of this chapter focusses on the current state-of-the-art methods in terms of pattern transfer, and highlights the issues faced in the field.

2.3 Pattern transfer: high-resolution etching

In nano-/micro-fabrication, materials are etched one of two ways: through wet etching or dry etching. The resultant etch is characterised by means of isotropy and selectivity. To achieve an anisotropic (directional) etch, the rate of vertical etching $r_V > 0$, whilst the rate of horizontal etching $r_H = 0$ (Figure 19a). Conversely for the less desired scenario of an isotopic etch, the rates are approximately equivalent (Figure 19a), with varying degrees of isotropy giving rise to varying degrees of mask undercutting. The selectivity S is defined as the rate of the substrate etch over the rate of the mask etch (Figure 19b), with poor selectivity defined as $S = 1$, whilst a good selectivity is achieved with $S > 4$. In a standard wet etch, liquid chemicals (etchants) dissolve material from the substrate with high selectivity, however due to the nature of the etching process, control over the directionality (isotropy) of the etch is low, and therefore undercutting of the mask is common. Dry etching, on the other hand, employs gaseous etchants. Three types of dry etching exist: pure sputtering, plasma etching and reactive ion etching (RIE). Sputter etching is a purely physical process, where high-energy directional ions bombard the surface; providing high anisotropy but low selectivity. In plasma etching, the use of reactive species results in higher selectivity but lower anisotropy. RIE is an ion-assisted reactive etching process (Figure 19c) and hence a combination of the two; having ions diffuse towards the surface where they absorb and selectively react to form a gaseous product (chemical etching), meanwhile bombardment of high-energy ions acts to increase the rate of surface adsorption, surface reaction or by-product removal (physical etching). This balance between chemical and physical etching yields both high selectivity and high anisotropy.

The generation of the plasma is typically achieved by applying a strong radio frequency (RF) electromagnetic field (13.56 MHz) to a gas. However, there are a number of ways in which the energy transfer to the gas can be achieved. Capacitively coupled plasma (CCP) sources comprise two electrodes which form the parallel plates of a capacitor (Figure 19ci). Between these two electrodes, reactive gases are fed into the chamber and are ionised by the oscillating electric field. One electrode is RF powered, whilst the other is grounded, and thus ions from the plasma are accelerated towards the powered electrode, creating a potential difference between the plasma and electrode. Inductively coupled plasma (ICP) etchers provide a higher density plasma, and comprise two sources of plasma power (Figure 19cii). The first, an ICP source delivers the energy transfer inductively via a coil which is wrapped around the RIE discharge region; creating an electric field that tends to circulate the plasma. The ICP coils control the plasma density and therefore the ion flux. A second CCP source controls the voltage between the wafer and the plasma; dictating ion energy and directionality. ICP etchers therefore enable independent control over ion flux and ion energy.

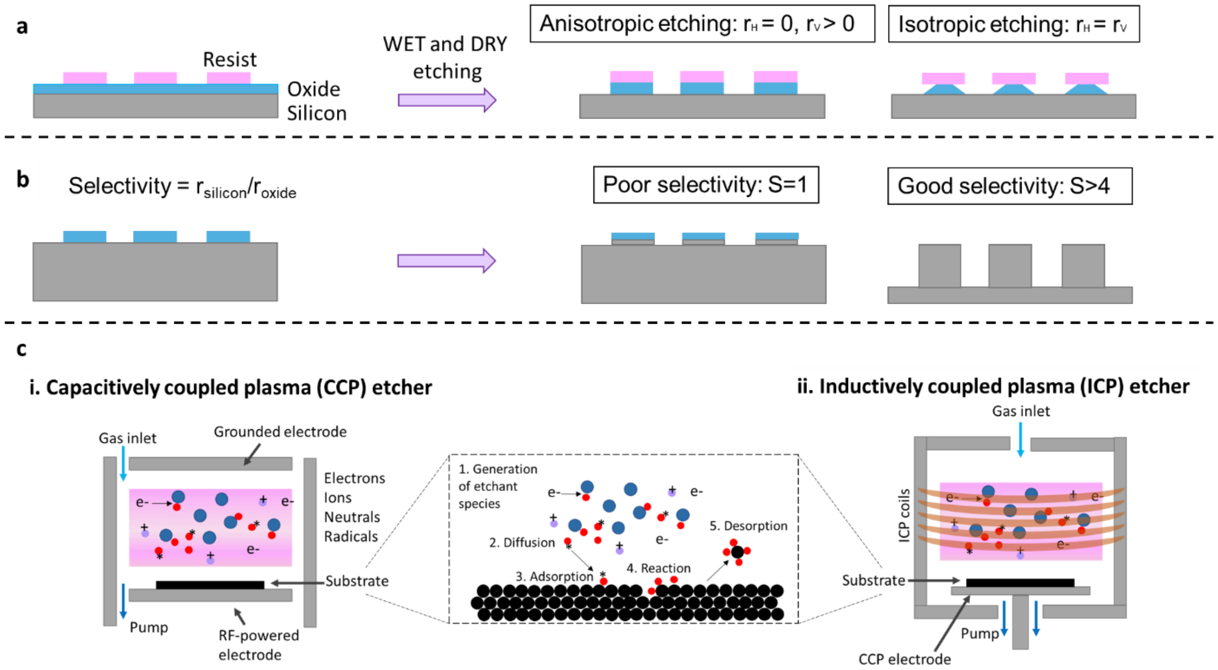
a
Resist
Oxide
Silicon
WET and DRY etching
Anisotropic etching: $r_H = 0$, $r_V > 0$
Isotropic etching: $r_H = r_V$
b
Selectivity = $r_{silicon}/r_{oxide}$
Poor selectivity: S=1
Good selectivity: S>4
c
i. Capacitively coupled plasma (CCP) etcher
Gas inlet
Grounded electrode
e-
Electrons
Ions
Neutrals
Radicals
Substrate
Pump
RF-powered electrode
1. Generation of etchant species
2. Diffusion
3. Adsorption
4. Reaction
5. Desorption
ii. Inductively coupled plasma (ICP) etcher
Gas inlet
ICP coils
Substrate
Pump
CCP electrode

Figure 19 | Etch characterisation and sources of plasma. **a,** The anisotropy of an etch depends on the horizontal r_H and vertical r_V etching rates. **b,** The selectivity of an etch is determined by the rate of substrate etching over the rate of mask degradation. **c,** Plasma etching can occur in a capacitively couple plasma (CCP) etcher with two parallel electrodes (i), or in an inductively couple plasma (ICP) etcher with ICP coils and a CCP electrode (ii).

Whilst RIE is not as scalable or as low cost as wet-etching, it is a well-established technique within the semiconductor electronics industry and is a staple piece of equipment within cleanrooms across the globe. More recently, RIE has attracted the attention and investment of glass manufacturer Corning for the fabrication of high-performance, multifunctional glass.[139]

The result of the interaction between the plasma and the surface depends on a number of factors: (i) the choice of feed gas, and therefore nature of the species produced, (ii) the pressure and power which determine the flux of the active species and positive ions, (iii) the bias power which determines the energy of the bombarding ions.[140] By adjusting these different parameters, self-masking can be induced when polymers formed in the plasma get deposited onto the surface and act as micro-etch masks.[141] Examples of mask-less glass and silicon etching have yielded a range of stochastic subwavelength structures (Figure 20),[141–144] however attaining control over the shape and dimensions is hard to achieve, and this can be detrimental for applications where reproducibility is critical, or for fundamental studies where one feature is varied systematically.

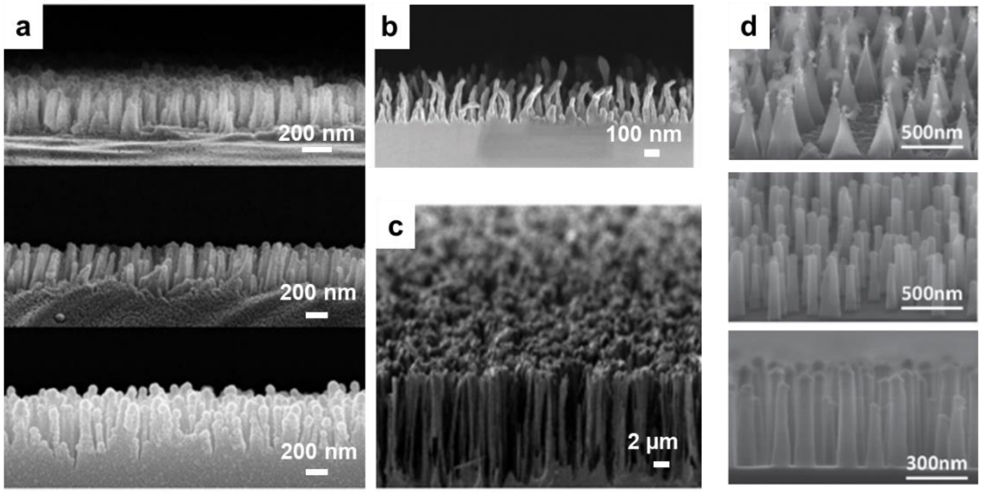

Figure 20 | Nanostructures generated through mask-less etching. **a,** subwavelength silica structures achieved through self-masked silica etching for 20 – 40 min.[141] **b,** Re-entrant silica nanostructures generated through RIE and PECVD using a Bayesian optimisation approach.[142] **c,** Silica grass generated through mask-less RIE.[143] **d,** Silicon nanostructures generated through simultaneous reactive ion synthesis and etching.[144]

2.3.1 Glass etching

Transferring the pattern from the polymeric etch-mask to the underlying glass substrate is a formidable step; particularly so for BCP lithography where the mask thickness ranges from 15-45 nm. Moreover, the complexity becomes further amplified for sub-100 nm pitch as the spacing in between structures is low, making it harder for etchant gases and high-energy ions to reach the base, and for etching by-products to be removed.

The challenge stems partially from the chemical and thermal stability of glass; which are paradoxically, the characteristics that make glass such an attractive material for many different applications. In order for a plasma species to etch a material, their interaction must lead to the formation of a stable volatile compound. Fluorine-based plasma does however, react with Si to form SiF_4, which has a boiling point of -86 °C, and is thus a stable volatile product. The most widely used fluorine-based gases for glass etching are fluorocarbons (CHF_3, CF_4, C_4F_8), which in addition to generating the etchant F, also generate CF_x radicals which tend to yield protective films (passivation). This is often viewed as an unwanted side effect as it can inhibit critical dimension control, and is often mitigated by increasing the energy of ion bombardment so that oxygen atoms can be released from SiO_2 to produce stable and volatile CO, CO_2, COF_2 species, thus burning away the film.[140] Alternatively O_2 is added into the gas feed, but can compromise the selectivity. A lesser used plasma for SiO_2 etching is SF_6 in combination with Ar, which does not induce the deposition of a protective film.

Therefore, for etching into glass using a BCP mask with a low pitch, there is an issue; using a plasma which does not deposit a protective film results in early depletion of the mask and low aspect ratio structures, however too much or uncontrolled deposition reduces the critical dimension control leading to distorted and inhomogeneous patterns. To overcome this issue, additional efforts have been made in the field to increase the required etch-contrast between mask and substrate, to surpass the low aspect ratios achieved by solely etching a soft mask into glass (Figure 21a). For instance, the use of organic-inorganic BCPs such as poly(isoprene-*block*-ferrocenyldimethylsilane), where the presence of Fe and Si in one of the nanodomains increases the etch contrast.[145] Alternatively, using all-organic BCPs, metals can be loaded selectively into one of the blocks through Sequential Infiltration Synthesis *via* Atomic Layer Deposition (ALD).[146] This route has enabled glass nanopillars of aspect ratio ~5 (Figure 21b).[147] A concept variation which does not require ALD, involves the infiltration of metal salts. For instance infiltrating iron salts into poly(styrene-*block*-4-vinylpyridine) after solvent annealing, which achieved aspect ratios of ~20 but with disordered patterns above ~4 (Figure 21c).[148] Gold salts have also been mixed with poly(styrene-*block*-2-vinylpyridine) in solution to form micelles loaded with a P2VP-gold core which are spin-coated onto the substrate, to yield well-defined gold nanoclusters (Figure 21d),[149] however the low thickness of the gold nanoclusters results in low aspect ratio structures (AR~2) upon etching (Figure 21e).[125] To increase the thickness and stability of the gold mask, electroless growth of gold has been performed after the self-assembly, and has arrived at aspect ratios ~20, but again with disordered structures above ~4 (Figure 21f).[150]

Whereas for BCP lithography where the thickness of the mask is limited to sub-45 nm, other lithographic techniques can employ thicker layers of photoresist for instance, to compensate for the degradation issue. Nonetheless, at the length scales of interest for multifunctionality, new issues arise; electrostatic attraction between neighbouring high aspect ratio masks can lead to buckling, and therefore hinders significant improvements.[151]

Whilst overall, metal masks improve the etching selectivity, they also introduce an additional step, cost, and potential source of contamination (diffusion into the substrate, non-volatile byproducts/debris deposition).[152] Therefore, there is a need to find alternative pathways to etch glass at high resolution, which make use of the plasma chemistry; altering the F/C ratio to change the plasma from etching to polymerising.

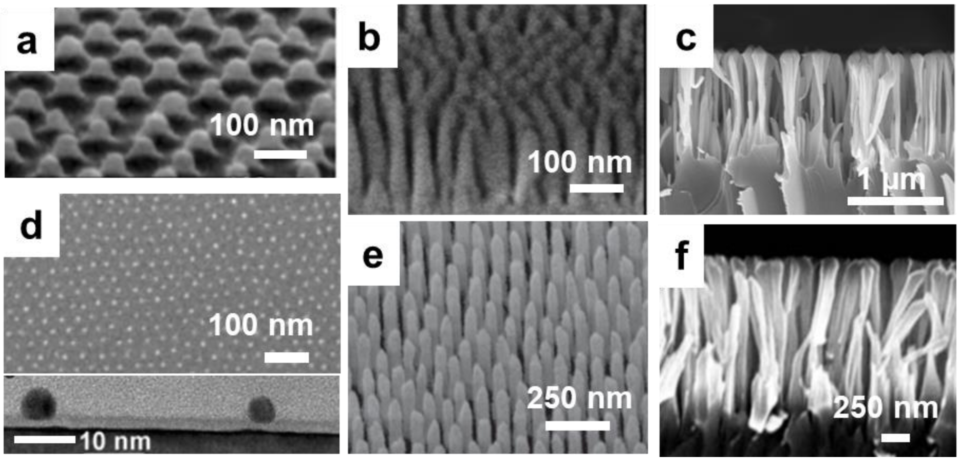

Figure 21 | SEM images of BCP-generated masks or the resulting glass nanostructures generated. **a,** Low aspect ratio glass nanopillars generated by BCP micelle lithography with unmodified poly(styrene-*block*-2-vinylpyridine)**.**[128] **b,** Glass nanopillars generated from a poly(styrene-*block*-methylmethacrylate) mask that has undergone Sequential Infiltration Synthesis of alumina.[147] **c,** Glass nanopillars generated from a poly(styrene-*block*-4-vinylpyridine) mask with infiltrated iron salts.[148] **d,** Top view and side view SEMs of well-defined gold nanoclusters generated from gold infiltration of poly(styrene-*block*-2-vinylpyridine).[153] **e,** Glass nanopillars generated from a gold-infiltrated mask.[125] **f,** Glass nanopillars generated from a thicker gold mask generated through electroless deposition.[150]

2.3.2 Silicon etching

Silicon etching is a well-described process with the bulk of the advancement having been driven by the semiconductor and microelectronics industry. Several different approaches have been developed to accommodate different fabrication needs, including: wet-etching, RIE, cryogenic etching and the Bosch process.[154,155] As with SiO_2, Si can be etched using fluorine-based plasma, however Si typically presents pure chemical etching behaviour with fluorine atoms. Thus, the Bosch process (DRIE) was invented to ensure anisotropic Si etching, through multiple cycles of passivation and etching (Figure 22a). Whilst this process has enabled the generation of very deep, anisotropic nanostructures, the periodic scalloping present on the sidewalls of structures is an inherent problem (Figure 22b). The scalloping effect can, for instance, degrade the performance of silicon diodes by introducing interface charge,[156] furthermore it can impact the optical properties by increasing the amount of scattering.[157] A few strategies have been developed to avoid scalloping, for example by introducing C_4F_8 into the etching step but with the result of a low etch rate,[156] or by performing a post-dry etching process by RIE with SF_6 plasma.[157]

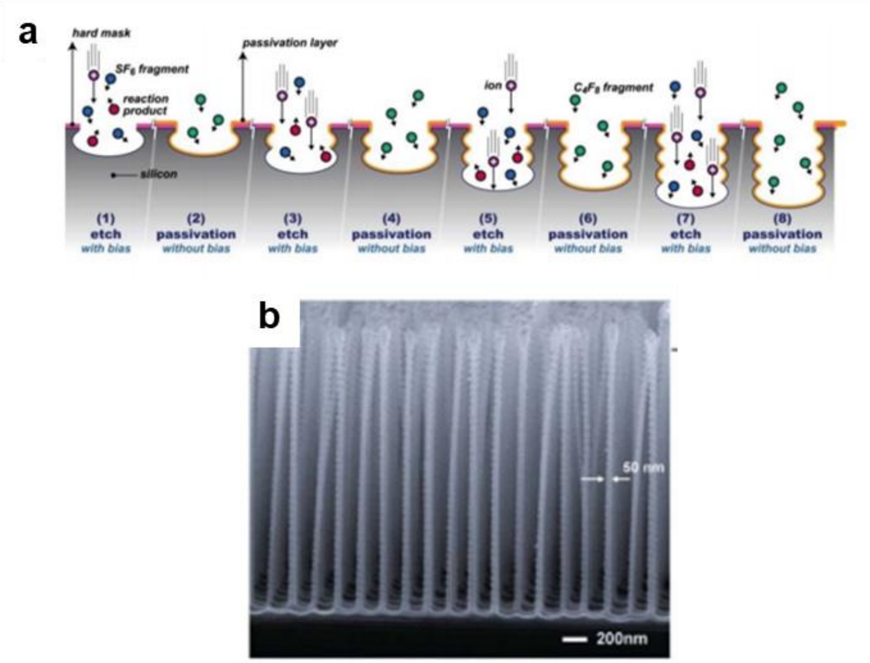
a
hard mask
SF₆ fragment
reaction product
silicon
passivation layer
ion
C₄F₈ fragment
(1) etch with bias
(2) passivation without bias
(3) etch with bias
(4) passivation without bias
(5) etch with bias
(6) passivation without bias
(7) etch with bias
(8) passivation without bias
b
50 nm
200nm

Figure 22 | Bosch silicon etching. **a,** Process flow of a typical Bosch process, consisting of alternating etch and passivation steps which give rise to the scalloping effect.[158] **b,** SEM image of silicon nanopillars with scalloping generated through a Bosch process.[159]

Whilst very high aspect ratios are beneficial for various functionalities, mechanical strength is also important and thus using DRIE to attain such deep structures is not necessary for multifunctional surfaces. For shallower etches, SF_6 plasmas have been used in combination with additive gases such as O_2. This ensures side-wall passivation with SiO_xF_y; important for anisotropic etching. Cl plasma can also be employed as a solution to anisotropic Si etching through means of ion bombardment; exposure to Cl plasma alone, without ion bombardment would not yield $SiCl_4$.

As with SiO_2 etching, there is an issue with selectivity between polymeric etch masks and Si; particularly for thin masks at reduced pitch. To enhance the etch contrast between a BCP mask and silicon, a number of strategies have been developed, for instance, choosing a silicon-containing BCP – such as PDMS – which under oxygen plasma converts into silicon oxycarbide, leaving a hard mask with enhanced mechanical and thermal stability.[145] This allowed for the fabrication of silicon nanopillars/nanoholes (Figure 23a, b).[114,160] Nonetheless, as the hard mask takes the dimensions of the BCP, the thickness remained very low, yielding an AR<2. Therefore additional layers such as chromium have been incorporated underneath the BCP, to attain higher AR~6.5 (Figure 23c).[161]

Alternatively, as seen before for SiO_2 etching, the constituent blocks of organic BCPs can be selectively infiltrated with metals/metal oxides,[47,162,163] to yield high AR arrays of nanopillars/cones/gratings (Figure 23 d,e,f). In these techniques however, the experimental conditions are delicate, demanding careful matching of precursor and block chemistry to obtain good infiltration efficiency, and in some instances requiring expensive equipment (atomic layer deposition). The cost and impracticality therefore represent a key limitation, with the additional potential introduction of metal contaminants into the chamber. Instead, using a thin 20-25 nm intermediate SiO_2 layer as a hard mask has resulted in high AR porous nanostructures (AR~10; Figure 23g),[164] albeit with limited success and control for more challenging geometries like pillars and cones; with the achieved AR<2, and little control over morphology (Figure 23h,i), owing to the previously mentioned challenges in SiO_2 (hard mask) etching combined with Si etching control.[128]

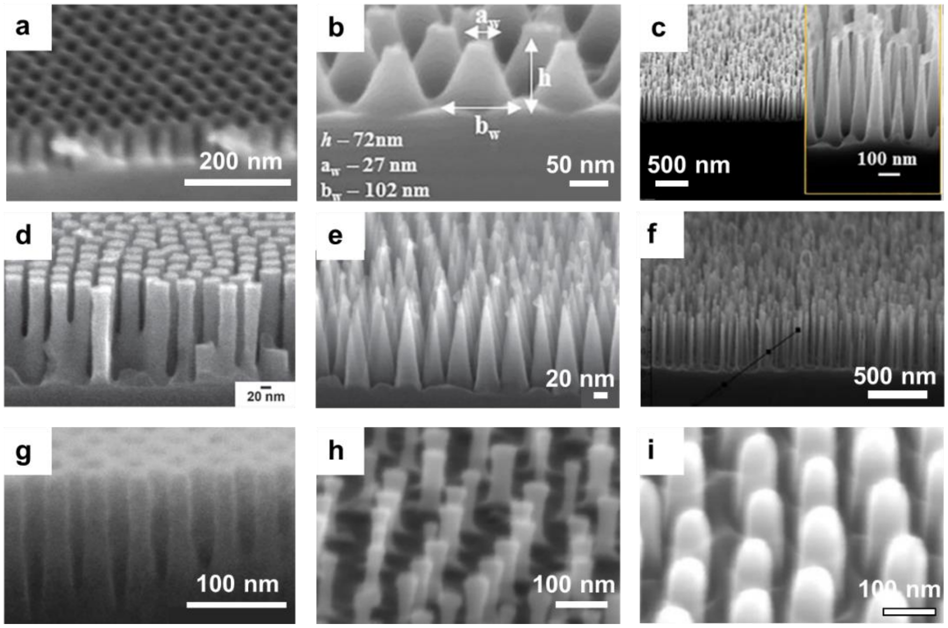

Figure 23 | SEM images of Si nanostructures generated by etching BCP masks, employing various strategies. **a,** Low aspect ratio nanoholes generated by oxidising a micro-phase separated film of PS-*b*-PDMS to yield a silicon oxycarbide hard mask, and subsequent etching into Si.[160] **b,** Low aspect ratio nanocones generated by oxidising a micro-phase separated film of PS-*b*-PDMS to yield a silicon oxycarbide hard mask, and subsequent etching into Si.[161] **c,** Higher aspect ratio nanocones generated using a silicon oxycarbide hard mask combined with an underlying layer of chromium.[161] **d,e,** cylindrical nanopillars (d) and sharp nanocones (e) generated through sequential infiltration synthesis of alumina into the PMMA domain of PS-*b*-PMMA.[47] **f,** High aspect ratio nanopillars generated by metal ion infiltration into the PEO block of PS-*b*-PEO, and subsequent etching into Si.[162] **g,** High aspect ratio nanoholes generated by BCP lithography using PS-*b*-PMMA and etching directly into an SiO_2 layer to create a hard mask for Si etching.[164] **h,i,** Nanopillars generated through BCP micelle lithography using PS-*b*-P2VP micelles and etching directly into an SiO_2 layer to create a hard mask for Si etching using SF_6/C_4F_8 (h) and Cl_2 (i) plasma.[128]

2.3.3 Summary

For both glass and silicon etching, the challenges which arise during the pattern transfer from the soft mask to the underlying substrate primarily stem from the low etch-contrast between the polymer mask and the underlying substrate. Whilst the focus has been on advancements in etching from a BCP mask, the dimensions and scale of these masks represent the more challenging scenarios for dry etching, and thus solutions found for these lengths scale can be applied to larger scales with more diverse morphologies.

3

REGENERATIVE SECONDARY MASK LITHOGRAPHY FOR MULTIFUNCTIONAL GLASS NANOCONES

This chapter is adapted from work published in Advanced Materials: 'Bioinspired Multifunctional Glass Surfaces Through Regenerative Secondary Mask Lithography'. The nanofabrication work was conducted by MM, TL, and myself over a number of years, and achieves high-resolution, high-aspect ratio glass etching of nanopillars from a BCP mask, by taking advantage of the plasma etching chemistry, and negating metal incorporation. The generated surfaces demonstrate broad multifunctionality; with optical measurements and modelling performed by MP and IP; antibacterial testing performed by MM and modelled by MM and myself; and wettability characterisation performed by MM and myself.

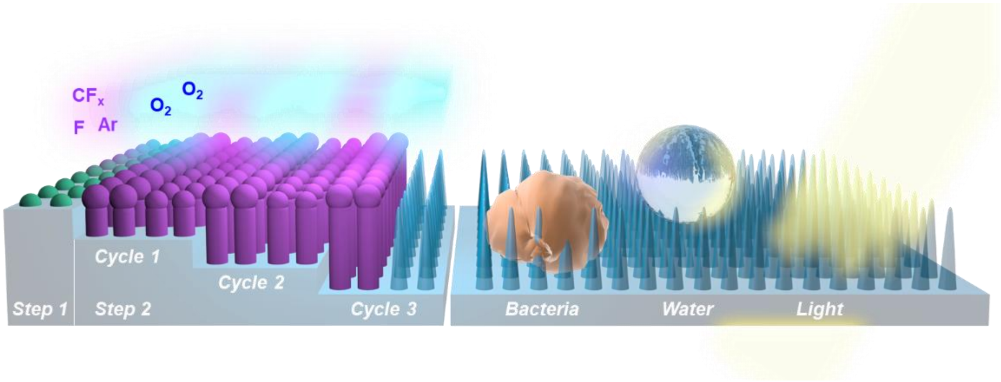

Schematic representation of the two-step cyclic etching process which embeds the BCP mask within a secondary protective mask which is controlled using oxygen plasma to ensure sufficient spacing, and then regenerated to achieve high aspect ratios. The generated arrays demonstrate mechano-bactericidal activity, water-repellence, and antireflectivity.

Adapted from: M. Michalska, S. K. Laney, T. Li, *et al*,. Bioinspired Multifunctional Glass Surfaces through Regenerative Secondary Mask Lithography, **Advanced Materials**, 2021, 2102175

3.1 Abstract

Nature-inspired nanopatterning offers exciting multifunctionality spanning antireflectance and the ability to repel water/fog, oils, and bacteria; strongly dependent upon nanofeature size and morphology. However, such patterning in glass is notoriously difficult, paradoxically, due to the same outstanding chemical and thermal stability that make glass so attractive. Here, Regenerative Secondary Mask Lithography is introduced and exploited to enable customized glass nanopillars through dynamic nanoscale tunability of the side-wall profile and aspect ratio (>7). The method is simple and versatile, comprising just two steps. Firstly, sub-wavelength scalable soft etch-masks (55-350 nm) are generated through an example of block copolymer micelles or nanoimprinted photoresist. Secondly, their inherent durability problem is addressed by an innovative cyclic etching, when the original mask becomes embedded within a protective secondary *organic* mask, which is tuned and regenerated, permitting dynamic nanofeature profiling with etching selectivity >1:32. It is envisioned that such structuring in glass will facilitate fundamental studies and be useful for numerous practical applications – from displays to architectural windows. To showcase the potential, glass features are tailored to achieve excellent broadband omnidirectional antireflectivity, self-cleaning, and unique antibacterial activity towards *Staphylococcus aureus*.

3.2 Introduction

Nature has evolved smart surfaces by organizing ordinary building blocks into sub-wavelength patterns to impart extraordinary properties, often of multifunctional character.[7,165,166] In this regard, bioinspired nanopatterning with purpose-tailored geometries (typically high-aspect ratio >1) has become a fast-evolving field, underpinning fundamental research and enabling novel applications from antireflective surfaces,[91,167] photonic membranes,[168] biological metamaterials,[169] de-icing[62] and dew-repelling coatings,[15] to mechano-bactericidal strategies.[84] Broadly, this multifunctionality is inherent to and bridged by the nanocone structure, yet such patterning in glass (SiO_2) remains a bottleneck due to its high chemical stability alongside structuring at the nanoscale itself, which becomes increasingly challenging to manage as the pattern resolution advances (pitch <100 nm). Attaining control over the pitch has, however, transpired to be necessary to advance existing, or unlock additional functionality; with theoretical models and experimental studies in silicon

Adapted from: M. Michalska, S. K. Laney, T. Li, *et al*,. Bioinspired Multifunctional Glass Surfaces through Regenerative Secondary Mask Lithography, **Advanced Materials**, 2021, 2102175

indicating that at these smaller length scales, nanocones are not only capable of resisting droplet impacts of higher velocity, but also of repelling water at the microscale – answering the need for antifogging surfaces.[15] Practically, this enables self-cleaning under various weather conditions permitting raindrops or dew to manage pollutants, for instance. Critical to the performance are also the profile and aspect ratio, where higher aspect ratio ensures smoother refractive index gradients, hence better antireflectance,[150] as well as it impacts flexibility of the cone, useful in boosting antimicrobial activity (e.g., aspect ratio ~10).[82] The latter functionality, widely demonstrated in other materials,[84] remains yet to be explored in glass; likely, due to the aforementioned structuring challenges.

Currently, such nanopatterning in glass is largely managed by multistep photolithographic processes[92] or somewhat simplified (de-wetting; mask-less) but at the expense of feature fine-control,[170–172] necessary to tune a combination of the properties. Additionally, despite pushing the resolution limits by deep-ultraviolet lithography or multiple patterning,[92,173] these complex strategies and costly equipment make such routes less appealing for mass-production when compared to self-assembling or imprinting methods. For example, block copolymers (BCPs) show a high-degree order at 10-100 nm scales (perfectly matching bio-patterns) and uniformity (m^2), while being economic and compatible with semiconductor technologies.[174] Similarly, nanoimprint lithography (NIL) generates high-resolution etch-masks in photoresists (down to tens nm), and can be scaled up into a continuous roll-to-roll process.[175] Ultimately, the material/device performance depends on the quality and aspect ratio of the pattern transferred into the glass *via* etching, which in turn depends on the mask's durability. To this end, the rapid BCP consumption as a soft mask alongside its limited height (tens nm), have been mitigated through a use of organic-organometallic BCPs[176] or Sequential Infiltration Synthesis;[146] by forming a hard mask via metal incorporation into a BCP block. This enables nanopillars with aspect ratio ~5.[147] A concept variation utilizing iron salt[148] or gold nanoparticles[149] led to the only reported aspect ratio ~20, however with disordered patterns above ~4.[150] Unlike BCP, a thicker photoresist mask can be imprinted (or nanospheres employed) to compensate the degradation issue. Yet at such scales, electrostatic attraction between adjacent mask sections leads to buckling, beyond certain mask thickness, hindering significant improvements.[151] Whilst overall metal masks improve etching selectivity, they introduce an additional step, cost, and potential source of contamination (diffusion into the substrate, non-volatile byproducts/debris deposition).[152] Evidently, with no other perceivable means to enhance the existing, but limited glass etching chemistry (fluorocarbon-based plasma accompanied by the formation of a carbopolymer etching-inhibitor layer), these mitigation routes were required and remain the state-of-the-art in soft mask-mediated glass nanofabrication. As such, developing a strategy to prevent soft mask degradation, compatible with scalable masking techniques, whilst erasing the need for soft-to-hard-mask conversion or mask thickening (limited for BCPs), represents a major materials and nanofabrication challenge.

Herein, we address this challenge and present facile templating of glass nanostructures (pillars/cones) of varying aspect ratio directly from the organic morphology (on the example of BCP and photoresist), with high selectivity (>1:32). At its core, our approach comprises just two steps (i) soft mask pre-patterning and (ii) our innovative cycling etching. We utilize H_2 addition into the glass etching chemistry (CHF_3/Ar) to trigger secondary (protective) mask formation around the original mask through well-controlled carbopolymer deposition. Importantly, the secondary mask is dynamic, as it can be reduced and regenerated, allowing side-wall profiling and multiple etching cycles (Figure 24a). We call this original mechanism *Regenerative Secondary Mask Lithography (RSML)*, which represents a generic solution for enhancing etching selectivity to elicit deep structures templated from thin soft masks, and can be applied to double-sided patterning. Finally, we achieve nanostructured glass with high transparency, broadband, haze-free, omnidirectional antireflectivity (>97.5% transmission calibrated to human eye response); impact-resistant superhydrophobicity (tested up to 4.4 m/s); and lastly, the first demonstrated antibacterial properties on a glass surface towards *S. aureus* with a competitive >81% killing efficiency.

3.3 Results and Discussion

3.3.1 Two-Step Fabrication – Regenerative Soft Mask Lithography (RSML)

Figure 24a-b show schematically the RSML process with corresponding scanning electron microscopy (SEM) images for an exemplary p=110 nm. It begins with surface pre-patterning. Here, pre-assembled block copolymer micelles comprised of PS-*b*-P2VP [poly(styrene-*block*-2vinylpyridine)] were spin-coated onto the substrate forming hexagonally-packed micellar bumps under ambient conditions [Figure 24a(1), Figure 25].[128]

Adapted from: M. Michalska, S. K. Laney, T. Li, *et al*,. Bioinspired Multifunctional Glass Surfaces through Regenerative Secondary Mask Lithography, **Advanced Materials**, 2021, 2102175

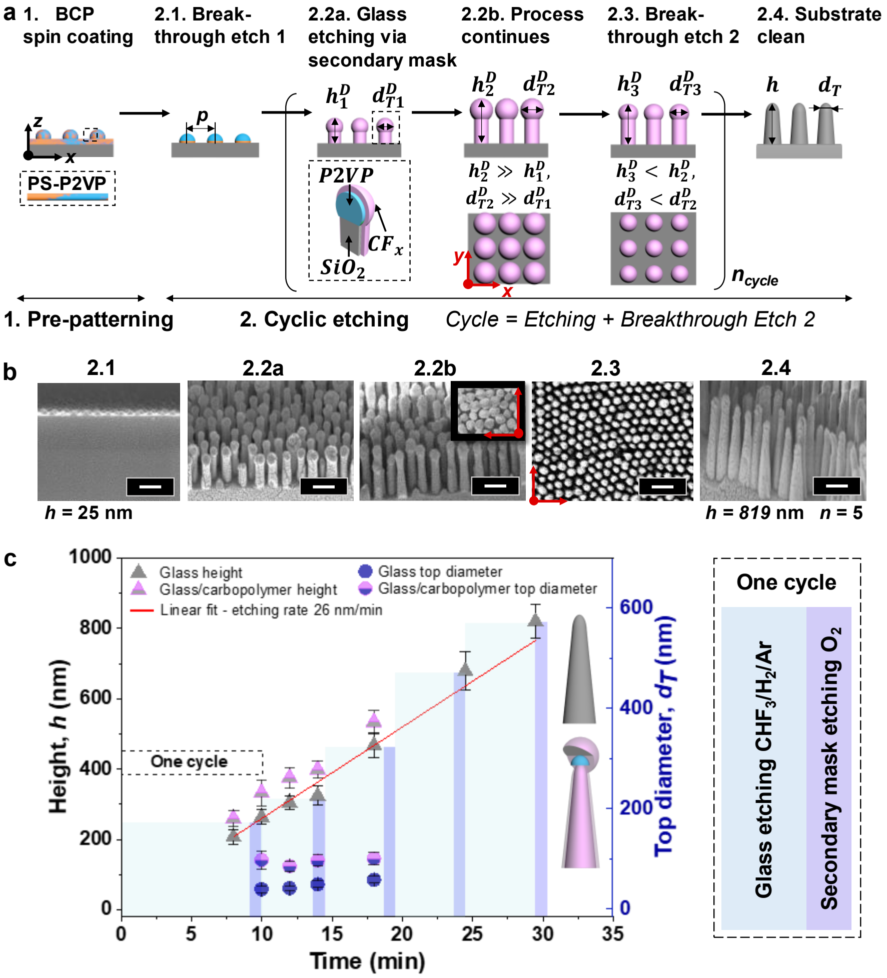

Figure 24 | Two-step fabrication process of glass nanopillars. **a,** Schematic illustration of regenerative secondary mask lithography consisting of: (Step 1) Surface pre-patterning using block copolymer (BCP) lithography, and (Step 2) cyclic reactive ion etching (RIE). Left to right: (1) Direct spin-coating of pre-assembled BCP micelles [micelle = P2VP core (blue) and PS matrix (orange)]. The second step proceeds entirely within the RIE chamber but is broken down here into sub-steps: (2.1) Breakthrough etch 1 using O_2 plasma to remove PS matrix; (2.2a-b) Anisotropic etching of glass (grey) during time *t*=a or b (b>a), using $CHF_3/H_2/Ar$ plasma, with simultaneous carbopolymer deposition (CF_x; pink) forming a secondary mask. The evolving pillars at time *t*=a, possess height $\boldsymbol{h_1^D}$ and top diameter $\boldsymbol{d_{T1}^D}$ (where superscript *D* refers to a structure with secondary mask), which both increase with the etching time until a maximum is reached (limited by $\boldsymbol{d_T^D}$) at time *t*=b; (2.3) Breakthrough etch 2 using O_2 plasma to refine the secondary mask; (2.4) Further etching with O_2 yields clean glass nanoarray. Steps (2.2-2.3) can be cycled *n* times to elicit structures of given *h*. Dashed lines indicate cross sections. **b,** Corresponding SEM images to the schematics (2.1-2.4), tilted 45° and top views. Five cycles result in glass pillars of *h*=819 nm. Scale bars 200 nm. **c,** An example of nanostructure evolution during *n*=5 cycles, monitored by changes in height and top diameter, with and without deposited carbopolymer.

Adapted from: M. Michalska, S. K. Laney, T. Li, *et al*,. Bioinspired Multifunctional Glass Surfaces through Regenerative Secondary Mask Lithography, **Advanced Materials**, 2021, 2102175

We explore four polymers (P) of M_w: P57, P100, P200, and P400 (M_w / kg mol^{-1} = 57-*b*-57, 109-*b*-90, 248-*b*-195, and 440-*b*-353, respectively), by dissolving the polymers in xylene isomers, and we find the most suitable dimensions of micelles and highly reproducible results for anhydrous *m*-xylene. Note, *p* and P refer to pitch and type of polymer, respectively. The phase segregation of the blocks is driven thermodynamically (molecular weight M_w, block ratio, composition, and degree of the blocks immiscibility) and kinetically (vapor pressure, humidity), providing a multiparameter space to accommodate specific applications.[129,174]

Characterization of the pattern by atomic force microscopy (AFM) revealed hexagonally-packed micelles of excellent uniformity, as shown in Figure 25a. The choice of solvent is extremely important. Here, we show the same P100 polymer dissolved in regular *m*-xylene, which results in micelles of a bimodal distribution (Figure 25b). Importantly, bimodality can enable binary or hierarchical structures, for instance, whereby two different diameters or heights of the feature can be achieved. Alternatively, a controlled disorder in the layout may be introduced by complete elimination of the second geometrical population during the subsequent etching. The height of the micelles is influenced by the humidity during the spin-coating process through swelling of the P2VP core with water, however as discussed later, the nature of our etching process ensures this is not problematic [the BCP mask is immediately embedded within a secondary mask during our *regenerative secondary mask lithography (RSML)* process, thus selectivity is maintained].

By varying spin speeds, a different pitch can be achieved as presented in Figure 25c for P57, P100, and P400. The chart nicely summarizes the achievable pitch range being ~50-300 nm. Note, for very high M_w, there is no linear dependence with respect to spin speeds and the pattern quality suffers when too rapid spin-casting is applied.

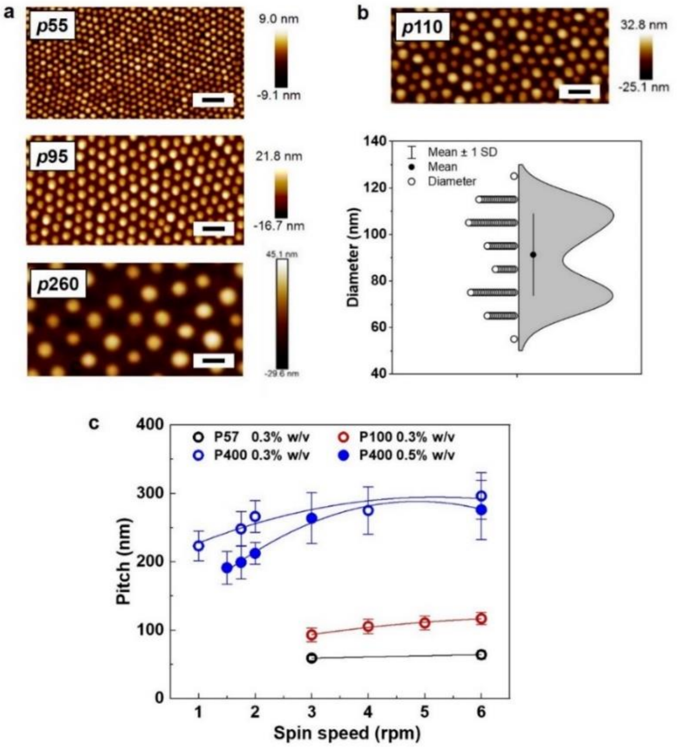

Figure 25 | Characterization of BCP patterns**. a,** AFM images presenting hexagonally-packed PS-*b*-P2VP micelles on glass substrates with three pitches *p*: 55, 95, and 260 nm. The resulting patterns of high quality were obtained by using 3% (w/v) solutions in anhydrous *m*-xylene with polymers of various molecular weight M_W: P57, P100, and P400, respectively; and their spin-coating at 3k, 6k, and 2k rpm, respectively. Scale bars are 200 nm. The color scales correspond to the height of the micelles. **b,** AFM image of P100 solution in regular *m*-xylene spin-coated at 6k rpm showing the pattern characterized by bimodal distribution, clearly indicated by the graph below (open circles refer to data). This example highlights the importance of solvent choice/quality. Additionally, it presents a pathway for bimodal structuring. **c,** Pitch as a function of spin speed for P57, P00, and P400 at the concentration of 3% w/v. Additionally, 2% w/v concentration of P400 is plotted showing how the range of the attainable dimensions can be further tuned. Note, with higher $M_{w,}$ there is no-linear dependence in respect to spin speeds.

The second step, aiming at pattern transfer into the substrate, proceeds in a single reactive ion etching (RIE) process. For understanding, it is broken down into sub-steps (2.1-4; Figure 24a), where oxygen plasma is firstly used as a breakthrough etch (2.1) to define mask diameter and uncover the underlying material to be etched by removing the PS matrix (Figure 26).

Adapted from: M. Michalska, S. K. Laney, T. Li, *et al*,. Bioinspired Multifunctional Glass Surfaces through Regenerative Secondary Mask Lithography, **Advanced Materials**, 2021, 2102175

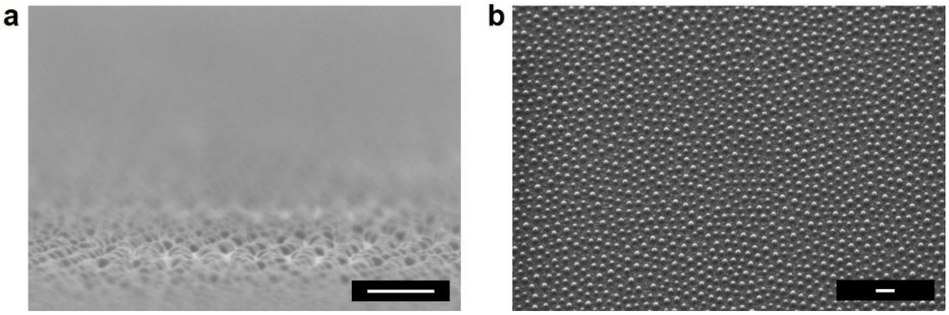

Figure 26 | BCP mask after breakthrough etch 1 (Step 2.1). SEM images of BCP P100 micelles spin-coated at 6k rpm and after 4 s of breakthrough etch 1 to remove PS matrix and uncover the underlying substrate to be etched. **a,** 2° tilted view. **b,** Top view. Note, hexagonal layout. Scale bars 200 nm.

Subsequently, we use fluorohydrocarbon plasma (CHF_3/Ar) to selectively etch SiO_2. The modest F/C ratio prompts moderate etching rates, critical for controlling etching profiles of narrow high-aspect ratio nanostructures (Figure 27). When using CHF_3 etching gas during SiO_2 plasma etching, the free fluorine radicals (F*) and other radicals such as CF_x* are generated according to the following reactions:

$$e^- + CHF_3 \rightarrow CHF_2^+ + F^* + 2e^- \qquad \textit{Eq. 17}$$

$$e^- + CHF_3 \rightarrow CF_2 + HF + e^- \qquad \textit{Eq. 18}$$

$$SiO_2 + xF^* \rightarrow SiF_x + O_2 \qquad \textit{Eq. 19}$$

$$3CF_x^* + 2O_2 \rightarrow CO + CO_2 + COF_2 \qquad \textit{Eq. 20}$$

$$3CF_x^* + 2SiO_2 \rightarrow 2SiF_x + CO + CO_2 + COF_2 \qquad \textit{Eq. 21}$$

During plasma-decomposition of the CHF_3 etchant, reactive fluorine atom F*, HF, and other radicals and ions are generated (*Eq. 17*-*Eq. 18*; Figure 27). The energetic heavy Ar ions cause the Si-O bonds to break, providing the disassociated silicon that can now react with fluorine radicals resulting in SiF_x formation (SiF_4 is volatile, hence it is evacuated from the chamber). Of note, the ion bombardment can also promote the desorption of some species chemisorbed on the surfaces, thus affecting the etch rate, degree of polymerization, as well as anisotropy. It can be seen in Eq. 19 that the silica etching consumes the F atom but frees the oxygen. The fluorocarbon CF_x radicals produced in Eq. 17 possess high sticking coefficients and typically deposit a polymer film on all surfaces, thus acting like an inhibiting layer for the further etching but also acting as promoters of anisotropic etching when depositing on the sidewalls. However, the release of oxygen leads to reactions with the polymer and formation of volatile CO, CO_2 and COF_2 which are consequently evacuated from the chamber. It also leads to a release of some F atoms – increasing the F/C ratio – and assisting with silica etching.[177] The F/C ratio is important to monitor with a general trend that the lower the ratio, the higher the concentration of CF_x species and thus the more polymerising the plasma.

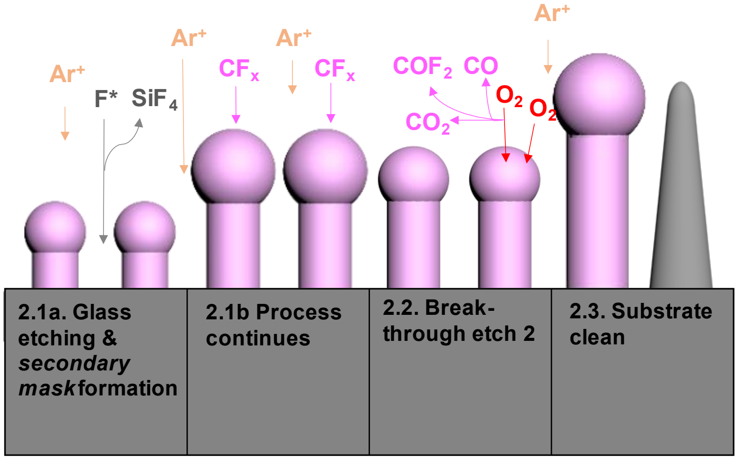

Figure 27 | A schematic of glass etching chemistry. Generation of the SiO_2 nanopillar through RSML is depicted. Starting from the BCP mask (not shown), the addition of H_2 into the etching chemistry (CHF_3/Ar) increases the generation of HF, thus lowering the F/C ratio; resulting in a more polymerizing plasma with increased CF_x deposition (2.1a-b). As the secondary mask builds up around the BCP to form mushroom-like structures, a brief oxygen plasma is applied which refines the diameter (2.2). This enables further etching to proceed, with self-regeneration of the mask to yield tall SiO_2 nanopillars. A final oxygen plasma removes the deposition to form high-aspect ratio SiO_2 nanopillars (2.3).

We add hydrogen (H_2) to the reaction, harnessing its ability to scavenge fluorine to form HF (aiding glass etching), and meanwhile lower the F/C ratio, thereby providing fluorocarbon species (CF_x) of high sticking probability.[178]

$$SiO_2 + 4HF \rightarrow SiF_4 + 2H_2O \qquad \textit{Eq. 22}$$

Under such conditions, fluorocarbon deposition (polymerization; CF_x), fluorocarbon etching (surface reaction; HF, F*) and ion-assisted glass etching (Ar^+) occur simultaneously. We take advantage of this shift in plasma character, from etching to more polymerizing, ensuring that the sidewalls are passivated and establish the conditions which induce secondary mask formation around the BCP originating from the CF_x, inhibiting its consumption (2.2a). Sidewall passivation

Adapted from: M. Michalska, S. K. Laney, T. Li, *et al*,. Bioinspired Multifunctional Glass Surfaces through Regenerative Secondary Mask Lithography, **Advanced Materials**, 2021, 2102175

encourages anisotropic etching by preventing lateral etching to yield steep sidewall profiles (the Bosch process for silicon etching is a prominent example), and occurs as a result of the fewer reactions experienced on the vertical sidewalls and lower probability of ion bombardment. In our case, not only does the polymer build-up occur on the sidewalls, but also on top of the structures yielding mushroom-like pillars. This shape originates from the BCP mask becoming embedded within the polymer, which we utilize here as a secondary mask in our RSML process. This mechanism prevents the BCP consumption and enables the etching selectivity.

Buildup control is obtained by adjusting the energy of Ar ions (vide infra). This etching advancement alone yields only moderate heights (~300 nm) as the growing mask becomes an obstacle in deeper etching, particularly for such high-resolution patterns (2.2b). Importantly, we find that it can be controllably reduced under a brief and mild oxygen plasma (2.3 – breakthrough etch 2), and can crucially *regenerate* in the following glass etching (discussed later).

To achieve high-aspect ratio nanostructures, this cycle (etching and breakthrough 2) needs to be repeated and optimized such that etching, deposition, and Ar ion sputtering rates (R^E, R^D, R^S, respectively) are balanced. Finally, complete CF_x removal (2.4) is achieved by applying a harsher oxygen plasma. Note in Figure 24b, how the initial organic mask with height h_{BCP}=25 nm yields glass nanopillars with impressive h>800 nm (five cycles), indicating the etching selectivity exceeds 1:32. Graphical representation of the heights and top diameters of the evolving structures with and without the deposited layer (h^D, h, d_T^D, d_T, respectively), quantitatively expresses, and further conceptualizes the process (Figure 24c). The BCP mask contributes to both h^D and d_T^D, and by assuming it is intact throughout, we can derive the deposition thickness at time *t* as $\Delta h = h_t^D - (h_t + h_{BCP})$ and $\Delta d_T = d_{T,t}^D - d_{BCP}$. To induce the secondary mask, R^D>R^S is required, yet for high profile anisotropy this difference should be modest (in this example, R^D = 4±1 nm/min), to ensure sufficient deposition protecting the BCP whilst enough physical bombardment to permit anisotropy (∝Ar flow). After the breakthrough etch, which reduces the secondary mask (and thus $d_T^D$and h^D), it becomes evident that during the subsequent etch the mask is regenerated, verified by a constant value at the end of each etch with average Δd_T=49±2 nm and Δh=45±4 nm.

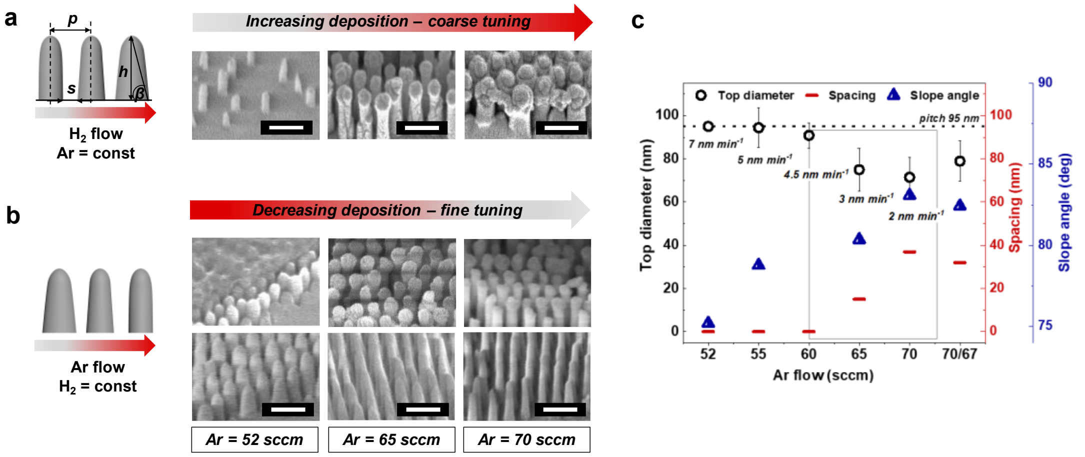

Figure 28 | Manipulation of etching/deposition gas composition for anisotropy control. **a-b,** Schematics with corresponding SEM images (45° tilt) showing major trends in tuning glass etching profiles – through sidewall angle *β* (tapering) – templated from BCPs when using $CHF_3/H_2/Ar$ plasma chemistry under varied H_2 and Ar flows, respectively. The pillar/cone profiles (height *h*, pitch *p*, and spacing *s*) are correlated with the degree of CF_x deposition (expressed as deposition rate R^D), which results in the secondary mask formation of diameter $\boldsymbol{d_T^D}$ visualized by corresponding SEM images presenting glass nanopillars with *p*=95 nm. Increasing H_2 flow (a), results in thickening of the secondary mask around the BCP, leading to a decrease in *β* and premature etch stop. Conversely, for increasing Ar flow (b) a stronger physical bombardment occurs resulting in smaller deposition and larger *β* which is seen more clearly after removal of the mask (bottom row of SEM images). We establish the process conditions by firstly testing H_2 flows until deposition occurs (coarse tuning). Secondly, Ar flow is used to fine-tune R^D and hence the profile, presented quantitatively by (c). **c,** Plot of $\boldsymbol{d_T^D}$, *s*, and *β* versus Ar flow. Overall, the closer *β* is to 90°, the more anisotropic the profile, and the maximum $\boldsymbol{d_T^D}$ is equivalent to the pitch (dotted line). The optimal process conditions are framed. Note, varying Ar *during* the process allows for further tuning resulting in base widening, for instance (70*=70 sccm followed by 67 sccm).

To explain this etching scenario, we detail in Figure 28 how to induce and manage the secondary mask which ultimately controls the profile anisotropy/tapering (yielding vertical pillars/tapered cones, respectively) – characterized by the slope angle *β* (see Figure 28a). When a substantial amount of H_2 is added ($CHF_3:H_2 \leq 3.3$), mushroom-like structures are formed around the mask at the top of the evolving nanostructures. At first glance, it seems surprising that the augmented deposition is formed solely around the mask. However, when ions hit the horizontal surfaces between the features, chemical reactions are induced by breaking the Si-O bonds. As opposed to the BCP, silicon reacts with fluorine while liberated oxygen burns the carbopolymer away as CO_x. This indicates the mechanism to be relatively generic and applicable to other organic masks which we discuss later. Careful choosing of the $CHF_3:H_2$ ratio is required as larger ratio decreases the

Adapted from: M. Michalska, S. K. Laney, T. Li, *et al*,. Bioinspired Multifunctional Glass Surfaces through Regenerative Secondary Mask Lithography, **Advanced Materials**, 2021, 2102175

deposition so that the BCP degrades quickly, distorting the pattern (Figure 28a). Conversely, too small a ratio (~2), augments the deposition, thus inhibiting etching.

We attempt to alternate these two processes (etching- or deposition-driven) to create a pseudo-Bosch switching route, being successful in silicon and providing some advances in glass etching, e.g., advanced cyclic etching method.[179,180] By altering H_2 content introduced to the gas feed (CHF_3:Ar 12 sccm: 38 sccm), broadly, we switch the plasma from etching to more polymerizing or *vice versa* (H_2 increase or decrease, respectively). When starting with higher H_2 ($CHF_3:H_2 = 3.0$, for instance), we induce self-masking originating from an excessive deposition of carbopolymer layer. By gradual hydrogen decrease (to $CHF_3:H_2 = 3.3$), we slowly reverse the plasma to become more etching so that the process behaves like a pseudo-Bosch silicon etching,[179] where the silicon anisotropic etching is alternated with the polymer passivation, which protects the sidewalls from the etching. Through such an approach, we successfully achieved nanopillars of $h = 840$ nm at $p = 200$ nm, as shown in Figure 29. However, at smaller pitch, this method was more challenging to control which prompted us to turn our attention onto process control by varying Ar content.

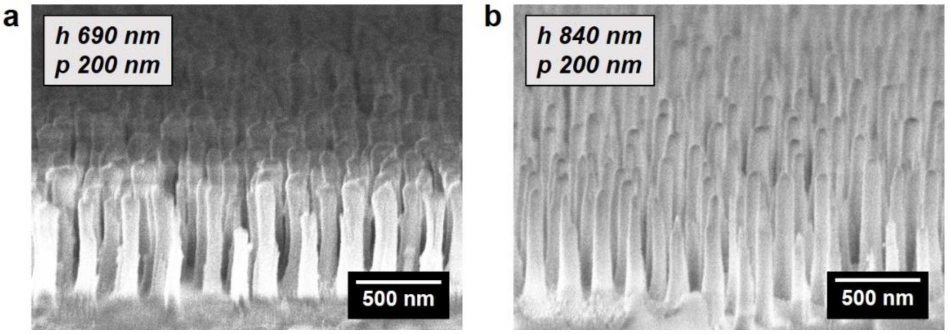

Figure 29 | Exemplary structures obtained by Pseudo-Bosch process. **a,b,** SEM images presenting glass nanopillars obtained by our pseudo-Bosch process. The structures were templated from BCP P200 (M_w / kg mol^{-1} = 248-*b*-185) with the resulting $p = 200$ nm. After the breakthrough etch 1 for 7 s, the glass etching was performed in three stages for 10, 10, and 5 min by decreasing H_2 from 4, 3.8, to 3.6 sccm respectively, under constant CHF_3:Ar = 12:38 sccm. Additionally, a step of oxygen clean followed by SF_6 etch for 1 min was performed in (b).

It is noteworthy that pseudo-Bosch approaches were also attempted in glass etching in order to address a problem of feature distortions during high-aspect ratio nanopattern generation (*e.g.*, twisting, tilting, surface roughening).[180] For example, advanced cyclic etching was proposed, where deposition and etching cycles were alternated, resulting in a successful etch of high-aspect ratio nanoholes from an amorphous carbon layer of 550 nm.[181] In another approach, the contact hole distortions caused by uncontrolled carbopolymer deposition at the oxide-mask interface were improved through introduction of an *in-situ* polymer removal step by oxygen.[182] However as mentioned above, controlling etching of nanopillars/cones at smaller pitch (<100 nm), templated from easily-degradable thin soft masks (~25 nm), poses its own set of challenges.

Instead, we anticipate that varying an inert gas such as Ar at fixed H_2 flow should affect ion bombardment and therefore when well-balanced, an R^S can be obtained that is a fraction slower that R^D. Secondary mask evolution and etching profile are dependent on the deposition rate R^D, and to allow for anisotropic/directional etching at the nanoscale, this value needs to be optimal; otherwise, the maximum height that structures can reach becomes quickly limited by the etch stop when: (i) d_T^D reaches maximum value, equivalent of pitch, or (ii) excessive tapering leads to bridging bases of the neighbouring pillar. The evolution of such an effect when $R^D \gg R^S$**,** and its consequences are depicted in Figure 30. After 4 min of etching, d_T^D approaches its maximum so the resulting pillars are still nicely separated. However, as the etching continues (8 min), an uneven structuring appears, manifested by the presence of pillar doublets connected by the common base (red arrow) and a non-linear baseline (dashed line). The determined R^D that led to the premature etch-stop is 10 nm/min.

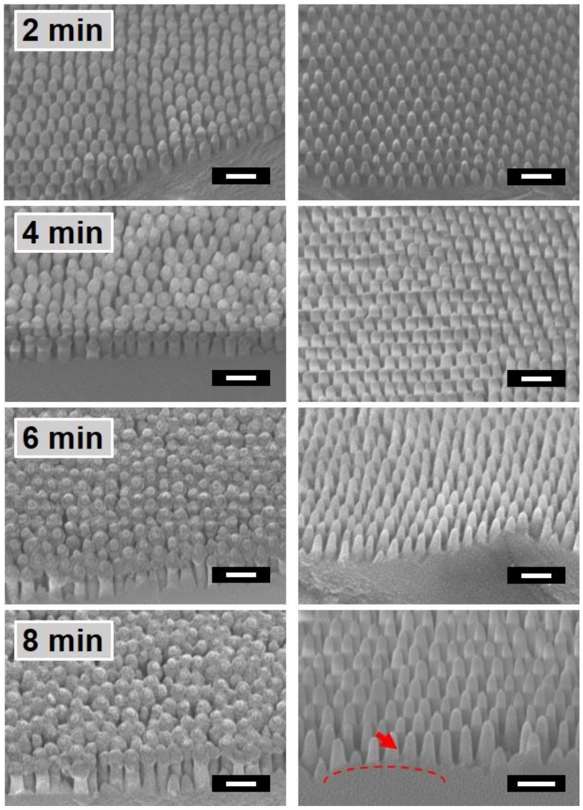

Figure 30 | Secondary mask evolution and structure tapering when $\boldsymbol{R^D} \gg \boldsymbol{R^S}$. SEM images 45°-tilted of the evolving glass nanopillars with deposition (secondary mask; left panel) and after O_2 clean (right panel). The structures were templated from BCP P100 with the resulting p = 95 nm. Due to the high R^D=8±1 nm/min, the secondary mask has reached its maximum diameter after 6 min. Additionally, both low etching directionality, which led to an increased tapering, and maximum $\boldsymbol{d_T^D}$ reached did not permit further etching to result in well-resolved array (8 min). Note uneven baseline (red dashed line) and red arrow indicating unseparated neighbouring pillars. Scale bar 200 nm.

By ensuring R^S is a fraction slower that R^D, we achieve more anisotropic etching through the downward ion channelling off the sidewalls, hence imparting higher R^E at the base allowing high-aspect ratio nanostructures to be formed within a non-switching process.[183] Indeed, we successfully control the secondary mask formation through precise adjustment of Ar flow (Figure 28b-c) to provide control over β – which in turn dictates the nanostructures height at certain pitch (etch stop), and can affect the mechanical stability.[184] We further quantify that approximately $2 \leq R^D < 5$ nm/min is optimal to form $\beta > 75°$.

Since we balance the processes by adjusting the R^S, it is important to elucidate its impact on the etching rate. Figure 31 presents data for the typical range of the values of Ar flow in use, and we can convincingly state that the effect of Ar flow is negligible across the studied conditions.

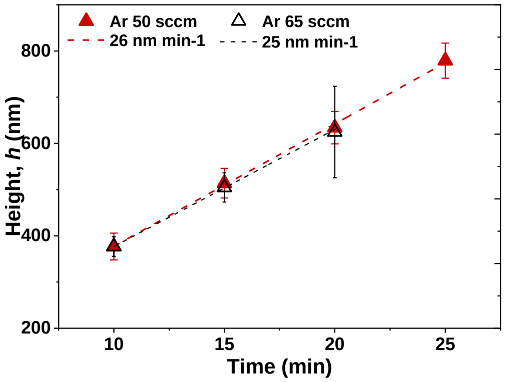

Figure 31 | The glass etching rates when varying argon flow. Nanopillars templated from BCP P400 were etched using two gas mixtures with variable content of Ar (CHF_3:H_2:Ar=3:1:10 and CHF_3:H_2:Ar=3:1:12; Ar 50 and 65 sccm, respectively). The etching rates were found independent from argon flow within the tested range.

Having reached a point where the d_T^D is approaching the pitch (due to $R^D > R^S$), we introduce a brief oxygen etch which enables diameter control through reduction of the secondary mask (Figure 32), hence permitting deeper etching. By knowing the O_2 R^E, d_T^D, and d_{BCP}, one can determine the necessary time for this breakthrough etch (Step 2.3) as shown in Figure 32b (inadequate = less space for further etching, excessive = mask degradation). Importantly, mild conditions are required to prevent mask distortion. The surface composition analysis obtained by XPS (Figure 32c) further confirms that initially (*t*=0 s; end of Step 2.2), only carbon and fluorine are present, in contrary to *t*=30 s where silicon and oxygen make up >90% of the entire composition (Step 2.4). Interestingly, a trace amount of nitrogen appears (~1%) throughout, originating from pyridine (P2VP), which is absent at the end of the etching; providing evidence the BCP is embedded within the CF_x structure.

Adapted from: M. Michalska, S. K. Laney, T. Li, *et al*,. Bioinspired Multifunctional Glass Surfaces through Regenerative Secondary Mask Lithography, **Advanced Materials**, 2021, 2102175

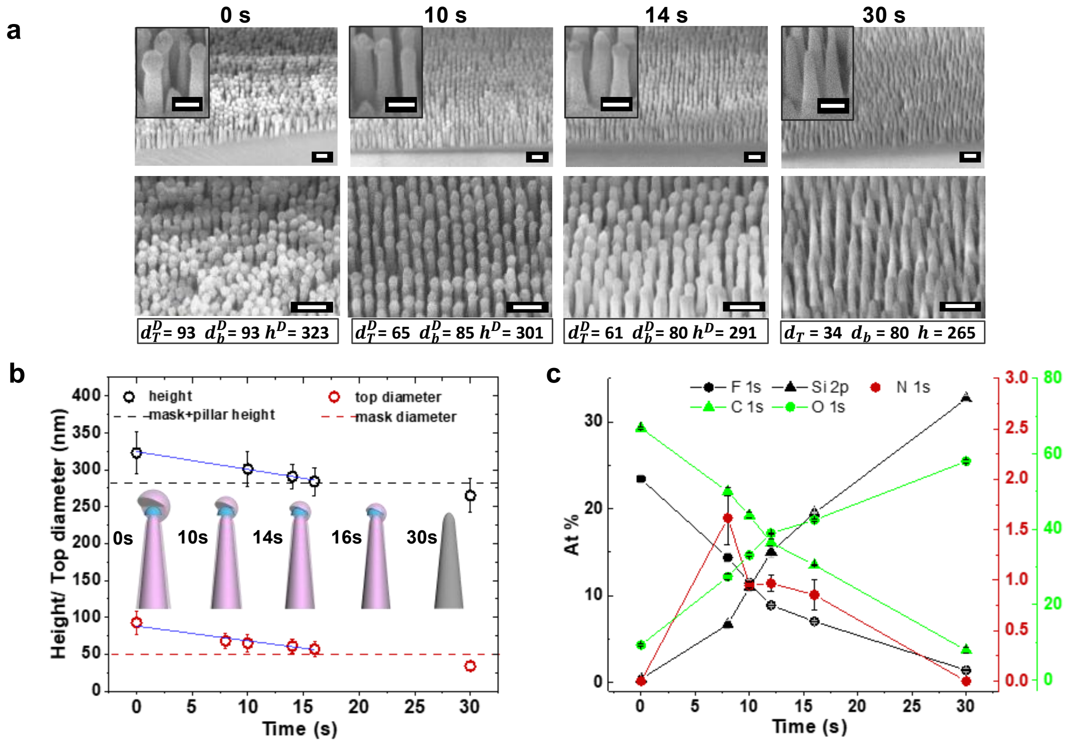

Figure 32 | Effect of secondary mask tuning. **a,** Temporal evolution of reducing carbopolymer under mild O_2 plasma, SEM micrographs tilted at 45°. Height, top and base diameters are determined ($\boldsymbol{h^D}$, $\boldsymbol{d_T^D}$, $\boldsymbol{d_b^D}$, respectively). **b,** Polymer reduction rate determined by plotting $\boldsymbol{h^D}$ and $\boldsymbol{d_T^D}$ as a function of O_2 etching time. Lateral and vertical rate were determined by linear fit and are 2.0±0.4 and 2.4±0.1 nm/s, respectively, hence indicating an isotropic etching. The rendered structures represent the changes in carbopolymer thickness where grey is a glass pillar, blue is the BCP (both blocks) mask, and pink is the deposited layer. **c,** Surface composition obtained from the survey spectra by X-ray photoelectron spectroscopy (XPS) for the series of the samples treated with varying O_2 etching time.

The great advantage of RSML-mediated glass nanostructuring is its straightforward nature. This enables flexibility and facile optimization to accommodate various masks and targeted topographies of certain pitch, aspect ratio, and feature shape (vertical/tapered sidewalls and round/sharp apex) – principal attributes to manage photons, water/oils, and/or cells. Note, the attainable pattern quality across a surface as shown in Figure 33 for exemplary nanostructures with aspect ratio 6 at *p* 95 and 110 nm.

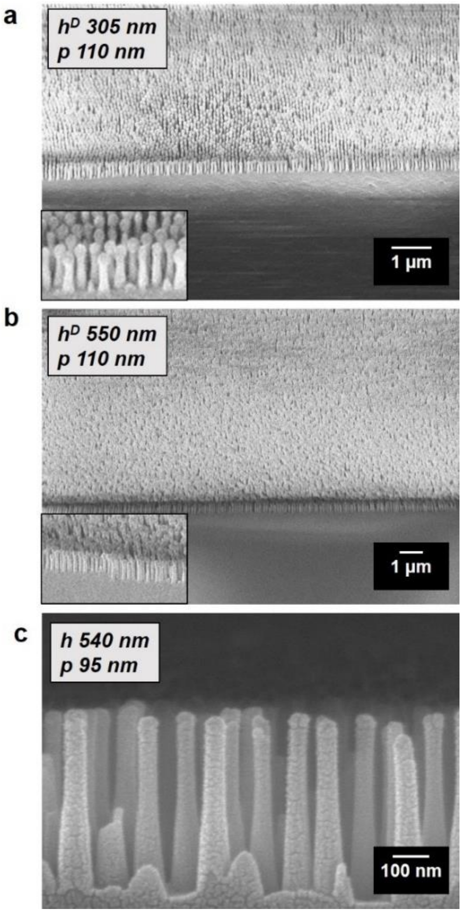

Figure 33 | Exemplary glass nanopillars. **a,b,** Glass nanopillars with *p*=110 nm at the end of cycle n = 1 (a) and n = 3 (b) showing the uniformity across the surface. **c,** Glass nanopillars with *p* = 95 nm and *h* = 540 nm obtained through our process. Note the even heights of the presented structures.

Applying now the concept to a mask of larger pitch (P400; *p*=260 nm), three different Ar flows were tested; 50, 55, and 65 sccm. Assessing the structures after 20 min of etching at these conditions, revealed that for Ar = 65 sccm, the process had reached a maximum, resulting in the complete removal of mask, and destruction of the glass pillars (SEM micrographs not shown). Proceeding instead with Ar = 50 sccm, which provides an R^D slightly greater than R^S, the structures were assessed after 10, 15, and 25 min, as shown in SEM images in Figure 34a-c; where the quality and uniformity of the obtained arrays is evident.

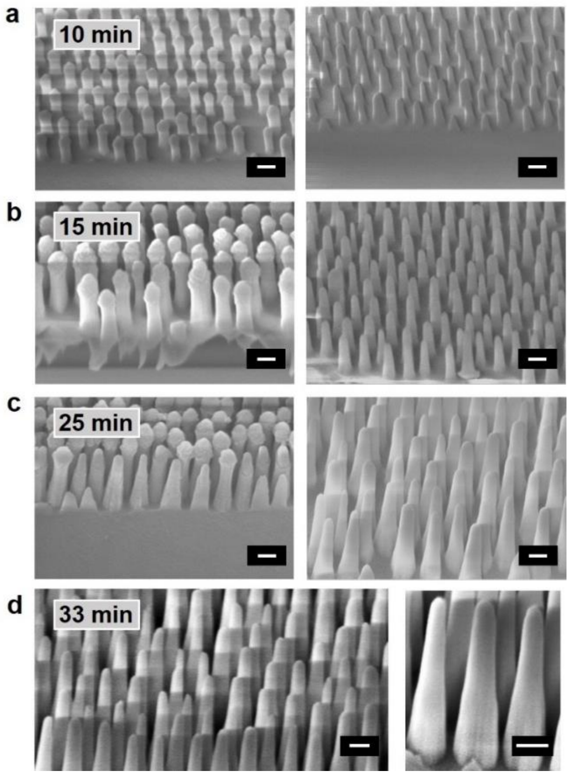

Figure 34 | Glass nanopillars templated from BCP P400. **a-c,** SEM tilted images of evolving glass nanopillars with carbopolymer deposition (left panel) and cleaned by O_2 plasma (right panel). The process was optimized for BCP P400 and resulting pitch *p*=260 nm. Nanopillars after 10 (a), 15 (b), and 25 min (c) of the first etching cycle were obtained by using CHF_3:H_2:Ar = 3:1:10. **d,** SEM tilted image of glass nanopillars. After 25 min, the breakthrough etch (18 s) was applied, and the second etching cycle for 8 min was followed using CHF_3:H_2:Ar = 3:1:11. The resulting structures possess *h* = 1080 µm. Scale bars 200 nm.

Additionally, the evolution of the height and top diameter with and without deposition over time is shown in Figure 35. In order to etch further, we performed an oxygen breakthrough of 18 s, which was calculated from the known etch rate, and the d_T^D. For the subsequent etch, the Ar flow was increased to 55 sccm for a further 8 min in order to induce greater anisotropy and obtain structures with a height >1 µm, possessing more vertical sides near the base, and tapered sides leading to the apex (Figure 34d).

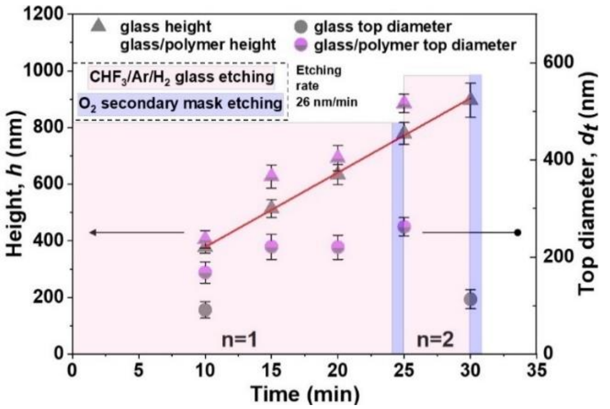

Figure 35 | Fabrication process of glass nanopillars templated from BCP P400. Example of nanostructure evolution during *n*=2 cycles, monitored by changes in height and top diameter, with and without deposited carbopolymer. The linear fit (red line) indicates etching rate of 26 nm/min.

The importance of the breakthrough etch 2 (reduction of secondary mask) is highlighted in Figure 36. Glass templated from P400 was etched for 25 min under Ar = 50 sccm (end of the first cycle), and next, 18 s of oxygen plasma was applied *or not* before proceeding with additional 7 min of glass etching (Figure 36a,b and Figure 36c,d, respectively). As can be seen, the secondary mask is smaller at the end of total etching in Figure 36a than that in Figure 36c, and the obtained structures are taller, well-separated, and with an even baseline (Figure 36b). The structures in Figure 36d, on the other hand, are shorter and exhibit an uneven baseline.

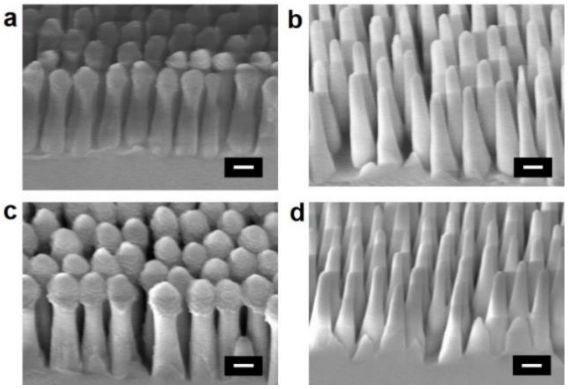

Figure 36 | Control experiment. **a**,**b** SEM images of the pillars with deposition and cleaned, respectively, which were templated from the BCP P400. At the end of the first cycle (n=1), the sample was subjected to the breakthrough etch 2 (18 s) to refine the secondary mask, and thus allow the subsequent etching cycle (n=2) to proceed. **c,d** SEM images of the pillars with deposition and cleaned, respectively, which were processed following the same recipe as (**a,b**) but without the breakthrough etch 2. Note the difference in deposition and uneven morphology

Adapted from: M. Michalska, S. K. Laney, T. Li, *et al*,. Bioinspired Multifunctional Glass Surfaces through Regenerative Secondary Mask Lithography, **Advanced Materials**, 2021, 2102175

of the resulting structures, highlighting necessity of the breakthrough etch 2. Additionally, pillars in (**d**) are shorter than those in (**b**), suggesting that etching stopped during this process. Scale bars 200 nm.

The above results have demonstrated how to successfully attain glass nanostructures from a BCP mask with sub-100 nm features and limited height through implementation of all the discussed process controls and RSML cycles. However, the principles of the method and its dynamic tunability can be leveraged in other pre-pattern scenarios (in respect to pitch and height), which we show on the example of photoresist. We use nanoimprint lithography (NIL) as an alternative approach to generate scalable etch-mask with sub-100 nm features, while also mitigating the shortcomings to yield a taller photoresist mask (Figure 37b; *h*~100 nm). Due to the greater initial height of the soft mask in comparison to BCP (here four times), less protection/deposition is required, and hence more sputtering is allowed during one cycle. Therefore, sufficient control of the secondary mask diameter can be attained through variation of the Ar flow, without necessitating an oxygen breakthrough to reduce it. However, if structures of greater diameter are sought, then multiple cycles would be required. Important to note however, is that although NIL permits soft masks of higher aspect ratio, above a certain threshold, an attractive force between pillars adjacent to each other induce tip-to-tip lateral collapse (Figure 37c); determined by the distance between the nanopillar masks, their surface energy, Young's modulus, and Poisson's ratio.[185] Consequently, the subsequent etching yields highly uneven structures (Figure 37c). Thus, the issue of soft mask degradation cannot be mitigated by merely increasing its height; again, confirming the need for RSML in this context.

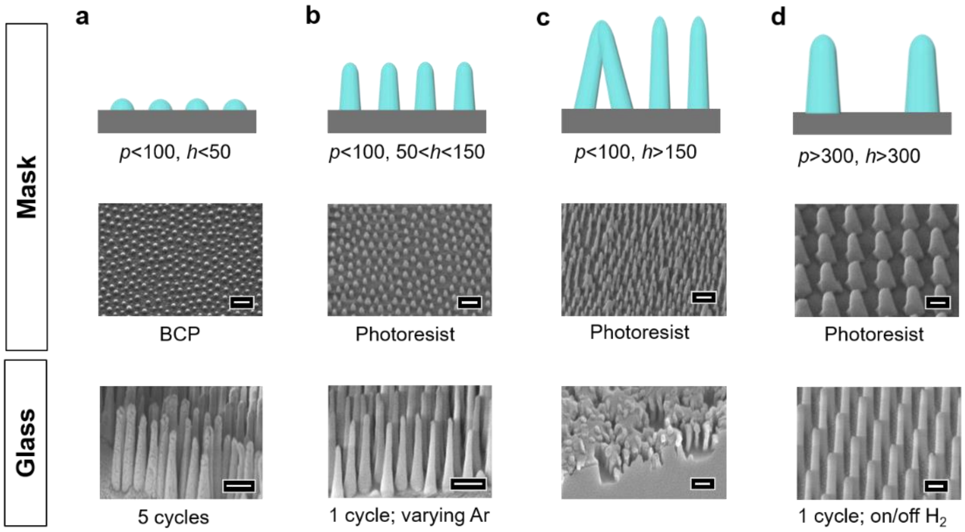

Figure 37 | RSML applicability. Schematics and 45°-tilted SEM images of soft masks of varying pitch/height (approximate ranges) and the resulting glass nanostructures obtained via RSML. Depending on the pre-pattern dimensions, the process was adapted accordingly. **a,** For BCP soft masks of *ca.* p<100 nm and h<50 nm, multiple cycles of RSML are required in order to attain high-aspect ratios as discussed in the main text. **b,** For photoresist masks with *ca.* p<100 nm but height within the range 50-150 nm, only one cycle of RSML with varying Ar flow is required to attain high aspect-ratios. **c,** Increasing the height of the photoresist mask to >150 nm leads to pillar-mask leaning, and upon etching gives rise to uneven structuring. **d,** For soft masks with greater pitch (*ca.* p>300 nm) and height (*ca.* h>300 nm), etching can proceed in one cycle by varying deposition (on/off). Scale bars = 200 nm.

Finally, we demonstrate the case for a photoresist mask with both a greater pitch and height (Figure 38ai; p=350 nm and h~380 nm). We etch initially in the absence of H_2 (Figure 38a) until there is significant mask consumption (Figure 38a(ii)), meaning any further etching under such conditions would result in pillar destruction. At this point, we introduce the RSML concept to induce a secondary mask (Figure 38a(iv)), and attain structures of higher aspect ratio. This also highlights that RSML can be implemented not only at the beginning of the process, but also part-way through in order to re-build a depleted mask.

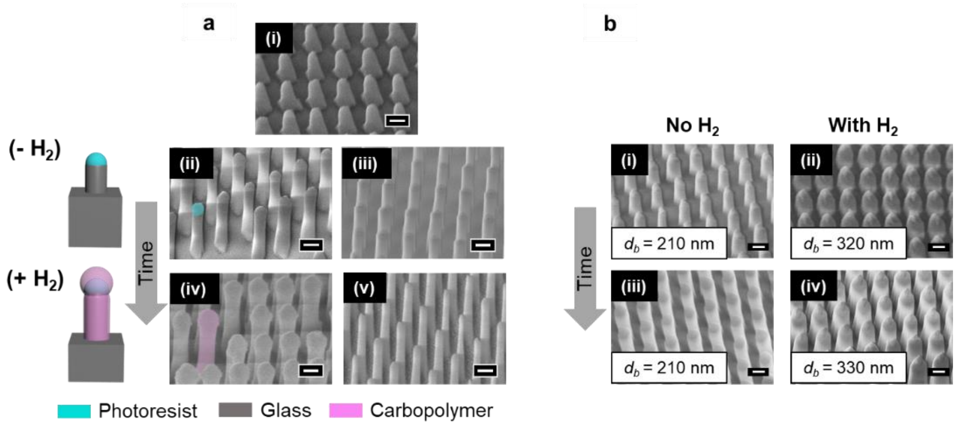

Figure 38 | The effect of an RSML-mediated etch on nanostructure diameter, using a photoresist mask. a, 45°-tilted SEM images and schematics of structures generated after etching from photoresist mask (i) with p=350 nm, h=380 nm, d_b=230 nm. Before (left) and after (right) oxygen cleaning, of glass nanopillars etched in the (ii) absence and (iv) presence of H_2. The added color in SEM images indicates how the depleted mask in (ii), limiting further etching, can be regenerated by using the RSML concept (iv) to increase its durability, which permits deeper etching. **b,** The same mask is etched for an initial 7 min followed by a further 7 min in the absence (i,iii) or presence (ii, iv) of H_2. Without H_2 present, the diameter of the nanopillar is observed to slightly decrease with respect to that of the mask. In contrast, when H_2 is present, a significant increase in the diameter of the nanopillars is observed, and continues to increase with the etch time. Scale bars = 200 nm.

Nonetheless, even for tall photoresist masks, applying RSML at the beginning of the process has the benefit of tuning the diameter of the structure. In Figure 38b, we highlight this effect through comparison of the nanostructure evolution in the presence or absence of H_2. The SEM micrographs reveal that without H_2, a slight decrease (~10%) in the base diameter (d_b) was observed compared to that of the mask, however the d_b is maintained as etching proceeds from 7 to 14 mins, indicating anisotropic etching. Nevertheless, the thin remaining mask (~20 nm) indicates further etching is not possible under these conditions. In contrast, with the addition of H_2 = 6 sccm, a ~40% increase in d_b was observed after 7 min (in respect to the mask), which rises by a further ~4% after a total of 14 min etching. This generates a tapered nanostructure profile, with a d_b (~330 nm) approaching the pitch (~350 nm). Overall, by interchanging the soft mask (BCP to photoresist), we demonstrate the versatility of RSML and highlight three scenarios where it can be employed: (i) to instantly increase the durability of a thin soft mask (*e.g.*, BCP), (ii) to re-build a depleted mask part-way through etching, and (iii) to tune the diameter and profile of the evolving nanostructure (originating from a thin or a thick mask).

Adapted from: M. Michalska, S. K. Laney, T. Li, *et al*,. Bioinspired Multifunctional Glass Surfaces through Regenerative Secondary Mask Lithography, **Advanced Materials**, 2021, 2102175

In order to test the mechanical stability of the nanopillars, we conducted tape-peel tests on two surfaces, differing in aspect ratio (AR) and solid fraction (f_s). Structures with a larger AR are known to have a lower mechanical stability[17] than those of smaller AR, therefore to compare, structures with an AR =2.5, and AR =5.5 were chosen (Figure 39). As the tape test was conducted without functionalizing the structures, it was anticipated that adhesion of the tape to the surface would be high owing to the larger contact area. Therefore, to further challenge the structures of lower AR, a sample with a high f_s was chosen ($f_s = 0.5$). The sample of higher AR, on the other hand, had a $f_s = 0.1$.

The (unfunctionalized) samples and a control (flat) sample were cleaned beforehand, and the tape (Scotch Magic TM tape) was applied by hand and flattened onto the surface using the back of a pair of tweezers. The tape was subsequently peeled from one edge of the sample using tweezers (Figure 39e). Removal of the tape from the low AR sample proved extremely challenging, with a very high adhesion causing the tape to tear. However eventual removal of the tape yielded a surface with a significant coverage of residual tape adhesive; which could be partially removed by sonication in acetone and IPA for ~5 min. The tape contacting the higher AR sample was less challenging to remove, and moreover the tape contacting the flat sample was easy to remove. Upon imaging of the samples under SEM (Figure 39c,d), it was revealed the pillars remained intact, however large areas remained embedded within the adhesive.

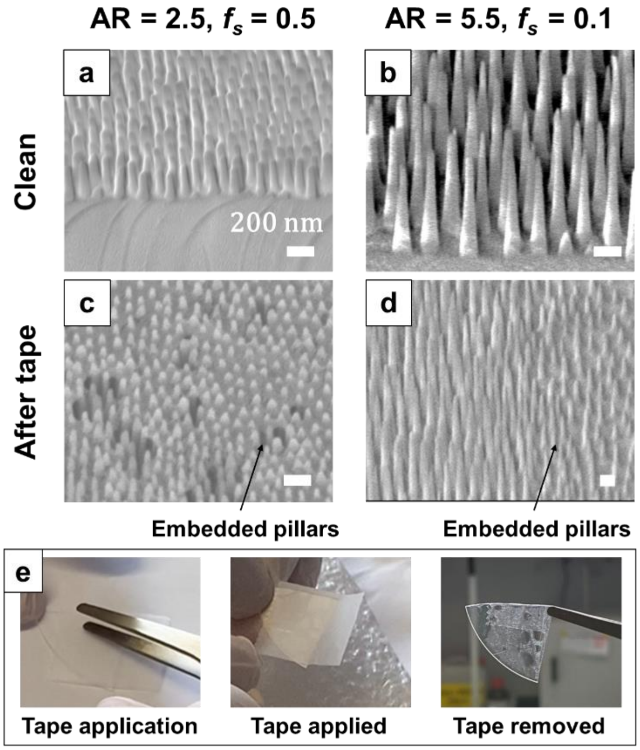

Figure 39 | Tape-peel test. **a,b,** Two unfunctionalized surfaces with nanopillars of AR =2.5 and solid fraction fs 0.5 (a), and AR = 5.5 with fs 0.1 (b) were imaged via SEM prior to the tape peel test. **c,d,** After the tape-peel test, samples were re-imaged via SEM revealing intact pillars with regions embedded in residual adhesive from the tape. **e,** Photographs showing how the tape-peel test was performed. Scale bars in a-d are 200 nm.

3.3.2 Application of Nanostructure Arrays

Through RSML, we now demonstrate the potential and quality of attainable topographies, particularly at reduced pitch (<100 nm), to accomplish high-performance multifunctionality including antireflectivity, high-transparency, superhydrophobicity, and antibacterial activity. We first optimize the nanocones to provide broadband antireflectivity over wide angles. Nanocones operate by adiabatically bridging the refractive index of the substrate with that of air (Figure 15a). Pitch and height are dimensions known to play key roles in discerning the minimum and maximum wavelengths for which reflectance is suppressed.[186] Through our model, a criterion of aspect ratio >2 was defined to effectively suppress reflectance across the visible range. Note, that if antireflection properties were to be maintained into the NIR, an aspect ratio of ~5 would be required, demonstrating the need for high aspect ratio structures.

Every substrate has two interfaces (air-glass and glass-air) where abrupt refractive index changes occur, therefore to further enhance the light transmission across a broad range of wavelength and incident angles, we perform double-sided patterning. In terms of fabrication, this is non-trivial, as it risks damaging the already patterned side, and furthermore the conditions of etching may be altered the second time round, meaning any deviations from the original recipe need to be accounted and compensated for. To minimize these issues, we developed the process shown in Figure 40. Here, we first spin-coat a layer of photoresist PR on side 2 (S1818 MICROPOSIT™, 3k rpm for 35 s; bake at 115 °C for 1 min), which serves to not only protect the glass from scratches, but also minimize alterations in etching conditions, as it ensures both etching processes proceed with an insulating layer of PR on the opposite side, in contact with the platen. The viscosity of the PR should be carefully chosen to allow sufficient pattern coverage. Polyvinyl alcohol (PVA) could be an alternative solution as well as a resist without photosensitivity. Following this, side 1 was cleaned with an acetone wipe and oxygen plasma, and then the BCP was spin-coated. The subsequent RSM lithography process was performed as described previously, with an oxygen plasma at the end to remove carbopolymer deposition, and sonication bath with acetone (three times, 2 min) to remove the protective PR layer on side 1 (nanostructured side), PR was spin-coated onto the etched surface for protection, and then on side 2, the surface was cleaned with an acetone wipe and oxygen plasma, and was subsequently spin-coated with BCP and etched as before. The resulting surface (Figure 40), structured on both sides was sonicated in acetone to remove the remaining PR.

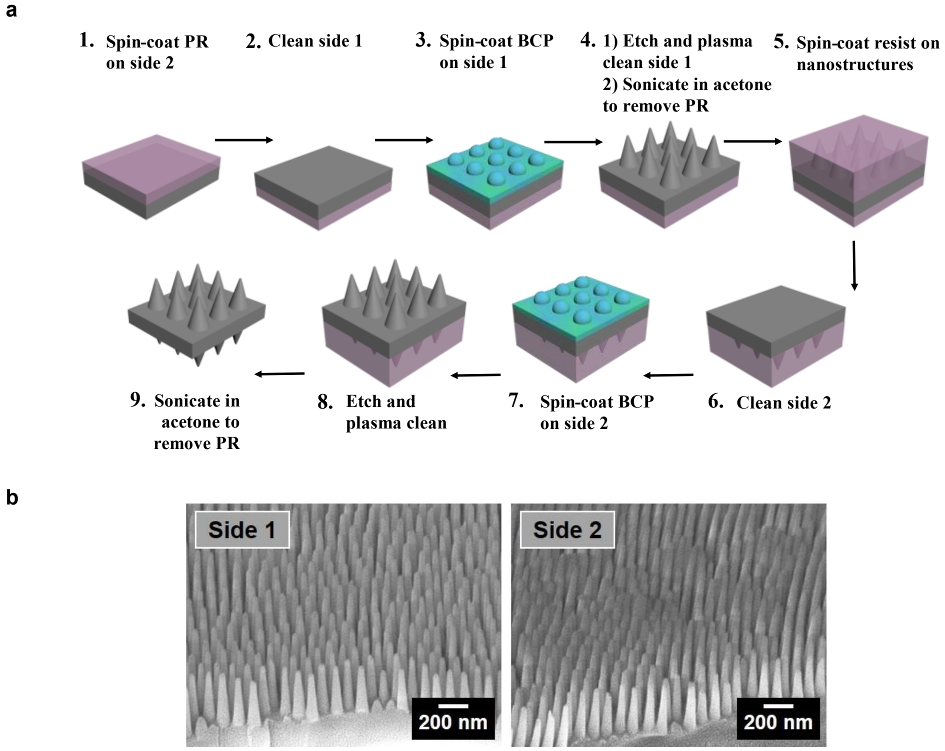
a
1. Spin-coat PR on side 2
2. Clean side 1
3. Spin-coat BCP on side 1
4. 1) Etch and plasma clean side 1
2) Sonicate in acetone to remove PR
5. Spin-coat resist on nanostructures
6. Clean side 2
7. Spin-coat BCP on side 2
8. Etch and plasma clean
9. Sonicate in acetone to remove PR
b
Side 1
Side 2
200 nm
200 nm

Figure 40 | Double-sided glass processing. **a,** Schematic illustration of the double-sided fabrication process consisting of: (1) Spin-coating of a thin photoresist PR layer onto side 2. (2) Flipping of sample, and cleaning side 1 using acetone and a brief oxygen plasma. (3) Spin-coating of BCP micelles onto side 1. (4) Cyclic etching to generate nanostructures, with final oxygen plasma to remove deposition, and sonication in acetone to remove PR from side 2. (5) Spin-coating a layer of PR onto the fabricated nanostructures for protection. (6) Cleaning of side 2 by an acetone wipe and brief oxygen plasma. (7) Spin-coating of BCP micelles onto side 2. (8) Etching to generate nanostructures through our cyclic etching process, with oxygen plasma to remove deposition. (9) Sonication of the sample in acetone to remove PR layer. **b,** SEM image of the resulting double-sided sample used for modelling. The dimensions are listed in the Table S1 below.

The reflectance of our double-sided sample with p = 95 nm, aspect ratio ~4 (Figure 41a), is measured as a function of wavelength and compared against the control (flat) substrate (Figure 41b). Evidently, the reflectance of the sample (~2.5%; calibrated against human photopic vision)[187] was considerably lower than the control (~6.8%) across the whole investigated spectral range. Notably for the chosen aspect ratio, reflectance was sustained to <2% in the near infrared (NIR) wavelengths up to 1100 nm (experimental limit), additionally unlocking NIR applications.[150] We measure the transmittance as a function of the incident angle (Figure 41c) and observe consistent antireflectivity up to 60°, establishing the robust broadband characteristics.[92,150,186,188–191]

Adapted from: M. Michalska, S. K. Laney, T. Li, *et al*,. Bioinspired Multifunctional Glass Surfaces through Regenerative Secondary Mask Lithography, **Advanced Materials**, 2021, 2102175

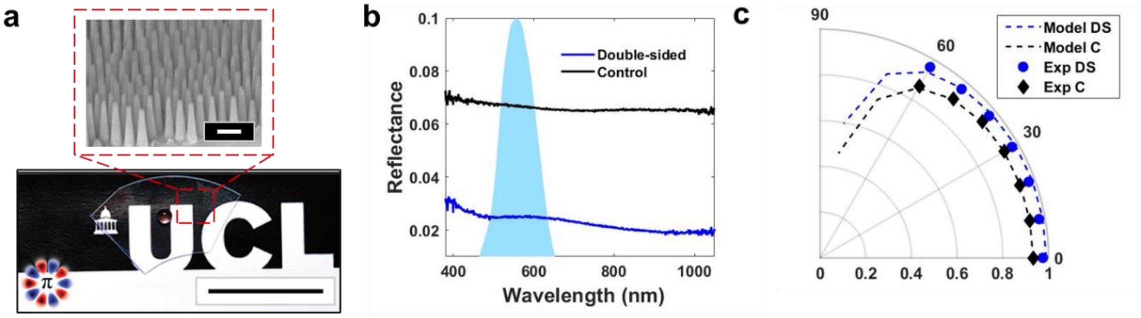

Figure 41 | Optical properties. **a,** Photograph and SEM image of a double-sided etched superhydrophobic glass after fluorosilane-coating (note the round shape of a water droplet). Scale bars 200 nm (SEM image) and 1 inch. **b,** Measured reflectance as a function of wavelength for flat quartz glass (control C; black) and double-sided nanocone sample (DS; blue). Photopic response of human eye is shown with light blue shaded area **c,** Measured and calculated transmission of C and DS samples as a function of incident angle for incoherent, unpolarized light, for photopic calibrated data.

Similarly to the optical requirements, engineering superhydrophobic nanocones with enhanced impact-resistance, is achieved through: small pitch, tapered geometry, and uniform structuring.[92] Crucial for preventing contact-line pinning, a minimized solid fraction was obtained through brief post-processing with diluted hydrofluoric acid (HF, 5%). The solid fraction $\emptyset_s$, was calculated for a hexagonal array as: $\emptyset_s = \frac{2\pi r^2}{p^2\sqrt{3}}$ (*Eq. 8*) where r = radius of curvature of the tip, p = pitch. Physically, the isotropic etching by HF sharpens the tips, whilst also reducing the height and diameter, depending on the process time (SEM images; Figure 42). The effect on wettability becomes clear when comparing the advancing contact angle θ_{adv} of P100 and P400 samples, with and without sharpening. There, θ_{adv} is plotted as a function of r/p, alongside values predicted by the Cassie-Baxter equation: $\cos\theta_{CB} = \emptyset_s(\cos\theta_E + 1) - 1$ (*Eq. 7*) where θ_E is the advancing contact angle on the corresponding smooth surface. Accordingly, we observe a substantial increase in advancing water contact angle (154° to 164°), and decrease in hysteresis (10° to 3°) for antireflective P100 – rendered superhydrophobic.

Adapted from: M. Michalska, S. K. Laney, T. Li, *et al*,. Bioinspired Multifunctional Glass Surfaces through Regenerative Secondary Mask Lithography, **Advanced Materials**, 2021, 2102175

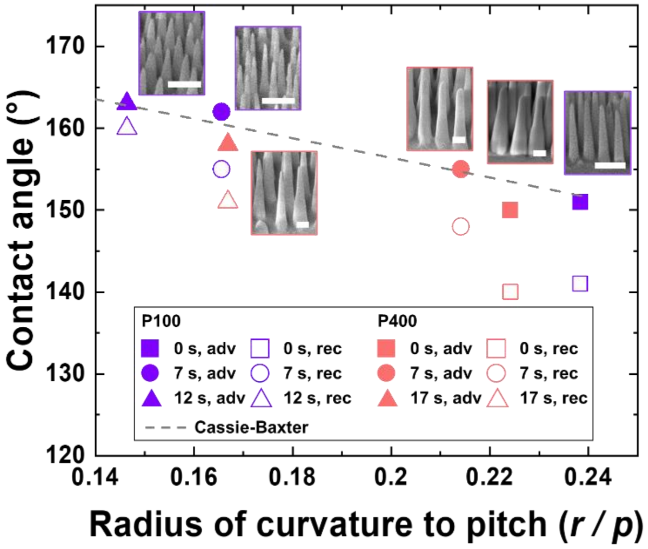

Figure 42 | The effect of sharpening on the sample wettability. Plot of the advancing and receding contact angles as a function of the radius of curvature to the pitch (*r* / *p*) with corresponding SEM images for the P400 (pink) and P100 (purple) samples with and without HF sharpening (0, 7 and 17s for P400, 0, 7 and 12s for P100). Plotted alongside is the Cassie-Baxter predicted trendline (grey dashed). Scale bars = 200 nm.

The coefficient of restitution of droplet bouncing ε also provides a good indication of the global hydrophobicity. It highlights surface inhomogeneities manifested as pinning points which result in a low elasticity. The droplet bouncing of the sharpened P100 with a θ^{a}_{adv}=163° was probed as a function of time (Figure 43) by releasing a droplet of r = 0.9 mm onto the sample from a height of 1 cm. This gave rise to an initial velocity V = 0.33 m/s and We =1.33, where We is the dimensionless Weber number which is a ratio between deforming inertial forces and stabilizing cohesive forces of a fluid. The coefficient ε can be inferred after each bounce using the following formula ε = V'/V, where V' and V are the velocities after and before the impact, respectively. At high velocity (first bounce), a modest elasticity was observed with ε = 0.5, however, the now decreased velocity of the second bounce (V = 0.13 m/s, We = 0.2) results in much greater elasticity, with ε = 0.90. This indicates the presence of a threshold velocity for bouncing, with greater velocities providing a larger degree of deformation and vibration (energy loss). Remarkably, the drop undergoes 17 bounces before coming to rest, with no further detachment from the surface.

Adapted from: M. Michalska, S. K. Laney, T. Li, *et al*,. Bioinspired Multifunctional Glass Surfaces through Regenerative Secondary Mask Lithography, **Advanced Materials**, 2021, 2102175

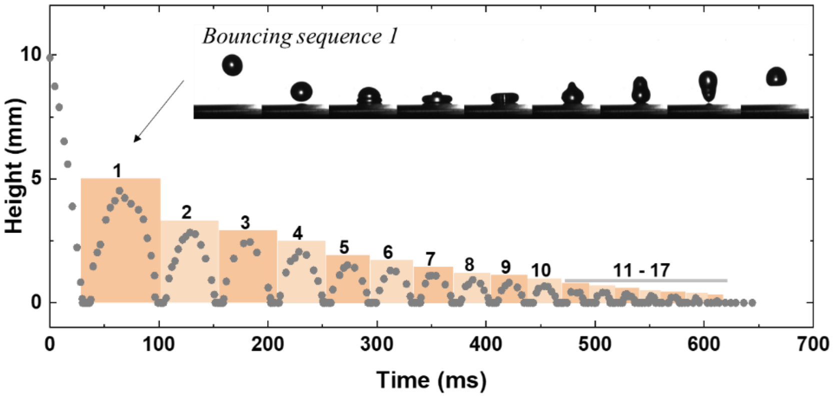

Figure 43 | Rebound characterization of a water droplet. Rebound height of a 3μL droplet on surface P100 vs time. The droplet was released from an initial height of 1cm, and bounces a remarkable 17 times. The inset shows an example bounce.

To investigate high-speed impacts, we deposit droplets of increasing velocity $V = 0.4\text{-}4.4$ m/s at room temperature and observe whether pinning occurs; at $V = 4.4$ m/s, P100 demonstrates no pinning. In a representative splashing sequence (Figure 44a), a droplet of $V = 2$ m/s contacts P100, spreading to a maximum diameter D_{max}. Comparison of droplet diameter D as a function of time for two samples varying in pitch, P100 and P400 ($p = 257$ nm), highlights no difference in the expansion process, and shows consistency relating to higher velocity impacts (greater deformation). During the retraction process – driven by the minimization of droplet surface area and solid-liquid contact – a shorter retraction time τ on P100 was observed, in agreement with previous reports relating to partial impalement.[192] Whilst the higher density of P100 nanostructures suggests a greater wetted area than P400, the reduced pitch yields a higher resistive capillary pressure P_c (which also increases with penetration depth z owing to the tapered profile). The degree of meniscus penetration z/h can be estimated through comparison of P_c with the water hammer pressure P_{WH} and Bernoulli pressure P_B generated by an impacting droplet. [17,47]

Adapted from: M. Michalska, S. K. Laney, T. Li, *et al*,. Bioinspired Multifunctional Glass Surfaces through Regenerative Secondary Mask Lithography, **Advanced Materials**, 2021, 2102175

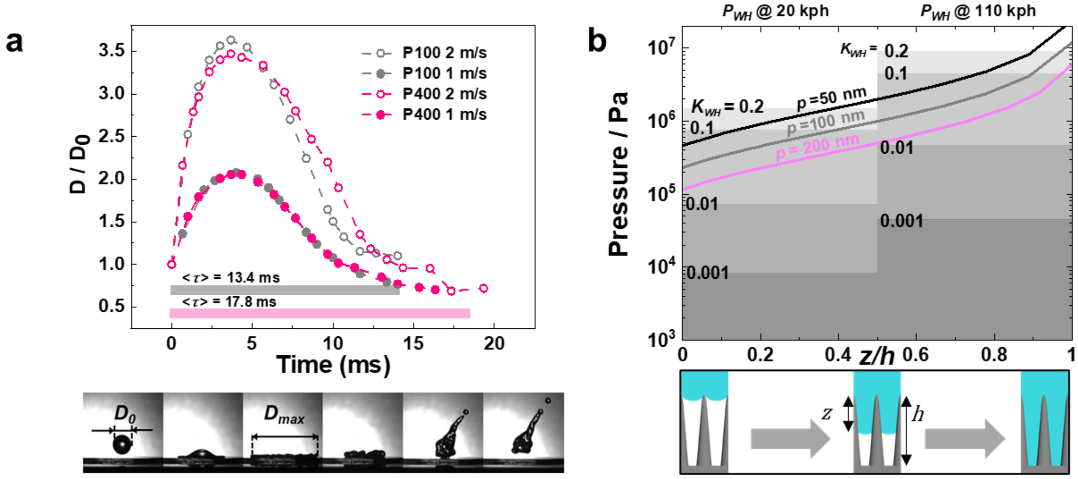

Figure 44 | Wettability characterisation. **a,** Bottom; Sequential images of a droplet impacting a surface with an initial diameter D_0 =2.7 mm, expanding to a maximum diameter D_{max} =9.45 mm as it spreads on the surface, followed by retraction and take-off. The corresponding plot of drop diameter versus time with the y-axis normalized to D_0 is shown for P100 (grey) and P400 (pink) at two impacting velocities: 1.0 m/s (dots) and 2.0 m/s (circles). The average contact time $<\tau>$ of the droplet with the surface is indicated to be 13.4 ms and 17.8 ms for P100 and P400, respectively. **b,** Calculated capillary pressure P_c plotted for nanocones of pitch 50, 100, and 200 nm, as a function of the penetration percentage (z/h), where z is the depth of meniscus penetration and h is the total height. The water hammer pressure generated at impacts of 20 and 110 kph are marked on the graph, with varying values for the water hammer pressure coefficient K_{WH}. The bottom row of schematics serves as a representation of the penetration depth z/h.

The water hammer pressure, which is the pressure surge caused when a moving droplet hits a surface forcing a momentum change, is an empirical parameter proportional to the water hammer pressure coefficient K_{WH}, which was found to vary largely with surface texture (0.001-0.2).[192,193] When considering K_{WH}=0.2 (generating the highest P_{WH}), it is calculated to be 0.6 MPa at a velocity of 2.0 m/s according to:[194]

$$P_{WH} \approx K_{WH} \rho c V_0 \qquad \textit{Eq. 23}$$

Where ρ is the density of water, c is the speed of sound in water, and V_0 is the impacting velocity of the droplet.

Simultaneously, pressure due to liquid compressibility is experienced as the droplet spreads, and is described by the Bernoulli equation to give a value of 2 kPa (supposing the velocity is still 2.0 m/s), according to:[46,194]

Adapted from: M. Michalska, S. K. Laney, T. Li, *et al*,. Bioinspired Multifunctional Glass Surfaces through Regenerative Secondary Mask Lithography, **Advanced Materials**, 2021, 2102175

$$P_B = {}^{\rho}/_{2} V_0^2 \qquad \textit{Eq. 24}$$

Comparing P_{WH} and P_B with the critical pressure required to force the liquid meniscus into the nanostructure, P_c, indicates whether the liquid penetrates (P_{WH} or P_B>P_c), or not (P_{WH} or P_B<P_c). P_c is obtained through:

$$P_c = \frac{4\pi\gamma r cos(\theta - \alpha)}{\sqrt{3}p^2 - 2\pi r^2} \qquad \textit{Eq. 25}$$

Where r and p are the radius and the pitch of the structure, θ is the advancing angle on the corresponding smooth surfaces, α is the cone angle, and γ is the interfacial tension of water (7.2 x 10^{-2} N m^{-1}).

When considering K_{WH} = 0.2 (generating the highest P_{WH}), the structures indeed should withstand an impact of *V* = 2.0 m/s so that *z/h* for P100 is ~30%, whereas for P400 it is ~60%.[47]

The significantly lower infiltration for P100 highlights the need for such resolution. In Figure 44b, the trend becomes even more apparent when comparing the P_c for nanostructures of reducing pitch (*p* = 200-50 nm) to the P_{WH} (with K_{WH} varying between 0.001-0.2) generated at speeds of 20 and 110 kph; commonly found in practical settings. Furthermore, nanocones of increasing aspect ratio are also calculated to withstand higher droplet impacts owing to the greater unfavourable contact experienced between the droplet and the functionalized nanocones for an aspect ratio of 5 (for instance) compared to an aspect ratio of 1 at the same penetration depth (Figure 45).

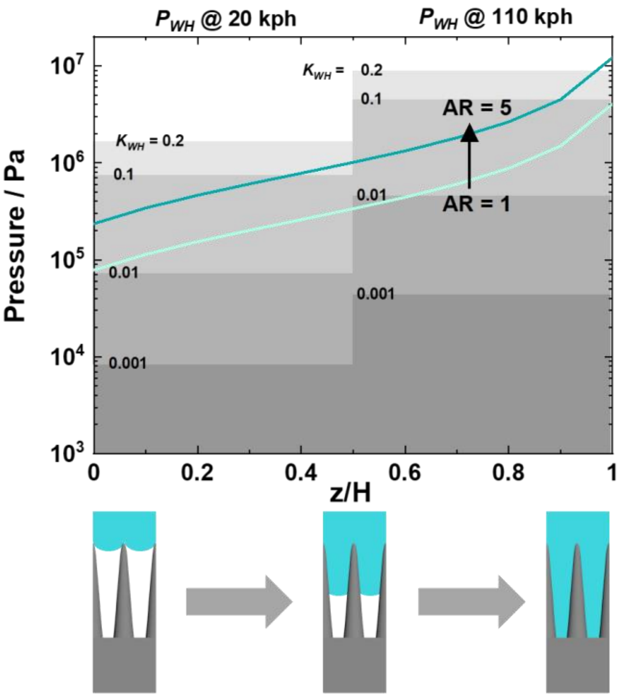

Figure 45 | Capillary pressure versus penetration percentage. Calculated capillary pressure P_c plotted for nanocones of aspect ratio 1 and 5, as a function of the penetration percentage (z/h), where z is the depth of meniscus penetration and h is the total height. The water hammer pressure generated at impacts of 20 and 110 kph are marked on the graph, with varying values for the water hammer pressure coefficient K_{WH}. The bottom row of schematics serves as a representation of the penetration depth z/h.

Clearly, a reduced pitch benefits the discussed functionalities, however predicting antibacterial properties is more complex due to the multitude of contributing factors including both material (aspect ratio/elasticity/shape/pitch)[14] and cellular features (rigidity/motility).[88] The non-trivial simulations have led to models which propose often opposite design criteria, with ambiguity concerning pitch but general agreement on the merits of sharper tips.[89] Here, we focus on the interactions with *S. aureus* (Gram-positive – highly-rigid and thus harder to inactivate than Gram-negative species),[89] and for guidance, calculate the pressure exerted on cells by various topographies.[90]

Unlike other approaches,[195,196] treatment of the interfacial energy gradient as the *driving force* promoting bacterial migration into the nanostructure, addresses the system in less abstract terms (energy as opposed to force).[90] The calculation of the interfacial energy gradient between cells and nanopillars follows the concept recently presented by Liu *at al.*,[90] with some adaptations. We focus here on the interactions with *S. aureus* possessing a volume of ~10^{-19} m^3, which was not considered in the reported study. Additionally, we investigate a hexagonally-packed array as opposed to square-packed[90] which results in an increase of surface roughness as well as solid fraction that is in contact with the cell.

Figure 46 illustrates schematically *S. aureus* cells, adhered to the flat (a) and structured surface with nanopillars (b). The pillars are characterized by pitch *p*, height *h*, and diameter *d*. Although *S. aureus* is considered a coccus, based on the SEM image processing, we treat its shape as a non-perfect sphere with a short segment *L* between two hemispheres. After cell adhesion to the surface, a flat base is formed of length *L* and width $2r_s$. The attached cell forms an adhesion angle with flat surface and nanopillars, θ_c and θ, respectively.

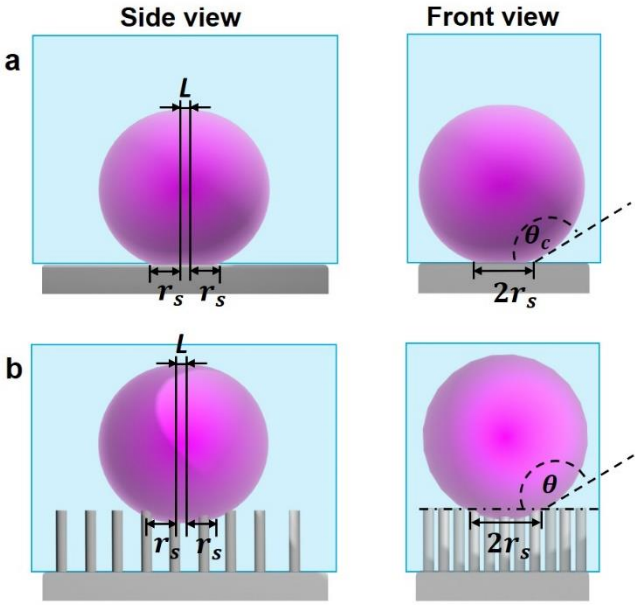

Figure 46 | Schematic of *S. aureus* adhered to the surface. **a,** The cell on flat surface is in contact with the substrate *via* flat base of the length *L* and width $2r_s$, and an adhesion angle $\boldsymbol{\theta_c}$. The three interfaces are observed between the cell (purple), solid (grey) and liquid (blue) **b,** The cell on nanostructured surface is in contact with the substrate *via* flat base of the length *L* and width $2r_s$, and an adhesion angle $\boldsymbol{\theta}$. In this study, $\boldsymbol{\theta_c = 150°}$ and $\boldsymbol{\theta = 157°}$, as measured by ImageJ.

In this model, the interfacial energy gradient which involves nanostructures and the attached cells is considered as the driving force F_d of bacteria into the nanostructure and it includes: (i) Gibbs free surface energy γ and (ii) deformation surface energy σ (which concerns all the changes related to when the cell wall deforms). For a hydrophilic nanostructured surface, there are solely liquid and solid interfaces beneath cell. Hence, the energy E can be expressed as follows:

$$E = A_{up}\sigma_{CL} + A_{bCL}\sigma_{CL} + \left[(r-f)A_{total} - \left(A_{bCS} - fA_{pCS}\right)\right]\gamma_{SL} + f\left(A_{total} - A_{pCS}\right)\gamma_{SL} + A_{bCS}\sigma_{CS} \qquad \textit{Eq. 26}$$

Where A_{up} – upper surface area of an adhered cell above the solid; A_{pCS} – adhered projection area between the cell and the solid surface; A_{total} – surface projection area including the cell; γ_{SL} – surface free energy of solid-liquid interface; σ_{CL} and σ_{CS} – deformation surface energy between cell and liquid or solid, respectively; r – Wenzel roughness; and f – solid fraction that is in contact with the cell.

The gradient E is derived in this model like for the case when droplet migrates towards the nanostructures, and can be written as follows:

$$F_d = -\frac{dE}{dx} = -\left(\frac{\partial E}{\partial x} + \frac{\partial E}{\partial \theta}\frac{\partial \theta}{\partial x}\right) \qquad \textit{Eq. 27}$$

Where $\frac{\partial E}{\partial x}$ corresponds to changing rate of the interfacial energy when cell moves towards the structure along x, whereas $\frac{\partial E}{\partial \theta}$ refers to changes when adhesion contact angle varies. Ultimately, the force can be expressed as:

$$F_d = \frac{r-1}{h}(\pi r_s^2 + 2r_sL)(\gamma_{SL} - \sigma_{CS}) + 2(\pi r_s + 2L)(1 - f)\sin\theta\,\sigma_{CL}\frac{sin\theta(1-cos\theta)\pi r_s^2 + (sin\theta - \theta cos\theta)(1+cos\theta)r_sL}{sin\theta(1-cos\theta)\pi r_s^2 + 2(sin\theta - \theta cos\theta)(1+cos\theta)r_sL} \qquad \textit{Eq. 28}$$

We calculate this force by using the following expressions for interfacial tension and deformation energies:

$$\gamma_{SL} = \frac{\gamma_{LG}}{2}\left(\sqrt{1 + sin^2\theta_w} - cos\theta_w\right) \qquad \textit{Eq. 29}$$

$$\sigma_{CS} = \frac{\sigma_{CL}}{2}\left(\sqrt{1 + sin^2\theta_C} - cos\theta_C\right) \qquad \textit{Eq. 30}$$

$$\gamma_{SL} = \frac{\sigma_{CL}}{2}\left(\sqrt{1 + sin^2\theta_C} + cos\theta_C\right) \qquad \textit{Eq. 31}$$

Adapted from: M. Michalska, S. K. Laney, T. Li, *et al*,. Bioinspired Multifunctional Glass Surfaces through Regenerative Secondary Mask Lithography, **Advanced Materials**, 2021, 2102175

Where θ_w is an intrinsic water contact angle of material substrate (here, PBS on fused silica, θ_w=70°).

Additionally, solid fraction and roughness for hexagonally-packed pattern are given by:

$$f = \frac{2\pi(\frac{d}{2})^2}{p^2\sqrt{3}} \qquad \textit{Eq. 32}$$

And

$$r = 1 + \frac{2\pi dh}{p^2\sqrt{3}} \qquad \textit{Eq. 33}$$

Having the force calculated, we can obtain the value of the pressure P which is exerted on cells by nanopillars using the following equation:

$$P = \frac{F_d}{(\pi r_s^2 + 2r_s L)f} \qquad \textit{Eq. 34}$$

Figure 47 presents the results of the pressure and driving force calculated for the topographies that vary in pitch and diameter in a range of 85-300 nm and 10-60 nm, respectively. The data indicate that indeed, the smaller the diameter (sharper the pillar) at the same pitch, the more pressure is exerted on the cells. Besides, the larger the pitch, the more pressure is generated. However, pitches as small as ~90 nm can be efficient as long as the diameter is small enough. Additionally, if that pressure is greater than the critical elastic stress of the cell wall (1 MPa in this case),[90] creep deformation occurs and depending on the deformation depth with respect to the height of nanopillars, penetration is possible or not.

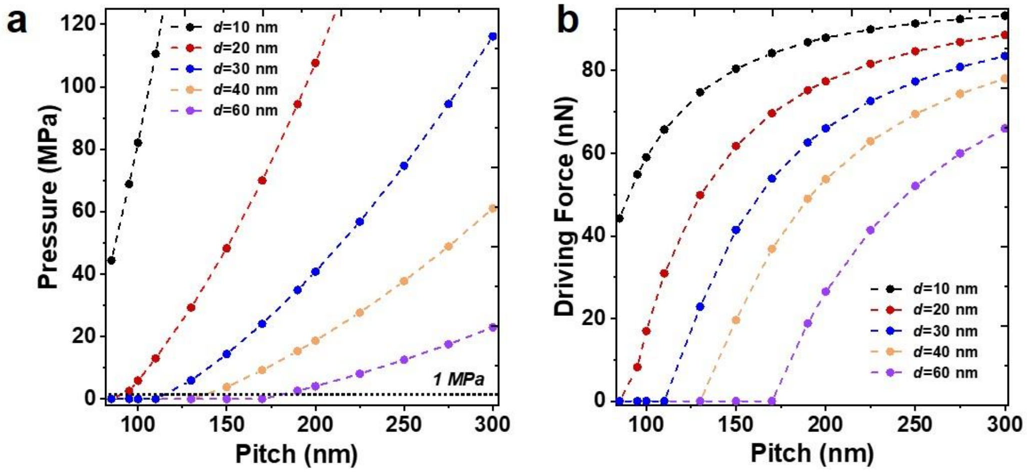

Figure 47 | Effect of geometry of nanopillars on the interactions with *S. aureus*. **a,** The calculated pressure acting on the cell as a function of pitch, with varied diameters (10-60 nm). **b,** The calculated force acting on the cell as a function of pitch.

For our P100 structures, (p=110 nm; d_T=21 nm), the model predicts a pressure of ~10 MPa indicating that creep deformation can occur with the potential to rupture given sufficient nanopillar height.

Experimentally, we investigate the antibacterial properties by viable counting and surface fluorescent imaging, where live and damaged/dead cells are visualized based on their membrane integrity (Figure 48a-c). Both measurements indicate significantly reduced numbers of viable bacteria after interacting with the nanostructures comparing to the control. The average proportion of non-viable cells on the surface is 81%, matching our theoretical predictions and previous results obtained with silicon (83-85%)[82] – this is the first demonstration of comparable activity with a glass substrate.

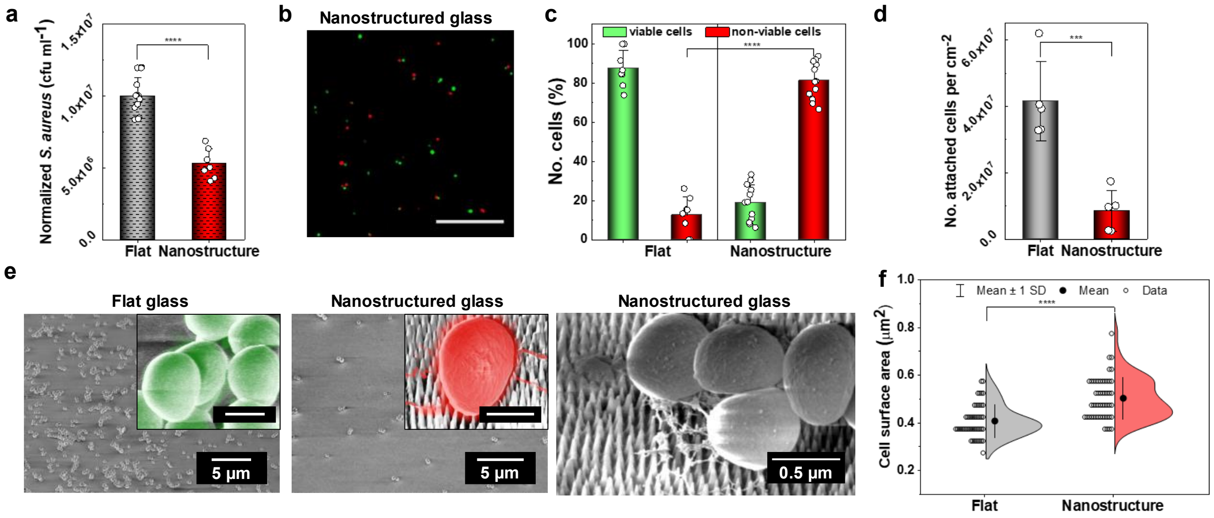

Figure 48 | Antibacterial properties of glass nanostructures. **a,** Number of viable *S. aureus* cells after interacting with flat (control) and nanostructured glass surface (nanopillars p=110 nm, h=230 nm, d_t=20 nm) in PBS for 18 h, assessed by viable counting. Nanostructures show a significant reduction in the number of viable bacteria with respect to the control (****P<0.0001, t-test, error bars show SD calculated from n=3 independent experiments containing replicates ≥3 – circular markers, the data were normalized to 1.0x10^7 colony forming units/ml). **b,** Fluorescent micrograph of *S. aureus* on nanostructured glass stained with LIVE/DEAD BacLight kit, where red dye indicates cells with compromised membranes (damaged/non-viable) and green dye indicates viable cells. Scale bar 20 µm. **c,** Plot showing antibacterial efficiency (81%, compared to 12% on the control) of the nanostructured glass expressed as a percentage of non-viable cells out of the total counted cells (****P<0.0001, t-test, error bars show SD, n=3 independent experiments). **d-f,** SEM imaging reveals marked differences in the number of attached bacteria to the flat and nanostructured surface (***P<0.001, t-test; (d)) and in the morphology of attached cells, as can be seen on SEM micrographs (e), which is quantitively determined by an increase in the average projected cell surface area (****P<0.0001, t-test; (f)). SEM micrographs are representative of three independent surfaces. Scale bars in insets 0.5 µm.

More advanced studies such as high-resolution imaging and changes in protein expression have recently shown that on different topographies or within the same, some bacteria can be impaled or deformed on nanopillars, and some exhibit an enhanced oxidative stress response, resulting in mechanically-ruptured and lysed cells or not.[14,89] This multitude of scenarios suggests that either

Adapted from: M. Michalska, S. K. Laney, T. Li, *et al*,. Bioinspired Multifunctional Glass Surfaces through Regenerative Secondary Mask Lithography, **Advanced Materials**, 2021, 2102175

several mechanisms exist at once for some structures, or one dominates, driven by a particularity of the topography-bacterium pair (and likely environment). Therefore, to elucidate the underlying mechanism, we further probe the surface by SEM imaging (Figure 48d-f) and discover the significantly lower number of adhered bacteria to the nanostructures than to the controls, also observing that ~50% of those attached cells are ruptured/lysed (see Methods). Amongst the bacteria that appear intact on the nanostructures, we note they appear flattened/deformed when resting on nanopillars, yet there are no clear signs of their disintegration (debris or cytosolic content visible). This can be attributed to cellular leakage (washed away), loss of turgor pressure, and/or stretching deformation upon adhesion (which likely is pre-(full) rupture provided the number of dead bacteria found by fluorescent imaging which scores viability based on the membrane integrity). Analysis of the average cell surface area and its distribution (Figure 48f; see Methods) reveals an increase, further confirming the bacteria are flattened. Nonetheless, although made of glass, we cannot exclude the role of pillar flexibility due to their fine size, to contribute to the overall performance *via* a recently proposed energy storage-release mechanism.[197] Overall, this demonstration of antibacterial glass indicates that at *p*~100 nm, *S. aureus* is killed with an efficiency matching the best reported structures in silicon, leading to bacteria lysis through stretch-and-rupturing and likely piercing, enhanced by the deflection of nanopillars. Further gains in performance are anticipated by adjusting the AR, however we reserve this investigation for future studies, and instead place emphasis on the potential of RSML as a fabrication tool in controllable nanoscale glass etching to achieve such functionalities.

3.4 Conclusions

In summary, we present a two-step fabrication concept to realize uniform nanostructures of varying aspect ratio with high-resolution in glass. This significantly simplifies current complex approaches while offering superior control – stemming from both the masking (pitch; mask type), and the etching, with *in-situ* secondary organic mask formation (tapering/diameter/height). Overall, this constitutes a generic solution for enhancing etching selectivity to elicit deep structures templated from thin soft masks. We anticipate these qualities to drive glass fabrication in both academic and industrial settings due to attainable feature dimensions (including <100 nm; aspect ratio >1), well-aligned with emerging trends in the design of multifunctional surfaces. We draw attention to the method potential by balancing optical transparency, water impact-resistance, and importantly, realize the first reported nanostructured glass surface capable of killing *S. aureus* with 81% efficiency. Despite the vast market for such antimicrobial product, scarce examples of nanostructuring exist in glass,[198] making RSML particularly important to drive this field forward, by providing the tools for systematic studies *via* tuning nanostructures shape and aspect ratio. Overall, the ability to simultaneously attain some or all of these properties may find use in applications including solar panels, high-rise glass buildings, food/therapeutics packaging and hospital/bathroom settings, to list a few.

3.5 Methods

Block copolymer (BCP) micelles preparation: BCP micelles of PS-*b*-P2VP [poly(styrene-*block*-2vinylpyridine), Polymer Source Inc.] were pre-assembled according to the previous report,[128] with certain adaptations. To accommodate pitch ranging from ~50-300 nm, four molecular weights were used: P57, P100, P200, and P400 corresponding to M_n (*10^3 g/mol): 57-*b*-57, 109-*b*-90, 248-*b*-195, and 440-*b*-353, respectively, with the following polydispersity index (M_w/M_n) values: 1.05, 1.08, 1.09, 1.18. The polymers were mixed with anhydrous *m*-xylene at the concentrations of 0.3-0.5% w/v by gentle stirring at 75°C for 16 h to form spherical micelles. Subsequently, the solutions were allowed to cool to room temperature (RT), filtered (PTFE 1 μm), and stored at 4°C.

Nanopillars fabrication in glass: The fabrication scheme is presented in Figure 24a. During the first step, the pre-assembled micelles were spin-coated for 30 s (SCS G3 Spin Coater) onto the pre-cleaned (acetone, isopropanol) glass wafer at RT (Fused silica JGS1, 2”-wafer, 500±25 μm; MicroChemicals GmbH). For P100, the typical spin speeds were 3 and 6k rpm, whereas for P400, we used 1-2k rpm. To register the pattern in glass, reactive ion etching (RIE) was conducted using PlasmaPro NGP80 RIE, Oxford instruments, at temperature of 20°C. First, breakthrough etch 1 was performed to tune diameter of the mask and remove PS matrix under O_2 (20 sccm), pressure 50 mTorr, and radio frequency (RF) power 50 W. Time varied between 3-14 s depending on the BCP used (e.g., 3 s for P57 and 4 s for P100). Subsequently, glass was etched using $CHF_3/H_2/Ar$ gases at flows 12-15, 0-6, and 45-75 sccm, respectively; under pressure of 30 mTorr and at RF power of 220 W. The optimal values were found to be 15, 5, and 65-70 sccm. Note, the Ar flow can be constant or varied to manage the deposition, diameter, and sidewall tapering. The etching depth was controlled by the etching time and could only proceed until secondary mask reached a maximum diameter equal to the pitch. If a taller structure was required, breakthrough etch 2 was performed under O_2 plasma (conditions as above) to reduce the diameter of the secondary mask (d_T^D). The time of this etch was estimated based on the d_T^Dvalue and etching rate (~2 nm/s). The typical values used were 10-16 s. This completes the first etch cycle which can be iterated until a desired height is reached. Eventually, the sample was cleaned under O_2 plasma (50 sccm, RF power 200 W) for 2 min. For very high-aspect ratios, an additional chamber clean between the cycles may be required due to continuous passivation of the reaction chamber.

Surface characterization: Topological characterization of BCP patterns (diameter, pitch) was evaluated using an Atomic Force Microscope (Dimension Icon-PT from Bruker AXS) in tapping mode in air at room temperature. The scanning speed was 1.00 Hz/s with 256 Samples/Line. The tips were NANOSENSORS™ PPP-NCHR, which have a tip radius curvature <10 nm, tip height 10-15 um, and are highly doped silicon with an Al coating on the detector side. The pitch was determined by using ImageJ (https://imagej.nih.gov/ij/) software with a nearest neighbor distance plugin. The scanning electron micrographs were taken by a Carl Zeiss XB1540 SEM and SmartSEM software (equipped with tilt correction) at 2-5 kV operating voltage. Prior to the imaging, the samples were sputter-coated with Au. For both AFM and SEM imaging, at least five independent fields were measured. ImageJ was used for statistical analysis of the nanostructure dimensions such as pitch, height, diameters (with 50 quantities measured). The chemical composition was characterized by X-ray photoelectron spectroscopy (XPS) with a Thermo Scientific K-Alpha Photoelectron Spectrometer using monochromatic Al kα radiation at 1486.6 eV. Survey scans were collected in the binding energy range of 100-1100 eV at a pass energy of 160 eV. CasaXPS version 2.3.16 software was used for peak fitting and binding energies were adjusted to adventitious carbon (284.5 eV) for charge correction.

Transmission/reflection Measurements: Transmission measurements were performed by attaching the samples to the input port of an integrating sphere (Labsphere) and illuminating the samples with a collimated white light source (Labsphere, KI-120 Koehler Illuminator). The output port of the integrating sphere was connected to a CCD spectrometer (Ocean Optics) by optical fiber. Measurements were taken at angles of incidence between 0-60° in intervals of 10° by rotating the imaging sphere and light source. Reference measurements were taken at each angle to consider the angular response of the setup. Since the samples are non-absorbing reflectance R was calculated as $R = 1 - T$. Beyond 60º, the signal-to-noise ratio originating from our experimental set-up degraded significantly, hindering the measurements. We therefore use our model, and expand the analysis up to 80º. We observe significant degradation above 60º in agreement with past results,[92,150] resulting from the z-component of the k-vector going to zero for grazing angles of incidence, thereby requiring very large aspect ratio to fulfil impedance matching conditions.[186]

Functionalization: The samples were first cleaned *via* sonication in acetone and isopropanol, and then subjected to an oxygen plasma (Diener Femto Plasma Etcher) in order to impart surface hydroxylation (5 min each, maximum of power generator). Immediately following this, they were immersed in a 2% v/v heptadecafluorotrimethoxysilane solution in anhydrous toluene at room temperature for 24 h, washed, and subsequently annealed at 120 °C for 30 min.

Wetting characteristics: Both advancing and receding contact angles were measured using a custom designed goniometry setup. The setup consists of syringe pump (Cole-Parmer Single-syringe infusion pump), a needle (BD PrecisionGlide™ needles, 21G), and an imaging device (Thorlab, model DCC1240). Droplets of ~30 µl were deposited onto the surfaces and further extracted using the syringe pump to measure advancing and receding contact angle, respectively. The videos taken during droplet deposition and extraction were processed through a Matlab script for contact angle measurements.[199]

Droplet bouncing was characterized by releasing a droplet of radius r=0.9 mm (~3 µl) from a pipette onto the sample from a height of 1 cm, giving rise to an initial velocity V=0.33 m/s and We=1.33. A high-speed camera (Phantom V411 fitted with a macro lens) was used to record and count the number of bounces. Freeze frames were taken, and the height of the droplet over time was measured using ImageJ.

Droplet impact experiments were carried out by dispensing droplets with an unperturbed radius r_0=1.35 mm from a needle (BD PrecisionGlide™, 21G) mounted at different heights to obtain a range of impact velocities, and recorded using a high-speed camera. Freeze frames were taken, and the diameter of the droplet as a function of time was measured using ImageJ.

Bacterial cultures: A model Gram-positive bacterium, *S. aureus* ATCC 6538 was used in this study as it is recommended by the ISO standard (International Organization for Standardization) JIS Z 2801 (2010) for assessing the antibacterial properties of materials. Bacteria were maintained frozen at -70°C and cultured on brain heart infusion (BHI) agar. To prepare the inoculum for application to the materials, bacteria were cultured to mid-exponential phase in BHI broth, aerobically, at 37 °C and with shaking at 250 rpm. The bacteria were recovered by centrifugation, washed twice in phosphate-buffered saline (PBS), and diluted to 10^7 colony forming units (cfu)/ml, unless stated otherwise.

Determination of bacterial viability: The antibacterial properties of the nanostructured surfaces were quantitatively evaluated using an adhesion based-assay. First, test surfaces and controls (flat fused silica; both 1 cm^2) were flame-sterilized and an inoculum volume of 25 µl ($2.5x10^5$ cfu) applied by dropping onto, followed by incubation for 18 h at room temperature (25 °C) in a high humidity achieved by placing soaked filter in the petri dish. Subsequently, the non-attached bacteria were washed off and collected, serially diluted to obtain 30-300 colonies per plate, spread on agar plates, and incubated at 37 °C for 18 h. Finally, the colonies were counted, and bactericidal efficiency (BE) determined according to the following equation: $BE = 100 - \left(\frac{V_x}{V_{ctrl}}\right) \cdot 100$, where *V*, *x*, and *ctrl* refer to the number of viable cells, experimental and control sample, respectively. The experiment was performed three times with 3-6 technical replicates.

The viability of the bacteria that remained attached onto the surfaces was evaluated by confocal laser scanning microscopy (CLSM) using LIVE/DEAD staining. The surfaces were rinsed with 1x Tris-buffered saline (TBS) to remove traces of the growth medium (known to quench the fluorophores), followed by staining with the LIVE/DEAD® BacLight™ kit (L7012, Invitrogen) per the instructions. The kit contains SYTO 9 (green) and propidium iodide (PI, red) dyes that stain the cells depending on their membrane integrity. Bacterial cells with intact membranes are stained green, whereas cells with a damaged membrane (that are considered to be damaged or dead) are stained red. Image acquisition was performed by means of a CLSM (BioRad Radiance2100, Zeiss, Welwyn Garden City, Herts, UK) with 60x objective, and Bio-Rad image analysis software. The cells were visualized by using 488 and 543 nm excitations and HQ515/30 and E600LP emission filters. Two colour channels, green and red, were acquired for each image. To remove the fluorescent background noise from the image, brightness levels in every channel were adjusted. The images were processed by ImageJ for BioRad CLSM imaging by counting cells from a minimum of five fields of view across each surface. The experiment was performed three times with two replicates. The bactericidal efficiency was expressed as a percentage of non-viable cells out of the total counted cells.

SEM imaging of cell-material interactions: Bacterial suspensions containing 10^9 cfu/ml (to generate statistically reliable data) were interacted with the samples for 18 h. Next, the samples were washed twice with 1×PBS, and subsequently fixed using 3% glutaraldehyde solution in 0.1M sodium cacodylate buffer (4 °C, 16 h). After fixation, samples were dehydrated in an ethanol series of 20%, 50%, 70%, 90%, and 100% (v/v) for 10 min each. Subsequently, the samples were immersed in hexamethyldisilazane[200] (HMDS, Sigma Aldrich) for 5 min, air-dried, sputter-coated with Au, and imaged using SEM (Carl Zeiss XB1540) at 2 kV. The images acquired were further analyzed in terms of (i) a number of cells adhered onto to the surface, (ii) the proportion of cells ruptured (when a clearly compromised membrane was observed and/or cellular content was present external to the cell), and (iii) an average cell surface area, A – to express quantitatively if there is a difference in bacterial morphologies between controls and tested samples. Here, clearly disintegrated or dividing bacteria with visible septum were dismissed. ImageJ was used to analyze the images and to accurately determine the surface area of each bacterium, the cells were treated as ellipses. Therefore, the semi-minor and semi-major axes (a and b, respectively) of 50 cells on both flat and nanostructured surfaces were measured, and the area was calculated according to following formula: $A = \pi ab$.

4

TUNEABLE SILICON NANOSTRUCTURING FOR MULTIFUNCTIONAL NANOSTRUCTURES, AND HIGHLY EFFICIENT ANTIFOGGING NANOCONES

This chapter is an amalgamation of two papers (1) in preparation and (2) published in Nature Communications which detail the fabrication route (with some illustrative functionality) and the antifogging behaviour, respectively. This work has very much been a collaborative effort; with fabrication work carried out by TL, MM, and myself; basic functional testing (wettability and optics) performed by TL and IP; and antifogging characterisation and theoretical modelling carried out by our collaborators in France: PL and DQ at École Polytechnique in Paris.

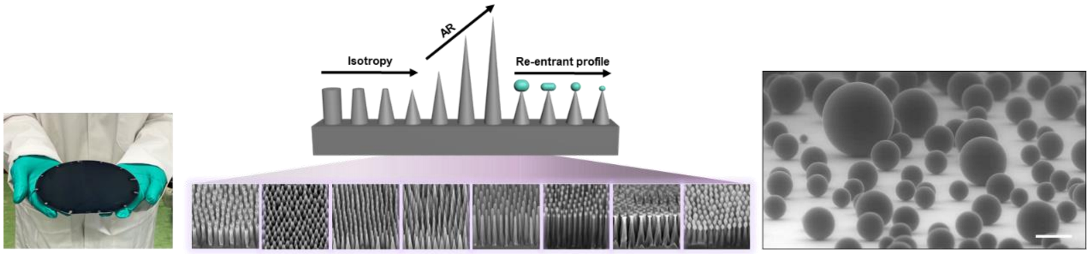

Representative images which demonstrate the scalability (6-inch wafer), the versatility in terms of nanostructure generation, and the antifogging ability (ESEM of condensing microdroplets sitting atop the nanocones; exhibiting very high contact angles and low adhesion).

Adapted from: (1) M. Michalska, S. K. Laney, T. Li, et al., A route to engineered high aspect-ratio silicon nanostructures through regenerative secondary mask lithography, 2021 (in preparation). (2) P. Lecointre, S. K. Laney, M. Michalska, T. Li, *et al.*, Unique and robust dew repelllency of nanocones, **Nature Communications**, 2021, 12, 3458

4.1 Fabrication

4.1.1 Abstract

Silicon nanostructuring imparts unique material properties including antireflectivity, antifogging/anti-icing, self-cleaning, and/or antimicrobial activity. Here, we present a versatile fabrication process to achieve high aspect ratio (>10), tailored silicon nanostructures (thin/thick pillars, sharp/truncated/re-entrant cones), of pitch down to ~50 nm. Our approach relies on pre-assembled block copolymer (BCP) micelles and their direct transfer into a glass hard mask of an arbitrary thickness, enabled by our recently reported regenerative secondary mask lithography. During this pattern transfer, the mask diameter can be also decreased or increased, to reach nanometer-scale inter-pillar spacing; constituting the first method to achieve such tunability without necessitating a different molecular weight BCP. Through hard mask modulation and adjusted silicon etch conditions, the morphology of nanopatterns can be customized. The process control and scalability enable uniform patterning of a 6"-wafer, and we verify the structural homogeneity through cross-wafer excellent antireflectivity (<5%) and water-repellency (advancing contact angle 158 °; hysteresis 1°).

4.1.2 Introduction

Nanopatterning of silicon to afford superior functionality and performance has become commonplace, with demonstrations spanning solar cells,[167,201] energy storage,[202] thermoelectrics,[203] sensors,[204] antibacterial[14,83] and special wetting surfaces.[15,192,205] To elicit the desired and new functionalities however, it is critical to control both the morphology and dimensions of nanofeatures while accommodating a continuous demand for higher resolution and aspect ratio (AR). Such requirements concurrent with method scalability, reliability, and compatibility with existing manufacturing processes are not trivial to achieve, bringing a necessity to advance nanofabrication techniques. In this regard, pattern transfer using block copolymers (BCPs) has been investigated due to their low cost, morphological diversity and proficiency in high resolution patterning (5-200 nm);[174,176,206] overcoming the limitations posed by photolithography and electron beam lithography, for instance.

Adapted from: M. Michalska, S. K. Laney, T. Li, et al., A route to engineered high aspect-ratio silicon nanostructures through regenerative secondary mask lithography, 2021 (in preparation).

Nonetheless, BCP lithography holds its own challenges related either to feasibility of morphology control or insufficient etching contrast. To overcome the former, substrate preparation (neutral brush layer), thermal/solvent annealing, and development steps have been adapted.[121,122,207] Here, conditions need to be carefully chosen, particularly during annealing to prevent de-wetting or undesired morphology formation.[114] This increases the complexity and cost of the fabrication, which constitutes a potential challenge for implementation in industry. Furthermore, control over pitch demands individual optimization for BCPs of different molecular weight M_w, limiting flexibility. Recently, an alternative BCP micelle lithography process was presented whereby pre-assembled solution-phase micelles of poly(styrene – *block* – 2-vinylpyridine) (PS-*b*-P2VP) were directly spin-coated onto a substrate, yielding micellar bumps which act as a topographic contrast.[127,128] This route negates the aforementioned steps, whilst enabling reduction of mask diameter, pitch fine-control through spin speed variation, and coarse-control through choosing a different M_w BCP (without individual optimization).

To achieve high AR nanostructures, a large etching contrast is required. Here, one common route is choosing a silicon-containing BCP – such as PDMS – which under oxygen plasma converts into silicon oxycarbide, leaving a hard mask with enhanced mechanical and thermal stability.[145] This allowed for fabrication of silicon nanopillars/nanoholes/re-entrant structures;[114,160] yet with an AR<2 due to the limited BCP thickness, therefore necessitating an additional layer such as chromium.[161] Alternatively, the constituent blocks of organic BCPs can be selectively infiltrated with metals/metal oxides,[47,162,163] to yield high AR arrays of nanopillars/cones/gratings. In these techniques however, the experimental conditions are delicate, demanding careful matching of precursor and block chemistry to obtain good infiltration efficiency, and in some instances requiring expensive equipment (atomic layer deposition). The cost and impracticality therefore represent a key limitation, with the additional potential introduction of metal contaminants into the chamber. Instead, using a thin 20-25 nm intermediate SiO_2 layer as a hard mask has resulted in high AR porous nanostructures (AR~10),[164] albeit with some success and control for more challenging geometries like pillars and cones; with the achieved AR<2, and little control over morphology.[128]

Herein, we present a library of precisely tailored Si nanostructures (pillars, cones, and re-entrant) with pitches ranging from ~50-260 nm. Using pre-assembled BCP micelles, we apply our recently reported regenerative secondary mask lithography (RSML) process[208] to transfer the pattern into an intermediate SiO_2 layer (hard mask) of an arbitrary thickness. Not only does this method solve the durability problem but it also uniquely allows the hard mask diameter to be increased as well as decreased without necessitating a different M_w BCP. Through modulation of the hard mask, alongside the Si etch conditions (Cl_2 flow, coil/platen power), high AR (>10) Si nanostructures can be generated with precisely tuned morphologies, permitting rational design. Finally, as a proof-of-concept, we demonstrate on a 6”-wafer scale that by engineering the surface nanostructures, an excellent antireflective and robust superhydrophobic surface with ultralow hysteresis (1°) is obtained.

4.1.3 Results And Discussion

Fabrication. A schematic of the strategy to fabricate Si nanostructures is shown in Figure 49 and it relies on BCP transfer into the SiO_2 hard mask, followed by pattern registration in the underlying Si. An SiO_2 layer of thickness T corresponding to the desired height h of the hard mask is first deposited on a silicon wafer. Subsequently, micelles of PS-*b*-P2VP are pre-assembled through dissolution in *m*-xylene and spin-coated to generate hexagonally-packed micellar bumps (step 1; Figure 49), as previously described.[128] The center-to-center distance (pitch, p) is determined predominantly through the M_w of each block, the solvent, and spin speed; and it ranges here from 56-257 nm as shown in scanning electron microscopy (SEM) images in Figure 49. A brief and mild oxygen breakthrough etch is performed to expose the underlying SiO_2 by removing the PS matrix (step 2). This step additionally provides an opportunity to decrease the mask diameter d but at the cost of its height h, lowering the etching contrast in classical approaches. However, the implementation of the RSML for SiO_2 etching in the third step overcomes this issue through inducing secondary mask formation, which acts as a protective layer enhancing BCP durability; hence enabling the pattern to be uniformly transferred through the entire thickness of the deposited SiO_2 layer. This allows for not only SiO_2 height control but also diameter control by varying H_2 content in the gas feed ($CHF_3/Ar/H_2$) so that, simply put, the higher the H_2 amount, the greater the

Adapted from: M. Michalska, S. K. Laney, T. Li, et al., A route to engineered high aspect-ratio silicon nanostructures through regenerative secondary mask lithography, 2021 (in preparation).

mask diameter, as shown schematically in Figure 49 (step 3). Further details are provided in the proceeding sections, where we demonstrate SiO_2 mask of h = 350 nm corresponding to an AR>3.

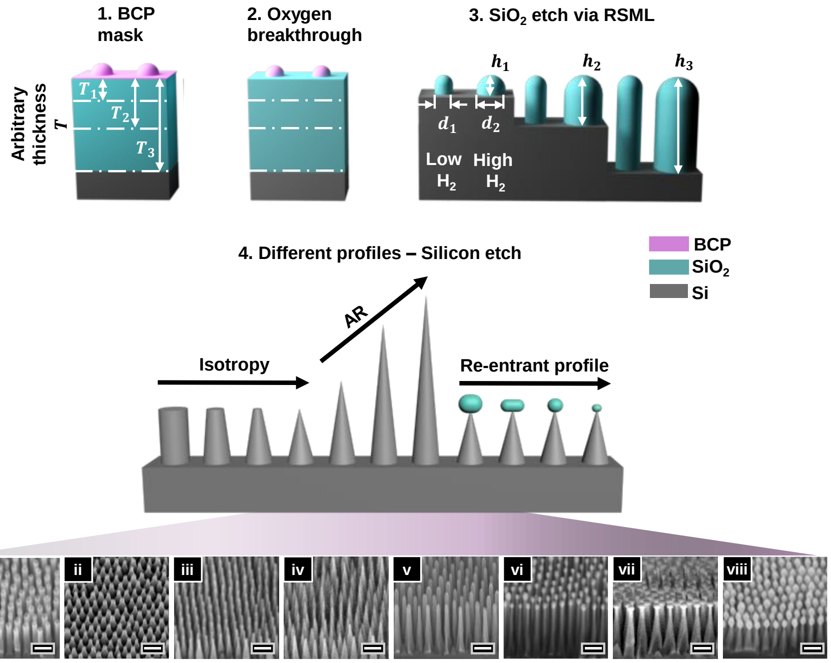
1. BCP mask
2. Oxygen breakthrough
3. SiO_2 etch via RSML
Arbitrary thickness T
T_1
T_2
T_3
h_1
h_2
h_3
d_1
d_2
Low H_2
High H_2
4. Different profiles – Silicon etch
BCP
SiO_2
Si
AR
Isotropy
Re-entrant profile
i
ii
iii
iv
v
vi
vii
viii

Figure 49 | Schematics of the four key process steps to generate a range of tailored Si nanostructures. Mask preparation (1-3) and pattern transfer (4). (1) Spin-coating of pre-assembled micelles to generate hexagonally-packed arrays with typical height h~20 nm; the substrate consists of Si with an SiO_2 layer of pre-determined thickness T; (2) Isotropic oxygen breakthrough etch to remove the PS matrix. Note, the diameter/height (d/h) of the bump can also be reduced at this stage; (3) Transfer of pattern into SiO_2 hard mask, where addition of H_2 gas into the etching chemistry protects the BCP mask through increased carbopolymer deposition. This enables the generation of hard masks with high ARs (h dependent on the T of deposited SiO_2 layer) and permits the d of the mask to be increased ($d_1<d_2$). (4) Etching into Si leads to a library of morphologies: with varying sidewall angle [isotropy; straight-walled pillars (**i**) and cones (**iv**)]; degree of truncation upon the mask removal (**ii-iv**); aspect ratio AR (**iv-vi**), as well as re-entrant profile (**vi-viii**). The pitch is 56 nm (**i**) and 110 nm (**ii-viii**). The end Si structures are engineered based on the h and d of SiO_2 mask, in addition to the etching conditions (coil and platen power/pressure/time). Scale bars are 200 nm.

The pattern transfer into the Si layer (Figure 49; step 4) is governed by a combination of the SiO_2 mask morphology (h/d), and the Si etch conditions. Here, we use Cl_2 plasma, with a characteristic etching selectivity >5, dependent on the coil/platen power, Cl_2 flow, and pressure. Through manipulation of the glass and Si etching, we realize high AR nanostructures with sophisticated sidewall profiles, including nanopillars, nanocones with truncated or sharp tips, re-entrant structures and nanopyramids, all of which are discussed separately in the following sub-sections.

Adapted from: M. Michalska, S. K. Laney, T. Li, et al., A route to engineered high aspect-ratio silicon nanostructures through regenerative secondary mask lithography, 2021 (in preparation).

Tuning the SiO_2 mask through RSML. Typically glass nanostructuring *via* RIE proceeds through a combination of; (i) chemical etching with a fluorocarbon plasma such as CHF_3, (ii) ion-assisted etching with an inert species such as argon, and (iii) simultaneous fluorocarbon deposition CF_x. However, as the etching chemistry stands (CHF_3/Ar), the deposition is not sufficient to prevent premature consumption of the non-robust organic BCP mask, thus culminating in very low AR of SiO_2 masks. Nonetheless, the addition of H_2 increases the formation of HF, in turn lowering the F/C ratio and generating a more polymerizing plasma (greater CF_x deposition). At such conditions, polymer build-up at the top of the structure can be induced,[208] embedding the BCP within a secondary organic mask; depicted schematically in Figure 50a,ii and shown in the SEM inset of Figure 50b. However, left unattended, over-deposition can block the path of bombarding ions and etching species, and prevent further etching. Therefore, in order to attain structures of higher AR, we apply a brief oxygen plasma which acts to controllably reduce the size of the secondary mask, allowing further etching at the base to proceed (Figure 50a,iii). During the subsequent etch, the mask regenerates as described in our previous work on patterning fused silica.[208] This cycle of etching followed by an oxygen breakthrough can be repeated numerous times to reach the desired AR. In Figure 50b, we demonstrate the achieved SiO_2 structures after 2 cycles with p = 110 nm, and h = 350 nm.

Adapted from: M. Michalska, S. K. Laney, T. Li, et al., A route to engineered high aspect-ratio silicon nanostructures through regenerative secondary mask lithography, 2021 (in preparation).

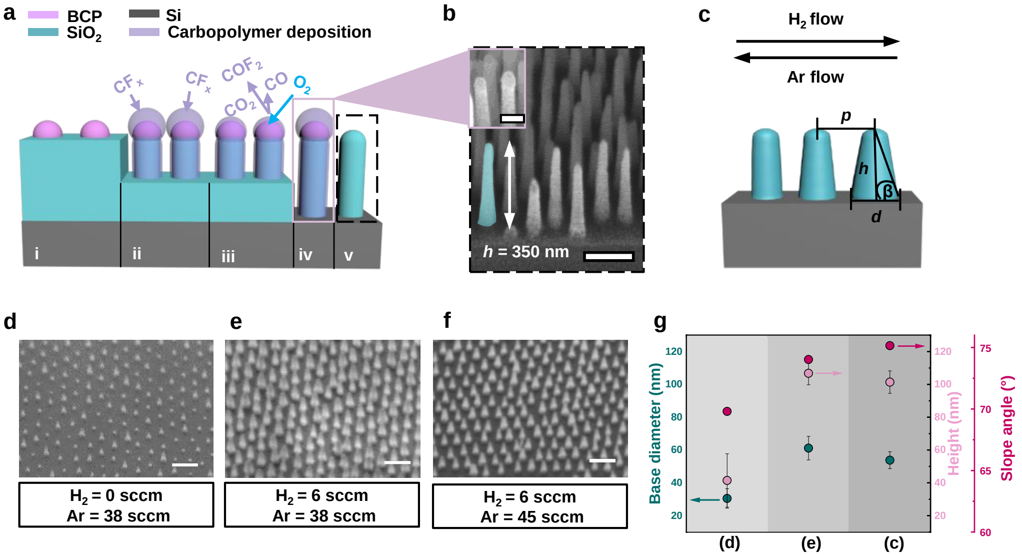

Figure 50 | Tuning of the SiO_2 hard mask height and shape. **a,** Schematic representation of the SiO_2 nanopillar generation through RSML. Starting from the BCP (i), the addition of H_2 into the etching chemistry (CHF_3/Ar) increases the generation of HF, thus lowering the F/C ratio; resulting in a more polymerizing plasma with increased CF_x deposition (ii). As the secondary mask builds up around the BCP to form mushroom-like structures, a brief oxygen plasma is applied which refines the diameter (iii). This enables further etching to proceed, with regeneration of the secondary mask to yield tall SiO_2 nanopillars (iv). A final oxygen plasma removes the deposition to form high AR SiO_2 nanopillar masks (v). **b,** SEM image of the generated hard mask with h = 350 nm, and p =1 10 nm (AR>3). The inset shows the structure as depicted in (iv) with polymer deposition remaining. Scale bar (inset) = 100 nm. **c,** Schematic representation of the effect of increasing H_2 or Ar flow, with key parameters depicted; height h, base diameter d, slope angle β, pitch p. **d-f,** SEM images of SiO_2 hard masks generated under varying H_2 and Ar flows with an initial SiO_2 thickness of 100 nm. No H_2 flow results in partial mask destruction with uneven topography (d). Maintaining the same Ar flow but increasing H_2 flow yields taller, more uniform SiO_2 pillars with a wide base diameter (e). Maintaining the same H_2 flow but increasing Ar flow, gives rise to similarly tall and uniform SiO_2 pillars, but with a narrow base diameter (f). **g,** Corresponding quantitative analysis of the change in base diameter, height and slope angle for the structures shown in SEM images d-f. Scale bars = 200 nm.

Not only does the altered etching chemistry permit high ARs through increased selectivity, but additionally enables the mask profile to be tuned so that the desired base diameter and anisotropy can be attained in order to well control the structure generation in Si. Profile control relies on the precise adjustment of H_2 and Ar flow, shown schematically in Figure 50c and in a series of SEM images in Figure 50d-f. Without H_2 (CHF_3:Ar = 1:3.2), the mask erosion quickly occurs resulting in non-uniform pattern transfer with a large h distribution, a small d, and low slope angle β (Figure

Adapted from: M. Michalska, S. K. Laney, T. Li, et al., A route to engineered high aspect-ratio silicon nanostructures through regenerative secondary mask lithography, 2021 (in preparation).

50d); as measured and quantitatively represented in Figure 50g. Introducing H_2 so that CHF_3:H_2:Ar = 2:1:6.3 (Figure 50e), yields 2.5-fold taller structures with a narrow distribution, twofold greater *d*, and larger *β*. Alternatively, achieving more anisotropic structures (even larger *β)* with a reduced *d* whilst retaining maximum *h*, is possible by decreasing carbopolymer deposition via stronger physical bombardment (increased Ar flow), so that CHF_3:H_2:Ar = 2:1:7.5 (Figure 50f).

Tuning the Si nanostructures. We next utilize the hard masks of varying diameters and heights, obtained from the same BCP template through modulation of RSML conditions, to elicit a range of designer nanostructures in silicon (Figure 51). For example, in Figure 51a, two generated hard masks of *d* = 60 and *d* = 112 nm, yield nanocones with ultra-sharp tips (i) and straight-walled nanopillars (ii) when the same etching conditions are applied (Cl_2 plasma; moderate power). It is noteworthy that ultra-sharp tips are often formed by thermal oxidation, followed by removal of the oxide layer.[209] Bypassing these steps therefore decreases process complexity. Whilst precisely controlled nanocone/nanopillar arrays present surfaces with invaluable properties (e.g., antireflective,[91] antifogging,[15] antibacterial[82]), unconventional morphologies, such as re-entrant structures, have been shown to display extraordinary omniphobic properties through manipulation of the direction of the liquid-vapor interface.[210] Starting from the same SiO_2 mask, but applying a reduced coil (<200 W) and particularly platen power (<15 W), we achieve mask undercutting which gives rise to nanopyramids of different re-entrant profiles (Figure 51a(iii, iv)). Here, the mask is observed to remain at the top of the structure and can be either stripped away or depleted through further etching leading to slender pillars of higher AR. More details on controlling the re-entrant profile are discussed in the following sections.

Adapted from: M. Michalska, S. K. Laney, T. Li, et al., A route to engineered high aspect-ratio silicon nanostructures through regenerative secondary mask lithography, 2021 (in preparation).

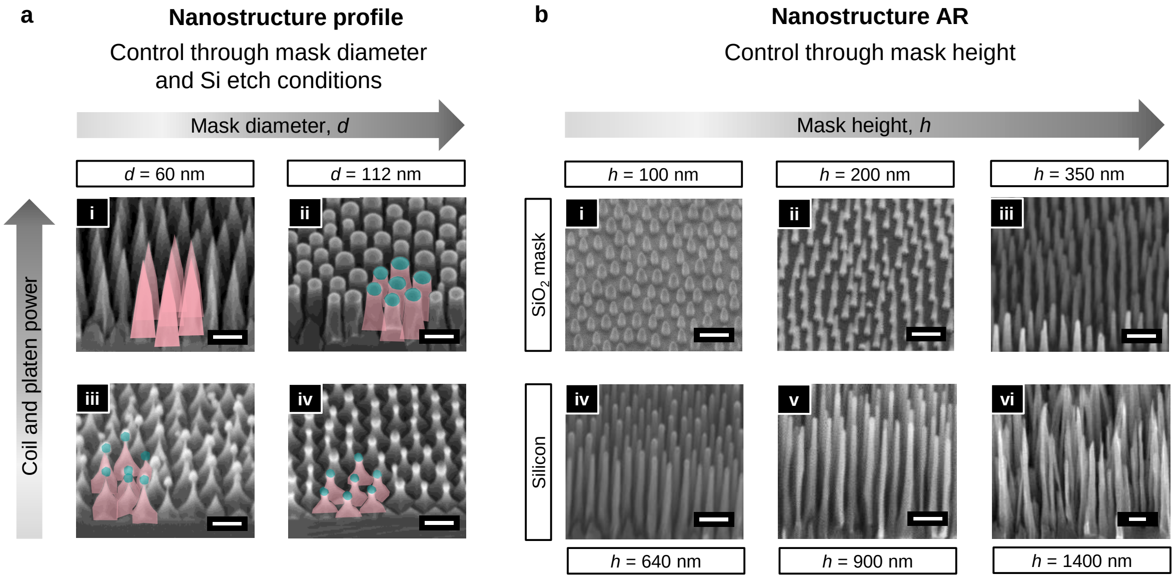
a
Nanostructure profile
Control through mask diameter and Si etch conditions
Mask diameter, d
d = 60 nm
d = 112 nm
Coil and platen power
i
ii
iii
iv
b
Nanostructure AR
Control through mask height
Mask height, h
h = 100 nm
h = 200 nm
h = 350 nm
SiO2 mask
Silicon
i
ii
iii
iv
v
vi
h = 640 nm
h = 900 nm
h = 1400 nm

Figure 51 | Tuning of nanostructure profile and aspect ratio. SEM images presenting an effect of the hard mask diameter (a) and height (b) on the pattern transfer into Si. **a,** Control over the nanostructure profile is obtained through a combination of the SiO_2 hard mask dimensions and the applied Si etching conditions (coil/platen power). Originating from the same BCP, Si nanocones (i) and straight-walled pillars (ii) were generated upon etching of a narrow (d = 60 nm) and wide (d = 112 nm) SiO_2 mask, respectively; and under a coil power of 300 W and platen power of 40 W. Nanopyramids (iii and iv) were similarly generated upon etching of the narrow and thin mask, but under a reduced coil (200 W) and platen (10 W) power. Both nanopyramids are similar, but the mask remaining in (iii) is very fragile and can be easily removed through HF treatment to yield short and sharp nanocones, whereas (iv) possesses considerable remaining hard mask. **b,** Control over the Si nanostructure's AR is provided through RSML-generated SiO_2 masks of varying height. SiO_2 masks of height 100 nm (i) and 200 nm (ii) were generated within one RSML cycle, whereas the mask of height 350 nm (iii) required two cycles. Etching of masks (i-iii) under coil power 300 W and platen power 40 W yields nanostructures (iv-vi) of heights 640, 900, and 1400 nm, respectively. Scale bars = 200 nm.

As in glass etching, a facile route for high aspect ratio silicon nanostructure generation has been absent, due to the lack of BCP mask durability. However, through RSML, we increase the AR of the SiO_2 hard mask, and overcome this issue. Figure 51b shows three hard masks of increasing *h* (100-350 nm), and the corresponding Si nanostructures etched under the same conditions. All structures are etched to the point of mask consumption to yield the highest AR (AR>10, Figure 51,vi), however this can introduce distortion. To avoid this therefore, etching should be stopped just prior to hard mask depletion, and followed by post-processing hard mask removal (e.g., HF treatment). Important to note, is that high AR hard masks, such as that shown in Figure 51b,iii,

Adapted from: M. Michalska, S. K. Laney, T. Li, et al., A route to engineered high aspect-ratio silicon nanostructures through regenerative secondary mask lithography, 2021 (in preparation).

can lead to bowing as a result of the mask weight and the AR of the Si structures. Nonetheless, the resulting Si nanograss (Figure 51b,vi) are likely to bring antireflective properties[9] or may be effective in antibacterial performance.[211]

The nanostructure design can also accommodate geometries with different levels of truncation, as highlighted in the SEM images in Figure 52. Figure 52a,i is the most truncated, with nanostructures displaying great similarities to those found on the wings of the Cicada.[7] Conversely, Figure 52a,iv possesses no truncation. Here, Si etching occurs in the same manner as the re-entrant structure generation (reduced coil (200 W) and platen (10 W) power), however it is stopped before complete undercutting of the hard mask occurs. The degree of truncation, therefore, is dictated by the etching time, with the top diameter of the truncated cone corresponding directly to the base diameter of the remaining hard mask.

The inset SEM images of Figure 52a show the structures before HF treatment; which is required to remove the remaining hard mask to attain truncated or sharp tops.

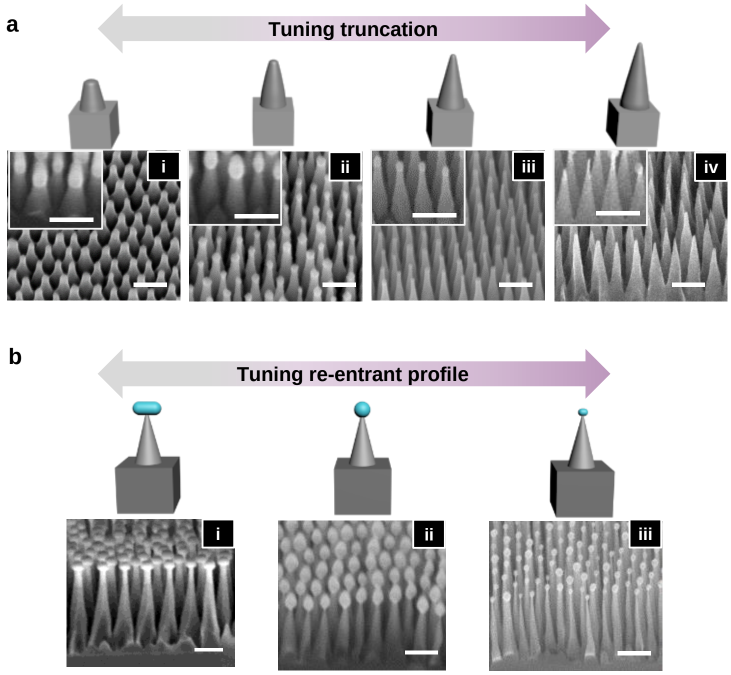

Figure 52 | Tuning of truncation and re-entrant profile. Si nanostructure morphology. **a,** SEM images and schematics of Si nanostructures with varying degrees of truncation – high (i) to low (iv) – generated by premature etch stop with subsequent HF treatment to remove the hard mask (inset shows structure before mask removal). The application of different etching time under the same isotropic etching conditions results in variable degrees of nanocone truncation.

Adapted from: M. Michalska, S. K. Laney, T. Li, et al., A route to engineered high aspect-ratio silicon nanostructures through regenerative secondary mask lithography, 2021 (in preparation).

b, Schematics and SEM images of the re-entrant nanostructures obtained under the same etching conditions but originating from a wide and flat (i) or a taller and tapered (ii) hard mask. (iii) Schematic and SEM image of a re-entrant nanostructure with a greater height and reduced hard mask generated from the same mask as in (ii) but under different etching conditions (more directional plasma). The application of the same (different) isotropic etching conditions to different (the same) shapes of the hard mask results in variable re-entrant profile. Scale bars = 200 nm.

Controlling the re-entrant profile is also possible as shown in Figure 52b, and relies predominantly on the dimensions of the hard mask. For example, Figure 52b,i originated from a flat and wide hard mask, whereas Figure 4b,ii originated from a taller and rounder hard mask. Nonetheless, the etching conditions and time also play a role. Here, Figure 52b,iii originating from the same mask as Figure 52b,ii was etched under higher coil/platen power and for a shorter time, yielding taller morphologies with less remaining hard mask. The slope angle β of the Si nanostructures can be tuned in a similar manner through control of the hard mask dimensions (shorter hard mask can elicit shorter, nanocones with a smaller β and *vice versa*), and through the Si etching conditions.

4.1.3.2 Applications.

The wealth of potential morphologies which can be reliably attained unlocks many functionalities through the ability of the nanostructure to manage the interactions with liquids, photons, and bacteria.[14,16,167] As an example, we therefore investigate the antireflectivity and superhydrophobicity of nanostructured silicon whilst presenting the method scalability by patterning the surface of a 6”-wafer. Figure 53a shows a large-area SEM image of the nanostructures clearly showcasing the pattern uniformity and a photograph demonstrating a uniform black color across the entire surface, with no visible reflections. To further demonstrate that there is consistent antireflectivity (also an indication of structural homogeneity) across the wafer, we measure the reflectance at the 5 locations marked in Figure 53b, and plot the absolute reflectance alongside that of the unstructured Si over the wavelength range 400-1000 nm (Figure 53c). This further demonstrates the quality of the pattern with an average reflectance of <5% and only slight variation across the wafer (<1%); meanwhile, the unstructured surface exhibits an average reflectance >40%. To render the wafer superhydrophobic, a thin layer of short-chain PDMS is grafted onto the surface,[212] and the wetting properties characterized by dynamic water contact angle measurements. Excellent superhydrophobicity is observed with high advancing (158

Adapted from: M. Michalska, S. K. Laney, T. Li, et al., A route to engineered high aspect-ratio silicon nanostructures through regenerative secondary mask lithography, 2021 (in preparation).

± 1°) and receding (157 ± 1°) contact angles and an ultralow contact angle hysteresis (1°). Such high water-repellence enables droplets to bounce off a surface multiple times with minimal dissipation of energy, and we observe a remarkable 19 bounces upon the release of water droplet (8 µl) from 1 cm height (Figure 53d).

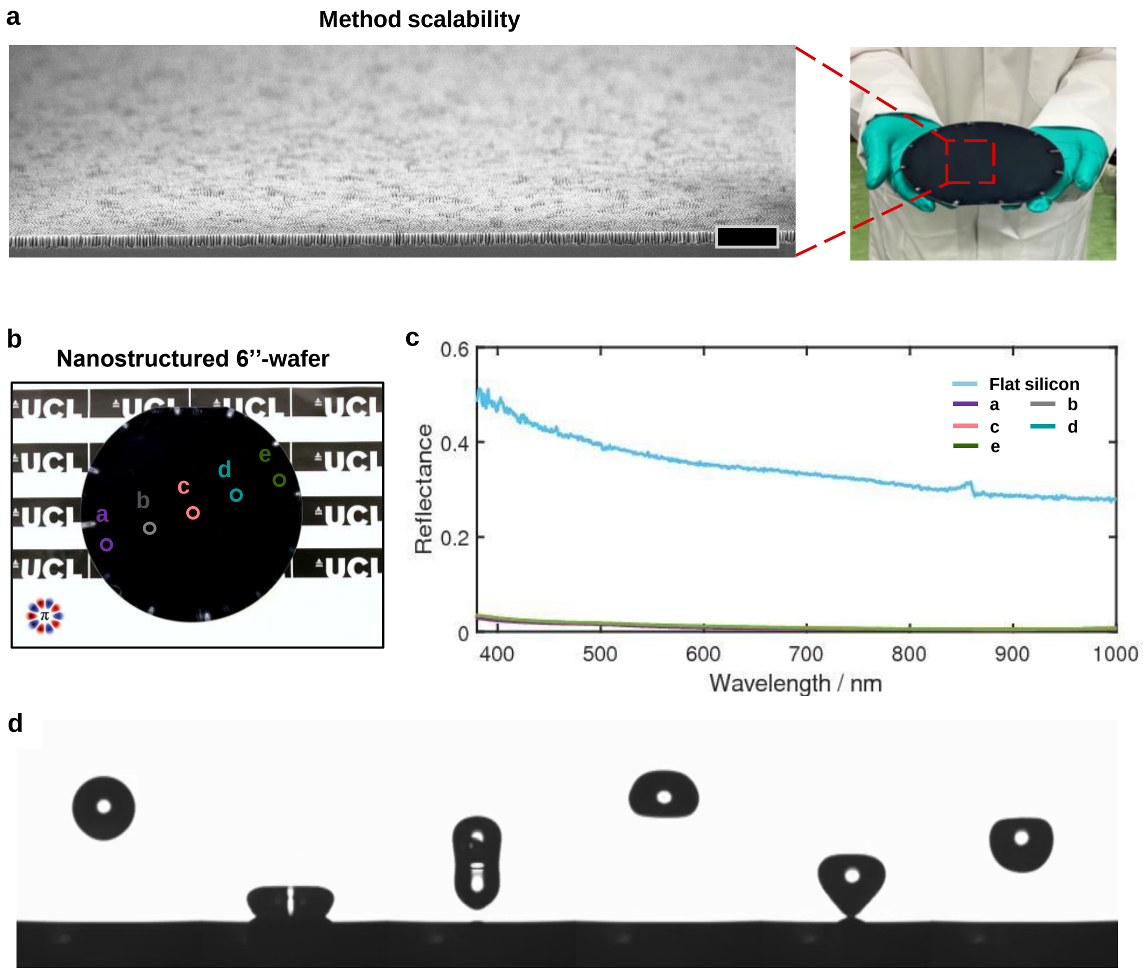

Figure 53 | Method scalability, optical properties, and wetting characteristics of the nanostructured silicon wafer. **a,** Large field of view SEM illustrating silicon nanostructures of AR~7 of the 6"-wafer (photograph), which demonstrates the scalability of the approach. Scale bar is 2 µm. **b,** Photograph of the nanostructured 6''-silicon wafer with the five locations marked where reflectance measurements were taken. **c,** Measured reflectance as a function of wavelength for flat silicon (control) and the nanostructured silicon at the five locations marked in (b). **d,** Sequential images of a droplet impacting the structured surface, with minimal dissipation of energy.

Adapted from: M. Michalska, S. K. Laney, T. Li, et al., A route to engineered high aspect-ratio silicon nanostructures through regenerative secondary mask lithography, 2021 (in preparation).

4.1.4 Conclusions

In summary, we have developed a fully tunable and simple fabrication route for a wide range of silicon nanostructure morphologies that vary in aspect ratio and shape at the length scales challenging to reach by conventional techniques. These multiple nanostructures originate from only one type of BCP micelle template, which we modulate further by RSML process so that various SiO_2 hard mask heights (>300 nm) and diameters (increase or decrease with respect to the original micelle) become available. The flexibility of the method stemming from numerous permutations of SiO_2 and Si etching conditions offers an easy to adapt platform for both Si nanopatterns as well as generation of SiO_2/Si heterostructures. Finally, we demonstrate the process scalability through patterning of 6”-wafer with nanopillars that can be utilized as highly antireflective and self-cleaning substrate. We envision the implementation of our approach to Si nanostructuring to be far-reaching, targeting applications which require large-scale, uniform patterning such as solar panels, anti-fogging/anti-bacterial surfaces, sensing, amongst many others.

4.1.5 Methods

Fabrication of silicon nanostructures.

SiO_2 deposition. A silicon wafer (MicroChemicals) was cleaned with acetone *via* sonication and subsequently washed with isopropanol. An SiO_2 layer of thickness 40, 70, 100, 200, or 350 nm was deposited on Si via plasma enhanced chemical vapor deposition (PECVD; STPS Multiplex) under low frequency RF with SiH_4 and O_2 vapor at 300°C.

BCP micelle preparation. BCP micelles of PS-*b*-P2VP [poly(styrene-*block*-2vinylpyridine), Polymer Source Inc.] were pre-assembled according to the previous report,[128] with certain adaptations. Three molecular weights were used for this study M_w / kg mol^{-1} = 57-*b*-57 (P57), 109-*b*-90 (P100), and 440-*b*-353 (P400) to accommodate pitches ranging from ~50-250 nm. The polymers were mixed with anhydrous m-xylene at concentrations of 0.3-0.5% w/v by gentle stirring at 75°C overnight. Subsequently, the solutions were allowed to cool to room temperature, filtered (PTFE 1 µm), and stored at 4°C.

SiO_2 hard mask preparation. First, pre-assembled micelles were spin-coated onto the Si/SiO_2 wafer at RT. Typical spin speeds for P400 ranged between 2-4k rpm, and for P100 and P57: 3-6k rpm. To register the pattern into SiO_2, reactive ion etching (RIE) was conducted using PlasmaPro NGP80 RIE, Oxford instruments, at temperature of 20°C. A breakthrough etch (3-14 s) was performed to remove the PS matrix and tune the diameter of the mask under O_2 (20 sccm), pressure 50 mTorr, and radio frequency (RF) power 50 W. Subsequently, glass was etched according to our recently reported RSML process[208] using CHF_3/H_2/Ar gases at flows 12-15, 0-6, and 38-45 sccm, respectively; under pressure of 30 mTorr and at RF power of 220

W. Control over the etching depth was obtained through the time, and to reach high aspect ratio, a breakthrough etch was performed under O_2 plasma (conditions as above) to reduce the diameter of the secondary mask. Etching of SiO_2 proceeded until reaching the underlying Si layer, at which point an O_2 clean was performed to remove the organic mask.

Si etching. The pattern from the hard mask was transferred into Si by means of an Advanced Silicon Etcher (ASE, STS MESC Multiplex ICP) under Cl_2 plasma. The conditions varied depending on the desired degree of anisotropy, with an anisotropic etch performed under coil power 300 W and platen power 40 W with Cl_2 flow of 20 sccm and pressure 3 mTorr. To obtain a less anisotropic profile (re-entrant), the etch was performed under a coil power of 150-200W and platen power 10-15W, with a Cl_2 flow of 20 sccm and pressure 3 mTorr. In some cases, a Cl_2 was mixed with SF_6 to increase the degree of hard mask undercutting.

Surface functionalization. In order to render surface superhydrophobicity, silanization was performed. The substrate was first cleaned *via* sonication in isopropanol and acetone, and subsequently treated with oxygen plasma to impart surface hydroxylation (5 min each). Short chain polydimethylsiloxane (PDMS) was grafted onto the surface, as previously reported,[212] using a 1:10:0.27 v/v/v ratio of dimethyldimethoxysilane : isopropanol : H_2SO_4 (>95%) mixture. The substrate was then placed on a hot plate (75°C) and the solution was drop casted atop for 15 s, followed by washing with deionised water, isopropanol, and toluene.

Adapted from: M. Michalska, S. K. Laney, T. Li, et al., A route to engineered high aspect-ratio silicon nanostructures through regenerative secondary mask lithography, 2021 (in preparation).

4.2 Antifogging

The nanostructure fabrication in this work follows the same protocol as described above, and was conducted at UCL by myself and MM. Probing and quantification of the antifogging properties and mechanism were conducted by PL and DQ, however I include them here for completeness.

4.2.2 Introduction

Spontaneous jumping of condensing droplets[54] has recently emerged as a promising solution for antifogging applications,[57,213,214] among many others.[215–220] For this to be achieved, droplets formed through condensation must exhibit large contact angles and minimal pinning to the substrate.[42,221] Whilst this is considered a challenge for micrometer scale droplets, cicada wing-inspired surfaces with nanocone arrays[16,17,57] have been shown to exhibit dew repellency and thus constitute a promising route to elicit special wetting properties at microscales.

During condensation, coalescence of neighbouring non-wetting droplets induces the conversion of surface energy into kinetic energy,[54] which possibly promotes droplets to jump away from the surface, hence providing antifogging behaviour. The proportion N of drops jumping after coalescence (rate of departure) is a measure of the antifogging efficiency, and it was found to exceed 90% on hydrophobic nanocones,[16] instead of at best 35% on previously reported textured materials.[16,222] This spectacular property was assumed to originate from the combination of texture scale (sub-micrometer), shape (conical) and density (dense array), without however, systematic experiments to verify this hypothesis. Hence it appears crucial to investigate *families* of conical structures in order to establish the versatility and universality of the antifogging efficiency of nanocones, and additionally explore where the boundary in performance extends to. We build a wide range of nanostructures (from pillar, to truncated, to sharp cone; Figure 54a), and first evidence the unique microwetting properties of sharp nanocones after observing condensed droplets by environmental scanning electron microscopy (ESEM). Subsequently, we focus on dew repellency and quantitatively discuss its control through texture size and shape design. To that end, we consider three families of nanocones; homothetic (differing in the pitch and height but with constant apex angle), extruded (differing in the height and apex angle but with constant pitch), and truncated (with a given design and different degrees of truncation).

Adapted from: P. Lecointre, S. K. Laney, M. Michalska, T. Li, *et al.*, Unique and robust dew repelllency of nanocones, **Nature Communications**, 2021, 12, 3458

4.2.3 Results and discussion

4.2.3.1 Imaging condensation at the microscale

Using block-copolymer self-assembly and plasma etching, nine centimetre-size arrays of nanocones (height h) were designed on a dense hexagonal lattice (pitch p). Two reference materials consisting of nanopillars (sample A) and nanocones (sample H1) were used to connect our findings to previous investigations.[16,47] Figure 54 shows the sample library. Family H refers to homothetic texture where the index ranks the relative size of structures, from lowest to highest pitch p (from 52 nm to 110 nm), at fixed aspect ratio $h/p = 2.2 \pm 0.2$. Family E is that of extruded cones, where materials are ranked from lowest to highest height (from 144 nm to 420 nm), at fixed $p = 110 \pm 5$ nm. The two families H and E intersect in one sample (H3/E2) with $p = 110$ nm and $h = 250$ nm. The cone sharpness $\Sigma = 1/2\tan^{-1}(p/2h)$, defined as the inverse of their apex angle β, varies in our study between 1 and 4. Finally, family T, includes truncated cones with same pitch $p = 110 \pm 5$ nm as in E, and it is classified from smallest to largest top diameter l (from 34 nm to 60 nm). Next, the resulting surfaces are rendered hydrophobic by vapor deposition of 1H,1H,2H,2H-perfluorodecyltrichlorosilane. Such a treatment on flat silicon yields an advancing contact angle $\theta_a = 120° \pm 2°$, a value that greatly increases to $\theta_a = 166° \pm 5°$ upon nanostructuring.

Adapted from: P. Lecointre, S. K. Laney, M. Michalska, T. Li, *et al.*, Unique and robust dew repelllency of nanocones, **Nature Communications**, 2021, 12, 3458

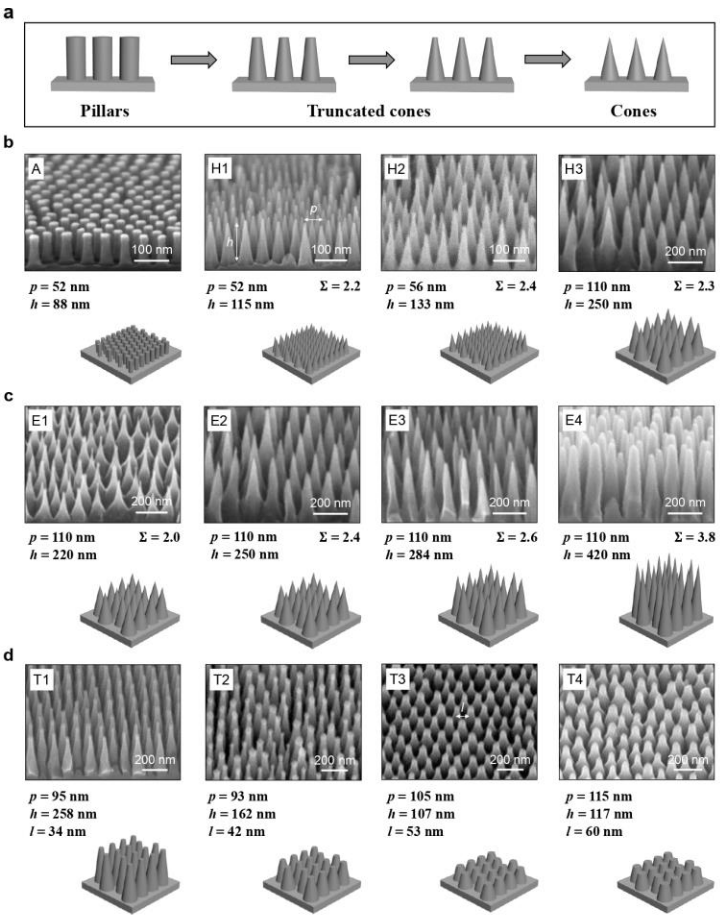
a
Pillars
Truncated cones
Cones
b
A
100 nm
p = 52 nm
h = 88 nm
H1
p
h
100 nm
p = 52 nm
Σ = 2.2
h = 115 nm
H2
100 nm
p = 56 nm
Σ = 2.4
h = 133 nm
H3
200 nm
p = 110 nm
Σ = 2.3
h = 250 nm
c
E1
200 nm
p = 110 nm
Σ = 2.0
h = 220 nm
E2
200 nm
p = 110 nm
Σ = 2.4
h = 250 nm
E3
200 nm
p = 110 nm
Σ = 2.6
h = 284 nm
E4
200 nm
p = 110 nm
Σ = 3.8
h = 420 nm
d
T1
200 nm
p = 95 nm
h = 258 nm
l = 34 nm
T2
200 nm
p = 93 nm
h = 162 nm
l = 42 nm
T3
200 nm
p = 105 nm
h = 107 nm
l = 53 nm
T4
200 nm
p = 115 nm
h = 117 nm
l = 60 nm

Figure 54 | Families of samples. **a,** Schematic illustrating the geometry transition from nanopillar, to truncated cone and finally, to sharp cone. **b-d,** Scanning electron microscopy (SEM) images and schematics corresponding to the three families of nanocones. For all surfaces, the cones with height h, pitch p, apex angle β and sharpness $\Sigma = 1/\beta$ are arranged on a dense hexagonal array and coated by a hydrophobic layer. **b,** A is a reference sample made of nanopillars with diameter $l = 30$ nm. H1 is the smallest nanoconical texture, H2 and H3 are homothetic (constant h/p), with a size ratio of 1.1 and 2.1, respectively. **c,** E1, E2, E3 and E4 are of equal pitch $p = 110$ nm and gradually extruded from E1 with $h = 144$ nm by a factor of 1.7, 2.0 and 2.9, respectively. Families H and E intersect: H3 and E2 are the same material. **d,** T1, T2, T3 and T4 have the same pitch but are truncated, with various top diameters l.

The adhesion of water to its substrate is quantified by the contact angle hysteresis, which we measure by slowly dispensing millimetre-size drops (Table 1).

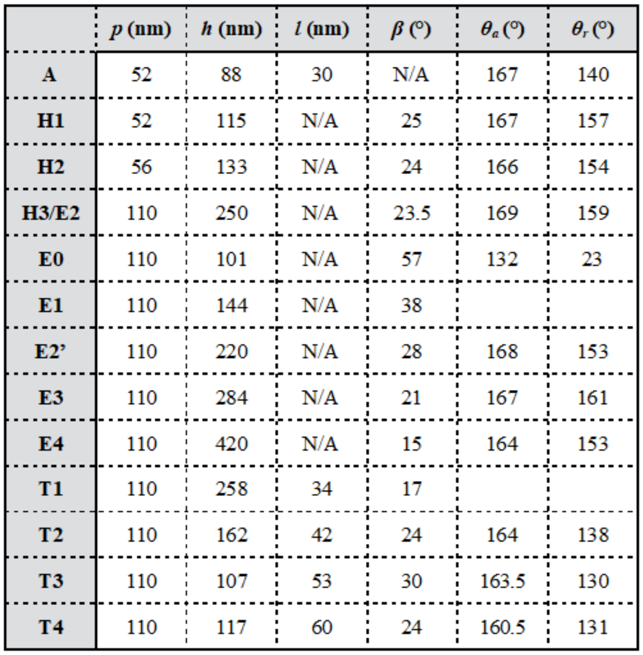

	p (nm)	h (nm)	l (nm)	β (°)	θ_a (°)	θ_r (°)
A	52	88	30	N/A	167	140
H1	52	115	N/A	25	167	157
H2	56	133	N/A	24	166	154
H3/E2	110	250	N/A	23.5	169	159
E0	110	101	N/A	57	132	23
E1	110	144	N/A	38		
E2'	110	220	N/A	28	168	153
E3	110	284	N/A	21	167	161
E4	110	420	N/A	15	164	153
T1	110	258	34	17		
T2	110	162	42	24	164	138
T3	110	107	53	30	163.5	130
T4	110	117	60	24	160.5	131

Table 1 | Characteristics of the nanotextured materials. Sample A comprises nanopillars, family H consists of homothetic cones, extruded cones E are more and more elongated and cones T are truncated. Families H and E have a common member called either H3 or E2. The cones (of angle β) are spaced with a pitch *p* and have a height *h* and possibly a top diameter *l*. In each family, the samples are ranked from lowest to largest characteristic size. Contact angles are measured with millimeter size water drops, and we provide both the advancing and receding values of these angles, measured with an uncertainty of ± 2°.

On the one hand, hysteresis is *ca.* 10° on samples H and E, a small value compared to the contact angles – the hallmark of repellent materials. All samples H and E have sharp structures favouring poor wetting, except E4 whose rounded and continuous top prevents contact lines from pinning, thereby providing wetting properties similar to sharper cones. On the other hand, hysteresis roughly triples to *ca.* 30° on nanopillars and truncated cones. We attribute this to the discontinuous edges at the top of these structures, which pins the contact line during receding motion. These differences can be amplified for microdrops: water condensing within nanopillars can remain trapped inside the vertical texture, which reinforces pinning and immobilizes droplets.[223] In contrast, water was assumed to spontaneously leave the core of dense nanocones: in such an asymmetric landscape, the nucleus lowers its surface energy by rising-up the structure to sit atop the cones, in the so-called Cassie state.[16,224–227] The expulsion of water nuclei from the conical texture is especially difficult to monitor directly, due to both the size (of order *p*) of the nuclei and

Adapted from: P. Lecointre, S. K. Laney, M. Michalska, T. Li, *et al.*, Unique and robust dew repelllency of nanocones, **Nature Communications**, 2021, 12, 3458

the short time (nanoseconds) anticipated for their displacement over the nanoscale height *h*. However, this scenario implies differences in the morphology of microdroplets growing on nanocones compared to those on nanopillars, and thus in their mobility – a property of paramount importance for antifogging.

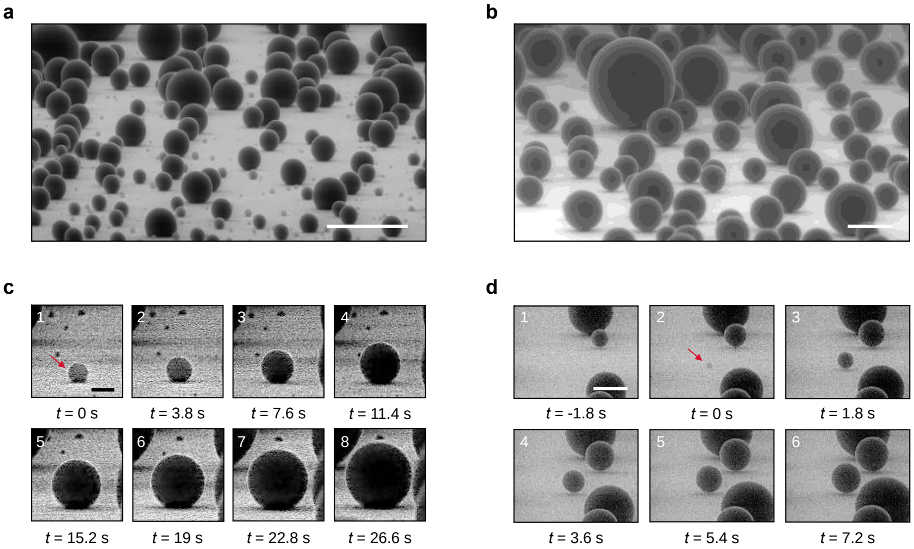

Figure 55 | Direct visualization of droplets condensing on nanotexture. **a,** ESEM images of water microdrops condensing on nanopillars (sample A; tilted by 85°). Drops adhere to the surface with contact angles no larger than 140°. The scale bar shows 20 µm. **b,** ESEM images of microdrops condensing on nanocones (sample E4; tilted by 80°). Contact angles are now ~170° for all drops (radii *r* between 1 µm and 23 µm). The scale bar shows 20 µm. **c,** Growth dynamics of an individual droplet (pointed by the arrow) on sample A. The drop is first pinned (images 1-3) with a contact angle increasing from 120° to 140°, after which it keeps this value. Images are separated by 3.8 s, substrate temperature is $T_s = -2.5$°C and chamber pressure $P = 600$ Pa. The scale bar shows 2 µm. **d,** Growth dynamics of a nucleus on sample E4. Starting with a contact angle of 130° ± 7° (image 2), the droplet quickly becomes a quasi-sphere with an angle of 171° ± 4°, proving a Cassie state even at a microscale. Images are separated by 1.8 s, temperature is $T_s = -1.5$°C and pressure $P = 700$ Pa. The scale shows 2 µm.

Condensing microdroplets can be observed directly by ESEM, whose high resolution and image sharpness enables us to visualize drops in the early stage of condensation and to access contact angles on the microscale (r > 350 nm). The operating conditions are carefully optimized to minimize heating,[228,229] contamination[230–232] and radiation damage.[233] The sample holder (60°-tilted copper bracket) can accommodate a wide tilting range (up to 90°), crucial to render a clear view of the evolving/resting droplets. Furthermore, the bracket is mounted on a Peltier cooling

Adapted from: P. Lecointre, S. K. Laney, M. Michalska, T. Li, *et al.*, Unique and robust dew repelllency of nanocones, **Nature Communications**, 2021, 12, 3458

stage and temperature and chamber pressure are controlled around -2 ± 1°C and $600 \pm 100\,\mathrm{Pa}$, respectively.

Images of water condensing either on nanopillars (sample A, Figure 55a) or nanocones (sample E4, Figure 55b) reveal marked differences: for all drop sizes, the apparent contact angle of water is much larger on E4 than on A. Water even seems to "levitate" on nanocones, with corresponding angles of $171° \pm 4°$. Furthermore Figure 55b shows a large collection of microdroplets (~70) all in this highly non-wetting state, and thus likely to be ultra-mobile despite their scale. These droplets are so close to being spherical that it proves extremely difficult to define a contact area. The micrographs captured on other nanocones (Figure S 1; see appendix), either sharp or truncated, are similar to that in Figure 55b, verifying this key observation applies to conical nanostructures.

The contact angle is also found to increase with the drop size, regardless the sample type, which can be seen both by (i) exploiting the droplet polydispersity (with radii spanning from ~1 µm to ~25 µm) displayed in Figure 55a and Figure 55b, or (ii) following individual condensation events, as pointed in Figure 55c and Figure 55d. In the first case, droplets with radius $r < 2$ µm have a typical contact angle of 120° on sample A and this value rises to ~140° for larger droplets. In the second case, the angle of a growing droplet also increases (Figure 55c), with successive growth modes[221,223]: starting at $r \approx 0.85\,\mu\mathrm{m}$ with $\theta = 120° \pm 5°$ (image 1), the nucleus retains a constant base area while its angle rises to $140° \pm 5°$ (images 2-3), a value maintained throughout (images 4-8). In contrast, the angle on surface E4 (Figure 55d) rapidly increases from $130° \pm 7°$ (for $r \approx 0.6\,\mu\mathrm{m}$, image 2) to its final value of $171° \pm 4°$ ($t > 3.6\,\mathrm{s}$, $r > 1.2\,\mu\mathrm{m}$, images 3-6).

Hence, we observe contrasting condensation patterns between both samples. On the one hand, contact angles on nanopillars are systematically smaller than those on nanocones and suffer from contact line pinning,[221,223] two facts that express deep solid/liquid interactions. On the other hand, apart from a short transient state, droplets on nanocones rapidly exhibit very high, macroscopic-like, contact angles. This strongly suggests a Cassie state triggered at a radius of $\sim 1\,\mu\mathrm{m}$, a unique behaviour at the scale where water generally penetrates pillar-like structures.

This first series of experiments can be condensed into one graph, by plotting the contact angle as a function of the droplet radius r (Figure S 2). Data are obtained by fitting the contour of drops by a circle of radius r completed by a base line with radius $l = r sin\theta$ so that these two independent measurements provide θ. In the experiments, the baseline progresses at a velocity $v = dl/dt$ ranging between 0.3 µm/s and 1 µm/s. Hence the capillary number $\eta v/\gamma$ (denoting η and γ as the viscosity and surface tension of water) is typically 10^{-8}, indicating a quasi-static regime for the advancing angle θ_a of water microdrops.

We first comment on the differences between pillars and cones. Figure S 2 consolidates the results noted in Figure 55, in that there is a distinct difference in contact angles between the samples, amounting to ~30° smaller contact angles on nanopillars than on nanocones at all radii r. Contact angles on truncated cones are slightly smaller than on sharp cones: despite the presence of flat areas at the cone tops, they maintain the high values characteristic of a Cassie state. In addition, the effect of drop size is confirmed for all samples: as r changes from micrometric to decamicrometric values, θ_a increases by ~30° and it plateaus at a value of $\theta_a = 141° \pm 3°$ on A, $\theta_a = 160° \pm 2°$ on T4 and $\theta_a = 171° \pm 3°$ on E4. Interestingly, these values differ from those measured with millimetric water drops, as shown by the dotted lines in Figure S 2. The discrepancy is especially large for sample A, where the “macroscopic” angle is $\theta_a = 167° \pm 3°$, a high value typical of a Cassie state. This confirms our former hypothesis: unlike deposited millimetric drops, condensing droplets partially grow within the A-texture and thus coexist with trapped water, a situation that renders the substrate more hydrophilic. Yet, the substrate remains globally hydrophobic, suggesting that condensing drops are in a partial Cassie state (that is, coexisting with a mixture of trapped water and trapped air).[221,223,234,235] At small radii, the lower contact angles agree with this scenario; if nuclei form inside the texture, the smaller the droplet, the more effectively hydrophilic the substrate.

At first glance, the situation with the nanocones is more surprising since the saturation value of the contact angle, $\theta_a = 171° \pm 3°$, is larger than the “macroscopic” value $\theta_a = 164° \pm 3°$. The effect is modest, yet systematic (despite error bars), as if the material exhibited an augmented hydrophobicity for r > 1.5 µm, a property of obvious practical interest in the context of anti-dew materials. At a millimetre-scale, gravity tends to flatten water, hence decreasing its apparent contact angle. The size of the gravity-driven contact of a non-wetting drop scales as $r^2\kappa$, denoting $\kappa^{-1} = (\gamma/\rho g)^{1/2}$ as the capillary length, ρ as the water density, and g as the gravity acceleration.[32] Weight can be neglected provided we have $r \sin\theta > r^2\kappa$, that is, $r < \kappa^{-1}\sin\theta \approx 600$ µm. This condition is largely fulfilled in Figure 55 and Figure S 2 for condensing drops, which can explain the difference between values of angles obtained at micrometric and millimetric scales. Macroscopic measurements of contact angles are performed with millimetric drops so that gravity increases the apparent solid/liquid contact, an artefact leading to an underestimation of high contact angles. This suggests that the genuine advancing angle is rather the one observed with condensing drops. For truncated cones, where angles are smaller, the discrepancy between micro- and milli-measurements is more modest, in good agreement with our arguments where the discrepancy increases with the value of the angle.

Small nuclei on nanocones also deserve a discussion. Below $r = 1.5$ µm (yet with $r > p$), the contact angle significantly decreases, which we interpret as an effect of Laplace pressure. To advance our understanding, we create a model for the depth of drop penetration within the structures, depending on the radius of the drop and on the cone geometry. The surface force opposing water penetration by distance z scales as $\gamma\beta z$ per cone,[239–241] where the apex angle is $\beta \sim p/h$ (Figure S 3).

Balancing the corresponding pressure $\sim\gamma\beta z/p^2$ by the Laplace pressure in the drop $\sim\gamma/r$ yields a depth $z \sim \Sigma p^2/r$, that is, hyperbolic in drop radius. This formula stresses another advantage of cones, namely their geometrical resistance to water penetration[47,239] expressed through their sharpness Σ. The distance z is nanometric and it quantifies the solid/liquid contact and thus determines the contact angle,[242,243] calculated using the Cassie equation,[42] $\cos\theta_a = -1 + \varphi_s(1 + \cos\theta_0)$, where $\theta_0 \approx 120°$ is the Young water contact angle on hydrophobic silicon, and φ_s the solid fraction in contact with water. The latter quantity is deduced from the surface areas A_{ls} and A_{la} of the liquid/solid and liquid/air contact whose analytic expressions[243] are given as a function of z according to *Eq. 35* (see also Figure S 3and Figure S 4).

$$z(r) = \frac{hr|\cos(\theta_0 - \beta/2)|}{p}\left[\sqrt{1 + \frac{2\sqrt{3}\,p^2}{\pi r^2 \cos^2(\theta_0 - \beta/2)}} - 1\right] \qquad \textit{Eq. 35}$$

Using our model, we demonstrate the case for E4 (solid line, Figure S 2), where we observe quantitative agreement with the data, explaining in particular why deviations only concern ultra-small drops, below 1.5 µm: above this size, water penetration *z* becomes negligible.

However, we observe limits in the antifogging ability terms of the cone profile (apex angle β) with very low (Figure S 4) and high (Figure S 5) apex angles resulting in water penetration. In the case of smaller cone angle β (very sharp needles), *Eq. 35* predicts that water penetrates the network of cones, as shown in Figure S 4b for β = 1° (black line), 10° (red line) and 15° (blue line). The penetration of water is physically due to the fact that a small apex angle cannot oppose water penetration, since the liquid then is not stopped by a significant surface area of solid as it is at larger β.

Another case of failure arises from large cone angles. Repellent materials are such that surface tension forces are oriented upwards to counter the pressure induced by liquid. The force exerted by the solid on the surface makes an angle π − θ0 + β/2 with the vertical, and it must be higher than π/2, hence yielding as a condition for superhydrophobicity: β < βc = 2θ0 – π. At large β, the capillary force acts downwards so as to push water inside the texture and to induce a sticky Wenzel state. In our case, we have θ0 ≈ 120° ± 2°, which yields a critical apex angle βc = 60°± 4°, since β-angles greater than $2\theta_0 - \pi \approx 60°$ prevent drops from sitting atop the cones.[242] Figure S 5 confirms that water penetrates cones with high apex angle (β = 57° ± 2°, Σ ≈ 1), which fully inhibits antifogging.

In contrast, all our samples have β-angles between 15° and 38°, which prevents the geometrical impregnation and defines what we call "sharp cones". All these observations and models can be finally put together to construct a "phase diagram" of antifogging (Figure S 6)

Here we collect our results and theoretical arguments in a phase diagram of jumping, based on the texture parameters *h*, *p*, *l* and Σ = 1/β. Three of those parameters can be tuned independently, so that the phase diagram is *a priori* three-dimensional, which complicates its readability. We thus simplify the diagrams by considering successively sharp cones (*l* = 0) and truncated cones.

Overall, the results from Figure 55 and Figure S 2 indicate the differences between the nanostructures, and reveal that droplets can remain in the Cassie state solely for nanocones and truncated nanocones, even on the microscale (Figure S 1). In contrast, the behaviour on nanopillars is consistent with previous studies, where condensation induces mixed states,[55,221,223,234,235] as shown in particular by Enright *et al.* who evidenced pinned wetted areas below microdroplets sitting on needles and pillars.[223] The latter effects are specific to condensing microdrops. Millimeter-size drops deposited on hydrophobic pillars are in a regular Cassie state, as evidenced by the larger value of the contact angle (Figure S 2).

4.2.3.2 Antifogging abilities

We now investigate the antifogging efficiency of nanocones and how it depends on their geometry. To achieve this, we visualise the breath figures resulting from condensation on our three families of nanocones and on pillars (Figure 56 and Figure S 7). The experiment relies on lowering the temperature of our samples below the dew point, to typically around 4°C. An inverted microscope (Nikon Eclipse Ti-U) equipped with a video-camera (Hamamatsu C11440) is used to observe how atmospheric water condenses. The supersaturation S (ratio between vapor pressure at room temperature and saturated vapor pressure at sample temperature) is here kept constant at a value $S = 1.6 \pm 0.2$.

An experiment lasts 30 minutes and images, with a size of 700 µm × 700 µm, are recorded every 2 seconds. We first observe the nucleation of multiple droplets, with an average density of nuclei per unit area of 1200 mm^{-2} on samples E and H; this value rises to 2300 mm^{-2} on samples T and up to 5600 mm^{-2} on pillars – showing that the presence of flat tops favours nucleation, in agreement with simulations by Xu *et al.* [224]. Nuclei grow and eventually coalesce with their neighbours, and we compare successive images to establish whether a coalescence is followed, or not, by a jump (sketched in Figure 57a in dark blue). This automated treatment allows us to quantify the jumping rate of a given sample, as a result of statistics performed over the few thousand coalescences that take place within 30 minutes. A coalescence event implies the merging of n droplets, where n is typically 2 – 5. The number of events decreases with n: the proportion of binary coalescences ($n = 2$) is of the order of 70%, while triple, quadruple and quintuple merging respectively concerns 20%, 6% and 3% of the events. A first overview of material performance can be gained through the global rate N_g, defined as the proportion of coalescences resulting in droplet jumps, irrespective of the value of *n.* This quantity is plotted as a function of time in Figure 57b, where each data point is an average made over one minute, that is, over *ca.* 100 coalescences. Considering absolute numbers of events (Figure S 8), it is observed that coalescences and jumps strongly correlate despite their fluctuations, justifying our choice of a rate of jumping as a metric of anti-fogging.

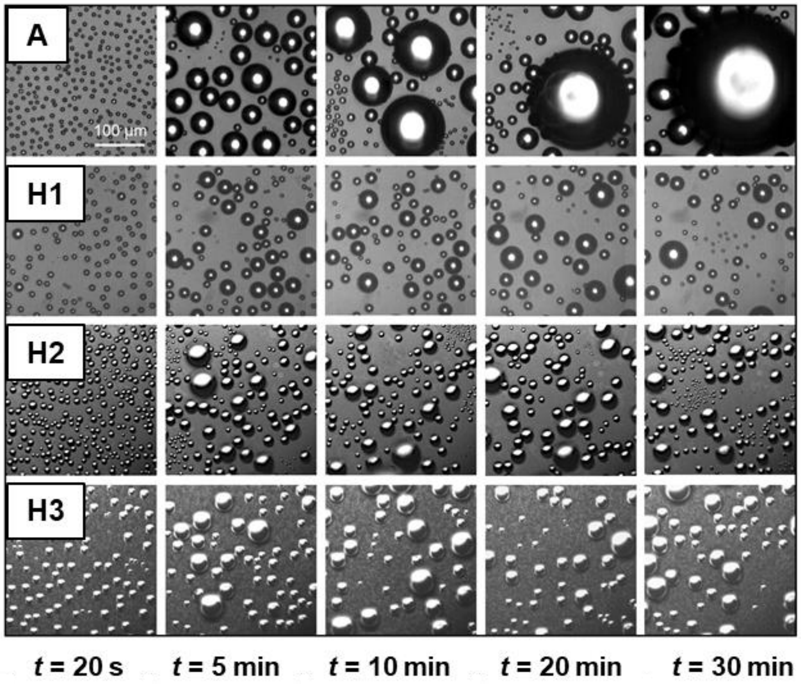

Figure 56 | Breath figures on pillars A and the homothetic family H (samples H1-H2-H3) under an optical microscope after 20 s, 5 min, 10 min, 20 min and 30 min. The room temperature is T = 21 ± 1°C, relative humidity RH = 52 ± 2% and sample temperature is T_s = 4 ± 1°C, which corresponds to a supersaturation S = 1.6 ± 0.2. Differences between pillars and sharp cones become apparent after 5 min: sample A is covered by larger and larger droplets while, for all structures H, growing droplets coalescing with their neighbours can jump off the surface, which results in similar breath figures with time and area fraction covered by droplets.

Adapted from: P. Lecointre, S. K. Laney, M. Michalska, T. Li, *et al.*, Unique and robust dew repelllency of nanocones, **Nature Communications**, 2021, 12, 3458

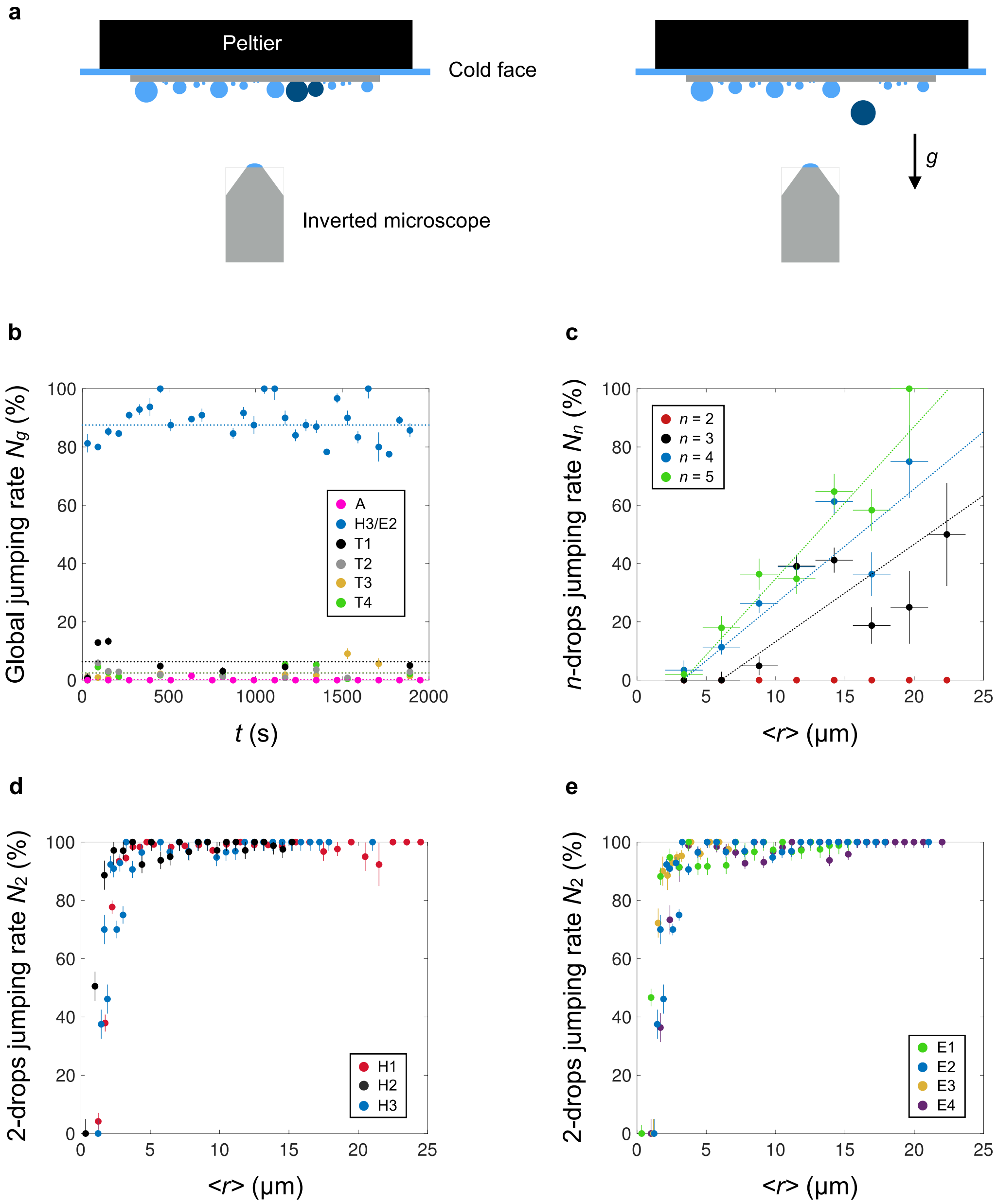

Figure 57 | Antifogging ability of nanocones. a, Schematic of the experiment: a sample is placed upside down on a Peltier cooler, which generates dew from atmospheric water. Droplets nucleate, grow and eventually coalesce, which we observe with an inverted optical microscope. We focus in particular on coalescing droplets (dark blue) and their possible takeoff from the material, from which we deduce the jumping rate of merging drops. **b,** Global jumping rate N_g as a function of time t: we consider all observed coalescences and average the proportion N_g that results in droplet jumps after merging, over one minute. For each series of data (obtained with pillar texture A, conical texture H3/E2 and truncated texture T1 to T4), we indicate with a dotted line the average value of N_g. The pink dots on the bottom show the jumping rate $N_g = 0.2\%$ for sample A. **c,** Jumping rate N_n of droplets on truncated cones T1 as a function of the mean radius

Adapted from: P. Lecointre, S. K. Laney, M. Michalska, T. Li, *et al.*, Unique and robust dew repelllency of nanocones, **Nature Communications**, 2021, 12, 3458

<r> of merging drops, after distinguishing the coalescences that imply $n = 2, 3, 4$ or 5 droplets. N_n increases with both n and <r>, explaining why a modest value of N_g can be accompanied by good antifogging abilities. Dotted lines are guides for the eyes. **d-e,** Jumping rate N_2 on sharp cones H/E for symmetric binary coalescences, for which merging radii do not differ by more than 20%. N_2 is plotted as a function of the average radius <r> for homothetic nanocones H1-H3 in **d** and for extruded cones E1-E4 in **e**. In both cases, the jumping rate plateaus at a constant value of 99 ± 1% above a critical radius $r_c \approx 1.5 \pm 0.4$ µm.

Despite fluctuations due to the huge polydispersity in drop sizes, the antifogging rate is stationary with an average value (Figure 57b; dotted line) that strongly depends on the texture. As expected from Figure 55 and Figure S 2 where drops were found to be quasi-spherical on cones and adhesive on pillars, we first note an extreme contrast between conical (sample H3, Figure 57b; blue dots) and cylindrical texture (sample A, pink dots on the abscissa axis), with respect to average values of N_g = 88% and 0.2%, as also captured through the sharp differences in the breath figures (Figure 56). Data obtained with all samples of H and E confirm the overall conclusions (Figure S 2), as well as observations performed after increasing the duration of the experiment by a factor of five or modifying the value of the supersaturation S.

Truncated cones provide an intermediate behaviour: N_g decays rapidly with the level of truncation, with an average value of 7% for T1 and of *ca.* 2% for the samples T2, T3 and T4. Hence truncated cones still have some capacity to repel dew, unlike sample A, despite similar contact angle hysteresis. We attribute this effect to the conical profile that might still promote nuclei to leave the interspace between structures and sit atop the texture.

However, judging the antifogging efficiency of truncated cones solely on the value of N_g can be grossly misleading. Whilst the global performance remains modest compared to that on H and E, breath figures on truncated cones, and especially T1, reveal no accumulation of water after 30 minutes (Figure S 7). Both the fraction occupied by water (~35%) and the radius of the largest drops (~30 µm) are comparable to that observed on nanocones H/E, in sharp contrast with the condensation on pillars (Figure 56). At first glance, the conjunction of low N_g and efficient water evacuation looks paradoxical. However, we can reconciliate this apparent contradiction by separating the jumping rates N_n for coalescences that imply n drops. These quantities are plotted in Figure 57c for the sample T1 as a function of the mean radius $<r> = \Sigma r_i/n$ of the merging drops, denoting r_i as the sizes of individual drops, with $1 \leq i \leq n$.

Each data corresponds to typically 40 events for which merging radii differ by no more than 30% for $n > 2$ (see data in Table S 1 and Table S 2 for T1 and T4, respectively). Figure 57c reveals an original antifogging mechanism, differing from the case for sharp cones (blue data in Figure 57b), where the high N_g implies that droplets jump irrespective of the value of n. The jumping rate N_2 for binary coalescences ($n = 2$) represents the majority of events, and it is found to be zero on truncated cones – thus explaining the origin for a low N_g. However, N_n increases markedly with both n ($n > 2$) and $<r>$, ultimately exceeding 50% for drop radii of ~20 µm at all $n \geq 3$. Smaller droplets suffer more from pining and triple, quadruple and quintuple merging events inject more surface energy than binary merging, which makes it possible to overcome the depinning barrier existing on truncated nanocones. Hence these structures can eventually exhibit a good antifogging ability, yet through a different mechanism than sharp cones: droplets grow for a longer time and are only evacuated when large enough and concentrated enough (which enables multiple coalescences), explaining why the samples are not saturated with water at long time.

We now contrast these results with those of the sharp nanocones H and E for which we focus on the jumping rate N_2 (Figure 57a and Figure S 9b), since the coalescence of two droplets (binary coalescences) provides a large enough conversion of surface energy to kinetic energy to overcome the low water adhesion and generate jumps. Furthermore, we restrict to symmetric coalescences (70% of the binary events), where the ratio between the radii of the two merging drops is between 0.8 and 1.2. As seen in Figure 57d and Figure 57e, the corresponding rate N_2 is about 100% for $r > 2$ µm, suggesting that the failure of jumping on sharp cones mainly arises from asymmetric merging that fails when injecting enough energy to prompt jumps. We split the results in two graphs that respectively display the antifogging efficiency N_2 for homothetic cones (samples H, Figure 57d) and for extruded cones (samples E, Figure 57e), both plotted as a function of $<r>$. Each data point is an average over typically 65 coalescences.

Remarkably, all results collapse on a single curve. In all cases, the jumping rate N_2 is typically 99% across a broad range of radii (from ∼2.5 µm to ∼25 µm, see also Figure S 10), with a few exceptions at large radius, a case where we have fewer coalescences (typically 10 to 20) so that one sticking event significantly affects the statistics. The very high rate of departure further confirms our assumption that microdroplets remain in the mobile Cassie state, and it generalizes the exceptional antifogging character of nanocones reported by Mouterde *et al.* on a unique sample:[16] the effect is found to be universal across a wide variety of cone geometries.

A second metric for antifogging is the drop radius r_c above which a water drop jumps. This quantity is found to be critical (within only 2 µm in radius $<r>$, N_2 varies from 0 to its maximum) and quasi-universal in the explored range of cone geometries. Defining r_c as the size at which we have $N_2 =$ 50%, we find $r_c = 1.8 \pm 0.2$ µm, 1.0 ± 0.3 µm and 1.6 ± 0.3 µm for samples H1, H2 and H3. For extruded cones E1 to E4, the critical radii are $r_c = 1.1 \pm 0.2$ µm, 1.6 ± 0.3 µm, 1.3 ± 0.3 µm and 1.9 ± 0.3 µm, respectively. These values are fairly constant, with changes comparable to the uncertainty of the measurement – a result also found on cones with similar size, yet convex instead of straight (Figure S 10). The typical critical size of jumping nicely agrees with the results in Figure S 2, where the contact angle was found to rapidly decay when the drop radius is below 1.5 µm – an effect we interpreted as resulting from the sinking of water inside the texture (*Eq. 35* and Figure S 4). The partial penetration of water in the substrate naturally increases its adhesion and thus impedes the mobility of droplets, preventing them from jumping. Interestingly, as seen in Figure S 10c, the quantity r_c was found to be larger on materials with a smaller jumping rate (nanoneedles), confirming the relevance of this parameter for quantifying antifogging.

4.2.4 Conclusion

In summary, the antifogging efficiency of sharp nanocones is shown to be universal across a vast range of texture sizes (50 – 420 nm), apex angles (15 – 38°) and cone shapes (straight/convex, with a sharp/round tip). Drops are observed to be quasi-spherical at microscales, which enables them to jump with a remarkable ~99% efficiency. The critical radius $r_c \sim 1.5$ µm of jump corresponds to the drop size at which we record a decrease of superhydrophobicity due to the partial penetration of water in the texture. Upon truncation, cones appear to lose some of their properties, with a smaller contact angle and global jumping rate. Nonetheless, condensing water is efficiently evacuated, which brings to light a new anti-fogging mechanism where, unlike binary merging, jumping is successful for triple, quadruple and quintuple coalescences. The antifogging efficiency also increases with drop size, so that most water can be swept from the surface. This finding should have technological implications: Firstly, it can be desirable to fabricate truncated structures to benefit from their higher mechanical resistance,[243] particularly for the case where we predominantly aim at evacuating decamicrometric drops as opposed to smaller ones. Secondly, sharp cones are likely to wear off over time, and it could previously be anticipated as an irreversible decay of the anti-dew behaviour. However, the clustered departures of drops might favour the persistence of the anti-dew property for blunt or broken tips, at least in the limit where hydrophilic tops (generated by the breaking of hydrophobic cones) play a marginal role.

To further advance the understanding, future research might focus on rigorously studying the jumping mechanism: we assumed here that it is related to the penetration of water inside the texture, but the exact threshold remains to be understood, in particular by accounting for the role of contact line pinning at the pillar tops. Another topic of interest concerns the effect of the cone design and chemistry upon the nucleation itself, a mechanism known to be influenced by surface properties, both chemical and physical. A final stimulating question concerns the increase in texture size: for cones in the micrometric or decamicrometric range, the dew drops will have sizes comparable to that of the texture, which should lead to new regimes of condensation and takeoff, preventing or delaying the antifogging effect.

4.2.5 Methods

4.2.5.1 Fabrication

Surfaces H2, H3, E0, E1, E2, E2', E3, E4, T1, T2, T3, T4.

These materials were produced by myself and Martyna Michalska according to the following fabrication steps:

(**1**) A layer of SiO_2 (44–100 nm) is deposited on a silicon wafer by plasma-enhanced chemical vapour deposition. The block-copolymer (BCP) poly(styrene-block-2-vinyl pyridine) (PS-b-P2VP) is self-assembled in m-xylene (0.4%) and subsequently spin-casted at 6000 rpm for 30 s resulting in a thin film. The obtained film comprises a well-ordered monolayer of hexagonally packed micelles, in which the molecular weight of each block dictates the distance between neighbouring micelles (pitch).

(**2**) A polymer breakthrough etch is performed in a PlasmaPro NGP80 Reactive Ion Etcher (RIE) at 20 °C under oxygen plasma in order to remove the polymer matrix. The remaining micellar bumps act as a topographic contrast for the subsequent SiO_2 etch.

(**3**) The micelle pattern is registered into the SiO_2 layer using CHF_3/Ar plasma etching: RF power 200 W, pressure 50 mTorr, CHF3/Ar 0.3. The SiO2 pattern acts as a hard mask for etching into the underlying Si.

(**4**) Dry Si etching is performed in an Advanced Silicon Etcher using chlorine plasma under low plasma power in order to achieve slow lateral etching and undercutting of the SiO_2 mask. The following conditions are used: Coil power 150–500 W, Platen power 10–60 W, pressure 3–6 mTorr, Cl_2 15–20 sccm.

(**5**) The remaining SiO_2 mask is stripped using hydrofluoric (HF) acid, to produce sharp tipped (H2–H3, E1–E4) or truncated cones (T1–T4), depending on the point at which the etching is stopped.

Surface A and H1.

In addition, we used as reference samples two materials produced at Brookhaven by A. Checco, A. Rahman and C.T. Black. The surface A is fabricated by combining block-copolymer self-assembly with anisotropic plasma etching in silicon, which provides large-area (cm^2) textures with ~10 nm feature size and long-range order. Posts, with diameter $l = 30$ nm and height $h = 88$ nm, are disposed on a rhombus network with side $p = 52$ nm. The surface H1 is fabricated using the same method as for sample A, but etching is made more isotropic, which provides the conical shapes.

ESEM procedures.

The dynamics of water condensation is imaged using a FEI Quanta 650 field emission gun (FEG) environmental scanning electron microscope of the Laboratoire de Mécanique des Solides at École Polytechnique by Pierre Lecointre.

The sample is mounted on a horizontal bracket for top images and a 60°-tilted copper bracket for tilted images. The support can be inclined up to 90° to provide a clear view of water droplets. The bracket is mounted on a thermoelectric (Peltier) cooling stage and both temperature and chamber pressure are controlled. Before every experiment, five purging cycles are performed, consisting in varying the pressure between 150 and 600 Pa, in order to remove any non-condensable gas. After this procedure, the sample is chilled at around −2 ± 1 °C for 2 min at a vapour pressure of 200 Pa. Water condensation is later achieved by increasing the chamber pressure to about 500–700 Pa. Low beam energies (10 keV) and 3.5 spot size were used to prevent all damage caused by ESEM. A SE detector (GSED) is selected for imaging as it yields better results than BSE detector. Tilting the sample influences the amount of secondary electrons produced, since a greater proportion of the interaction volume is then exposed. Consequently, emission at edges is particularly high and they appear brighter than flat surfaces. The detector potential is set at 330 ± 30 V (bias between 55 and 65) in order to prevent e-beam charging: the electric field magnitude increases with the bias, hence surface potential is more important for high bias. This parameter was found to be crucial for limiting wettability changes during condensation. Higher bias led to the complete wetting of condensing droplets, which might be due to the destruction of the hydrophobic layer. Finally, the electron beam working distance is set around 5 mm. Recordings were performed at various frame rates, varying from 0.3 to 4.6 fps.

Contact-angle measurements.

Contact angles are deduced from imaging by extracting from image analysis the drop radius r and the contact radius ∼ (radius of the apparent contact area of the drop with the surface). The contact angle θ is simply deduced from the geometric relationship $\sin\theta = \lambda/r$. Since drops arising from condensation are inflating, these experiments provide the so-called advancing contact angle. When slowly inflating a drop, this angle corresponds to the value observed at the contact line when this line starts moving (that is, once the drop is not pinned any more). We denote the velocity of the contact line as v. The typical rate of inflation is chosen so as to reach a quasi-static limit for the contact angle, corresponding to capillary numbers $\eta v/\gamma$ (denoting η and γ as the viscosity and surface tension of water) smaller than 10−3. In our experiment, we are indeed in the inflating mode, since drops are growing owing to the condensation from the atmospheric water. The velocity v of the contact line as drops grow (in Figure 55c, for instance) is between 0.3 and 1 µm/s, so that the capillary number for water is 10−8, indeed in quasi-static limit.

Antifogging efficiency of nanotexture: experimental set-up.

The experimental setup is defined in Figure 57a. The breath figure is observed with a microscope (Nikon Eclipse Ti-U) equipped with a video-camera (Hamamatsu C11440). Samples are placed upside down, so that departing drops do not re-deposit on the material, which would complicate the analysis of the antifogging effect. We can wonder whether gravity might detach droplets (with radius r). To that end, we compare its magnitude to the force induced by adhesion by introducing the Bond number $Bo \approx \rho g r2/\gamma \sin\theta a (\cos\theta r - \cos\theta a)$. The maximum observed radius of drops condensing on nanocones is 35 µm (owing to the high antifogging efficiency), which yields a Bond number $Bo \approx 0.01$ for $\theta a \approx 165°$ and $\theta r \approx 150°$. Hence gravity can be neglected in our setup, in agreement with the observation that drops never depart without coalescing with their neighbours.

Adapted from: P. Lecointre, S. K. Laney, M. Michalska, T. Li, *et al.*, Unique and robust dew repelllency of nanocones, **Nature Communications**, 2021, 12, 3458

5

SPACER DEFINED INTRINSIC MULTIPLE PATTERNING FOR COMPLEX NANOARRYS WITH MULTIFUNCTIONAL SURFACE PROPERTIES

This chapter is an amalgamation of two papers published in ACS Nano and Langmuir which detail the fabrication route for single nanotubes and complex nanoarrays (with some illustrative optical functionality) and the delayed depletion of lubricant from a nanotube surface, respectively. The fabrication was carried out by TL and myself, the optical properties of the surface were characterised and modelled by FR, MP and IP, the SLIPS were fabricated and characterised by myself with assistance in the experiment design from MM, JO and MKT.

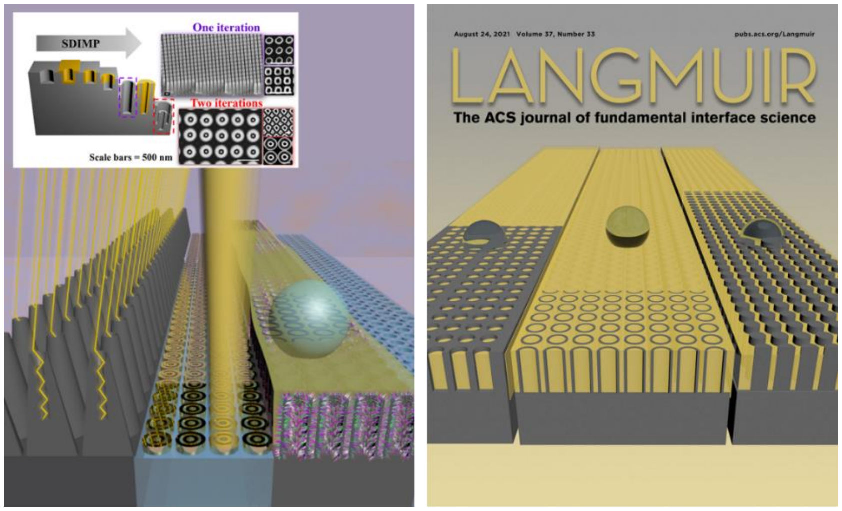
SDIMP
One iteration
Two iterations
Scale bars = 500 nm
August 24, 2021 Volume 37, Number 33
pubs.acs.org/Langmuir
LANGMUIR
The ACS journal of fundamental interface science

Left: Graphic representation of the types of nanostructures that can be generated through SDIMP, and the tested or anticipated properties (inset shows the fabrication process.) Right: Cover art accepted into Langmuir, depicting the enhanced lubricant retention properties of nanotubes compared to nanoholes and nanopillars.

Adapted from: S. K. Laney, T. Li, M. Michalska, *et al.*, Spacer Defined Intrinsic Multiple Patterning, **ACS Nano**, 2020, 14, 12091-12100

5.1 Fabrication

5.1.1 Abstract

Periodic nanotube arrays render enhanced functional properties through their interaction with light and matter, but to reach optimal performance for technologically prominent applications, *e.g.*, wettability or photonics, structural fine-tuning is essential. Nonetheless, a universal and scalable method providing independent dimension control, high aspect-ratios, and the prospect of further structural complexity, remains unachieved. Here, we answer this need through an atomic layer deposition (ALD)-enabled multiple patterning. Unlike previous methods, the ALD-deposited spacer is applied *directly* on the pre-patterned target substrate material, serving as an etching mask to generate a multitude of *tailored nanotubes*. By concept iteration, we further realize concentric and/or binary nanoarrays in a number of industrially important materials such as silicon, glass, polymers. To demonstrate the achieved quality and applicability of the structures, we probe how nanotube fine-tuning induces broadband antireflection, and present a surface boasting extremely low reflectance of <1% across the wavelength range 300-1,050 nm.

5.1.2 Introduction

The proliferation of interest in periodic nanostructured surfaces has driven significant advancements in nanofabrication techniques, leading to their successful implementation into energy storage devices,[244] solar cells,[91,245] sensing,[246] and special wetting surfaces.[247] Whilst the collective interactions of many sub-components within an array, and the resultant surface properties are well studied for pillars, cones or holes, more complex designs allude to more exotic phenomena. For example, superior control over localisation of electromagnetic fields can be achieved,[248–250] if only the complexity of sub-components is tuned adequately. In particular, nanotubes; hybrid structures of nano-holes within pillars that amalgamate the best attributes from each (high surface area yet low solid fraction), are gaining significant attention due to their widespread applicability spanning solar cells,[251] batteries,[252,253] sensing/SERS,[254–256] molecule delivery systems,[257] smart surfaces,[258] and nanocatalysis.[259] Despite the progress to achieve nanotube arrays, expanding on their complexity (*e.g.*, concentric/binary structures) alongside advanced feature control and large-scale fabrication, remains a synthetic bottleneck.

Adapted from: S. K. Laney, T. Li, M. Michalska, *et al.*, Spacer Defined Intrinsic Multiple Patterning, **ACS Nano**, 2020, 14, 12091-12100

Some advances have been made to address these shortcomings, like colloidal templating in combination with metal sputtering and reactive ion etching (RIE),[260,261] and a recently reported multi-patterning technique.[98] Although the latter is scalable and harnesses nanometer-scale dimension control, shape tunability and binary structure generation is limited; yet desired in many applications, where subtle structural changes often drastically impact on overall performance.[262] Latest advancements in binary nanoarray generation have emerged through anodic aluminum oxide templating, allowing highly controlled optimisation of the morphology and/or material, but at the cost of complicated fabrication.[248] Well-defined hollow nanostructures (*e.g.*: nanotubes, nanovolcanos) have been achieved *via* secondary electron lithography induced by ion-beam milling, however this too suffers from scalability.[263] One method that has gained the attention of the semiconductor industry, is spacer defined double patterning (SDDP), which uses ALD instead of multistep lithographic processes to overcome the resolution limit and reduce fabrication steps, thus better complying with high volume manufacturing.[264–266] In SDDP, a highly conformal ALD-deposited film-spacer is applied to a sacrificial pattern (photoresist or hard mask) and etched anisotropically so that the spacer sidewalls serve as an etching mask, resulting in a pitch half of the original. For 1D gratings, SDDP is a well-established method, with double iterations often performed to further multiply pattern resolution.[264] However, despite the low process complexity, only few examples of SDDP onto 2D patterns (holes/pillars) to generate nanotubes – a morphology otherwise challenging to obtain – have been reported.[259,267,268] Yet still, these demonstrations do not harness the full dimensional control, nor do they expand on the structural complexity through further iterations.

To that end, we present an alternative branch of ALD-assisted etching, namely *spacer defined intrinsic multiple patterning* (SDIMP), to generate wafer-scale tailored nanotubes, as well as complex nanoarrays.. Unlike previously reported spacer deposition on 2D-patterns, we first etch nanoholes or nanopillars of varying aspect-ratio (AR=1-6) into the target substrate material (Si or SiO_2), and directly deposit the Al_2O_3-spacer, as opposed to performing ALD earlier, on the photoresist/hard mask itself (Figure 58 further highlights the differences between SDDP and SDIMP). This generates intrinsic, rather than free-standing nanotubes which provides excellent control over pattern integrity and height.

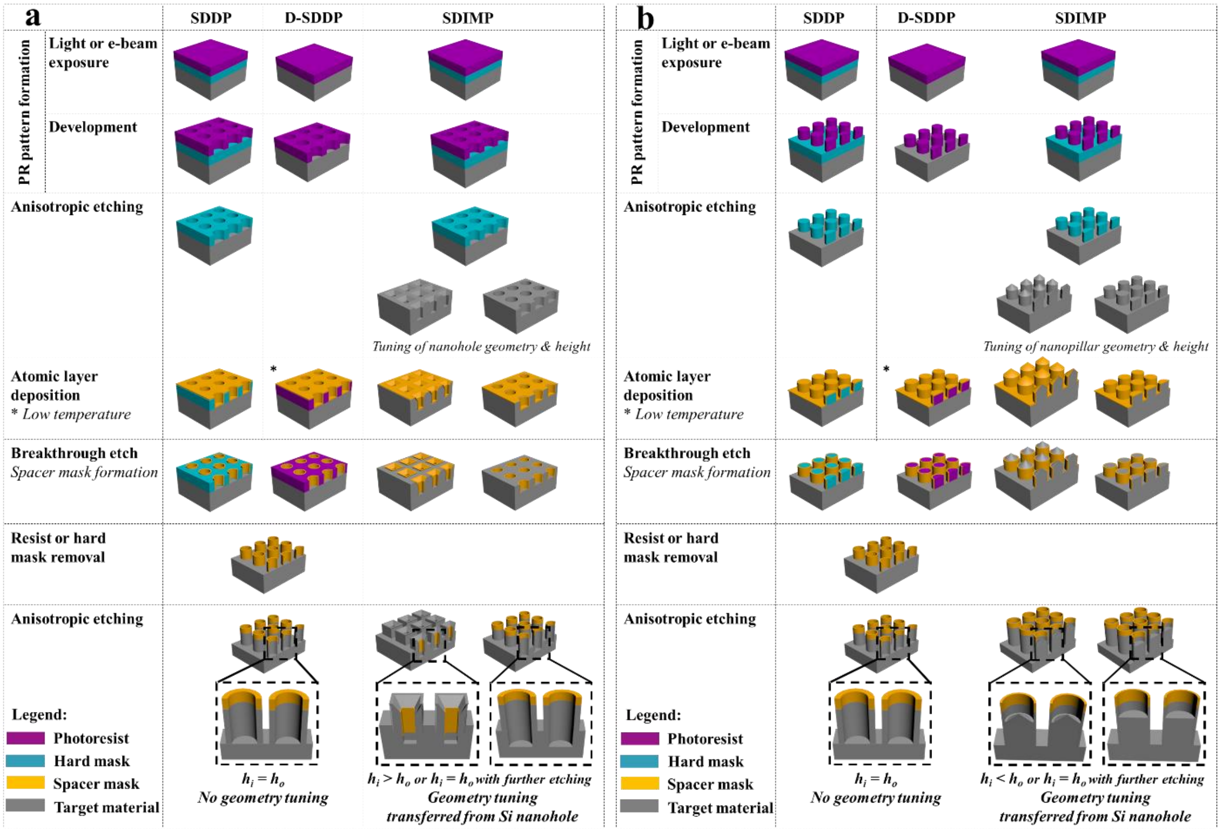
a
SDDP
D-SDDP
SDIMP
PR pattern formation
Light or e-beam exposure
Development
Anisotropic etching
Tuning of nanohole geometry & height
Atomic layer deposition
* Low temperature
*
Breakthrough etch
Spacer mask formation
Resist or hard mask removal
Anisotropic etching
Legend:
Photoresist
Hard mask
Spacer mask
Target material
$h_i = h_o$
No geometry tuning
$h_i > h_o$ or $h_i = h_o$ with further etching
Geometry tuning
transferred from Si nanohole
b
SDDP
D-SDDP
SDIMP
PR pattern formation
Light or e-beam exposure
Development
Anisotropic etching
Tuning of nanopillar geometry & height
Atomic layer deposition
* Low temperature
*
Breakthrough etch
Spacer mask formation
Resist or hard mask removal
Anisotropic etching
Legend:
Photoresist
Hard mask
Spacer mask
Target material
$h_i = h_o$
No geometry tuning
$h_i < h_o$ or $h_i = h_o$ with further etching
Geometry tuning
transferred from Si nanohole

Figure 58 | Schematics highlighting the differences between SDIMP and SDDP/D-SDDP methods for circular patterns. Here, SDIMP is spacer defined intrinsic multiple patterning; SDDP is spacer defined double patterning; and D stands for direct. **a,** Starting from a nanohole morphology and **(b)** starting from a nanopillar morphology in PR. In SDIMP, the pattern is transferred from the hard mask to the target material *via* anisotropic etching, whereby tuning of the morphology can be introduced [**(a)** square with crown, or circular nanoholes and **(b)** nanopencils or flat nanopillars]. The ALD-deposited spacer is then applied directly onto the pre-patterned target material, resulting in the conformal layer following the tuned nanohole/pillar geometry. As shown, this is not possible for either SDDP or D-SDDP as the nanohole/pillar pattern is only transferred to the hard mask or PR, respectively. The subsequent etching of the ALD-coated nanostructures results in nanotubes with, for SDIMP varying inner and outer height with possible extension to equal heights, whereas for SDDP and D-SDDP typically nanotubes with equal heights are achieved (modifications in some cases are possible, however the control is poor).

By virtue of a comprehensive mechanistic understanding, we first demonstrate independent control over nanotube dimensions; pitch/spacing, height, and diameter – already leading to binary nanoarrays, and also show structure replication into polymers. Advancing the control further, we

Adapted from: S. K. Laney, T. Li, M. Michalska, *et al.*, Spacer Defined Intrinsic Multiple Patterning, **ACS Nano**, 2020, 14, 12091-12100

tune the morphology; geometry, tapering and internal structuring. Furthermore, by performing a second SDIMP iteration, an expansive library of complex nanostructures can be achieved and we demonstrate some as a proof-of-concept; fabricated in a large-scale yet straightforward manner. Finally, we illustrate photonics as one of the many potential applications, with an exemplar tailored nanotube array achieving efficient broadband antireflection; <1%, 300-1,050 nm. Given the ability to engineer unlimited combinations of feature sizes and dimensions through one or more iterations, we envision SDIMP to be a general route for the fabrication of complex meta-nanostructures targeting applications in SERS and optical trapping, for instance.

5.1.3 Results And Discussion

5.1.3.1 Spacer defined intrinsic multiple patterning

Figure 59 details the fabrication process of the silicon (Si; target material) nanotube arrays, which can have two distinct starting points; photoresist (PR) nanopillars (Figure 1a) or nanoholes (Figure 59b).

Adapted from: S. K. Laney, T. Li, M. Michalska, *et al.*, Spacer Defined Intrinsic Multiple Patterning, **ACS Nano**, 2020, 14, 12091-12100

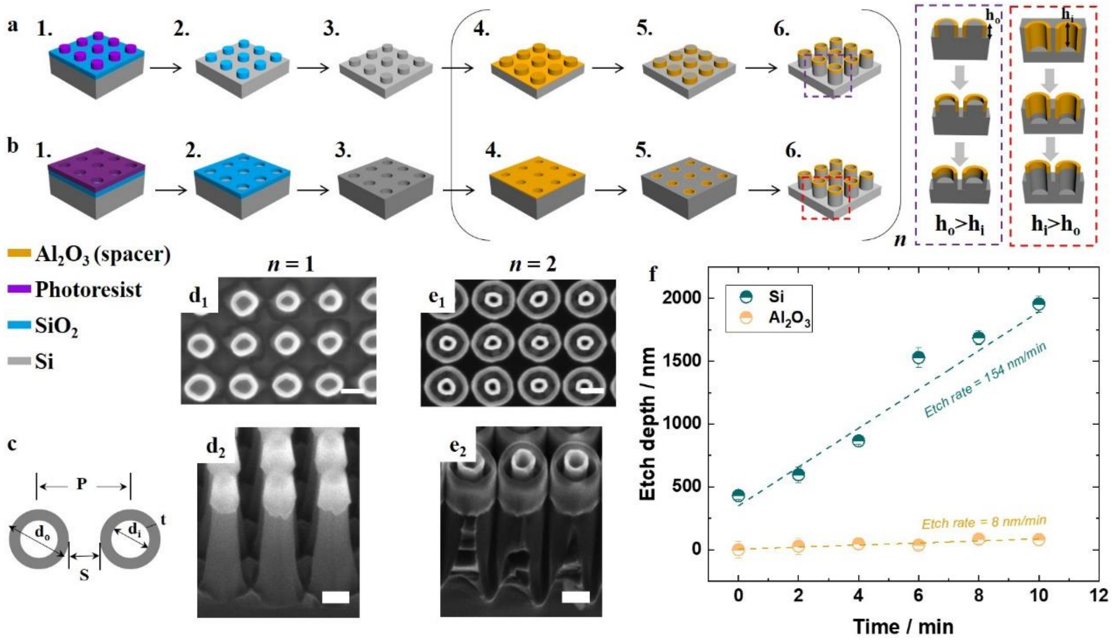

Figure 59 | Nanotube fabrication process and tuning of the pitch and height. **a,b** Schematics of the fabrication process starting from photoresist pillars (a) or holes (b). From left to right: (Step 1) PR pattern; (Step 2) Etching the underlying SiO_2 layer using the PR mask; (Step 3) Etching silicon using the SiO_2 as a hard mask; (Step 4) Depositing conformal layer of Al_2O_3 *via* ALD; (Step 5) Etching Al_2O_3 to consume horizontal deposition but leave vertical (sidewall) deposition; (Step 6) Etching into silicon using spacer-sidewalls as a hard mask [outer sidewalls of pillar (a) or inner sidewalls of hole (b)]; Steps 4-6 can be iterated n times to obtain numerous complex nanostructures. Schematics on the right-hand side illustrating the difference in inner and outer height (h_i and h_o, respectively) of the end nanotube when starting from a nanopillar array (purple) or nanohole array (red). **c,** Top view schematic indicating the notation to describe nanotube arrays, where *S*=spacing, *P*=pitch, d_o=outer diameter, d_i=inner diameter, *t*=thickness of tube corresponding to ALD thickness. **d_1,e_1**, Top view and **d_2,e_2**, side view SEM images of nanostructures after one or two iterations (n=1,2). **f,** Graph highlighting the selectivity of the process, with etch rates for Si (154 nm/min) and Al_2O_3 (8 nm/min) giving rise to a selectivity ~20 for an example nanotube array, originating from a pillar morphology. Scale bars = 200 nm.

The evolution of the structures (Step 1-6) is presented in a collection of scanning electron microscopy images (SEM; Figure 60) which begins from the generation of PR pattern (Figure 59, Step 1), with detailed information on specific conditions/times/thicknesses/dimensions given in Table 2-Table 5 in the Methods section. A Si wafer with a thin layer of deposited glass (SiO_2) is coated with PR and then patterned *via* laser interference lithography to achieve periodically-ordered square or hexagonally close-packed PR nanopillars or nanoholes. Note, *any* lithographic

Adapted from: S. K. Laney, T. Li, M. Michalska, *et al.*, Spacer Defined Intrinsic Multiple Patterning, **ACS Nano**, 2020, 14, 12091-12100

method can be used to pattern the PR, thus enabling various pitches and geometric arrangements (periodic or non-periodic). Step 2 uses a fluorine (F) based RIE to register the pattern into the SiO_2 layer. This acts as a hard mask in Step 3 when chlorine (Cl) plasma is used to etch into Si (selectivity ~10:1) which, distinctive of SDIMP (see Figure 58), permits the generation of intrinsic nanohole/pillars of high aspect-ratio greater than four. Step 4 involves ALD-coating the attained Si arrays in a layer of aluminium oxide (Al_2O_3=spacer) of predetermined thickness (*t*). The subsequent RIE takes place in a single step, however to understand the mechanism, it is broken down into two parts; (i) a breakthrough etch which acts to anisotropically remove a horizontal spacer layer equal to *t*, to attain exposed Si inside and outside a tube of Al_2O_3 (Step 5), and (ii) a selective etch using vertical spacer sidewalls as a mask (Step 6). Due to the high etch selectivity under Cl plasma (>15:1), evidenced in Figure 59f with an obtained selectivity ~20, the Al_2O_3-coated sidewalls etch more slowly than Si, thus enabling the transfer of the pattern into Si and the generation of high-aspect ratio nanotube arrays (where high AR at the nanoscale is defined as >1). Note, other RIE processes could be easily employed such as pseudo-Bosch recipe utilizing SF_6/C_4F_8 gases,[269] given the process is selective. The etching proceeds until the mask consumption, or alternatively the residual spacer can be removed by hydrofluoric acid.

Adapted from: S. K. Laney, T. Li, M. Michalska, *et al.*, Spacer Defined Intrinsic Multiple Patterning, **ACS Nano**, 2020, 14, 12091-12100

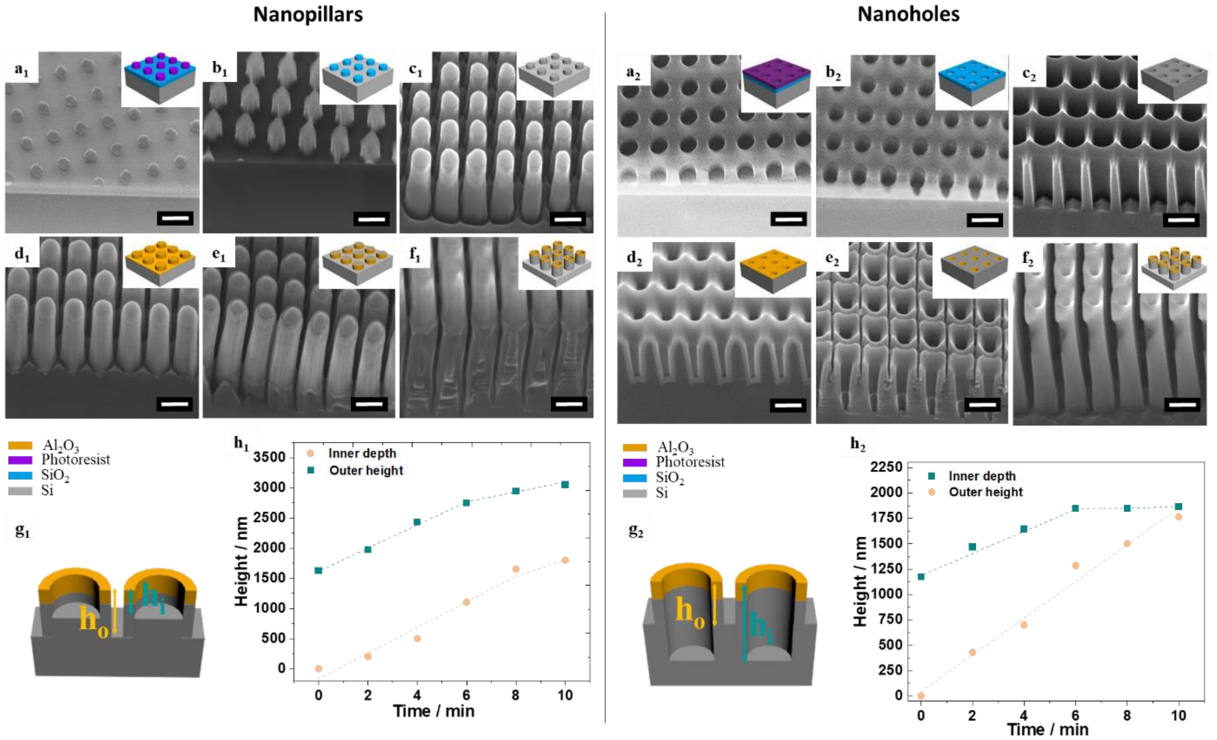

Figure 60 | Corresponding SEM images (45° tilted) to the fabrication scheme in when starting from photoresist nanopillar morphology (left) or nanohole morphology (right). a, Photoresist pattern. **b,** Etching the underlying SiO_2 layer using the photoresist mask. **c,** Etching silicon using the SiO_2 as a hard mask. **d,** Depositing conformal layer of aluminium oxide *via* ALD. **e,** Etching Al_2O_3 to the point where the horizontal deposition is consumed and only vertical deposition remains. **f,** Etching into silicon using the vertical deposition as a mask. **g,** Schematic indicating how the evolution of the inner and outer height was measured in (**h**) in which we present how these heights change for a nanotube originating from a pillar (left), which possesses an inherently larger initial h_o than h_i and nanohole (right) which possesses an inherently larger initial h_i than h_o. Scale bar = 500 nm.

The main criterion for SDIMP is to select materials with high etching contrast (selectivity) in an anisotropic RIE process.[270] To demonstrate this versatility, we show similar nanotube formation in glass using CHF_3/Ar chemistry during RIE with either PR or Al_2O_3 mask (Figure 61a-f). Additionally, we show replication of the structure in photoresist *via* nanoimprint lithography (NIL; Figure 61h), as well as generation of an inverse nanotube morphology with hierarchical features in polyurethane acrylate *via* soft lithography (Figure 61g). These serve as examples for either

Adapted from: S. K. Laney, T. Li, M. Michalska, *et al.*, Spacer Defined Intrinsic Multiple Patterning, **ACS Nano**, 2020, 14, 12091-12100

further scaling-up (NIL) or to provide inspiration for additional applications requiring flexible substrates.

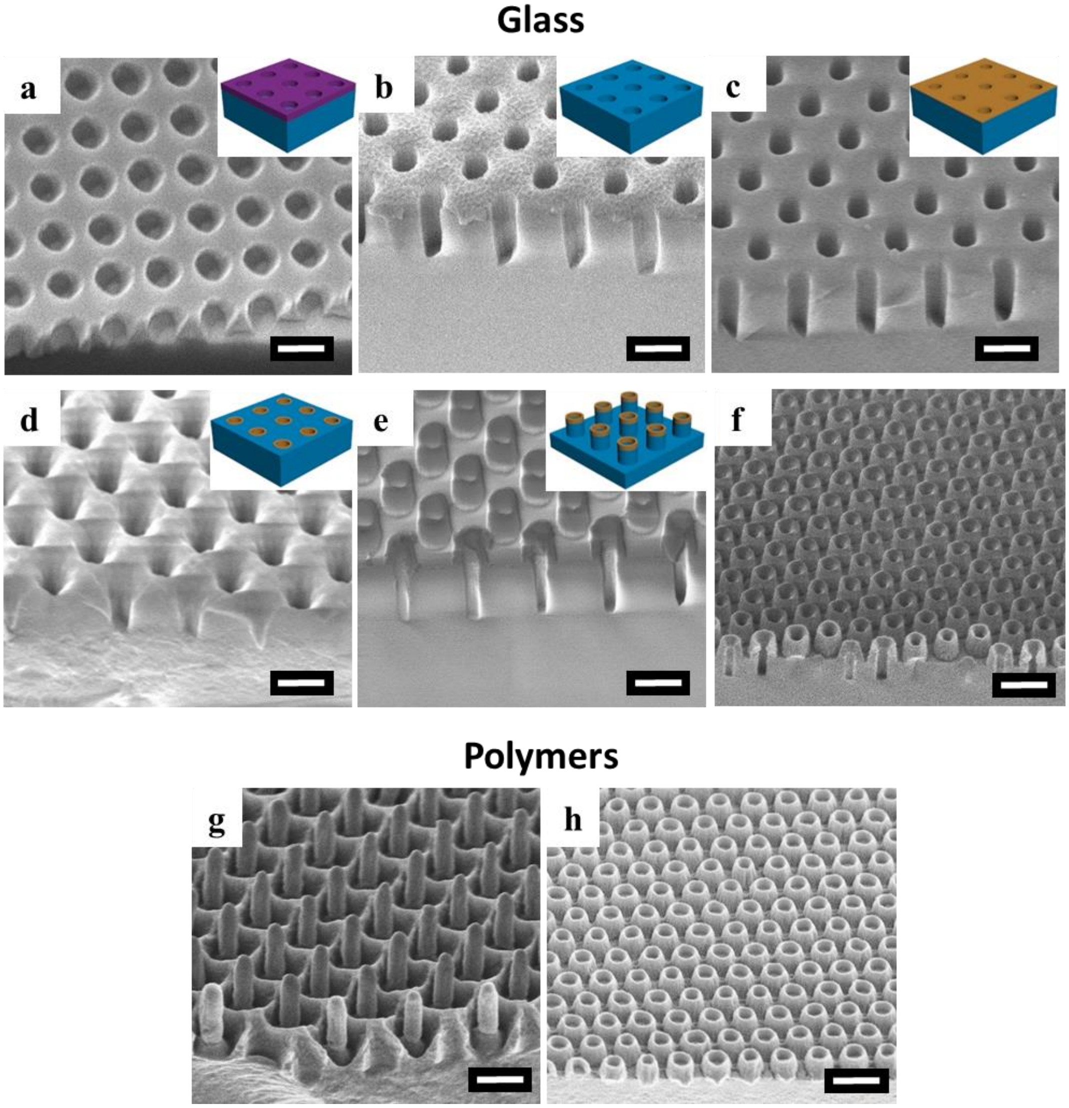

Figure 61 | Corresponding SEM images (45° tilted) to the fabrication of nanotubes in glass and imprints into polymers. a, Photoresist holes on SiO_2 substrate. **b,** Etched nanohole arrays into SiO_2. **c,** Nanoholes coated with 30 nm layer of Al_2O_3. **d,** Breakthrough etch. **e,** Further etch using the vertical deposition as a mask. **f,** Additional glass nanotube example but with hexagonal arrangement. **g,** Inverse nanotubes imprinted in polyurethane acrylate (PUA) *via* soft lithography. **h,** Photoresist nanotubes made *via* nanoimprint lithography. Scale bar = 500nm.

SDIMP could also readily be expanded to other semiconducting (*e.g.*: Ge, GaAs, InP, ZnO *etc.*), oxide (*e.g.*: HfO_2, ZrO_2, TiO_2, MgO, and Sc_2O_3 *etc.*) and nitride materials (SiN). Note, for low selectivity pairs, *e.g.*, TiO_2-silicon processed under chlorine plasma,[271] for instance, SDIMP is possible but will result in low aspect ratio structures.

If, however, a free-standing TiO_2 nanostructure is needed, one could use our reported process to generate a sacrificial template of a given complexity in silicon. Subsequently, one could deposit TiO_2 onto the template and perform SF_6 isotropic etching (selectivity as high as 66,000:1) to completely remove the sacrificial layer, resulting in a complex TiO_2 pattern.[272]

5.1.3.2 One SDIMP iteration – mechanism of control

To achieve designer complex nanostructures, the challenge lies in an effective control of each sub-dimension. We therefore begin with breaking down the levels of independent control attainable through one SDIMP iteration. First, we tune the nanostructure size (pitch/spacing, height, diameter) and then delve into a more advanced level of control over the morphology (geometry, tapering). We demonstrate further how, through intelligent design and collective tuning of features, additional complexity can be introduced.

The pitch (*P*, defined in Figure 59c) and spatial arrangement of the nanoarrays is dictated by the lithographic method used – here LIL – providing flexibility in defining this parameter. Two nanotube arrays of P = 350 and 560 nm are shown in Figure 62 demonstrating excellent pattern resolution of the end nanotube which is an attribute of the precise techniques involved: ALD and plasma etching.

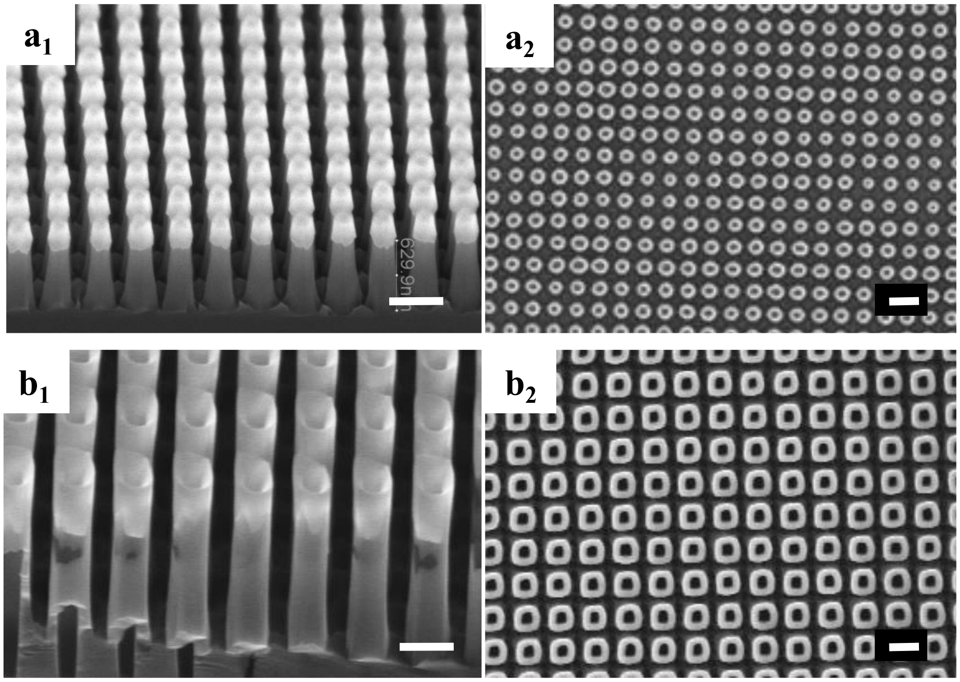

Figure 62 | SEM images of nanotubes generated at two different pitches. a, 350 nm pitch. **b,** 560 nm pitch. Scale bars = 500 nm.

Similarly, the lithographic method determines the morphology of the PR; nanopillar or nanohole. By deliberately choosing one starting morphology, the relation between the outer and inner height of the tube (h_o and h_i, respectively) can be addressed, and the evolution is shown schematically on the right-hand side of Figure 1a. We monitor this evolution for exemplary nanotubes originating from nanopillars and nanoholes in Figure 60, where it can be seen that h_o becomes greater than h_i in a former case and $h_i>h_o$ in the latter. However, other factors such as RIE lag[273] (lower etching rates at smaller feature sizes and *vice versa*) can alter the expected evolution of h_o and h_i.

Whilst nanotubes of high aspect-ratio can be generated, with the highest AR of ~6 attained in this study (Figure 60f$_1$), low aspect-ratio 2D nanorings can also be realised. Independent control of the inner diameter is gained when starting from nanohole morphology and depositing Al_2O_3 of precise thickness (Figure 63a,c) with subsequent etching to generate the nanotubes (Figure 63b,d). Control of the outer diameter is equivalently obtained when starting from nanopillars with a possible extension towards connected or binary nanoarrays (Figure 63e,f), as a consequence of Al_2O_3 deposition when criterium of t >(S/2) is met. Additionally, this enables a change in the spatial arrangement.

We now show more advanced control over the nanotube geometry, in addition to combining the acquired understanding to create more intricate structural changes. Unlike the PR mask, the robustness of the SiO_2 hard mask facilitates finer geometry tuning, as it withstands a wider range of RIE conditions. For example, it allows for achieving both circular and square nanoholes in Si (Figure 63g,i), by varying RIE power. The morphological change arises from angular ion distribution, whereby ions impact and scatter from the evolving feature. Consequently, not only more angular (square) nanoholes are created, but also facets at the top of the hole and trenching at the base (Figure 64), and this becomes more apparent with greater RIE power and longer process time.[274] This additional level of flexibility and control carries through to the nanotube due to the conformal nature of ALD, allowing cylindrical or cuboid nanotubes to be formed (Figure 63h,j).

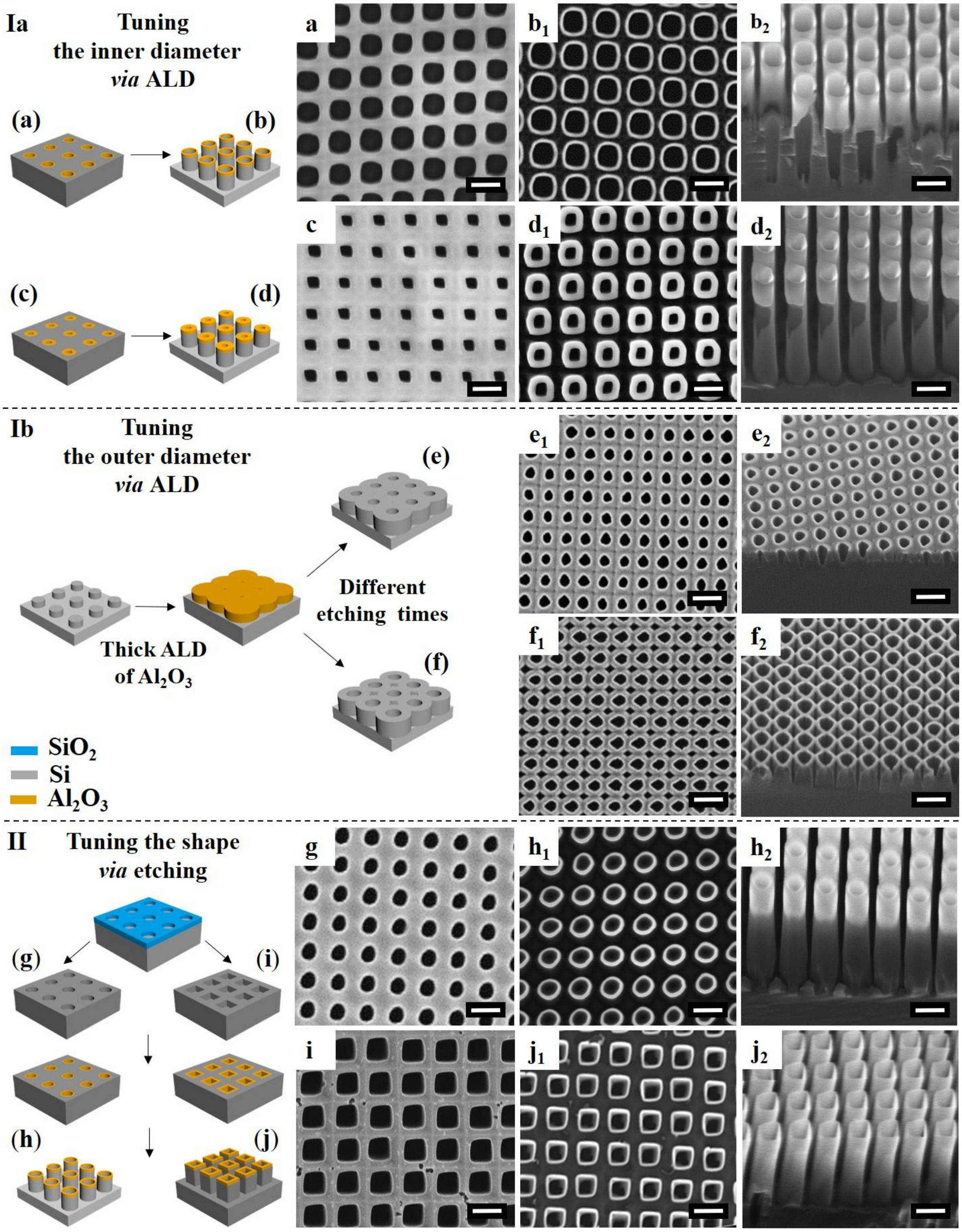
Ia
Tuning the inner diameter *via* ALD
(a)
(b)
(c)
(d)
a
b1
b2
c
d1
d2
Ib
Tuning the outer diameter *via* ALD
Thick ALD of Al2O3
Different etching times
(e)
(f)
e1
e2
f1
f2
SiO2
Si
Al2O3
II
Tuning the shape *via* etching
(g)
(i)
(h)
(j)
g
h1
h2
i
j1
j2

Figure 63 | Fine-tuning the nanotube dimensions during one SDIMP iteration. SEM images (top views labelled as x or x_1; and 45° tilted labelled as x_2) demonstrating examples of how the

Adapted from: S. K. Laney, T. Li, M. Michalska, *et al.*, Spacer Defined Intrinsic Multiple Patterning, **ACS Nano**, 2020, 14, 12091-12100

shape of the tube can be tuned at different stages in the fabrication process. **Ia,Ib,** Schematic and corresponding SEMs of tuning inner and outer diameter. **Ia,** When starting from the same nanohole structure but differing in the ALD thickness; (a)=30 nm, (c)=90 nm, tubes with thinner (b) or thicker walls (d) are achieved. **Ib,** When starting from the same pillars, coated with thick spacer layer, but differing in etching time, connected (e) or binary arrays (f) are generated. Note that thickness of deposited layer must correspond to at least half of the pillar spacing. **II,** Schematic and corresponding SEMs of tuning the shape of nanostructures. When starting from the same SiO_2 hard mask, but altering the silicon etch conditions (coil/platen power and time), cylindrical (g) or square holes (i) are generated. The subsequent ALD process and etch results in cylindrical tubes (h) or cuboid tubes (j). Scale bar = 500 nm.

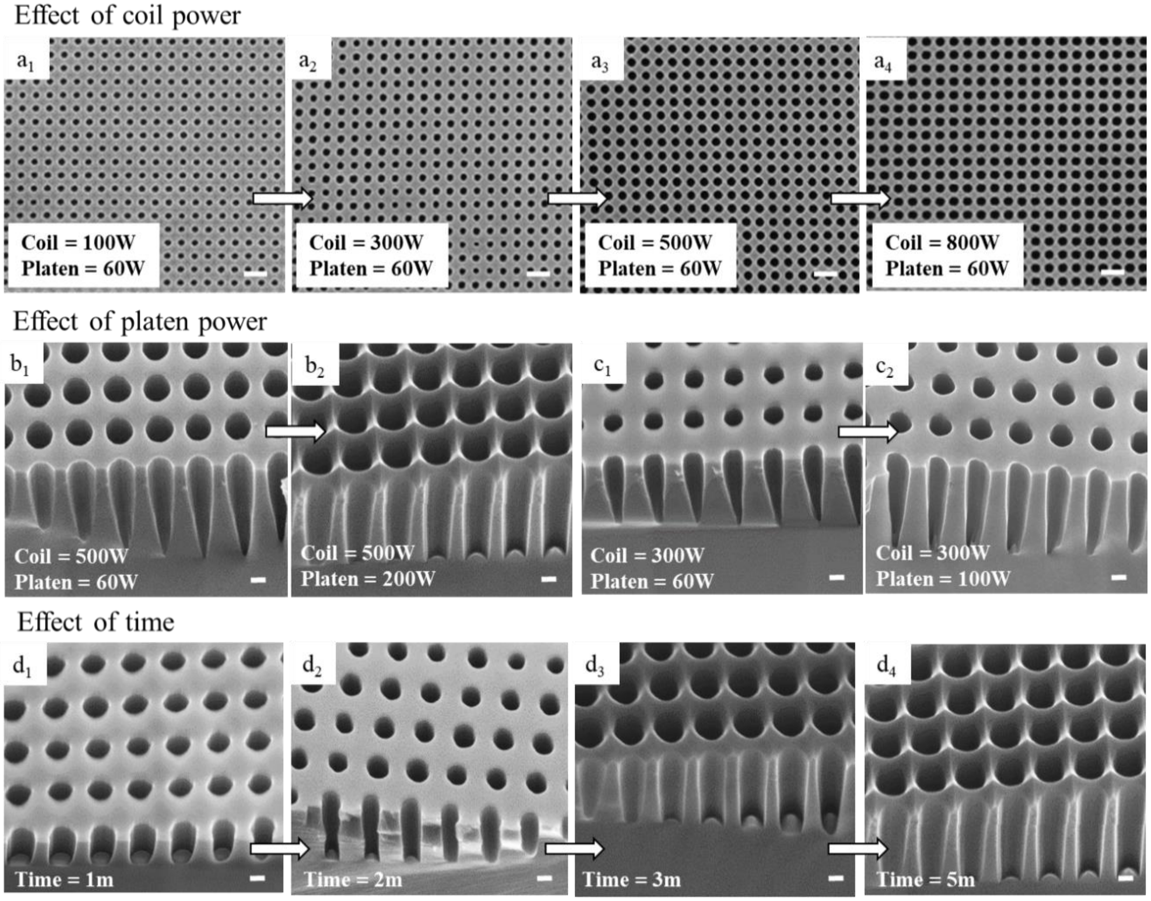
Effect of coil power
a1
a2
a3
a4
Coil = 100W Platen = 60W
Coil = 300W Platen = 60W
Coil = 500W Platen = 60W
Coil = 800W Platen = 60W
Effect of platen power
b1
b2
c1
c2
Coil = 500W Platen = 60W
Coil = 500W Platen = 200W
Coil = 300W Platen = 60W
Coil = 300W Platen = 100W
Effect of time
d1
d2
d3
d4
Time = 1m
Time = 2m
Time = 3m
Time = 5m

Figure 64 | Investigation into the effect of coil power, platen power and time for the fabrication of the nanohole arrays in Si. a, The effect of coil power is investigated starting from 100 W to 800 W at a constant platen power of 60 W for a time of 5 min. **b,** The effect of platen power is investigated starting from 60 W to 200 W at constant coil power of 500 W and time 5 min. **c,** The effect of platen power is investigated from 60 W to 100 W at constant coil power of 300 W and time 5 min. **d,** The effect of time is investigated starting from 1 to 5 min at a constant coil power of 500 W and platen 200 W. Scale bar for (a) is 1 µm, for (b-d) is 200 nm.

By taking advantage of the aforementioned tuning mechanisms, the discussed facet formation in the Si nanohole materialises as a crown structure. This feature can be further preserved and transferred into the nanotube through (i) a thick layer of Al_2O_3 and (ii) mild post-ALD etching conditions, which also gives rise to outer sidewall tapering (Figure 65). The necessity for such a high degree of morphological control is critical for optical properties as discussed in the Applications section.

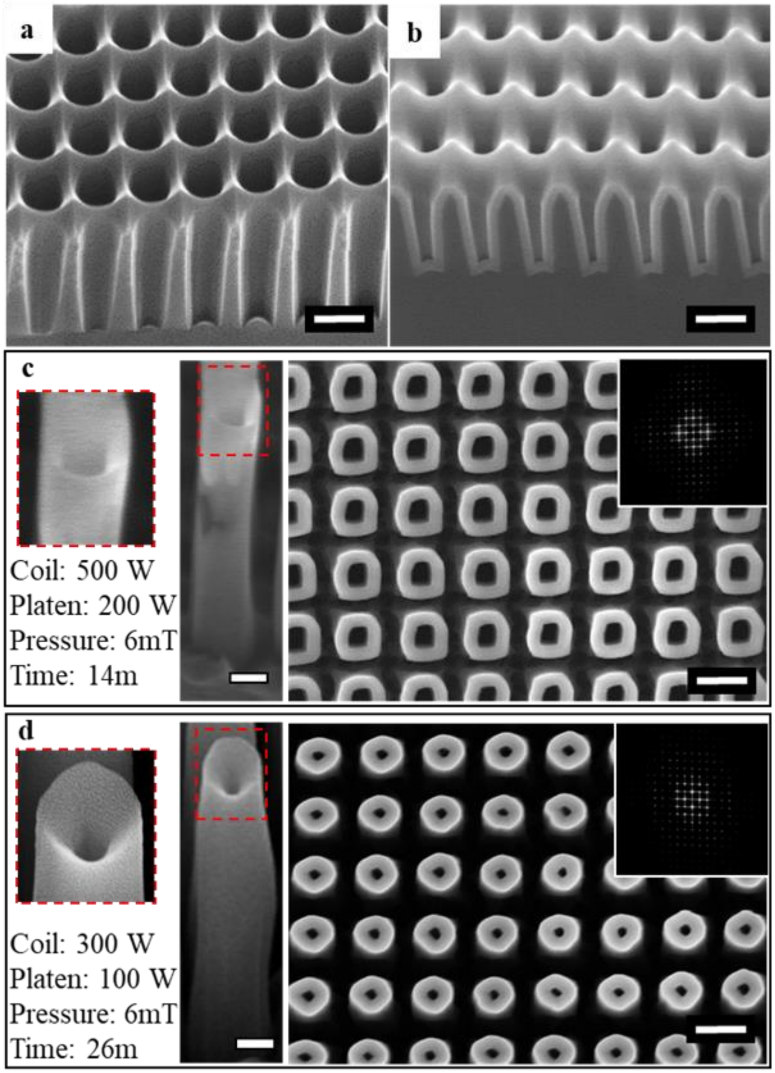

Figure 65 | Tuning the transfer of the crown structure to the nanotube, and the outer and inner tapering. a, SEM image of the nanohole array with crown structure present at the **b,** top. SEM image of the same nanohole array with 90 nm layer of Al_2O_3 deposited. **c,** Harsh and **d,** mild etching conditions applied to (b) result in anisotropic or tapered etching of the inner and outer nanotube walls, respectively (side view SEM). Additionally, the post-ALD etching results in either removal (c) or preservation (d) of the crown (side and top view SEM.) The Fast Fourier Transform (FFT; inset), indicates that the order which originated from the LIL patterning, is preserved through to nanotube formation. Scale bars (a,b,d,f) = 500 nm, (c,e) = 200 nm.

5.1.3.3 Two SDIMP iterations – complex structures

Unlike previously demonstrated spacer defined quadruple patterning (SDQP),[264] where the additional iteration requires a different spacer material, we repeat SDIMP in the same manner, providing a proof-of-concept of higher complexity structures created through multiple iterations. However, owing to the now more densely-confined features, the etching conditions may need an adjustment to converge to the same quality between iterations and prevent pattern distortions likely caused by high-energy ions reflecting off the greater surface area, for instance. As an example, we note non-equivalent roundness of the inner and outer rings of the concentric structures in Figure 66b, calculated to be 0.89±0.06 and 0.95±0.08, respectively (where 1 corresponds to the perfect circle). Here, we demonstrate some of the myriad of designs, and start from the same cylindrical nanotube array, but vary the thickness of the second ALD, to determine whether concentric or connected concentric nanotubes are formed (Figure 66b and c, respectively). Alternatively, by starting from a nanotube with a smaller inner radius and large spacing, the second ALD can result in nanotubes with an internal nanopillar (Figure 66e). Performing the second iteration on a structure such as the porous binary nanoarray in Figure 63f, enables extruding binary nanostructure to be achieved (Figure 66g).

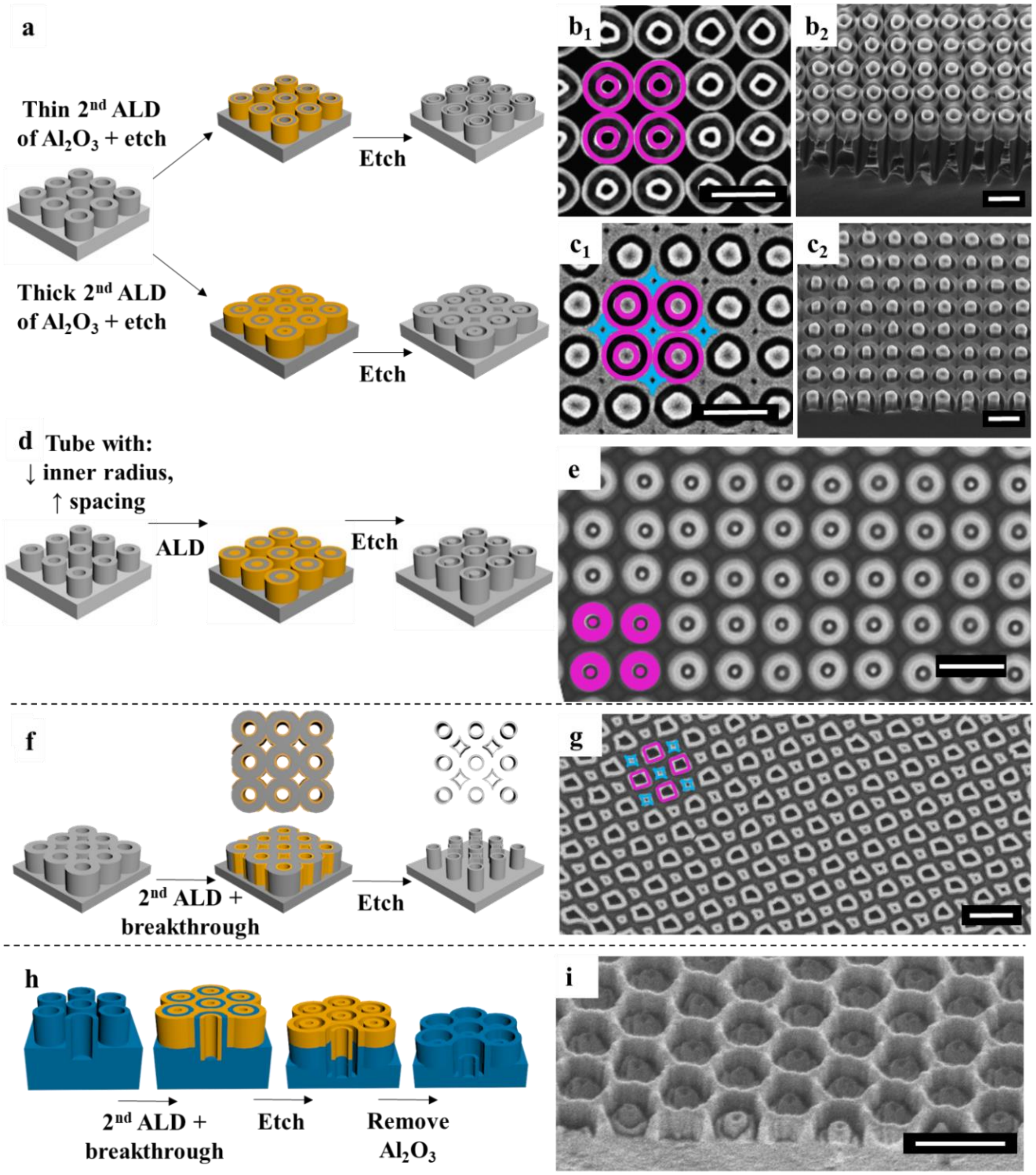
a
Thin 2nd ALD
of Al2O3 + etch
Etch
Thick 2nd ALD
of Al2O3 + etch
Etch
b1
b2
c1
c2
d Tube with:
↓ inner radius,
↑ spacing
ALD
Etch
e
f
2nd ALD +
breakthrough
Etch
g
h
2nd ALD +
breakthrough
Etch
Remove
Al2O3
i

Figure 66 | Exemplary complex structures by two SDIMP iterations. Schematics and corresponding SEM images show some of the possible structures when the second SDIMP process is conducted. Structural units are schematically depicted and bicolour refers to morphologically-binary structures. **a,** When starting from the same nanotube structure, but depositing a thinner or thicker spacer layer in the subsequent ALD and etch, concentric nanotubes (**b**) or connected concentric nanotubes (**c**) are generated. **d,** When starting from a nanotube with a reduced inner radius and greater spacing, a nanotube with an internal pillar can be created (**e**). **f,** When starting from connected nanotube arrays, the subsequent ALD and etch

Adapted from: S. K. Laney, T. Li, M. Michalska, *et al.*, Spacer Defined Intrinsic Multiple Patterning, **ACS Nano**, 2020, 14, 12091-12100

can generate extruding binary nanoarrays (**g**), note the schematic is simplified for the case where the inner tube is circular, as opposed to square which is seen in the corresponding SEM. **h,** When starting from nanotubes with a greater inner depth than outer height, multilevel concentric structures are generated (**i**) and in this case have been fabricated in glass to emphasise the process versatility. Scale bars = 500 nm.

Note also, through careful design, multilevel concentric structures can be fabricated by taking advantage of the inner/outer height difference of the starting nanotube: for $h_i > h_o$ see Figure 66h,i. Also noteworthy in Figure 66i is the spatial arrangement (hexagonally-packed) and the glass (rather than silicon) substrate. This emphasises the fact that numerous exotic nanostructures can be achieved in different materials by simple and scalable means, by virtue of the countless ALD/RIE combinations. Our proof-of-concept demonstration of double SDIMP offers a simple route to generate highly complex structures with advanced control over feature sizes (sub-10 nm gaps; Figure 67), which we anticipate to attract great interest for application in optical trapping whereby micro-/nanoscopic objects are physically held and moved with nanometric position using a highly focussed laser beam.[275,276] Moreover, for aperture based nano-optical tweezers, ultranarrow slits on the order of tens of nanometers are beneficial for boosting the efficiency, signifying the potential of this technique for optical trapping.[277–279] Another prospective application of the achievable structures through SDIMP, is Surface-Enhanced Raman Scattering (SERS). Through metallisation of our structures, surface plasmons can be channelled or concentrated to greatly enhance the signal when detecting single molecules. Alternatively, they can be used to generate smooth patterned metals *via* known template stripping technique, which utilizes the phenomenon of the poor adhesion and good wettability of noble metals on glass or silicon.[280]

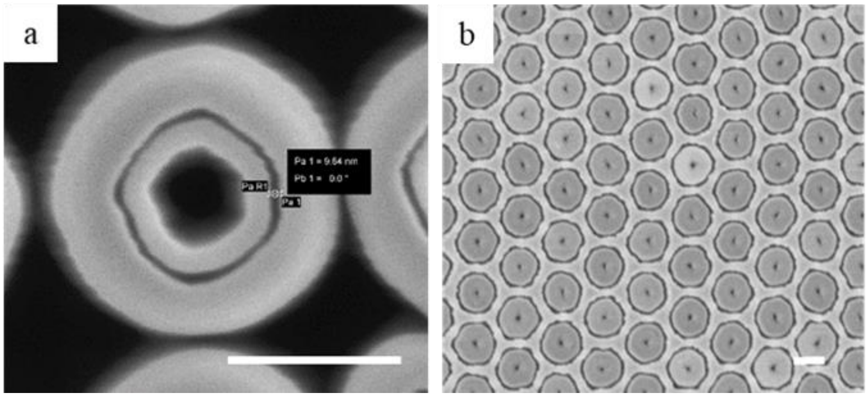

Figure 67 | Further nanostructures generated through two SDIMP iterations. a,b, Top view SEM images of nanostructures achieved with an incomplete final etch which led to very narrow gaps between the Al_2O_3 spacer layers; (a) Si concentric tubes with gap ~9 nm, (b) Glass embedded nano-doughnuts with gaps ~ 10nm. Such narrow gaps are highly desired for application in optical trapping. Scale bar = 200 nm.

5.1.4 Applications – broadband antireflection

Antireflective properties imparted by silicon nanostructuring have been largely explored as a method to improve the light trapping efficiency in optoelectronic devices.[251,281] Here, the enhanced material performance is typically attributed to the subwavelength features and the co-action of various mechanisms which include coupling with localized or waveguided photonic modes[18] in addition to the induced refractive index gradient between air and the substrate.[282] Whilst arrays comprising Si nanowires,[283] nanocones,[281] nanotips,[284] or nanotubes[251] have shown a reduced reflection, typically one mechanism dominates; and furthermore, antireflection is only observed in partial regions of the solar spectrum ($\lambda \sim 250$-2500 nm). Because these structures hold a single geometrical feature, to achieve broadband antireflectance, a large AR (>30:1) is required;[285,286] but at the cost of structure durability. An alternative path to render such properties relies on expanding feature hierarchy,[262,287] so that each feature now can interact with a specific part of the spectrum.

Therefore, both independent dimension control and the possibility to iterate our SDIMP method make it particularly suitable for the development of complex nanostructures with broadband antireflective properties. Here, as an example we show a nanotube array with subwavelength dimensions, additionally possessing crowned features at the top. Upon measurement of the fabricated surface (visually assessed as exceptionally black) using an integrating sphere (see

Methods), we indeed find a very low reflectance of an average 1.0% between 350-550 nm and 0.7% for 550-1,050 nm, which translates to 0.9% overall (Figure 68c, magenta dashed line).

To elucidate the contribution of structural components to the high value of the measured antireflectance, we simulate four similar geometries with varying complexity (Figure 68c): straight-walled tube (black curve), tapered tube (red), tapered pillar with a top crown (orange), and tapered tube with a top crown (yellow). It is clear that with increasingly complex geometric features, the reflectance is further supressed. For instance, the straight-walled tube array shows an average reflectance of 12.1% which is comparatively lower than that from a flat substrate, but still large compared to previously achieved nanostructured Si surfaces. By reshaping the tube through adding tapered sidewalls, the reflectance is significantly reduced across 500-900 nm wavelength range, and the average reflectance decreases to 5.1%. Removing the central hole and adding a top crown to the previous structure (orange curve) shows further improvements of the antireflective properties; lower reflectance overall and on average 2.2% as compared to the previous cases. Finally, by adding a central hole to the previous structure to obtain a tapered tube with a top crown (yellow curve), light couples to the waveguiding modes into the tubular structure, achieving an extra reduction in reflectance (1.5% average). Further suppression of reflectance to the levels observed in the experiments (0.9%) could be attributed to the small roughness at the walls of the tubes (Figure 68b). We note that these findings corroborate well with the very recent study on the natural surfaces of the wings of papilionid butterflies[262] where a 16-fold suppression of reflectance was similarly attributed to the existence of steep ridges surrounding a nanohole (crowned tapered nanostructures). Although the exact role of the size and shape of the hole in such structures is still under debate (with ambiguity regarding absorption management at non-normal incidence angle), it is clear that generally two shapes come into play – spherical and square, both of which can be attained by SDIMP.

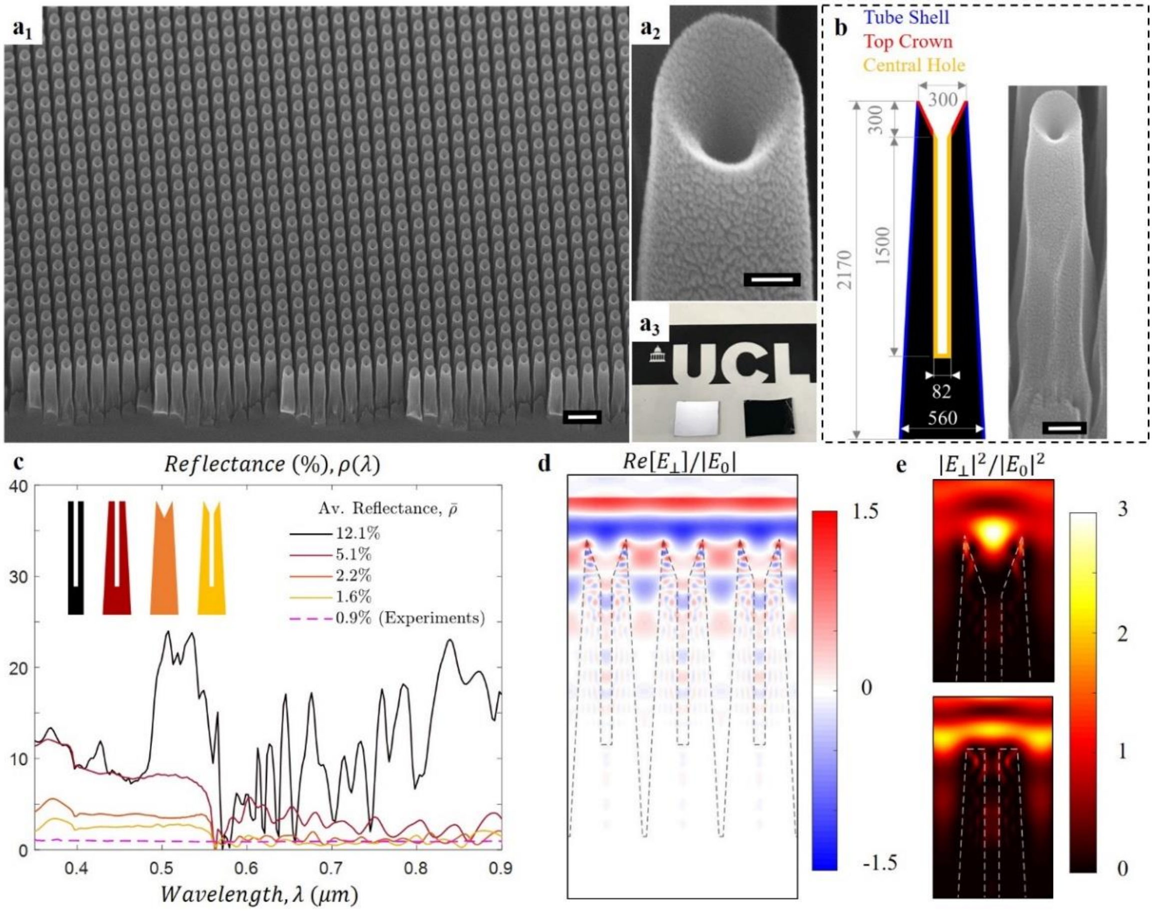

Figure 68 | Antireflective study of silicon nanotube arrays. **a$_1$,a$_2$,** Side view SEM images of the fabricated silicon nanotube arrays highlighting the scale of fabrication (a$_1$) and crown structure (a$_2$). (a$_3$) Photograph of a plain piece of Si (left) next to the sample comprising the crowned-nanotube array (right, ~6 cm^2), to visually highlight the ultra-black properties. **b,** Schematic with accompanying SEM image of the nanotube considered in the simulation, together with its overall dimensions (nm). The three main geometrical components of the nanotube (*i.e.*, Tube Shell, Top Crown and Central Hole) are highlighted in the figure for reference. **c,** Reflectance at normal incidence as obtained from measurements (magenta dashed line), and simulations for four different geometries: straight-walled tube (black curve), tapered tube (red curve), tapered pillar with a top crown (orange curve), and tapered tube with a top crown (yellow curve). **d,e,** Distribution of the electric field perpendicular to the plane of incidence ($E_{\perp}$) for a planewave at 400 nm wavelength and normal incidence. **d,** Real part of the normalised electric field ($Re[E_{\perp}]/|E_0|$) for crowned tapered tube arrays. **e,** Normalised electric field energy density ($|E_{\perp}|^2/|E_o|^2$) at the tip of a crowned tapered tube (upper) and regular tapered tube (lower). Scale bars: a$_1$ = 1 um, a$_2$ = 100 nm, b = 200 nm.

Adapted from: S. K. Laney, T. Li, M. Michalska, *et al.*, Spacer Defined Intrinsic Multiple Patterning, **ACS Nano**, 2020, 14, 12091-12100

Building on from our simulations, the electric field distribution of tapered tubes and tapered crown tubes (Figure 68d,e) indicate further that the top crown is a critical element to supress the reflectance of light at small wavelengths (300-560 nm) as it allows for the efficient coupling of light into the structure. Numerical simulations at oblique angles of incidence for s and p polarisations (Figure 69) reveal that reflectance remains below 5% for angles as large as 50°, and most of the light at wavelengths 350-500 nm is being absorbed by the tubes before reaching the substrate. This shows that localized modes at the crown top and waveguided modes in the central hole are the major mechanisms contributing in this range. For longer wavelengths on the other hand, most absorption occurs within the substrate, which indicates that the structures act to gradually match the impedance between air and Si in this spectral range. Through this example, concomitantly with the merits of other attainable complex structures by iterative SDIMP, we believe that our technology holds a great potential for future designs of perfect absorbers. Additionally, to the best of our knowledge, this represents the only reported synthetic analogue of ultra-black crowned tapered nanostructures similar to those found on the papilionid butterfly, further reinforcing potential of SDIMP.

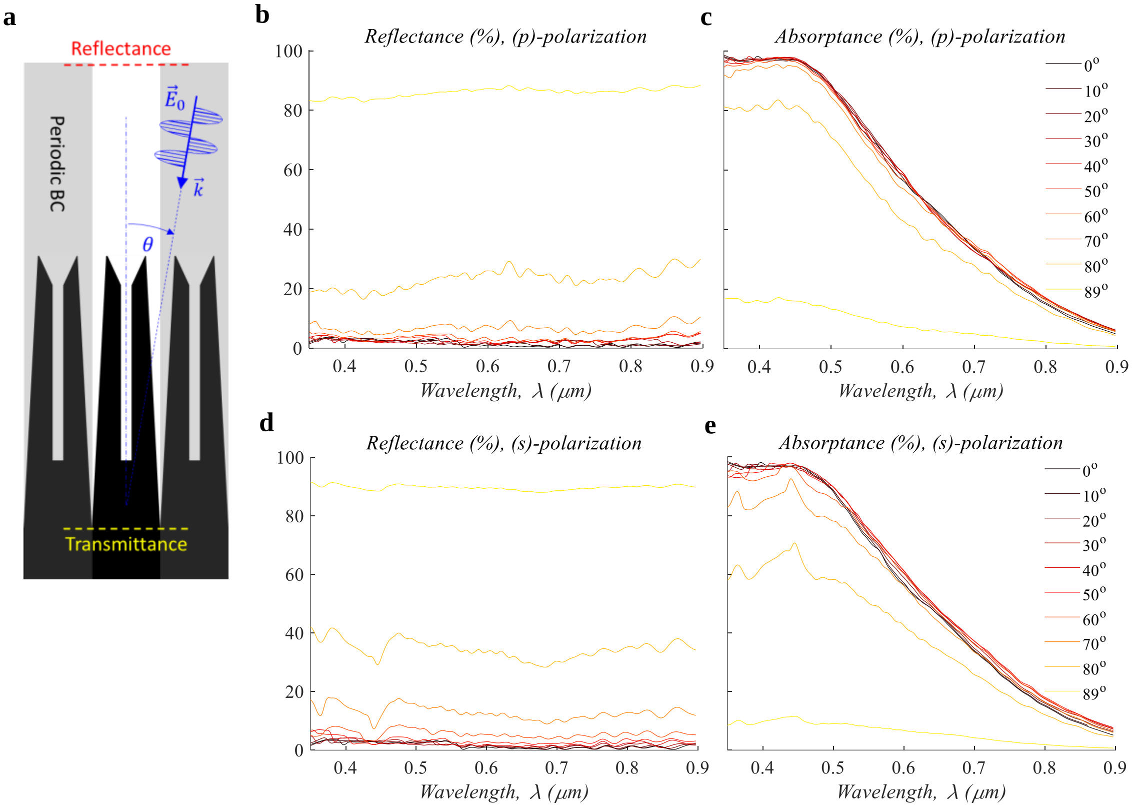

Figure 69 | Optical properties of the tapered nanotube with a top crown at oblique angle of incidence. a, Schematic of the simulation set up. The angle of incidence is defined by $\boldsymbol{\theta}$. Unless stated otherwise, light is polarized parallel to the plane of incidence (p-polarization). Periodic boundary conditions based on a square lattice were considered (gray shade). In order to quantify the absorption of Electromagnetic (EM) waves by the nanotubes, the power flux was monitored above and below the nanotubes, to meassure reflection and transmission of EM-waves, respectively. **b,** Reflectance and **c,** Absorptance of p-polarized of EM waves as a function of the angle of incidence. **d,** Reflectance and **e,** Absorptance of s-polarized of EM waves as a function of the angle of incidence.

5.1.5 Conclusion

In this work, we present spacer defined intrinsic multiple patterning as an enabling platform technology for the fabrication of nanotube arrays with independent control of the overall geometries. The versatility of SDIMP stems from the vast availability of photolithographic and self-assembly methods for initial patterning, and numerous target material-spacer pairs of high etching contrast at various RIE processes. This allows for nearly no limit on feature dimensions and spatial arrangement (periodic or not), as well as on material choice, enabling tunable and high-

Adapted from: S. K. Laney, T. Li, M. Michalska, *et al.*, Spacer Defined Intrinsic Multiple Patterning, **ACS Nano**, 2020, 14, 12091-12100

quality structures, evidenced by the photonic properties of the ‘crowned’ nanotube array. Further, as a proof-of-concept, we advance the structural complexity through an additional iteration, and envision many far-reaching applications spanning metamaterials, wettability, biotechnology, and sensing amongst others.

5.1.6 Methods

Nanotube fabrication through one SDIMP iteration. The fabrication process flow is provided in Figure 59. First, silicon wafer (MicroChemicals) was cleaned with acetone *via* sonication and subsequently washed with isopropanol. SiO_2 layer (70 nm or 100 nm) was deposited on Si *via* plasma enhanced chemical vapor deposition (PECVD; STPS Multiplex) under low frequency RF with SiH_4 and O_2 vapor at 300°C.

(Step 1) An initial photoresist pattern (holes or pillars) was generated by laser interference lithography (LIL) using a Lloyd's mirror interferometer set. A primer layer (TI Prime, Microchemicals) was first applied *via* spin-coating (6,000 rpm for 30s and baked at 120°C for 90 s) in order to improve resist adhesion. Photoresist (ma-N 405, Microresist technology) was diluted 1:1 with MIBK (4-methyl-2-pentanone) and spin coated onto the wafer at 3,000 rpm for 30s. Soft baking was carried out in an oven at 100°C (3 min). Square- or hexagonally-packed pillars or holes were generated by means of one or two mirrors using the free-space UV-laser with beam diameter of ~1 mm (IK3201R-F by Kimmon; Class 3B; 25 mW; 325 nm; CW; single mode TEM00). After exposure (pillars; 60 s, holes; 90 s), the photoresist was developed using AZ 726 MIF (Microchemicals) for 30 s. After the pattern was established, a brief oxygen breakthrough was applied to expose underlying material (SiO_2 – hard mask) to be etched (Table 3-Table 4 for conditions/times).

To generate initial PR pattern, virtually any technique can be employed. In this study, alternatively, UV nanoimprint lithography (NIL) was utilised (for details see Methods – NIL).

(Step 2) To register the PR pattern into the hard mask, reactive ion etching (RIE) was conducted using CHF_3/Ar plasma at temperature of 20°C (PlasmaPro NGP80 RIE, Oxford instruments). After etching, residual PR was removed by O_2 RIE.

(Step 3) Using the hard mask, the pattern was transferred into the underlying Si layer by means of Advanced Silicon Etcher (ASE, STS MESC Multiplex ICP) using Cl plasma. Typically, etching was performed until mask consumption. Note, excessive SiO_2 mask on Si can be removed by hydrofluoric acid (HF). Detailed etching conditions for both RIE processes (Steps 2-3) to generate each nanostructure are listed in Table 3-Table 5.

(Step 4) Prior to atomic layer deposition (ALD) of Al_2O_3 spacer, the surfaces were subjected to an RCA cleaning process to remove organic and ionic contaminants. Subsequently, the deposition of Al_2O_3 was conducted in Savannah G2 S200 (Ultratech), using alternating exposures of trimethylaluminum (97%, Aldrich) and deionised water at 200°C with N_2 gas purge steps in between. The exposure and purge time for both precursors used in this study were 0.015 s and 3 s, respectively. Ten cycles of the process equal 1 nm (see Table 3 for deposition thickness).

(Step 5) The breakthrough etch was conducted using Cl plasma (Table 3, Table 5) to remove the horizontal deposition (equivalent to the deposition thickness; 10 nm/min) whilst revealing vertically aligned spacer mask.

(Step 6) The subsequent etch was continued using Cl plasma (Table 3, Table 5) either until spacer mask depletion or until the desired height was reached. The remaining Al_2O_3 mask was removed by HF.

Complex nanostructures fabrication through two SDIMP iterations. The fabricated single nanotubes were cleaned according to the RCA cleaning process, and placed in the ALD chamber. The second ALD and etch were performed as described before.

For concentric nanotubes (Figure 66b), PR pillars (P = 350 nm) were generated atop of Si with deposited 70 nm of SiO_2 layer. The primer layer and negative-tone PR were applied as described above (Step 1). The Lloyd's set up comprised of one mirror, and the sample was rotated 90° after each exposure (30 s). Development was performed in undiluted AZ-MIF-726 for 90 s. To register the PR nanopillars into the SiO_2 hard mask, RIE was performed (Oxford instruments) with CHF_3/Ar plasma for 90 s. To transfer the pattern from hard mask to Si, RIE (STS) was performed using Cl plasma for 3 min (for both RIE conditions – see Table 4). The sample was cleaned and placed in the ALD chamber, where 40 nm of Al_2O_3 was deposited. Subsequently, the sample was subjected to RIE with Cl plasma for 7 min, at which point it was cleaned and placed back into ALD chamber for a further 25 nm of Al_2O_3 deposition. The final etch was performed for 11.5 min under Cl plasma.

For fabrication of the other demonstrated complex nanostructures through two iterations, please refer to Table 6; the process only differs in etching time and deposition thickness.

Characterisation. Scanning electron microscopy (SEM) was performed using a Field Emission Zeiss Ultra Plus scanning electron microscope with a Gemini column operating at an accelerating voltage of 2-20 kV. Glass samples were coated with a thin layer of gold *via* sputter deposition to minimize charging. ImageJ (https://imagej.nih.gov/ij/) was used for statistical analysis of the nanostructure dimensions such as pitch, height, diameters. Additionally, roundness of some structures was characterized ($roundness = \frac{4 \cdot A}{\pi \cdot a^2}$, where A is the surface area and a is major axis; ImageJ) to describe feature shape and compare uniformity.

Soft lithography. The mold substrate was functionalised with a PDMS brush layer as described above, in order to ease separation. Preparation of the poly(urethane acrylate) (PUA) solution was carried out according to a previously reported method.[288] Briefly, the PUA solution was prepared by thorough mixing of 30 wt% of trimethylolpropane ethoxylate triacrylate (409073, Sigma) with respect to the diacrylate prepolymer (Ebecryl 284, Allnex). Subsequently, photo initiators Irgacure 184 (1-Hydroxy-cyclohexyl-phenyl-ketone, 30472119, BASF) and Darocur (2-Hydroxy-2-methylpropiophenone, 405655, Sigma) were added at 1.5 wt% with respect to the combined weight. Finally, a releasing agent (TEGO® Rad 2200N) was added at 1 wt%. The prepared solution was mixed and degassed, and stored in a refrigerator protected from light. The sample was drop casted with the solution and cured for 20 s under a high intensity UV laser (365 nm, CS2010 UV Curing System, ThorLabs), followed by 10-hour curing under low intensity UV light.

NIL. Having generated a pattern with the desired pitch and orientation *via* LIL, and transferred this into Si, NIL was employed to facilitate quick and reproducible pattern replication into PR for further substrates. To generate a positive-tone replica of the pattern, a two-step nanoimprint was conducted. The NIL process was performed on EITRE® 3 (Obducat). Prior to imprinting, the master mold was functionalised with polydimethylsiloxane (PDMS) brush layer according to a previously reported method,[289] to facilitate a demolding process. Briefly, oxygen plasma was applied to activate the surface which was subsequently grafted with short chain PDMS using 1:10:0.27 v/v/v ratio of dimethyldimethoxysilane : isopropanol : H_2SO_4 (>95%) mixture. The substrate was placed on a hot plate (75°C) and the solution was drop casted atop for 15 s, followed by washing with deionised water, isopropanol and toluene. The intermediate polymer (IPS, Obducat) stamping process was operated at 145°C and 20 bar for 20 s. Transfer of the negative pattern into the photoresist (STU-7, Obducat) was operated at 70°C and 40 bar for 240 s with 120 s of UV curing.

Ultraviolet – visible light spectroscopy measurements. Reflection measurements were taken at 8° off normal incidence. The sample was attached to a port of an integrating sphere (Labsphere) and illuminated using a white light source (KI-120 Koehler Illuminator, Labsphere). Light levels were measured using a fibre coupled spectrometer (QEPro, Ocean Optics) and calibrated against a diffuse reflectance standard (SRS-02-10, Spectralon, Labsphere).

Optical Simulation. Numerical simulations at normal incidence and electric field distribution (Figure 4) were obtained from Finite Difference Time Domain (FDTD) method, using FDTD 3D Electromagnetic Simulator, Lumerical Inc. (https://www.lumerical.com/products/fdtd/). Optical properties at oblique angle of incidence (Figure 69), were obtained from Rigorous Coupled Wave Analysis (RCWA) method using the software package S4.[290] In all the simulations, periodic boundary conditions on a square lattice were considered, and the power flux was monitored above and below the nanotubes structure to quantify reflection and transmission, respectively. The refractive index of silicon was obtained from a previous report.[291]

Table 2 | Nanotube dimensions

Sample	**Pitch (*P*) nm**	**Spacing (*S*) nm**	**Outer height, (h_o) nm**	**Inner height (h_i) nm**	**Thickness (*t*) nm**	**Inner tube radius (r_i) nm**
Figure 59d	350	159 ± 9	800 ± 30	N/A	25	54 ± 6
Figure 63b	560	86 ± 12	893 ± 20	1623 ± 9	30	186 ± 16
Figure 63d	560	150 ± 15	1510 ± 20	1750 ± 14	90	89 ± 5
Figure 63e	350	0	370 ± 8	N/A	120	55 ± 7
Figure 63f	350	0	455 ± 11	N/A	120	109 ± 8
Figure 63h	560	162 ± 14	1721 ± 16	1743 ± 11	30	143 ± 11

Figure 63j	560	168 ± 18	1224 ± 14	2302 ± 17	30	147 ± 6

Table 3 | Nanotube fabrication: (i) etching times and (ii) thicknesses of SiO_2 or Al_2O_3 deposition

Sample	**SiO_2 thickness / nm**	**O_2 etch / s**	**CHF_3/Ar etch / min**	**Cl_2 etch / min**	***t* ALD / nm**	**Cl_2 etch / min**
Figure 59d	70	8	3.5	4	25	8
Figure 63b	200	10	9	5	30	9
Figure 63d	200	10	9	15	90	14
Figure 63e	70	30	1.5	3	150	17
Figure 63f	70	30	1.5	3	120	16
Figure 63h	200	10	9	15	30	5
Figure 63j	200	10	9	5	30	16

Table 4 | Nanotube etching conditions – Oxford RIE

<table>
<tr><th colspan="5">Oxford RIE conditions – capacitively coupled plasma</th></tr>
<tr><td rowspan="2">Oxygen breakthrough</td><td>Pressure / mTorr</td><td colspan="2">RF Power / W</td><td>O_2 / sccm</td></tr>
<tr><td>50</td><td colspan="2">100</td><td>50</td></tr>
<tr><td rowspan="2">SiO_2 etch</td><td>Pressure /mTorr</td><td>RF Power / W</td><td>CHF_3 / sccm</td><td>Ar /sccm</td></tr>
<tr><td>50</td><td>200</td><td>12</td><td>38</td></tr>
</table>

Table 5 | Nanotube etching conditions – ICP STS

Sample	**1st Si etch**				**Breakthrough etch**				**Further etch**			
	Coil /W	Platen /W	P /mTorr	t /min	Coil /W	Platen /W	P /mTorr	t /min	Coil /W	Platen /W	P /mTorr	t /min

Figure 59d	300	40	6	4					300	40	6	8
Figure 59e	500	200	6	5	300	40	3	9	500	200	6	5
Figure 63b	500	200	6	5	300	40	3	3	300	100	6	6
Figure 63d	500	200	6	5	300	40	3	9	500	200	6	5
Figure 63e	300	40	6	3					300	40	6	17
Figure 63f	300	40	6	3					300	40	6	16
Figure 63h	500	60	6	15	300	40	3	3	500	200	6	5
Figure 63j	300	100	6	5					300	100	6	16

Table 6 | Iterative SDDP structure fabrication

Sample	**SiO_2 thickness /nm**	**O_2 / s**	**CHF_3/Ar etch / min**	**Cl_2 etch / min**	**ALD / nm**	**Cl_2 etch / min**	**ALD / nm**	**Cl_2 etch / min**
Figure 66b	70	38	1.5	3	40	7	25	11.5
Figure 66c	70	40	1.5	2	60	9	80	14
Figure 66e	70	45	1.7	1	45	7.5	30	6
Figure 66g	70	30	1.5	3	120	16	30	5
	O_2 / s	**CHF_3/Ar etch / min**	**ALD / nm**	**Cl_2 etch / min**	**CHF_3/Ar etch / min**	**ALD / nm**	**Cl_2 etch / min**	**CHF_3/Ar etch / min**
Figure 66i	12	10	40	3	10	30	3	10

5.2 Slippery Liquid Infused Porous Surfaces

5.2.1 Abstract

Slippery Liquid Infused Porous Surfaces (SLIPS) are an important class of repellent materials, comprising micro/nano-textures infused with a lubricating liquid. Unlike superhydrophobic surfaces, SLIPS do not rely on a stable air-liquid interface and thus can better manage low surface tension fluids, are less susceptible to damage under physical stress, and are able to self-heal. However, these collective properties are only efficient as long as the lubricant remains infused, which has proved challenging. We hypothesized that, in comparison to a nanohole and nanopillar morphology, the 'hybrid' morphology of a hole within a nanopillar, namely a nanotube, would be able to retain and redistribute lubricant more effectively; owing to capillary forces trapping a reservoir of lubricant within the tube, whilst lubricant between tubes can facilitate redistribution to depleted areas. By virtue of recent fabrication advances in Spacer Defined Intrinsic Multiple Patterning (SDIMP), we fabricated an array of silicon nanotubes, and equivalent arrays of nanoholes, and nanopillars (pitch; 560 nm, height; 2 μm). After infusing the nanostructures (pre-rendered hydrophobic) with lubricant Krytox 1525, we probed the lubricant stability under dynamic conditions and correlated the degree of the lubricant film discontinuity to changes in the contact angle hysteresis. As a proof-of-concept, the durability test, which involved consecutive deposition of droplets onto the surface amounting to 0.5 liters, revealed a 2-fold and 1.5-fold enhancement of lubricant retention in nanotubes, in comparison to nanopillars and nanoholes respectively; showing a clear trajectory for prolonging the lifetime of a slippery surface.

5.2.2 Introduction

Liquid repellent surfaces have been an active area of research for some decades, with a predominant focus on superhydrophobic lotus inspired-structures.[15,292–294] An upsurge of interest in pitcher plant-inspired surfaces, known as Slippery Liquid Infused Porous Surfaces (SLIPS), has been observed ever since their introduction in 2011.[58] This family of non-wettable surfaces which

Adapted from: S. K. Laney, T. Li, M. Michalska, *et al*., Delayed Lubricant Depletion of Slippery Liquid Infused Porous Surfaces Using Precision Nanostructures, **Langmuir**, 2021, 37, 33, 10071-10078

comprise a thin lubricating layer trapped within surface roughness, resides at the forefront of the literature, having consistently been shown to succeed where their gas-cushioned counterparts fail; in repelling organic liquids or complex mixtures with low surface tension, sustaining no damage under physical stress, and an ability to self-heal.[59,60] Prized for their anti-adhesive nature, SLIPS bestow interfacial properties that are highly desired across a broad range of applications including anti-icing,[61,62] drag-reducing properties,[63] heat transfer,[64] anti-fouling coatings in the marine[65] and medical sectors,[66,67] non-stick packaging,[68] and droplet manipulation.[69]

To achieve liquid repellence, SLIPS essentially exploit the immiscibility of lubricants with other liquids. A low surface energy lubricant is infused into the surface structure, and the lubricant forms the interface with the immiscible working liquids (e.g., water, ethanol), as opposed to the solid surface, thus resulting in very low contact angle hysteresis (minimal adhesion). In order to attain these properties, three criteria need to be met: (i) the solid substrate must have a higher affinity for the lubricant over the droplet, (ii) the lubricant and the working fluid must be immiscible, (iii) the lubricant must wick into, spread and stably adhere within the structure.[58,70] The prime source of failure for SLIPS lies in this third criterion and the poor ability of the structure to retain the lubricant leading to drainage of the lubricant layer causing contact line pining of the working fluid on the exposed solid structures.[71,72] Exploiting the physical interaction between the lubricant and the structure is, therefore, crucial for its retention.

In this regard, recent fabrication capabilities, propelled in part by the design and manufacture of superhydrophobic surfaces, have given rise to an expansive array of possible nano- and micro-architectures.[14,15] Nonetheless, efforts to design a structure capable of enhanced lubricant retention are still on-going, with the effect of geometric surface parameters on lubricant retention under flow highlighted as an area requiring further work.[295] Maximizing the capillary forces, which hold the lubricant within the structure against the action of gravity and shear force, is clearly an important consideration. Such capillary forces are only generated when the sizes of the features are smaller than the capillary length of the lubricating liquid.[296] Whilst micro-roughness typically satisfies this criterion, under high shear conditions the effective capillary length of the lubricant reduces to micron length scales (~ µm), thereby permitting lubricant depletion, and exposing the underlying microstructures.[297] Conversely for nanostructures, the lubricant layer remains stable until the thickness reduces to a size comparable to the feature height.[298] Additionally, the capillary pressure which retains the lubricant is much greater for nanostructures, owing to the inverse relationship with the spacing between structural domains (nanointerstices).[299] Of course, all nanostructured surfaces do not perform equally, and further probing of nanostructure features has elucidated the benefits of a closed-cell system (*i.e.* nanoholes/pores),[298] as opposed to an open-cell system (interconnected networks *i.e.* nanopillars).[300] Here, the isolated domains of lubricant act as a physical barrier to depletion,[72] however paradoxically, this retention can prevent replenishment and self-healing. As the lubricant layer thins, a surface with a lower solid fraction (minimized flat areas where capillary forces cannot act) can benefit SLIPS performance, owing to fewer sites for water contact line pinning.[301] Intermolecular forces can also be maximized through increasing the surface area (roughness) of the nanostructures.[297] Based on these considerations, it is necessary to generate a nanostructure which has a low solid fraction, a high roughness, and the ability to simultaneously retain and replenish lubricant. One well-studied example which satisfies these criteria is an inverse colloidal monolayer, where structural dimensions and corresponding roughness are determined by the nanoparticle size.[298] Another such structure is a hybrid between a nanopillar (NP) and a nanohole (NH); namely, a nanotube (NT), where enhanced tunability stems from decoupling the individual nano-feature dimensions (height, spacing, wall thickness). Recent advances in atomic layer deposition-assisted processes, such as Spacer Defined Intrinsic Multiple Patterning (SDIMP),[167] have enabled the controlled fabrication of such nanotube structures; creating an opportunity for further studies.

For the first time, we fabricate and functionalize a silicon nanotube sample and compare its ability to retain lubricant (Krytox 1525 – fluorinated oil immiscible with most working fluids)[302] with nanohole and nanopillar samples of equivalent dimensions, under dynamic conditions with water as the working fluid. To test the stability of the lubricant within each structure, we perform two different tests and correlate the degree of the lubricant film discontinuity to changes in the contact angle hysteresis (CAH). Firstly, we performed a shear tolerance test which revealed all nanostructures were able to retain the lubricant through capillary action up to the tested 10k rpm; yielding no significant changes in CAH. Secondly, we designed and performed a harsher droplet shedding test, with consecutive deposition of small droplets at moderate rates (~16 µl, 2 drops/s;

known to challenge the lubricant retention, as opposed to larger volumes or continuous flow and higher rates)[302] onto the tilted surface amounting to 0.5 liters. We observe a 2-fold and 1.5-fold enhancement of lubricant retention in nanotubes, in comparison to nanopillars and nanoholes, respectively.

5.2.3 Results And Discussion

To systematically probe the lubricant retention capabilities of the three nanostructures, we employ a nanotube array originating from a previous investigation, focused on its excellent antireflective properties.[167] We fabricated corresponding arrays of nanoholes and nanopillars with equivalent pitch (560 nm), heights (~2 µm), and top diameters (~300 nm), as listed in Table 7. The nanotube dimensions, with comparable intra- and inter-tube spacing, allow for both lubricant retention and redistribution, whilst the high surface roughness provided by an AR~7 increases the inherent resistance to shear. Laser interference lithography, plasma etching and for the nanotubes, subsequent ALD-assisted processing (SDIMP)[167] were employed to generate the nanostructure arrays as seen in Figure 1a-c. Here, SDIMP allows for freedom in the nanotube design, whereby the inter- and intra-tube spacing can be realized with ALD precision.

As discussed, the water repellence of a SLIPS is attributed to the water-immiscible lubricant film held within and above the surface of a porous structure, yet, characteristics of the underlying porous structure play an important role in the droplet mobility, redistribution characteristics, and capillary retention.[299] As the lubricant film begins to deplete, the mobility of a droplet (sliding speed) is known to be reduced on a surface with a larger solid fraction $\emptyset_S$; the fraction of the solid that is exposed to the working fluid (water in this example). Characterization of the three nanostructures revealed a $\emptyset_S$ of 0.1 for nanotubes, 0.7 for nanoholes and 0.2 for nanopillars, providing initial indications that droplet mobility may be most hindered on the nanoholes. In terms of lubricant redistribution, broadly speaking, structures able to hold a greater volume of lubricant per unit area (nanotubes > nanopillars > nanoholes; Table 7) benefit from the increased capacity to redistribute and replenish depleted areas (provided the lubricant is not isolated, as is the case for the nanoholes). It is also known that surfaces possessing a greater degree of roughness *R* (calculated total surface area of the structure over the projected area), are able to entrap oil more effectively through a combination of capillary and van der Waals forces.[297] Indeed, there is a critical roughness value (R_{crit}) which needs to be exceeded in order for a lubricant film to be thermodynamically stable, predicted by:[298]

$$R > \frac{\gamma_{LW}}{\gamma_L cos\theta_L - \gamma_W cos\theta_W} \qquad [Eq.\ 36]$$

For the case of a water droplet as the working fluid and Krytox 1525 as the lubricant, $R_{crit} > 1.2$. All surfaces exceed this threshold (Table 7) indicating that without external perturbances, the lubricant would be stably adhered within all nano-structured surfaces.

To further quantify the effect of structure theoretically, we determined the difference in energy between two possible configurations, as previously described:[58] (1) the structure is fully wet by water (E_W) and (2) the structure is fully wet by lubricant in the presence (E_{LW}) or absence (E_L) of water. To ensure the structure is preferentially wet by the lubricant as opposed to water, $\Delta E_{LW} = E_W - E_{LW} > 0$, and $\Delta E_L = E_W - E_L > 0$. Values are shown in Table 7 and indicate that all structures far exceed the criteria but moreover the tubes are shown theoretically to be most stable.

Table 7 | Dimensions of the nanostructures of the same pitch (560 nm) and calculated values for the roughness R, solid fraction $\emptyset_S$, capacity for lubricant per cm^2 V, the difference in energy when the structure is fully wet by the lubricant in the presence $\Delta \boldsymbol{E_{LW}}$ or absence of water $\Delta \boldsymbol{E_L}$.

Morphology	**Height / nm**	**Diameter / nm**	R	$\emptyset_S$	V **/ ml**	ΔE_{LW}	ΔE_L
Nanotubes	1994 ± 28	Inner: 238 ± 9 Outer: 311 ± 10	11.9	0.10	1.8×10^{-4}	*515*	*618*
Nanoholes	1771 ± 36	348 ± 13	7.2	0.70	5.4×10^{-5}	*291*	*394*
Nanopillars	1857 ± 30	292 ± 12	6.4	0.21	1.5×10^{-4}	*254*	*357*

For the SLIPS preparation, all samples were treated similarly, and were first rendered hydrophobic through functionalization with a silane (PFDTES), as depicted schematically in Figure 70d and detailed in the experimental section. The apparent advancing (θ_{adv}^{a}) and receding (θ_{rec}^{a}) water contact angles and the CAH served as indicators of the successful modification from hydrophilic

(θ^{a}_{adv}<10°) to hydrophobic upon silane-functionalization, resulting in $\theta^{a}_{adv,Tube}$=155°±1, $\theta^{a}_{adv,Hole}$=145°±2, and $\theta^{a}_{adv,Pillar}$=148°±2 with CAH of 30°±2, 145°±2 and 18°±2, respectively (Figure 71a,b). After immersion of the surfaces in the lubricant, with infiltration into the structure encouraged by the hydrophobic coating as well as vacuum degassing, excess lubricant was removed through means of wicking onto an absorbent cloth over a period of 24 h. Measurement of the advancing contact angle revealed equivalent wetting behavior across the sample set with $\theta^{a}_{adv,Tube,Hole,Pillar} \approx$ 120° and CAH < 3° (Figure 71a,b). The lubricant is observed to form a wetting ridge (lubricant meniscus surrounding the droplet; Figure 72b) and based on the interfacial tensions of the lubricant-water pair, cloaking of the droplet by the lubricant is expected as the spreading coefficient, calculated according to:

$$S_{LW} = \gamma_W - (\gamma_L + \gamma_{WL}) \qquad \textit{[Eq. 37]}$$

Is calculated to be 2.704 based on the values in Table 11, indicating it is energetically favourable to spread on water, thus giving rise to cloaking. The ramifications of cloaking are discussed elsewhere,[303] however as the aim is to compare the effect of nanostructure on performance rather than lubricant, it is not considered pertinent.

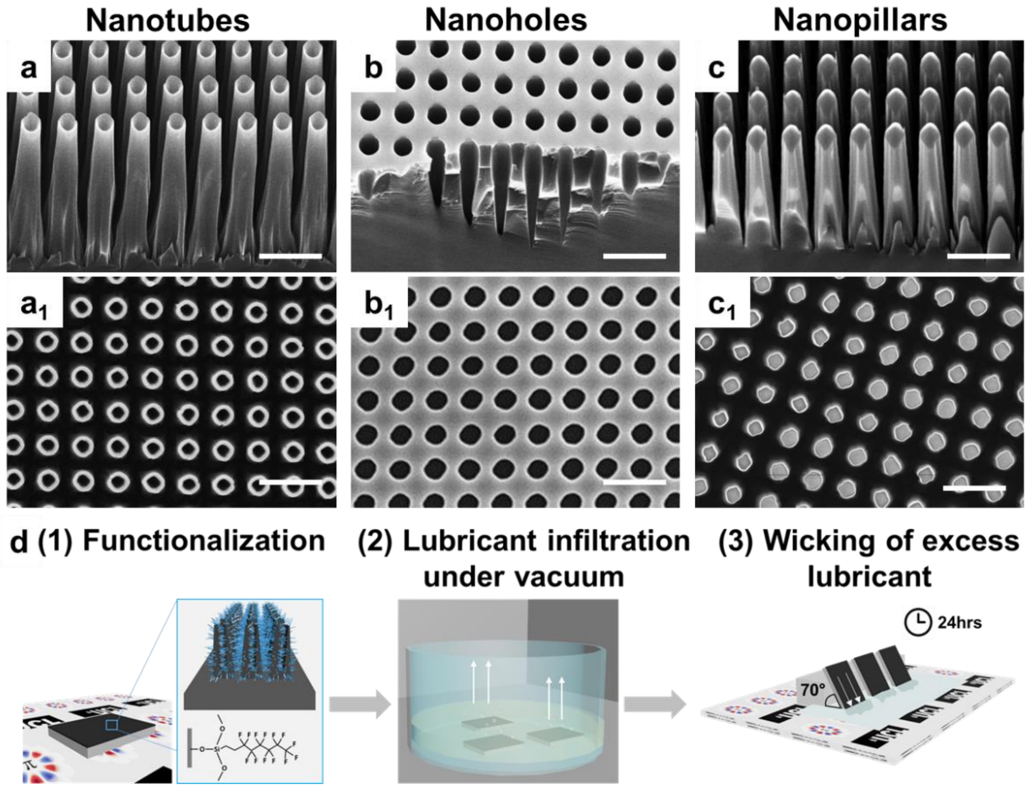

Figure 70 | a-c, Side view and, (a_1-c_1) top view SEM images of the nanotube, nanohole, and nanopillar structures, respectively. Scale bars = 1 µm. **d,** Schematic of the SLIPS samples preparation flow: (1) functionalization with PFDTES; (2) infusion of the lubricant into the nanostructures by submersion and subsequent degassing under vacuum; (3) wicking of excess lubricant by tilting the samples at an angle of 70° atop of an absorbent cloth for a duration of at least 24 h.

One of the tests frequently performed to assess the durability of a slippery surface, namely a shear tolerance test, involves subjecting the surfaces to increasing centrifugal forces (spin speeds) and comparing the resultant water CAH (Figure 71c). After being subjected to a speed of 1k rpm for 1 min, the CAH remained below 5° indicating a continuous lubricant film was still present. Increasing the speed further up to 10k rpm also revealed no significant increase in the CAH for each of the surfaces; consistent with previous studies on nanostructured surfaces.[298] Under these conditions capillary forces are responsible for trapping the lubricant film, and remain effective so long as the capillary length k^{-1} of the lubricant remains greater than the length scale of the nanostructures ($k^{-1} = \sqrt{\frac{\gamma}{\rho g}}$ where γ is the surface tension, and ρ is the density of the fluid, and g the gravitational acceleration). In the absence of spinning, the capillary length of Krytox 1525 is ~1 mm. However, as the spin rate increases, the capillary length decreases and ultimately reaches a value of ~tens µm at 10k rpm; thus, the lubricant remains trapped within a nanostructured surface, as previously reported.[297]

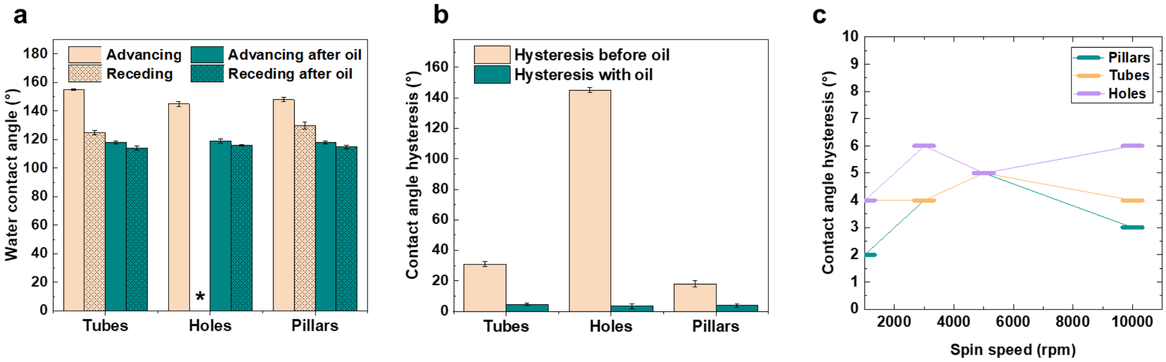

Figure 71 | a, Advancing and receding water contact angles on the three different structured silanized surfaces before (orange) and after (green) lubricant infiltration indicating the higher advancing contact angles on the silanized surfaces without lubricant (the asterisk indicates pinning) and the reduced contact angles that are consistent across the three, after lubricant infiltration. **b,** Water contact angle hysteresis of the three structured silanized surfaces before and after lubricant infiltration. After lubricant infiltration, all three surfaces display very low CAH (< 5°). **c,** Water contact angle hysteresis on the three different lubricated nanostructured samples after the shear tolerance test. The spin rate starts at 1k rpm and increases to 10k rpm for a time of 60s at each speed.

Although capillary forces are able to hold the lubricant within the structure whilst being subjected to high shear forces, the conditions that a SLIPS would experience when deployed are typically much harsher. Even the seemingly simple motion of a droplet being shed from a slippery surface invokes a complex interplay of surface tensions within a four-phase system. Therefore, we designed a system whereby small droplets (16 µl) were deposited from a height of 1 cm onto the surfaces, which were tilted at 45°. A small droplet volume and moderate rate of deposition (2 droplets/s) were chosen to challenge the surfaces' ability to retain lubricant; with droplets of greater volume, or continuous streams suppressing lubricant depletion by minimizing the formation of a lubricant cloaking layer and large wetting ridge, and similarly increasing the deposition rate is another known strategy for reducing wetting ridge formation. Contact angle hysteresis was measured at different intervals, across 5 different locations of the sample: left, middle top (where the droplet is deposited), center (where the drop slides), middle bottom and right. A schematic of the experimental setup and location of the measured points is shown in Figure 72a. The results are plotted in Figure 72c as contour maps, where the *x*- and *y*-axes indicate the location on the sample, and the *z*-axis contains information on the CAH.

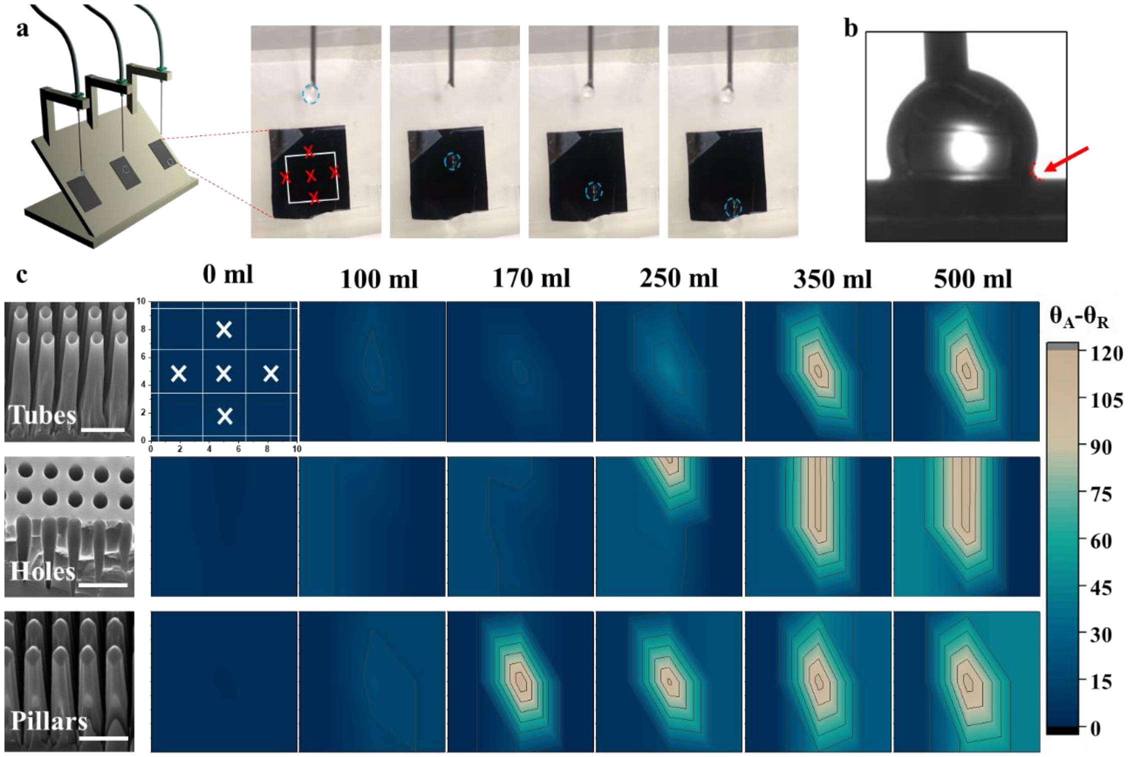

Figure 72 | a, Schematic representation of the experimental setup for the droplet shedding tests; whereby needles deposited water droplets onto the surface. A corresponding photograph highlights the locations where measurements of CAH were taken (marked with a red cross). Later photographs show the progression of a droplet as it leaves the needle, lands on the surface and slides down. **b,** Photograph of a water droplet deposited onto a lubricant infused surface, with formation of a wetting ridge (outlined in red). **c,** Results from the droplet shedding test. Contour maps represent the change in CAH across each surface, with the x- and y-axes mapping the location of the measurement on the sample (as shown in the above photograph), and the z-axis represents the CAH. The CAH was measured after a known volume of water had been deposited, up to 0.5 litres. Scale bars = 1 µm.

From the test, three key observations were made: (i) drainage from the nanopillars occurred first and at the center point; (ii) drainage from nanoholes occurred next but at the point of droplet deposition; (iii) drainage from the nanotubes occurred last and at the center point. Considering the morphologies, the open structure of nanopillars allows for free redistribution of the lubricant, resulting in recovery until drainage becomes significant. At which stage, pinning and depinning of the water contact line on the exposed nanostructure slows the traversing droplet, resulting in coalescence of the successive droplet at the center point (see CAH increase). This serves to amplify lubricant depletion at this location due the increasing wetting ridge; which, owing to its negative curvature and thus Laplace pressure, draws in more lubricant over time.[71,304] Following coalescence, the now larger droplet gains velocity and slides off the surface, removing lubricant as it does so.

For nanoholes, pinning is observed at the point of droplet deposition after 250 ml and continues to deteriorate in line with droplet propagation. Within the hole, capillary forces are much greater than the surface tension force pulling up the wetting ridge hence the lubricant is retained, however the thin layer of lubricant covering the large solid fraction is easily displaced by the shearing motion and the capillary suction force exerted by a deposited or sliding droplet.[305] Moreover, the absence of an interconnected structure prevents recovery; thus, degradation occurs first where the droplet is deposited. The droplet is observed to remain at the deposition location until a successive droplet drops down and coalesces to it.

The nanotubes, having elements of both nanopillars and nanoholes, displays the best lubricant retention, and does not exhibit pinning until 350 ml has been deposited, with the location of the pinning site equivalent to the nanopillars. A combination of factors may contribute to the longevity of the lubricant layer; firstly the open structure which aids the redistribution of lubricant to depleted areas, secondly the reservoir within the tube which is retained through capillary action, thirdly the low solid fraction which renders the surface the least hindering in terms of droplet mobility, and finally, the larger volume of lubricant held per unit area compared to nanopillars (20% more) and nanoholes (230% more), also facilitating redistribution.

Adapted from: S. K. Laney, T. Li, M. Michalska, *et al*., Delayed Lubricant Depletion of Slippery Liquid Infused Porous Surfaces Using Precision Nanostructures, **Langmuir**, 2021, 37, 33, 10071-10078

As an additional layer to our experiment, we weighed the three samples before lubricant infiltration, after lubricant infiltration and at regular intervals of water deposition, with weights normalized to the dry weight (no lubricant) of surfaces of equivalent area (Figure 73). Upon infiltration, the weight of the three surfaces increased by ~2.5%. Infiltration of lubricant into the structure alone would account only for an increase in weight of ~0.3%, thus indicating a lubricant film of ~18 µm is present. Water was deposited on the surfaces in the same manner as the test presented in Figure 72. The largest decrease in weight for all three nanostructured surfaces was observed after the first 150 ml of water was passed over the surface; attributed to the easy removal of the loosely held lubricant film above the structures. Nonetheless differences between structures were observed after 150 ml, consistent with the CAH measurements in Figure 72c; whereby nanopillars are seen to deteriorate fastest, with the lubricant film being removed to expose the nanostructures at a location in the pathway of the droplet. The nanohole and nanotube surfaces exhibit similar decreases in the weight after deposition of 150 and 250 ml of water, however after 350 ml, the weight of the nanohole surface is seen to rapidly decrease and subsequently plateau (similarly to the nanopillars); signaling that the lubricant in the pathway of the droplet has been removed. The nanotube surface on the other hand exhibits a more gradual decrease in the weight, and does not decrease to the same level as that of the nanohole or nanopillar surface after 500 ml.

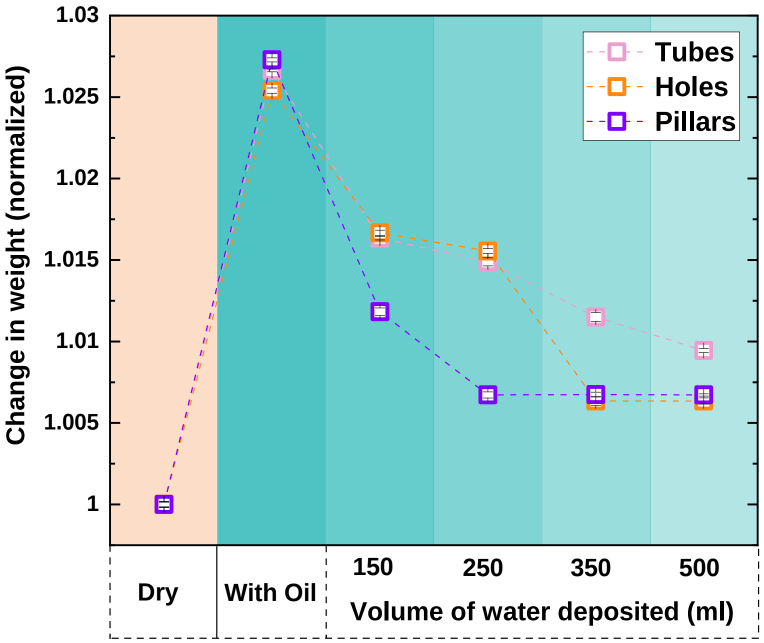

Figure 73 | The observed change in weight of the three nanostructured samples after lubricant infiltration and subsequent water deposition, normalized to the dry weight (prior to lubricant infiltration).

5.2.4 Conclusion

In summary, we present proof-of-concept experiments which demonstrate how by simply tuning the morphology of the nanostructure, the lifetime of a slippery surface can be extended. The fabricated nanotube sample displayed a 2-fold enhancement in lubricant retention in comparison to nanopillars when subjected to a harsh droplet shedding test. A likely explanation being that, as the lubricant layer thinned, the low solid fraction of the nanotubes enabled greater droplet mobility; decreasing the time the droplet spent on the surface and thus reducing the volume of lubricant entrained within the wetting ridge.[71] Furthermore, the capillary forces holding the lubricant within the tube prevented shear-driven lubricant removal from these areas, meanwhile lubricant outside of the tube facilitated redistribution to depleted areas (deposition location). Whilst we have focused solely on the role of the nanostructure in lubricant retention, the choice of the lubricant itself can also enhance the lifetime; with lubricants of higher viscosities having been shown to impede drainage,[306] and non-cloaking lubricant-working fluid combinations preventing additional

Adapted from: S. K. Laney, T. Li, M. Michalska, *et al*., Delayed Lubricant Depletion of Slippery Liquid Infused Porous Surfaces Using Precision Nanostructures, **Langmuir**, 2021, 37, 33, 10071-10078

lubricant removal with each shed droplet.[303] Overall, with modern-day fabrication capabilities (e.g. SDIMP) providing vast freedom in nanostructure design, we envision that further optimization in the nanotube fabrication (concentric or quadruple nanotubes, lowering of the pitch) can elicit even greater lubricant retention, and our preliminary results will help to pave the way to achieve durable SLIPS surfaces. Furthermore, as previously demonstrated SDIMP-generated structures can be successfully imprinted into polymer films, enabling large-scale production and wide applicability.

5.2.5 Methods

Nanostructure fabrication. The nanostructures of hole, pillar and tube morphologies were fabricated according to our SDIMP method.[167] Detailed etching conditions for all RIE processes are listed Table 8-Table 10.

Nanostructure characterization. Scanning Electron Microscopy (SEM) was performed using a Field Emission Zeiss Ultra Plus scanning electron microscope with a Gemini column operating at an accelerating voltage of 2-20 kV. ImageJ (https://imagej.nih.gov/ij/) was used for statistical analysis of the nanostructure dimensions such as pitch, height, diameters.

Surface functionalization. The samples were immersed in 1H,1H,2H,2H-Perfluorodecyltrimethoxysilane (PFDTES) in anhydrous toluene (2% v/v) at room temperature for 24 h, and subsequently annealed at 120°C for 30 min.

Lubricant infiltration. An excess of lubricant was poured atop the surfaces which were then placed in a low-pressure vacuum chamber (pressure ~0.001 atm) for 1 h. To remove the excess lubricant, the surfaces were tilted at 70° under ambient conditions for 24 h, with an absorbent cloth placed underneath.

Contact angle measurements. Both advancing and receding contact angles were measured using a custom designed goniometry setup. The setup consists of a syringe pump (Cole-Parmer Single-syringe infusion pump), a needle (BD PrecisionGlide™ needles, 18G), and an imaging device (Thorlab, model DCC1240). Droplets of approximately 20 µl were deposited onto the surfaces and further extracted using the syringe pump to measure the advancing and receding contact angle, respectively. The videos taken during droplet deposition and extraction were processed through a

Matlab script for contact angle measurements,[199] which is available from the corresponding author upon reasonable request.

The shear tolerance test. The samples, 2 x 2 cm^2, were prepared with an initial excess of lubricant on the surface and affixed onto individual glass microscope slides, 2.5 cm from the center of the slide, with a piece of flat silicon affixed at the opposite end to ensure balancing of the slide. The slide containing the sample was then placed onto the spin coater (SCS G3 Spin Coater). The samples were subjected to increasing spin speeds from 1k to 10k rpm for 60 s at a ramping rate of 3.2. The contact angle hysteresis (CAH) was measured after each spinning cycle (three repeat measurements) and was used to indicate the loss of lubricant from the structure.

Droplet shedding test. Samples were placed on a 45°-tilted stage with needles placed 1 cm from the sample, connected via tubing to a water reservoir and automatic pump (see Figure 72a for schematic). Droplet volume (16 µl) was measured by weighing a known number of water droplets (repeated three times) and using the density of water. The water flow (2 droplets/s) was chosen to be slow enough to ensure single droplets landed on the surface rather than a constant stream, but fast enough so that all points could be collected in one day to avoid effects ranging from self-healing to evaporation. Figure 72a illustrates the setup and shows the five locations on the sample where CAH measurements were taken. Only one point was taken on the left and right of the sample as these areas were not in the pathway of the droplet, however tests were performed to ensure there was no difference across the left side (top, middle and bottom) and right side (top, middle and bottom).

Weighing experiment. Samples were weighed before infiltration. The next weight measurement was taken after infiltration and drainage of excess lubricant. Subsequently, measurements were taken after dropwise deposition (according to the protocol in the droplet shedding test) of 150, 250, 350, and 500 ml water. Weights of the three samples were normalized to the surface area, and to the corresponding ‘dry’ weight.

Table 8 | Etching times and deposition thickness for nanostructure generation

Sample	SiO_2 thickness / nm	O_2 etch / s	CHF_3/Ar etch / min	Cl_2 etch / min	*t* ALD / nm	Cl_2 etch / min
Nanoholes	200	5	9	10	N/A	N/A
Nanopillars	200	5	6	10	N/A	N/A
Nanotubes	200	5	9	5	30	10

Table 9 | Oxford RIE etching conditions for SiO_2 mask etching

Oxford RIE conditions – capacitively coupled plasma				
Oxygen breakthrough	**Pressure / mTorr**	**RF Power / W**	**O_2 / sccm**	
	50	100	50	
SiO_2 etch	**Pressure /mTorr**	**RF Power / W**	**CHF_3 / sccm**	**Ar /sccm**
	50	200	12	38

Table 10 | STS etching conditions for Si etching

ASE, STS MESC Multiplex conditions – inductively coupled plasma								
Sample	**1st Si etch**				**2nd Si etch**			
	Coil /W	Platen /W	P /mTorr	t /min	Coil /W	Platen /W	P /mTorr	t /min
Nanoholes	300	40	3	10	N/A	N/A	N/A	N/A
Nanopillars	300	100	3	10	N/A	N/A	N/A	N/A
Nanotubes	500	200	3	5	300	100	3	10

Table 11 | Interfacial energy values

	Surface tension / mN/m
(Krytox 1525)[303] γ_L	19
(DI water) γ_W	72.2
Krytox-Water γ_{LW}[303]	50.5

Adapted from: S. K. Laney, T. Li, M. Michalska, *et al*., Delayed Lubricant Depletion of Slippery Liquid Infused Porous Surfaces Using Precision Nanostructures, **Langmuir**, 2021, 37, 33, 10071-10078

6

CONCLUSIONS AND OUTLOOK

6.1 Conclusions

This thesis centres around the development of novel fabrication routes for the well-controlled, scalable, and versatile nanostructuring of glass, silicon and polymers to achieve surface multifunctionality. As multifunctionality is the driving force for each class of nanostructures, theoretical investigations are conducted into the optimal morphology/dimensions for each functionality targeted, and experimental testing is performed.

In Chapter 1, the key functionalities of interest are outlined; wetting phenomena (superhydrophobicity, antifogging, slippery surfaces), antireflectivity, and bactericidal action, and the basic principles governing each functionality are explained. At the end of this chapter, the types of structures that are capable of bestowing such properties are introduced, and the fabrication requirements in terms of shape and pitch are established.

This leads into Chapter 2, in which the current state-of-the-art fabrication routes are presented, and the operational principles are explained. This chapter is broken down into lithographic techniques and methods for pattern transfer. Emphasis is placed on the current limitations when using scalable polymeric masks of high resolution, but typically of low aspect ratio, in combination with reactive ion etching. The drawbacks of the solutions presented in the literature are examined and the need for alternative solutions is highlighted.

In Chapter 3, Regenerative Secondary Mask Lithography (RSML) is presented as a route to achieve high-resolution, high-aspect ratio glass etching of nanopillars from a BCP mask, by taking advantage of the plasma etching chemistry, and negating metal incorporation. The presented structures are able to balance optical transparency, water impact-resistance, and importantly, realize the first reported nanostructured glass surface capable of killing *S. aureus* with 81% efficiency. The work also highlights the versatility of RSML by its application to photoresist masks; which do not suffer from the same initial low aspect ratios, but do become depleted during etching. The method is anticipated to drive glass fabrication in both academic and industrial settings due to attainable feature dimensions (including <100 nm; aspect ratio >1), well-aligned with emerging trends in the design of multifunctional surfaces, and find use in applications including solar panels, high-rise glass buildings, food/therapeutics packaging and hospital/bathroom settings, to list a few.

Chapter 4 builds on the work of RSML, by using the technique to generate glass hard masks of varying shape and height, in order to etch into silicon and create a library of different nanostructures. Basic functional testing of the wetting properties and antireflectivity are presented of a 6-inch wafer; highlighting the scalability and uniformity of the techniques. Subsequently, by using this method to fabricate different families of silicon nanocones with systematically varied heights, angles, pitches, and truncation, the chapter proceeds to present the antifogging abilities; investigated through environmental electron microscopy and modelling. It is seen that for all samples within the sharp cone sub-set, microdroplets adopt a highly non-adhesive state, even at radii as low as 1.5 µm, contrasting with the behaviour on pillars where pinning results in impedance of droplet ejection. For truncated cones, opposing characteristics (pinning and a high degree of hydrophobicity) lead to a different, yet efficient, mechanism of dew ejection that requires multiple coalescences.

Chapter 5 deviates from the fabrication of nanocones and their variants, and instead explores more unusual nano-geometries by taking advantage of spacer patterning. By applying a spacer material directly onto pre-patterned silicon nanostructures, Spacer Defined Intrinsic Multiple Patterning (SDIMP) presents a means to precisely control the shape and aspect ratio of the end nanotubes. Further iterations are shown to yield more complex structures, with capabilities to attain concentric arrays with gaps on the order of a few nm; creating the potential for optical trapping or Surface Enhanced Raman Scattering. A nanotube array with fine-tuned features (top crown, tapered outer walls, inner hole) is shown to display remarkable anti reflectivity, and simulations reveal the how the individual features work together to supress light reflectance at different wavelength ranges. Further functionality of the nanotubes is demonstrated in the second half of Chapter 5, when their ability to retain lubricant as a Slippery Liquid Infused Porous Surface (SLIPS) is investigated and compared to conventional nanoholes and nanopillars through dynamic water droplet shedding tests. Contact angle hysteresis measurements in combination with sample weighing are used to determine the degree of lubricant depletion and reveal a 2-fold improvement in retention for nanotubes when compared to nanopillars.

Together, these new/improved fabrication processes provide a platform from which to create tailored nanostructures capable of targeting a multitude of different applications. The fabrication techniques are chosen for their scalability, simplicity and precision, as these are the characteristics sought after when it comes to commercial up-scaling.

6.2 Future Outlook

Despite the rapid advances in both technology and scientific understanding, we remain many steps behind nature in terms of pattern complexity and scale of production. However, for such biological materials, the limited resources and compositions available are likely the driving force for such intricate surface nanopatterns; and this is where we have an advantage.

Nowadays, material properties are not fixed, and instead can be manipulated by understanding the chemistry. For instance, glass; a rigid, brittle material that has been used in windows since the end of the first century, has been reimagined over the past century. By using an ion-exchange process, tougher more durable glass has been created on large scales and employed in the majority of smart phones (Corning Gorilla Glass 6). Through a fusion draw process, ultra-thin (100 µm) glass sheets have been manufactured which can be spooled into rolls owing to their flexibility (Corning Willow Glass). Flexible glass opens up the possibility of roll-to-roll processing, and thus large-scale nanopatterned glass surfaces are a possibility if integrated with roll-to-roll NIL.

Historically, glass has been a passive participant in buildings of various construction – chosen principally for its optical transparency and chemical/thermal stability; making it an ideal candidate for windows and doors. However, in recent years, glass has taken a more active role in the built environment, as companies have begun to realise the potential of this ubiquitous material. NSG

Pilkington have, for instance, developed a commercially available glass coated in an antimicrobial agent that operates through photocatalysis (Pilkington SaniTise); reducing the risk of antimicrobial transmission on exterior and interior glass surfaces. However, such coatings require a certain level of UV exposure in order to be effective, and are thus impractical in certain settings and geographical locations. The mechano-bactericidal glass demonstrated in Chapter 3, therefore holds great promise – either acting solely through contact killing or through a dual chemical and physical approach if incorporating titanium dioxide for instance. In addition to the commercial prospects, the fabrication control achievable through RSML can drive fundamental studies into the mechanism behind the killing and elucidate further the role played by pitch, homogeneity, shape and height. And by the equivalent fabrication in silicon, and imprinting in polymers, the role of the material properties can be determined.

The glass and silicon nanostructures can also incorporate additional active materials such as vanadium dioxide (VO_2) to create, for instance, thermochromic windows with self-cleaning and antireflective properties; providing a step change in the current application space. As mentioned in Chapter 5, nanostructures with precisely controlled nano-spacings can act as aperture based nano-optical tweezers[277–279] in which micro-/nanoscopic objects are physically held and moved with nanometric position using a highly focussed laser beam.[275,276] Another prospective application of the achievable structures through SDIMP, is Surface-Enhanced Raman Scattering (SERS). Through metallisation of our structures, surface plasmons can be channelled or concentrated to greatly enhance the signal when detecting single molecules.

In terms of fabrication, by capitalising on the control achieved through silicon etching for instance (Chapter 4 and 5), soft lithography or NIL can be employed to replicate the pattern from the 'master' into polymeric materials which can be applied as films. It is also envisioned that larger scale production in polymers can be achieved through direct polymeric etching.[307] Excitingly, machine learning has been recently piloted to guide nanofabrication.[142] This could assist in harnessing the multi-dimensional parameter space for etching of different materials, and automatically tailor the fabrication to the functionalities targeted.

With the enormous inspiration from nature, the advances in material development, large-scale production, the fusion of approaches (chemical and physical), and the introduction of artificial intelligence, it is only a matter of time before such nanostructured surfaces find their way into our daily lives. As mentioned, their applicability spans antifogging windscreens, headlights, and endoscopic lenses, to oil-repelling phone screens, to antimicrobial high-touch surfaces and antibiofouling ship hulls, to smart windows with thermochromic properties. However these applications are only scraping the surface of their potential, and new up-and-coming areas of research in radiative cooling or augmented reality for instance, could greatly benefit from such novel fabrication routes.

6.3 Summary of contributions

Owing to the highly interdisciplinary nature of the work presented in this thesis, it has been very much a collaborative effort, and would not have been possible without the persons mentioned in the acknowledgements, and throughout. To summarise the contributions: The fabrication processes have been developed by myself, MM, and TL, with support from IP; the basic wettability characterisation was conducted by myself, MM and TL; the optical characterisation and modelling was carried out by MP, FR and IP; the antifogging characterisation and modelling was performed by PL, and DQ; the SLIPS testing was conducted by myself, with support from MM, JO and MKT.

Bibliography

(1) United Nations Global Issues https://www.un.org/en/global-issues (accessed Sep 16, 2021).

(2) Lelieveld, J.; Evans, J. S.; Fnais, M.; Giannadaki, D.; Pozzer, A. The Contribution of Outdoor Air Pollution Sources to Premature Mortality on a Global Scale. *Nature* **2015**, *525* (7569), 367–371.

(3) Boretti, A.; Rosa, L. Reassessing the Projections of the World Water Development Report. *npj Clean Water* **2019**, *2* (1), 15.

(4) Intelligence, N.; Report, C. NICR 2013-05 US Nat Resources 2020, 2030 2040. **2020**, No. July 2013.

(5) World Health Organisation, *Report; Antimicrobial Resistance*; **2020**.

(6) Neill, J. O. ’. Antimicrobial Resistance: Tackling a Crisis for the Health and Wealth of Nations The Review on Antimicrobial Resistance Chaired. **2014**, No. December.

(7) Ivanova, E. P.; Hasan, J.; Webb, H. K.; Truong, V. K.; Watson, G. S.; Watson, J. A.; Baulin, V. A.; Pogodin, S.; Wang, J. Y.; Tobin, M. J.; Löbbe, C.; Crawford, R. J. Natural Bactericidal Surfaces: Mechanical Rupture of Pseudomonas Aeruginosa Cells by Cicada Wings. *Small* **2012**, *8* (16), 2489–2494.

(8) Shi, Y.; Ilic, O.; Atwater, H. A.; Greer, J. R. All-Day Fresh Water Harvesting by Microstructured Hydrogel Membranes. *Nat. Commun.* **2021**, *12* (1), 2797.

(9) Teng, F.; Li, N.; Liu, L.; Xu, D.; Xiao, D.; Lu, N. Fabrication of Ordered Si Nanopillar Arrays for Ultralow Reflectivity. *RSC Adv.* **2016**, *6* (19), 15803–15807.

(10) Lotus leaf http://www.hk-phy.org/atomic_world/lotus/lotus01_e.html (accessed Jun 4, 2021).

(11) Mccarty, M. Butterfly https://commons.wikimedia.org/w/index.php?curid=5221997 (accessed Jun 4, 2021).

(12) Otas32. Moth eye https://www.deviantart.com/otas32/art/Moth-eye-close-up-270336394%0A (accessed Jun 4, 2021).

(13) Vidu, R.; Rahman, M.; Mahmoudi, M.; Enachescu, M.; Poteca, T. D. Nanostructures : A Platform for Brain Repair and Augmentation. **2014**, *8* (June), 1–24.

(14) Michalska, M.; Gambacorta, F.; Divan, R.; Aranson, I. S.; Sokolov, A.; Noirot, P.; Laible, P. D. Tuning Antimicrobial Properties of Biomimetic Nanopatterned Surfaces. *Nanoscale* **2018**, *10* (14), 6639–6650.

(15) Lecointre, P.; Laney, S.; Michalska, M.; Li, T.; Tanguy, A.; Papakonstantinou, I.; Quéré, D. Unique and Universal Dew-Repellency of Nanocones. *Nat. Commun.* **2021**, *12* (1), 3458.

(16) Mouterde, T.; Lehoucq, G.; Xavier, S.; Checco, A.; Black, C. T.; Rahman, A.; Midavaine, T.; Clanet, C.; Quéré, D. Antifogging Abilities of Model Nanotextures. *Nat. Mater.* **2017**, *16* (6), 658–663.

(17) Park, K.-C.; Choi, H. J.; Chang, C.-H.; Cohen, R. E.; McKinley, G. H.; Barbastathis, G. Nanotextured Silica Surfaces with Robust Superhydrophobicity and Omnidirectional Broadband Supertransmissivity. *ACS Nano* **2012**, *6* (5), 3789–3799.

(18) Brongersma, M. L.; Cui, Y.; Fan, S. Light Management for Photovoltaics Using High-Index Nanostructures. *Nat. Mater.* **2014**, *13* (5), 451–460.

(19) Briscoe, B. J.; Galvin, K. P. The Effect of Surface Fog on the Transmittance of Light. *Sol. Energy* **1991**, *46* (4), 191–197.

(20) San-Juan, M.; Martín, Ó.; Mirones, B. J.; De Tiedra, P. Assessment of Efficiency of Windscreen Demisting Systems in Electrical Vehicles by Using IR Thermography. *Appl. Therm. Eng.* **2016**, *104*, 479–485.

(21) Lawrentschuk, N.; Fleshner, N. E.; Bolton, D. M. Laparoscopic Lens Fogging: A Review of Etiology and Methods to Maintain a Clear Visual Field. *J. Endourol.* **2010**, *24* (6), 905–913.

(22) Ene, A.; Teodosiu, C. Studies Dealing with Defogging and De-Icing Phenomena on Vehicles' Windshield: A Review. *IOP Conf. Ser. Earth Environ. Sci.* **2021**, *664* (1), 012071.

(23) Zhang, T.; Gao, C.; Gao, Q.; Wang, G.; Liu, M.; Guo, Y.; Xiao, C.; Yan, Y. Y. Status and Development of Electric Vehicle Integrated Thermal Management from BTM to HVAC. *Appl. Therm. Eng.* **2015**, *88* (5988), 398–409.

(24) Cao, L.; Jones, A. K.; Sikka, V. K.; Wu, J.; Gao, D. Anti-Icing Superhydrophobic Coatings. *Langmuir* **2009**, *25* (21), 12444–12448.

(25) Li, Y.; Zhang, J.; Yang, B. Antireflective Surfaces Based on Biomimetic Nanopillared Arrays. *Nano Today* **2010**, *5* (2), 117–127.

(26) Philipps, S.; Warmurth, W. *Photovoltaics Report*; **2020**.

(27) Tiedje, T.; Yablonovitch, E.; Cody, G. D.; Brooks, B. G. Limiting Efficiency of Silicon Solar Cells. *IEEE Trans. Electron Devices* **1984**, *31* (5), 711–716.

(28) Green, M. A. Limits on the Open-Circuit Voltage and Efficiency of Silicon Solar Cells Imposed by Intrinsic Auger Processes. *IEEE Trans. Electron Devices* **1984**, *31* (5), 671–678.

(29) Andreani, L. C.; Bozzola, A.; Kowalczewski, P.; Liscidini, M.; Redorici, L. Silicon Solar Cells: Toward the Efficiency Limits. *Adv. Phys. X* **2019**, *4* (1), 1548305.

(30) Yang, R.; Liu, J.; Lin, L.; Qu, Y.; Zheng, W.; Lai, F. Optical Properties and Thermal Stability of Colored Solar Selective Absorbing Coatings with Double-Layer Antireflection Coatings. *Sol. Energy* **2016**, *125*, 453–459.

(31) Zhou, C.; Li, T.; Song, Y.; Zhou, S.; Wang, W.; Zhao, L.; Li, H.; Tang, Y.; Diao, H.; Gao, Z.; Duan, Y.; Li, Y. SiOx(C)/SiNx Dual-Layer Anti-Reflectance Film Coating for Improved Cell Efficiency. *Sol. Energy* **2011**, *85* (11), 3057–3063.

(32) Saidan, M.; Albaali, A. G.; Alasis, E.; Kaldellis, J. K. Experimental Study on the Effect of Dust Deposition on Solar Photovoltaic Panels in Desert Environment. *Renew. Energy* **2016**, *92*, 499–505.

(33) Marmur, A. The Lotus Effect: Superhydrophobicity and Metastability. *Langmuir* **2004**, *20* (9), 3517–3519.

(34) Gao, X.; Yan, X.; Yao, X.; Xu, L.; Zhang, K.; Zhang, J.; Yang, B.; Jiang, L. The Dry-Style Antifogging Properties of Mosquito Compound Eyes and Artificial Analogues Prepared by Soft Lithography. *Adv. Mater.* **2007**, *19* (17), 2213–2217.

(35) NEINHUIS, C. Characterization and Distribution of Water-Repellent, Self-Cleaning Plant Surfaces. *Ann. Bot.* **1997**, *79* (6), 667–677.

(36) Arzt, E.; Quan, H.; McMeeking, R. M.; Hensel, R. Functional Surface Microstructures Inspired by Nature – From Adhesion and Wetting Principles to Sustainable New Devices. *Prog. Mater. Sci.* **2021**, *119* (February).

(37) Eberle, P.; Tiwari, M. K.; Maitra, T.; Poulikakos, D. Rational Nanostructuring of Surfaces for Extraordinary Icephobicity. *Nanoscale* **2014**, *6* (9), 4874–4881.

(38) Ivanova, E. P.; Linklater, D. P.; Werner, M.; Baulin, V. A.; Xu, X.; Vrancken, N. The Multi-Faceted Mechano-Bactericidal Mechanism of Nanostructured Surfaces. **2020**, *117* (23).

(39) de Gennes, P.-G.; Brochard-Wyart, F.; Quere, D. Contact Between Three Phases: Wetting. In *Capillarity and Wetting Phenomena. Drops, Bubbles, Pearls, Waves*; Springer Science + Business Media Inc.: New York, **2004**; pp 15–28.

(40) Young, T. An Essay on the Cohesion of Fluids. *Philos. Trans. R. Soc. London* **1805**, *95* (0), 65–87.

(41) Wenzel, R. N. Resistance of Solid Surfaces to Wetting by Water. *Ind. Eng. Chem.* **1936**, *28* (8), 988–994.

(42) Cassie, A. B. D.; Baxter, S. Wettability of Porous Surfaces. *Trans. Faraday Soc.* **1944**, *40*, 546.

(43) Johnson, R. E.; Dettre, R. H. Contact Angle Hysteresis. In *Advances in Chemistry*; **1964**; pp 112–135.

(44) Balu, B.; Breedveld, V.; Hess, D. W. Fabrication of “Roll-off” and “Sticky” Superhydrophobic Cellulose Surfaces-via Plasma Processing. *Langmuir* **2008**, *24* (9), 4785–4790.

(45) Zhang, X.; Shi, F.; Niu, J.; Jiang, Y.; Wang, Z. Superhydrophobic Surfaces: From Structural Control to Functional Application. *J. Mater. Chem.* **2008**, *18* (6), 621–633.

(46) Reyssat, M.; Pépin, A.; Marty, F.; Chen, Y.; Quéré, D. Bouncing Transitions on Microtextured Materials. *Europhys. Lett.* **2006**, *74* (2), 306–312.

(47) Checco, A.; Rahman, A.; Black, C. T. Robust Superhydrophobicity in Large-Area Nanostructured Surfaces Defined by Block-Copolymer Self Assembly. *Adv. Mater.* **2014**, *26* (6), 886–891.

(48) Durán, I. R.; Laroche, G. Current Trends, Challenges, and Perspectives of Anti-Fogging Technology: Surface and Material Design, Fabrication Strategies, and Beyond. *Prog. Mater. Sci.* **2019**, *99* (June 2017), 106–186.

(49) Yuan, J.; Yan, S.; Zhang, X. Superhydrophilic Antifogging Broadband Antireflective Coatings with Worm-like Nanostructures Fabricated by One Dip-Coating Method and Calcination. *Appl. Surf. Sci.* **2020**, *506* (November 2019), 144795.

(50) Choi, M.; Xiangde, L.; Park, J. H.; Choi, D.; Heo, J.; Chang, M.; Lee, C.; Hong, J. Superhydrophilic Coatings with Intricate Nanostructure Based on Biotic Materials for Antifogging and Antibiofouling Applications. *Chem. Eng. J.* **2017**, *309*, 463–470.

(51) Rose, J. W. Dropwise Condensation Theory and Experiment: A Review. *Proc. Inst. Mech. Eng. Part A J. Power Energy* **2002**, *216* (2), 115–128.

(52) Dorrer, C.; Rühe, J. Condensation and Wetting Transitions on Microstructured Ultrahydrophobic Surfaces. *Langmuir* **2007**, *23* (7), 3820–3824.

(53) Varanasi, K. K.; Hsu, M.; Bhate, N.; Yang, W.; Deng, T. Spatial Control in the Heterogeneous Nucleation of Water. *Appl. Phys. Lett.* **2009**, *95* (9), 094101.

(54) Boreyko, J. B.; Chen, C. H. Self-Propelled Dropwise Condensate on Superhydrophobic Surfaces. *Phys. Rev. Lett.* **2009**, *103* (18), 2–5.

(55) Miljkovic, N.; Enright, R.; Nam, Y.; Lopez, K.; Dou, N.; Sack, J.; Wang, E. N. Jumping-Droplet-Enhanced Condensation on Scalable Superhydrophobic Nanostructured Surfaces. *Nano Lett.* **2013**, *13* (1), 179–187.

(56) Chen, X.; Wu, J.; Ma, R.; Hua, M.; Koratkar, N.; Yao, S.; Wang, Z. Nanograssed Micropyramidal Architectures for Continuous Dropwise Condensation. *Adv. Funct. Mater.* **2011**, *21* (24), 4617–4623.

(57) Wisdom, K. M.; Watson, J. A.; Qu, X.; Liu, F.; Watson, G. S.; Chen, C.-H. Self-Cleaning of Superhydrophobic Surfaces by Self-Propelled Jumping Condensate. *Proc. Natl. Acad. Sci.* **2013**, *110* (20), 7992–7997.

(58) Wong, T.-S. S.; Kang, S. H.; Tang, S. K. Y. Y.; Smythe, E. J.; Hatton, B. D.; Grinthal, A.; Aizenberg, J. Bioinspired Self-Repairing Slippery Surfaces with Pressure-Stable Omniphobicity. *Nature* **2011**, *477* (7365), 443–447.

(59) Papadopoulos, P.; Mammen, L.; Deng, X.; Vollmer, D.; Butt, H. J. How Superhydrophobicity Breaks Down. *Proc. Natl. Acad. Sci. U. S. A.* **2013**, *110* (9), 3254–3258.

(60) Lv, P.; Xue, Y.; Shi, Y.; Lin, H.; Duan, H. Metastable States and Wetting Transition of Submerged Superhydrophobic Structures. *Phys. Rev. Lett.* **2014**, *112* (19).

(61) Prakash, C. G. J.; Prasanth, R. Recent Trends in Fabrication of Nepenthes Inspired SLIPs: Design Strategies for Self-Healing Efficient Anti-Icing Surfaces. *Surfaces and Interfaces* **2020**, *21* (September), 100678.

(62) Kreder, M. J.; Alvarenga, J.; Kim, P.; Aizenberg, J. Design of Anti-Icing Surfaces: Smooth, Textured or Slippery? *Nat. Rev. Mater.* **2016**, *1* (1).

(63) Lee, S. J.; Kim, H. N.; Choi, W.; Yoon, G. Y.; Seo, E. A Nature-Inspired Lubricant-Infused Surface for Sustainable Drag Reduction. *Soft Matter* **2019**, *15* (42), 8459–8467.

(64) Preston, D. J.; Lu, Z.; Song, Y.; Zhao, Y.; Wilke, K. L.; Antao, D. S.; Louis, M.; Wang, E. N. Heat Transfer Enhancement during Water and Hydrocarbon Condensation on Lubricant Infused Surfaces. *Sci. Rep.* **2018**, *8* (1), 1–9.

(65) Amini, S.; Kolle, S.; Petrone, L.; Ahanotu, O.; Sunny, S.; Sutanto, C. N.; Hoon, S.; Cohen, L.; Weaver, J. C.; Aizenberg, J.; Vogel, N.; Miserez, A. Preventing Mussel Adhesion Using Lubricant-Infused Materials. *Science (80-.).* **2017**, *357* (6352), 668–673.

(66) Howell, C.; Grinthal, A.; Sunny, S.; Aizenberg, M.; Aizenberg, J. Designing Liquid-Infused Surfaces for Medical Applications: A Review. *Adv. Mater.* **2018**, *30* (50), 1–26.

(67) Sotiri, I.; Overton, J. C.; Waterhouse, A.; Howell, C. Immobilized Liquid Layers: A New Approach to Anti-Adhesion Surfaces for Medical Applications. *Exp. Biol. Med.* **2016**, *241* (9), 909–918.

(68) Brown, P. S.; Bhushan, B. Liquid-Impregnated Porous Polypropylene Surfaces for Liquid Repellency. *J. Colloid Interface Sci.* **2017**, *487*, 437–443.

(69) Wang, W.; Timonen, J. V. I.; Carlson, A.; Drotlef, D. M.; Zhang, C. T.; Kolle, S.; Grinthal, A.; Wong, T. S.; Hatton, B.; Kang, S. H.; Kennedy, S.; Chi, J.; Blough, R. T.; Sitti, M.; Mahadevan, L.; Aizenberg, J. Multifunctional Ferrofluid-Infused Surfaces with Reconfigurable Multiscale Topography. *Nature* **2018**, *559* (7712), 77–82.

(70) Villegas, M.; Zhang, Y.; Abu Jarad, N.; Soleymani, L.; Didar, T. F. Liquid-Infused Surfaces: A Review of Theory, Design, and Applications. *ACS Nano* **2019**, *13* (8), 8517–8536.

(71) Kreder, M. J.; Daniel, D.; Tetreault, A.; Cao, Z.; Lemaire, B.; Timonen, J. V. I.; Aizenberg, J. Film Dynamics and Lubricant Depletion by Droplets Moving on Lubricated Surfaces. *Phys. Rev. X* **2018**, *8* (3), 031053.

(72) Wexler, J. S.; Jacobi, I.; Stone, H. A. Shear-Driven Failure of Liquid-Infused Surfaces. *Phys. Rev. Lett.* **2015**, *114* (16), 168301.

(73) Zhao, J.; Green, M. A. Optimized Antireflection Coatings for High-Efficiency Silicon Solar Cells. *IEEE Trans. Electron Devices* **1991**, *38* (8), 1925–1934.

(74) Dubey, R. S.; Ganesan, V. Fabrication and Characterization of TiO2/SiO2 Based Bragg Reflectors for Light Trapping Applications. *Results Phys.* **2017**, *7*, 2271–2276.

(75) Cai, J.; Qi, L. Recent Advances in Antireflective Surfaces Based on Nanostructure Arrays. *Mater. Horizons* **2015**, *2* (1), 37–53.

(76) Yao, L.; He, J. Recent Progress in Antireflection and Self-Cleaning Technology – From Surface Engineering to Functional Surfaces. *Prog. Mater. Sci.* **2014**, *61*, 94–143.

(77) Rodvold, K. A.; McConeghy, K. W. Methicillin-Resistant Staphylococcus Aureus Therapy: Past, Present, and Future. *Clin. Infect. Dis.* **2014**, *58* (suppl 1), S20–S27.

(78) Datta, R.; Huang, S. S. Risk of Infection and Death Due to Methicillin-Resistant Staphylococcus Aureus in Long-Term Carriers. *Clin. Infect. Dis.* **2008**, *47* (2), 176–181.

(79) Wandiyanto, J. V.; Cheeseman, S.; Truong, V. K.; Kobaisi, M. Al; Bizet, C.; Juodkazis, S.; Thissen, H.; Crawford, R. J.; Ivanova, E. P. Outsmarting Superbugs: Bactericidal Activity of Nanostructured Titanium Surfaces against Methicillin- and Gentamicin-Resistant Staphylococcus Aureus ATCC 33592. *J. Mater. Chem. B* **2019**, *7* (28), 4424–4431.

(80) Stapleton, P. D.; Taylor, P. W. Methicillin Resistance in Staphylococcus Aureus: Mechanisms and Modulation. *Sci. Prog.* **2002**, *85* (1), 57–72.

(81) Sánchez-Gómez, S.; Martinez-de-Tejada, G. Antimicrobial Peptides as Anti-Biofilm Agents in Medical Implants. *Curr. Top. Med. Chem.* **2017**, *17* (5), 590–603.

(82) Ivanova, E. P.; Linklater, D. P.; Werner, M.; Baulin, V. A.; Xu, X.; Vrancken, N.; Rubanov, S.; Hanssen, E.; Wandiyanto, J.; Truong, V. K.; Elbourne, A.; Maclaughlin, S.; Juodkazis, S.; Crawford, R. J. The Multi-Faceted Mechano-Bactericidal Mechanism of Nanostructured Surfaces. *Proc. Natl. Acad. Sci.* **2020**, *117* (23), 12598–12605.

(83) Ivanova, E. P.; Hasan, J.; Webb, H. K.; Gervinskas, G.; Juodkazis, S.; Truong, V. K.; Wu, A. H. F.; Lamb, R. N.; Baulin, V. A.; Watson, G. S.; Watson, J. A.; Mainwaring, D. E.; Crawford, R. J. Bactericidal Activity of Black Silicon. *Nat. Commun.* **2013**, *4* (1), 2838.

(84) Linklater, D. P.; Baulin, V. A.; Juodkazis, S.; Crawford, R. J.; Stoodley, P.; Ivanova, E. P. Mechano-Bactericidal Actions of Nanostructured Surfaces. *Nature Reviews Microbiology*. Springer US January 17, 2021, pp 8–22.

(85) Hazell, G.; Fisher, L. E.; Murray, W. A.; Nobbs, A. H.; Su, B. Bioinspired Bactericidal Surfaces with Polymer Nanocone Arrays. *J. Colloid Interface Sci.* **2018**, *528*, 389–399.

(86) Zahir, T.; Pesek, J.; Franke, S.; Van Pee, J.; Rathore, A.; Smeets, B.; Ramon, H.; Xu, X.; Fauvart, M.; Michiels, J. Model-Driven Controlled Alteration of Nanopillar Cap Architecture Reveals Its Effects on Bactericidal Activity. *Microorganisms* **2020**, *8* (2), 186.

(87) Singh, J.; Jadhav, S.; Avasthi, S.; Sen, P. Designing Photocatalytic Nanostructured Antibacterial Surfaces: Why Is Black Silica Better than Black Silicon? *ACS Appl. Mater. Interfaces* **2020**, *12* (18), 20202–20213.

(88) Jindai, K.; Nakade, K.; Masuda, K.; Sagawa, T.; Kojima, H.; Shimizu, T.; Shingubara, S.; Ito, T. Adhesion and Bactericidal Properties of Nanostructured Surfaces Dependent on Bacterial Motility. *RSC Adv.* **2020**, *10* (10), 5673–5680.

(89) Jenkins, J.; Mantell, J.; Neal, C.; Gholinia, A.; Verkade, P.; Nobbs, A. H.; Su, B. Antibacterial Effects of Nanopillar Surfaces Are Mediated by Cell Impedance, Penetration and Induction of Oxidative Stress. *Nat. Commun.* **2020**, *11* (1), 1626.

(90) Liu, T.; Cui, Q.; Wu, Q.; Li, X.; Song, K.; Ge, D.; Guan, S. Mechanism Study of Bacteria Killed on Nanostructures. *J. Phys. Chem. B* **2019**, *123* (41), 8686–8696.

(91) Rahman, A.; Ashraf, A.; Xin, H.; Tong, X.; Sutter, P.; Eisaman, M. D.; Black, C. T. Sub-50-Nm Self-Assembled Nanotextures for Enhanced Broadband Antireflection in Silicon Solar Cells. *Nat. Commun.* **2015**, *6* (1), 5963.

(92) Park, K. C.; Choi, H. J.; Chang, C. H.; Cohen, R. E.; McKinley, G. H.; Barbastathis, G. Nanotextured Silica Surfaces with Robust Superhydrophobicity and Omnidirectional Broadband Supertransmissivity. *ACS Nano* **2012**, *6* (5), 3789–3799.

(93) del Barrio, J.; Sánchez-Somolinos, C. Light to Shape the Future: From Photolithography to 4D Printing. *Adv. Opt. Mater.* **2019**, *7* (16), 1900598.

(94) Pargen, S.; Willems, C.; Keul, H.; Pich, A.; Möller, M. Surfactant-Free Synthesis of Polystyrene Nanoparticles Using Oligoglycidol Macromonomers. *Macromolecules* **2012**, *45* (3), 1230–1240.

(95) Jiang, P.; Bertone, J. F.; Hwang, K. S.; Colvin, V. L. Single-Crystal Colloidal Multilayers of Controlled Thickness. *Chem. Mater.* **1999**, *11* (8), 2132–2140.

(96) Gu, Z. Z.; Fujishima, A.; Sato, O. Fabrication of High-Quality Opal Films with Controllable Thickness. *Chem. Mater.* **2002**, *14* (2), 760–765.

(97) Wang, D.; Möhwald, H. Rapid Fabrication of Binary Colloidal Crystals by Stepwise Spin-Coating. *Adv. Mater.* **2004**, *16* (3), 244–247.

(98) Xu, X.; Yang, Q.; Wattanatorn, N.; Zhao, C.; Chiang, N.; Jonas, S. J.; Weiss, P. S. Multiple-Patterning Nanosphere Lithography for Fabricating Periodic Three-Dimensional Hierarchical Nanostructures. *ACS Nano* **2017**, *11* (10), 10384–10391.

(99) Jiang, P.; McFarland, M. J. Large-Scale Fabrication of Wafer-Size Colloidal Crystals, Macroporous Polymers and Nanocomposites by Spin-Coating. *J. Am. Chem. Soc.* **2004**, *126* (42), 13778–13786.

(100) Jibowu, T. Nano-Spherical Lithography for Nanopatterning. *Front. Nanosci. Nanotechnol.* **2016**, *2* (5), 1–5.

(101) Rahman, F. *Vistas in Nanofabrication*; Pan Stanford, **2012**.

(102) Wang, Y.; Zhang, M.; Lai, Y.; Chi, L. Advanced Colloidal Lithography: From Patterning to Applications. *Nano Today* **2018**, *22*, 36–61.

(103) Acikgoz, C.; Hempenius, M. A.; Huskens, J.; Vancso, G. J. Polymers in Conventional and Alternative Lithography for the Fabrication of Nanostructures. *Eur. Polym. J.* **2011**, *47* (11), 2033–2052.

(104) Chou, S. Y. Sub-10 Nm Imprint Lithography and Applications. *J. Vac. Sci. Technol. B Microelectron. Nanom. Struct.* **1997**, *15* (6), 2897.

(105) Chou, S. Y.; Krauss, P. R.; Renstrom, P. J. Imprint Lithography with 25-Nanometer Resolution. *Science (80-.).* **1996**, *272* (5258), 85–87.

(106) Austin, M. D.; Ge, H.; Wu, W.; Li, M.; Yu, Z.; Wasserman, D.; Lyon, S. A.; Chou, S. Y. Fabrication of 5nm Linewidth and 14nm Pitch Features by Nanoimprint Lithography. *Appl. Phys. Lett.* **2004**, *84* (26), 5299–5301.

(107) M., M.; Mohame, K. Three-Dimensional Patterning Using Ultraviolet Nanoimprint Lithography. In *Lithography*; InTech, **2010**.

(108) Vogler, M.; Wiedenberg, S.; Mühlberger, M.; Bergmair, I.; Glinsner, T.; Schmidt, H.; Kley, E.-B.; Grützner, G. Development of a Novel, Low-Viscosity UV-Curable Polymer System for UV-Nanoimprint Lithography. *Microelectron. Eng.* **2007**, *84* (5–8), 984–988.

(109) Lan, H.; Ding, Y. Nanoimprint Lithography. In *Lithography*; InTech, **2010**.

(110) Tan, H. Roller Nanoimprint Lithography. *J. Vac. Sci. Technol. B Microelectron. Nanom. Struct.* **1998**, *16* (6), 3926.

(111) Kooy, N.; Mohamed, K.; Pin, L.; Guan, O. A Review of Roll-to-Roll Nanoimprint Lithography. *Nanoscale Res. Lett.* **2014**, *9* (1), 320.

(112) Ahn, S. H.; Guo, L. J. High-Speed Roll-to-Roll Nanoimprint Lithography on Flexible Plastic Substrates. *Adv. Mater.* **2008**, *20* (11), 2044–2049.

(113) Bates, F. S.; Fredrickson, G. H. Block Copolymer Thermodynamics: Theory and Experiment. *Annu. Rev. Phys. Chem.* **1990**, *41* (1), 525–557.

(114) Li, T.; Wang, Z.; Schulte, L.; Hansen, O.; Ndoni, S. Fast & Scalable Pattern Transfer via Block Copolymer Nanolithography. *RSC Adv.* **2015**, *5* (124), 102619–102624.

(115) Schacher, F. H.; Rupar, P. A.; Manners, I. Functional Block Copolymers: Nanostructured Materials with Emerging Applications. *Angew. Chemie - Int. Ed.* **2012**, *51* (32), 7898–7921.

(116) Bates, F. S.; Fredrickson, G. H. Block Copolymers—Designer Soft Materials. *Phys. Today* **1999**, *52* (2), 32–38.

(117) Förster, S.; Plantenberg, T. From Self-Organizing Polymers to Nanohybrid and Biomaterials. *Angew. Chem. Int. Ed. Engl.* **2002**, *41* (5), 689–714.

(118) Kim, J. K.; Yang, S. Y.; Lee, Y.; Kim, Y. Functional Nanomaterials Based on Block Copolymer Self-Assembly. *Prog. Polym. Sci.* **2010**, *35* (11), 1325–1349.

(119) Orilall, M. C.; Wiesner, U. Block Copolymer Based Composition and Morphology Control

in Nanostructured Hybrid Materials for Energy Conversion and Storage: Solar Cells, Batteries, and Fuel Cells. *Chem. Soc. Rev.* **2011**, *40* (2), 520–535.

(120) Zhang, L. F.; Eisenberg, a. Formation of Crew-Cut Aggregates of Various Morphologies from Amphiphilic Block Copolymers in Solution. *Polym. Adv. Technol.* **1998**, *9* (May), 677–699.

(121) Gotrik, K. W.; Hannon, A. F.; Son, J. G.; Keller, B.; Alexander-Katz, A.; Ross, C. A. Morphology Control in Block Copolymer Films Using Mixed Solvent Vapors. *ACS Nano* **2012**, *6* (9), 8052–8059.

(122) Sinturel, C.; Vayer, M.; Morris, M.; Hillmyer, M. A. Solvent Vapor Annealing of Block Polymer Thin Films. *Macromolecules* **2013**, *46* (14), 5399–5415.

(123) Sinturel, C.; Vayer, M.; Morris, M.; Hillmyer, M. A. Solvent Vapor Annealing of Block Polymer Thin Films. *Macromolecules* **2013**, *46* (14), 5399–5415.

(124) Yang, Q.; Loos, K. Perpendicular Structure Formation of Block Copolymer Thin Films during Thermal Solvent Vapor Annealing: Solvent and Thickness Effects. *Polymers (Basel).* **2017**, *9* (10).

(125) Lohmüller, T.; Aydin, D.; Schwieder, M.; Morhard, C.; Louban, I.; Pacholski, C.; Spatz, J. P. Nanopatterning by Block Copolymer Micelle Nanolithography and Bioinspired Applications. *Biointerphases* **2011**, *6* (1), MR1–MR12.

(126) Spatz, J. P.; Mössmer, S.; Hartmann, C.; Möller, M.; Herzog, T.; Krieger, M.; Boyen, H. G.; Ziemann, P.; Kabius, B. Ordered Deposition of Inorganic Clusters from Micellar Block Copolymer Films. *Langmuir* **2000**, *16* (2), 407–415.

(127) Krishnamoorthy, S.; Manipaddy, K. K.; Yap, F. L. Wafer-Level Self-Organized Copolymer Templates for Nanolithography with Sub-50 Nm Feature and Spatial Resolutions. *Adv. Funct. Mater.* **2011**, *21* (6), 1102–1112.

(128) Krishnamoorthy, S.; Gerbig, Y.; Hibert, C.; Pugin, R.; Hinderling, C.; Brugger, J.; Heinzelmann, H. Tunable, High Aspect Ratio Pillars on Diverse Substrates Using Copolymer Micelle Lithography: An Interesting Platform for Applications. *Nanotechnology* **2008**, *19* (28), 285301.

(129) Krishnamoorthy, S.; Pugin, R.; Brugger, J.; Heinzelmann, H.; Hinderling, C. Tuning the Dimensions and Periodicities of Nanostructures Starting from the Same Polystyrene-Block-Poly(2-Vinylpyridine) Diblock Copolymer. *Adv. Funct. Mater.* **2006**, *16* (11), 1469–1475.

(130) Brueck, S. R. J. Optical and Interferometric Lithography -Nanotechnology Enablers. In *Proceedings of the IEEE*; **2005**; Vol. 93, pp 1704–1721.

(131) Yang, X. L.; Cai, L. Z.; Wang, Y. R.; Liu, Q. Interference Technique by Three Equal-Intensity Umbrellalike Beams with a Diffractive Beam Splitter for Fabrication of Two-Dimensional Trigonal and Square Lattices. *Opt. Commun.* **2003**, *218* (4–6), 325–332.

(132) Campbell, M.; Sharp, D. N.; Harrison, M. T.; Denning^3, R. G.; Turber®eld, A. J.

Fabrication of Photonic Crystals for the Visible Spectrum by Holographic Lithography; **2000**.

(133) Cai, L. Z.; Yang, X. L.; Wang, Y. R. Formation of a Microfiber Bundle by Interference of Three Noncoplanar Beams. *Opt. Lett.* **2001**, *26* (23), 1858–1860.

(134) Wolferen, H. van; Abelman, L. Laser Interference Lithography. In *Lithography: Prinnciples, Processes and Materials*; Hennessy, T., Ed.; Nova Science Publishers Inc., **2011**; pp 133–148.

(135) O'Reilly, T. B.; Smith, H. I. Linewidth Uniformity in Lloyd's Mirror Interference Lithography Systems. *J. Vac. Sci. Technol. B Microelectron. Nanom. Struct.* **2008**, *26* (6), 2131–2134.

(136) Kulkarni, D. D.; Field, D. A.; Cutshall, D. B.; Harriss, J. E.; Harrell, W. R.; Sosolik, C. E. Probing Kinetically Excited Hot Electrons Using Schottky Diodes. *J. Vac. Sci. Technol. B, Nanotechnol. Microelectron. Mater. Process. Meas. Phenom.* **2017**, *35* (3), 03D103.

(137) Dorney, K.; Castellanos, S.; Larsen, E.; Holzmeier, F.; Singh, D.; Vandenbroeck, N.; Simone, D. De; Schepper, P. De; VaglioPret, A.; Bargsten, C.; Cousin, S. L.; Raymondson, D.; Rinard, E.; Ward, R.; Kaptyen, H.; Nuytten, T.; der Heide, P. Van; Petersen, J. Lloyd's Mirror Interference Lithography below a 22-Nm Pitch with an Accessible, Tabletop, 13.5 Nm High-Harmonic EUV Source. In *Novel Patterning Technologies 2021*; Panning, E. M., Ed.; SPIE, **2021**; Vol. 11610.

(138) Wang, L.; Wang, Z.-H.; Yu, Y.-H.; Sun, H.-B. Laser Interference Fabrication of Large-Area Functional Periodic Structure Surface. *Front. Mech. Eng.* **2018**, *13* (4), 493–503.

(139) Tulli, D.; Hart, S. D.; Mazumder, P.; Carrilero, A.; Tian, L.; Koch, K. W.; Yongsunthon, R.; Piech, G. A.; Pruneri, V. Monolithically Integrated Micro- and Nanostructured Glass Surface with Antiglare, Antireflection, and Superhydrophobic Properties. *ACS Appl. Mater. Interfaces* **2014**, *6* (14), 11198–11203.

(140) Cardinaud, C. Fluorine-Based Plasmas: Main Features and Application in Micro-and Nanotechnology and in Surface Treatment. *Comptes Rendus Chim.* **2018**, *21* (8), 723–739.

(141) Ye, X.; Jiang, X.; Huang, J.; Geng, F.; Sun, L.; Zu, X.; Wu, W.; Zheng, W. Formation of Broadband Antireflective and Superhydrophilic Subwavelength Structures on Fused Silica Using One-Step Self-Masking Reactive Ion Etching. *Sci. Rep.* **2015**, *5* (August), 1–10.

(142) Haghanifar, S.; McCourt, M.; Cheng, B.; Wuenschell, J.; Ohodnicki, P.; Leu, P. W. Creating Glasswing Butterfly-Inspired Durable Antifogging Superomniphobic Supertransmissive, Superclear Nanostructured Glass through Bayesian Learning and Optimization. *Mater. Horizons* **2019**, *6* (8), 1632–1642.

(143) Haghanifar, S.; Gao, T.; Rodriguez De Vecchis, R. T.; Pafchek, B.; Jacobs, T. D. B.; Leu, P. W. Ultrahigh-Transparency, Ultrahigh-Haze Nanograss Glass with Fluid-Induced Switchable Haze. *Optica* **2017**, *4* (12), 1522.

(144) Chen, Y.; Xu, Z.; Gartia, M. R.; Whitlock, D.; Lian, Y.; Liu, G. L. Ultrahigh Throughput Silicon Nanomanufacturing by Simultaneous Reactive Ion Synthesis and Etching. *ACS Nano* **2011**, *5* (10), 8002–8012.

(145) Nunns, A.; Gwyther, J.; Manners, I. Inorganic Block Copolymer Lithography. *Polymer (Guildf).* **2013**, *54* (4), 1269–1284.

(146) Peng, Q.; Tseng, Y.-C.; Darling, S. B. B.; Elam, J. W. W. A Route to Nanoscopic Materials via Sequential Infiltration Synthesis on Block Copolymer Templates. *ACS Nano* **2011**, *5* (6), 4600–4606.

(147) Liapis, A. C.; Rahman, A.; Black, C. T. Self-Assembled Nanotextures Impart Broadband Transparency to Glass Windows and Solar Cell Encapsulants. *Appl. Phys. Lett.* **2017**, *111* (18), 183901.

(148) Alabi, T. R.; Yuan, D.; Bucknall, D.; Das, S. Silicon Oxide Nanowires: Facile and Controlled Large Area Fabrication of Vertically Oriented Silicon Oxide Nanowires for Photoluminescence and Sensor Applications. *ACS Appl. Mater. Interfaces* **2013**, *5* (18), 8932–8938.

(149) Glass, R.; M ller, M.; Spatz, J. P. Block Copolymer Micelle Nanolithography. *Nanotechnology* **2003**, *14* (10), 1153–1160.

(150) Diao, Z.; Kraus, M.; Brunner, R.; Dirks, J.-H.; Spatz, J. P. Nanostructured Stealth Surfaces for Visible and Near-Infrared Light. *Nano Lett.* **2016**, *16* (10), 6610–6616.

(151) Glassmaker, N. J.; Jagota, A.; Hui, C.-Y.; Kim, J. Design of Biomimetic Fibrillar Interfaces: 1. Making Contact. *J. R. Soc. Interface* **2004**, *1* (1), 23–33.

(152) Green, T. A. Gold Etching for Microfabrication. *Gold Bull.* **2014**, *47* (3), 205–216.

(153) Glass, R.; M ller, M.; Spatz, J. P. Block Copolymer Micelle Nanolithography. *Nanotechnology* **2003**, *14* (10), 1153–1160.

(154) Bestwick, T. D.; Oehrlein, G. S.; Angell, D. Cryogenic Reactive Ion Etching of Silicon in SF 6. *Appl. Phys. Lett.* **1990**, *57* (5), 431–433.

(155) Laermer, F.; Schlip, A. Method of Anisotropically Etching Silicon, 1996.

(156) Voss, L. F.; Shao, Q.; Conway, A. M.; Reinhardt, C. E.; Graff, R. T.; Nikolic, R. J. Smooth Bosch Etch for Improved Si Diodes. *IEEE Electron Device Lett.* **2013**, *34* (10), 1226–1228.

(157) Park, J. S.; Kang, D.-H.; Kwak, S. M.; Kim, T. S.; Park, J. H.; Kim, T. G.; Baek, S.-H.; Lee, B. C. Low-Temperature Smoothing Method of Scalloped DRIE Trench by Post-Dry Etching Process Based on SF6 Plasma. *Micro Nano Syst. Lett.* **2020**, *8* (1), 14.

(158) Roozeboom, F.; van den Bruele, F.; Creyghton, Y.; Poodt, P.; Kessels, W. M. M. Cyclic Etch/Passivation-Deposition as an All-Spatial Concept toward High-Rate Room Temperature Atomic Layer Etching. *ECS J. Solid State Sci. Technol.* **2015**, *4* (6), N5067–N5076.

---

(159) Morton, K. J.; Nieberg, G.; Bai, S.; Chou, S. Y. Wafer-Scale Patterning of Sub-40 Nm Diameter and High Aspect Ratio (>50:1) Silicon Pillar Arrays by Nanoimprint and Etching. *Nanotechnology* **2008**, *19* (34), 345301.

(160) Li, T.; Wang, Z.; Schulte, L.; Ndoni, S. Substrate Tolerant Direct Block Copolymer Nanolithography. *Nanoscale* **2016**, *8* (1), 136–140.

(161) Rasappa, S.; Hulkkonen, H.; Schulte, L.; Ndoni, S.; Reuna, J.; Salminen, T.; Niemi, T. High Molecular Weight Block Copolymer Lithography for Nanofabrication of Hard Mask and Photonic Nanostructures. *J. Colloid Interface Sci.* **2019**, *534*, 420–429.

(162) Ghoshal, T.; Senthamaraikannan, R.; Shaw, M. T.; Holmes, J. D.; Morris, M. A. In Situ Hard Mask Materials: A New Methodology for Creation of Vertical Silicon Nanopillar and Nanowire Arrays. *Nanoscale* **2012**, *4* (24), 7743–7750.

(163) Kamcev, J.; Germack, D. S.; Nykypanchuk, D.; Grubbs, R. B.; Nam, C.-Y.; Black, C. T. Chemically Enhancing Block Copolymers for Block-Selective Synthesis of Self-Assembled Metal Oxide Nanostructures. *ACS Nano* **2013**, *7* (1), 339–346.

(164) Guarini, K. W.; Black, C. T.; Zhang, Y.; Kim, H.; Sikorski, E. M.; Babich, I. V. Process Integration of Self-Assembled Polymer Templates into Silicon Nanofabrication. *J. Vac. Sci. Technol. B Microelectron. Nanom. Struct.* **2002**, *20* (6), 2788.

(165) Xia, F.; Jiang, L. Bio-Inspired, Smart, Multiscale Interfacial Materials. *Adv. Mater.* **2008**, *20* (15), 2842–2858.

(166) Raut, H. K.; Ganesh, V. A.; Nair, A. S.; Ramakrishna, S. Anti-Reflective Coatings: A Critical, in-Depth Review. *Energy Environ. Sci.* **2011**, *4* (10), 3779–3804.

(167) Laney, S. K.; Li, T.; Michalska, M.; Ramirez, F.; Portnoi, M.; Oh, J.; Tiwari, M. K.; Thayne, I. G.; Parkin, I. P.; Papakonstantinou, I. Spacer-Defined Intrinsic Multiple Patterning. *ACS Nano* **2020**, *14* (9), 12091–12100.

(168) Narasimhan, V.; Siddique, R. H.; Lee, J. O.; Kumar, S.; Ndjamen, B.; Du, J.; Hong, N.; Sretavan, D.; Choo, H. Multifunctional Biophotonic Nanostructures Inspired by the Longtail Glasswing Butterfly for Medical Devices. *Nat. Nanotechnol.* **2018**, *13* (6), 512–519.

(169) Higgins, S. G.; Becce, M.; Belessiotis-Richards, A.; Seong, H.; Sero, J. E.; Stevens, M. M. High-Aspect-Ratio Nanostructured Surfaces as Biological Metamaterials. *Adv. Mater.* **2020**, *32* (9), 1903862.

(170) Infante, D.; Koch, K. W.; Mazumder, P.; Tian, L.; Carrilero, A.; Tulli, D.; Baker, D.; Pruneri, V. Durable, Superhydrophobic, Antireflection, and Low Haze Glass Surfaces Using Scalable Metal Dewetting Nanostructuring. *Nano Res.* **2013**, *6* (6), 429–440.

(171) Haghanifar, S.; McCourt, M.; Cheng, B.; Wuenschell, J.; Ohodnicki, P.; Leu, P. W. Creating Glasswing Butterfly-Inspired Durable Antifogging Superomniphobic Supertransmissive, Superclear Nanostructured Glass through Bayesian Learning and Optimization. *Mater.*

Horizons **2019**, *6* (8), 1632–1642.

(172) Papadopoulos, A.; Skoulas, E.; Mimidis, A.; Perrakis, G.; Kenanakis, G.; Tsibidis, G. D.; Stratakis, E. Biomimetic Omnidirectional Antireflective Glass via Direct Ultrafast Laser Nanostructuring. *Adv. Mater.* **2019**, *31* (32), 1–8.

(173) Park, J.-S.; Zhang, S.; She, A.; Chen, W. T.; Lin, P.; Yousef, K. M. A.; Cheng, J.-X.; Capasso, F. All-Glass, Large Metalens at Visible Wavelength Using Deep-Ultraviolet Projection Lithography. *Nano Lett.* **2019**, *19* (12), 8673–8682.

(174) Nie, Z.; Kumacheva, E. Patterning Surfaces with Functional Polymers. *Nat. Mater.* **2008**, *7* (4), 277–290.

(175) Liddle, J. A.; Gallatin, G. M. Nanomanufacturing: A Perspective. *ACS Nano* **2016**, *10* (3), 2995–3014.

(176) Lammertink, R. G. H.; Hempenius, M. A.; van den Enk, J. E.; Chan, V. Z. H.; Thomas, E. L.; Vancso, G. J. Nanostructured Thin Films of Organic-Organometallic Block Copolymers: One-Step Lithography with Poly(Ferrocenylsilanes) by Reactive Ion Etching. *Adv. Mater.* **2000**, *12* (2), 98–103.

(177) Mohamed, K.; Alkaisi, M. M. Investigation of a Nanofabrication Process to Achieve High Aspect-Ratio Nanostructures on a Quartz Substrate. *Nanotechnology* **2013**, *24* (1), 015302.

(178) Chan, C.-M.; Ko, T.-M.; Hiraoka, H. Polymer Surface Modification by Plasmas and Photons. *Surf. Sci. Rep.* **1996**, *24* (1–2), 1–54.

(179) Marty, F.; Rousseau, L.; Saadany, B.; Mercier, B.; Français, O.; Mita, Y.; Bourouina, T. Advanced Etching of Silicon Based on Deep Reactive Ion Etching for Silicon High Aspect Ratio Microstructures and Three-Dimensional Micro- and Nanostructures. *Microelectronics J.* **2005**, *36* (7), 673–677.

(180) Huang, S.; Shim, S.; Nam, S. K.; Kushner, M. J. Pattern Dependent Profile Distortion during Plasma Etching of High Aspect Ratio Features in SiO 2. *J. Vac. Sci. Technol. A* **2020**, *38* (2), 023001.

(181) Cho, S.-W.; Kim, J.-H.; Kim, S.; Shin, E. W.; Kim, C.-K. Reduction in the Diameter of Contact Holes with a High Anisotropy and Aspect Ratio. *ECS J. Solid State Sci. Technol.* **2015**, *4* (7), P226–P231.

(182) Kim, J. K.; Lee, S. H.; Cho, S. Il; Yeom, G. Y. Study on Contact Distortion during High Aspect Ratio Contact SiO 2 Etching. *J. Vac. Sci. Technol. A Vacuum, Surfaces, Film.* **2015**, *33* (2), 021303.

(183) Saffih, F.; Con, C.; Alshammari, A.; Yavuz, M.; Cui, B. Fabrication of Silicon Nanostructures with Large Taper Angle by Reactive Ion Etching. *J. Vac. Sci. Technol. B, Nanotechnol. Microelectron. Mater. Process. Meas. Phenom.* **2014**, *32* (6), 06FI04.

(184) Wang, D.; Sun, Q.; Hokkanen, M. J.; Zhang, C.; Lin, F. Y.; Liu, Q.; Zhu, S. P.; Zhou, T.; Chang, Q.; He, B.; Zhou, Q.; Chen, L.; Wang, Z.; Ras, R. H. A.; Deng, X. Design of Robust

Superhydrophobic Surfaces. *Nature* **2020**, *582* (7810), 55–59.

(185) Choi, M. K.; Yoon, H.; Lee, K.; Shin, K. Simple Fabrication of Asymmetric High-Aspect-Ratio Polymer Nanopillars by Reusable AAO Templates. *Langmuir* **2011**, *27* (6), 2132–2137.

(186) Stavenga, D. G.; Foletti, S.; Palasantzas, G.; Arikawa, K. Light on the Moth-Eye Corneal Nipple Array of Butterflies. *Proc. Biol. Sci.* **2006**, *273* (1587), 661–667.

(187) Mbise, G. W.; Bellac, D. Le; Niklasson, G. A.; Granqvist, C. G. Angular Selective Window Coatings: Theory and Experiments. *J. Phys. D. Appl. Phys.* **1997**, *30* (15), 2103–2122.

(188) Siddique, R. H.; Gomard, G.; Hölscher, H. The Role of Random Nanostructures for the Omnidirectional Anti-Reflection Properties of the Glasswing Butterfly. *Nat. Commun.* **2015**, *6* (1), 6909.

(189) Deparis, O.; Khuzayim, N.; Parker, A.; Vigneron, J. Assessment of the Antireflection Property of Moth Wings by Three-Dimensional Transfer-Matrix Optical Simulations. *Phys. Rev. E* **2009**, *79* (4), 041910.

(190) Mitsas, C. L.; Siapkas, D. I. Generalized Matrix Method for Analysis of Coherent and Incoherent Reflectance and Transmittance of Multilayer Structures with Rough Surfaces, Interfaces, and Finite Substrates. *Appl. Opt.* **1995**, *34* (10), 1678.

(191) Katsidis, C. C.; Siapkas, D. I. General Transfer-Matrix Method for Optical Multilayer Systems with Coherent, Partially Coherent, and Incoherent Interference. *Appl. Opt.* **2002**, *41* (19), 3978.

(192) Maitra, T.; Tiwari, M. K.; Antonini, C.; Schoch, P.; Jung, S.; Eberle, P.; Poulikakos, D. On the Nanoengineering of Superhydrophobic and Impalement Resistant Surface Textures below the Freezing Temperature. *Nano Lett.* **2014**, *14* (1), 172–182.

(193) Kwon, H.-M.; Paxson, A. T.; Varanasi, K. K.; Patankar, N. A. Rapid Deceleration-Driven Wetting Transition during Pendant Drop Deposition on Superhydrophobic Surfaces. *Phys. Rev. Lett.* **2011**, *106* (3), 036102.

(194) Deng, T.; Varanasi, K. K.; Hsu, M.; Bhate, N.; Keimel, C.; Stein, J.; Blohm, M. Nonwetting of Impinging Droplets on Textured Surfaces. *Appl. Phys. Lett.* **2009**, *94* (13), 2–5.

(195) Pogodin, S.; Hasan, J.; Baulin, V. A.; Webb, H. K.; Truong, V. K.; Phong Nguyen, T. H.; Boshkovikj, V.; Fluke, C. J.; Watson, G. S.; Watson, J. A.; Crawford, R. J.; Ivanova, E. P. Biophysical Model of Bacterial Cell Interactions with Nanopatterned Cicada Wing Surfaces. *Biophys. J.* **2013**, *104* (4), 835–840.

(196) Xue, F.; Liu, J.; Guo, L.; Zhang, L.; Li, Q. Theoretical Study on the Bactericidal Nature of Nanopatterned Surfaces. *J. Theor. Biol.* **2015**, *385*, 1–7.

(197) Linklater, D. P.; De Volder, M.; Baulin, V. A.; Werner, M.; Jessl, S.; Golozar, M.; Maggini, L.; Rubanov, S.; Hanssen, E.; Juodkazis, S.; Ivanova, E. P. High Aspect Ratio Nanostructures Kill Bacteria via Storage and Release of Mechanical Energy. *ACS Nano*

2018, *12* (7), 6657–6667.

(198) Han, S.; Ji, S.; Abdullah, A.; Kim, D.; Lim, H.; Lee, D. Superhydrophilic Nanopillar-Structured Quartz Surfaces for the Prevention of Biofilm Formation in Optical Devices. *Appl. Surf. Sci.* **2018**, *429*, 244–252.

(199) Peng, C.; Chen, Z.; Tiwari, M. K. All-Organic Superhydrophobic Coatings with Mechanochemical Robustness and Liquid Impalement Resistance. *Nat. Mater.* **2018**, *17* (4), 355–360.

(200) Braet, F.; De Zanger, R.; Wisse, E. Drying Cells for SEM, AFM and TEM by Hexamethyldisilazane: A Study on Hepatic Endothelial Cells. *J. Microsc.* **1997**, *186* (1), 84–87.

(201) Savin, H.; Repo, P.; von Gastrow, G.; Ortega, P.; Calle, E.; Garín, M.; Alcubilla, R. Black Silicon Solar Cells with Interdigitated Back-Contacts Achieve 22.1% Efficiency. *Nat. Nanotechnol.* **2015**, *10* (7), 624–628.

(202) Fukata, N.; Subramani, T.; Jevasuwan, W.; Dutta, M.; Bando, Y. Functionalization of Silicon Nanostructures for Energy-Related Applications. *Small* **2017**, *13* (45), 1701713.

(203) Elyamny, S.; Dimaggio, E.; Magagna, S.; Narducci, D.; Pennelli, G. High Power Thermoelectric Generator Based on Vertical Silicon Nanowires. *Nano Lett.* **2020**, *20* (7), 4748–4753.

(204) Li, T.; Wu, K.; Rindzevicius, T.; Wang, Z.; Schulte, L.; Schmidt, M. S.; Boisen, A.; Ndoni, S. Wafer-Scale Nanopillars Derived from Block Copolymer Lithography for Surface-Enhanced Raman Spectroscopy. *ACS Appl. Mater. Interfaces* **2016**, *8* (24), 15668–15675.

(205) Laney, S. K.; Michalska, M.; Li, T.; Ramirez, F. V; Portnoi, M.; Oh, J.; Thayne, I. G.; Parkin, I. P.; Tiwari, M. K.; Papakonstantinou, I. Delayed Lubricant Depletion of Slippery Liquid Infused Porous Surfaces Using Precision Nanostructures. *Langmuir* **2021**, acs.langmuir.1c01310.

(206) Darling, S. B. Directing the Self-Assembly of Block Copolymers. *Prog. Polym. Sci.* **2007**, *32* (10), 1152–1204.

(207) Black, C. T.; Guarini, K. W.; Ruiz, R.; Sikorski, E. M.; Babich, I. V.; Sandstrom, R. L.; Zhang, Y. Polymer Self Assembly in Semiconductor Microelectronics. In *2006 International Electron Devices Meeting*; IEEE, **2006**; Vol. 51, pp 1–4.

(208) Michalska, M.; Laney, S. K.; Li, T.; Portnoi, M.; Mordan, N.; Allan, E.; Tiwari, M. K.; Parkin, I. P.; Papakonstantinou, I. Bioinspired Multifunctional Glass Surfaces Through Regenerative Secondary Mask Lithography. *Adv. Mater.* **2021**, 1–26.

(209) Choi, C.-H.; Kim, C.-J. Fabrication of a Dense Array of Tall Nanostructures over a Large Sample Area with Sidewall Profile and Tip Sharpness Control. *Nanotechnology* **2006**, *17* (21), 5326–5333.

(210) Telecka, A.; Li, T.; Ndoni, S.; Taboryski, R. Nanotextured Si Surfaces Derived from Block-

Copolymer Self-Assembly with Superhydrophobic, Superhydrophilic, or Superamphiphobic Properties. *RSC Adv.* **2018**, *8* (8), 4204–4213.

(211) Linklater, D. P.; Juodkazis, S.; Crawford, R. J.; Ivanova, E. P. Mechanical Inactivation of Staphylococcus Aureus and Pseudomonas Aeruginosa by Titanium Substrata with Hierarchical Surface Structures. *Materialia* **2019**, *5* (October 2018), 100197.

(212) Wang, L.; McCarthy, T. J. Covalently Attached Liquids: Instant Omniphobic Surfaces with Unprecedented Repellency. *Angew. Chemie Int. Ed.* **2016**, *55* (1), 244–248.

(213) Watson, G. S.; Gellender, M.; Watson, J. A. Self-Propulsion of Dew Drops on Lotus Leaves: A Potential Mechanism for Self Cleaning. *Biofouling* **2014**, *30* (4), 427–434.

(214) Watson, G. S.; Schwarzkopf, L.; Cribb, B. W.; Myhra, S.; Gellender, M.; Watson, J. A. Removal Mechanisms of Dew via Self-Propulsion off the Gecko Skin. *J. R. Soc. Interface* **2015**, *12* (105).

(215) Boreyko, J. B.; Zhao, Y.; Chen, C. H. Planar Jumping-Drop Thermal Diodes. *Appl. Phys. Lett.* **2011**, *99* (23), 1–3.

(216) Zhang, Q.; He, M.; Chen, J.; Wang, J.; Song, Y.; Jiang, L. Anti-Icing Surfaces Based on Enhanced Self-Propelled Jumping of Condensed Water Microdroplets. *Chem. Commun.* **2013**, *49* (40), 4516–4518.

(217) Boreyko, J. B.; Collier, C. P. Delayed Frost Growth on Jumping-Drop Superhydrophobic Surfaces. *ACS Nano* **2013**, *7* (2), 1618–1627.

(218) Boreyko, J. B.; Chen, C. H. Vapor Chambers with Jumping-Drop Liquid Return from Superhydrophobic Condensers. *Int. J. Heat Mass Transf.* **2013**, *61* (1), 409–418.

(219) Miljkovic, N.; Preston, D. J.; Enright, R.; Wang, E. N. Electrostatic Charging of Jumping Droplets. *Nat. Commun.* **2013**, *4*, 1–9.

(220) Zhang, K.; Liu, F.; Williams, A. J.; Qu, X.; Feng, J. J.; Chen, C. H. Self-Propelled Droplet Removal from Hydrophobic Fiber-Based Coalescers. *Phys. Rev. Lett.* **2015**, *115* (7), 074502.

(221) Rykaczewski, K. Microdroplet Growth Mechanism during Water Condensation on Superhydrophobic Surfaces. *Langmuir* **2012**, *28* (20), 7720–7729.

(222) Rykaczewski, K.; Paxson, A. T.; Anand, S.; Chen, X.; Wang, Z.; Varanasi, K. K. Multimode Multidrop Serial Coalescence Effects during Condensation on Hierarchical Superhydrophobic Surfaces. *Langmuir* **2013**, *29* (3), 881–891.

(223) Enright, R.; Miljkovic, N.; Al-Obeidi, A.; Thompson, C. V; Wang, E. N. Condensation on Superhydrophobic Surfaces: The Role of Local Energy Barriers and Structure Length Scale. *Langmuir* **2012**, *28* (40), 14424–14432.

(224) Xu, W.; Lan, Z.; Peng, B.; Wen, R.; Ma, X. Heterogeneous Nucleation Capability of Conical Microstructures for Water Droplets. *RSC Adv.* **2015**, *5* (2), 812–818.

(225) Xu, W.; Lan, Z.; Peng, B. L.; Wen, R. F.; Ma, X. H. Effect of Nano Structures on the Nucleus Wetting Modes during Water Vapour Condensation: From Individual Groove to Nano-Array Surface. *RSC Adv.* **2016**, *6* (10), 7923–7932.

(226) Zhang, B.; Chen, X.; Dobnikar, J.; Wang, Z.; Zhang, X. Spontaneous Wenzel to Cassie Dewetting Transition on Structured Surfaces. *Phys. Rev. Fluids* **2016**, *1* (7), 1–11.

(227) Wen, R.; Lan, Z.; Peng, B.; Xu, W.; Yang, R.; Ma, X. Wetting Transition of Condensed Droplets on Nanostructured Superhydrophobic Surfaces: Coordination of Surface Properties and Condensing Conditions. *ACS Appl. Mater. Interfaces* **2017**, *9* (15), 13770–13777.

(228) Rykaczewski, K.; Scott, J. H. J.; Fedorov, A. G. Electron Beam Heating Effects during Environmental Scanning Electron Microscopy Imaging of Water Condensation on Superhydrophobic Surfaces. *Appl. Phys. Lett.* **2011**, *98* (9), 1–3.

(229) Rykaczewski, K.; Scott, J. H. J. Methodology for Imaging Nano-to-Microscale Water Condensation Dynamics on Complex Nanostructures. In *ACS Nano*; **2011**; Vol. 5, pp 5962–5968.

(230) Bozso, F.; Avouris, P. Thermal and Electron-Beam-Induced Reaction of Disilane on Si(100)-(2×1). *Phys. Rev. B* **1988**, *38* (6), 3943–3947.

(231) Aronov, D.; Rosenman, G.; Barkay, Z. Wettability Study of Modified Silicon Dioxide Surface Using Environmental Scanning Electron Microscopy. *J. Appl. Phys.* **2007**, *101* (8), 1–5.

(232) Aronov, D.; Molotskii, M.; Rosenman, G. Electron-Induced Wettability Modification. *Phys. Rev. B - Condens. Matter Mater. Phys.* **2007**, *76* (3), 1–12.

(233) Royall, C. P.; Thiel, B. L.; Donald, A. M. Radiation Damage of Water in Environmental Scanning Electron Microscopy. *J. Microsc.* **2001**, *204* (3), 185–195.

(234) Miljkovic, N.; Enright, R.; Wang, E. N. Effect of Droplet Morphology on Growth Dynamics and Heat Transfer during Condensation on Superhydrophobic Nanostructured Surfaces. *ACS Nano* **2012**, *6* (2), 1776–1785.

(235) Rykaczewski, K.; Osborn, W. A.; Chinn, J.; Walker, M. L.; Scott, J. H. J.; Jones, W.; Hao, C.; Yao, S.; Wang, Z. How Nanorough Is Rough Enough to Make a Surface Superhydrophobic during Water Condensation? *Soft Matter* **2012**, *8* (33), 8786–8794.

(236) Bird, J. C.; Dhiman, R.; Kwon, H.-M.; Varanasi, K. K. Reducing the Contact Time of a Bouncing Drop. *Nature* **2013**, *503* (7476), 385–388.

(237) Gauthier, A.; Symon, S.; Clanet, C.; Quéré, D. Water Impacting on Superhydrophobic Macrotextures. *Nat. Commun.* **2015**, *6*, 8001.

(238) Liu, Y.; Moevius, L.; Xu, X.; Qian, T.; Yeomans, J. M.; Wang, Z. Pancake Bouncing on Superhydrophobic Surfaces. *Nat. Phys.* **2014**, *10* (7), 515–519.

(239) Checco, A.; Ocko, B. M.; Rahman, A.; Black, C. T.; Tasinkevych, M.; Giacomello, A.; Dietrich, S. Collapse and Reversibility of the Superhydrophobic State on Nanotextured Surfaces. *Phys. Rev. Lett.* **2014**, *112* (21).

(240) D'Urso, B.; Simpson, J. T.; Kalyanaraman, M. Emergence of Superhydrophobic Behavior on Vertically Aligned Nanocone Arrays. *Appl. Phys. Lett.* **2007**, *90* (4), 1–3.

(241) Lobaton, E. J.; Salamon, T. R. Computation of Constant Mean Curvature Surfaces: Application to the Gas-Liquid Interface of a Pressurized Fluid on a Superhydrophobic Surface. *J. Colloid Interface Sci.* **2007**, *314* (1), 184–198.

(242) Dorrer, C.; Rühe, J. Wetting of Silicon Nanograss: From Superhydrophilic to Superhydrophobic Surfaces. *Adv. Mater.* **2008**, *20* (1), 159–163.

(243) Schneider, L.; Laustsen, M.; Mandsberg, N.; Taboryski, R. The Influence of Structure Heights and Opening Angles of Micro-and Nanocones on the Macroscopic Surface Wetting Properties. *Sci. Rep.* **2016**, *6* (February), 1–9.

(244) Liu, C.; Gillette, E. I.; Chen, X.; Pearse, A. J.; Kozen, A. C.; Schroeder, M. A.; Gregorczyk, K. E.; Lee, S. B.; Rubloff, G. W. An All-in-One Nanopore Battery Array. *Nat. Nanotechnol.* **2014**, *9* (12), 1031–1039.

(245) Wallentin, J.; Anttu, N.; Asoli, D.; Huffman, M.; Aberg, I.; Magnusson, M. H.; Siefer, G.; Fuss-Kailuweit, P.; Dimroth, F.; Witzigmann, B.; Xu, H. Q.; Samuelson, L.; Deppert, K.; Borgstrom, M. T. InP Nanowire Array Solar Cells Achieving 13.8% Efficiency by Exceeding the Ray Optics Limit. *Science (80-.).* **2013**, *339* (6123), 1057–1060.

(246) Gibson, S. J.; van Kasteren, B.; Tekcan, B.; Cui, Y.; van Dam, D.; Haverkort, J. E. M. M.; Bakkers, E. P. A. M. A. M.; Reimer, M. E. Tapered InP Nanowire Arrays for Efficient Broadband High-Speed Single-Photon Detection. *Nat. Nanotechnol.* **2019**, *14* (5), 473–479.

(247) Chu, K.-H.; Xiao, R.; Wang, E. N. Uni-Directional Liquid Spreading on Asymmetric Nanostructured Surfaces. *Nat. Mater.* **2010**, *9* (5), 413–417.

(248) Wen, L.; Xu, R.; Mi, Y.; Lei, Y. Multiple Nanostructures Based on Anodized Aluminium Oxide Templates. *Nat. Nanotechnol.* **2017**, *12* (3), 244–250.

(249) Das Gupta, T.; Martin-Monier, L.; Yan, W.; Le Bris, A.; Nguyen-Dang, T.; Page, A. G.; Ho, K.-T.; Yesilköy, F.; Altug, H.; Qu, Y.; Sorin, F. Self-Assembly of Nanostructured Glass Metasurfaces via Templated Fluid Instabilities. *Nat. Nanotechnol.* **2019**, *14* (4), 320–327.

(250) Kuznetsov, A. I.; Miroshnichenko, A. E.; Brongersma, M. L.; Kivshar, Y. S.; Luk'yanchuk, B. Optically Resonant Dielectric Nanostructures. *Science (80-.).* **2016**, *354* (6314), aag2472.

(251) Jeong, H.; Song, H.; Pak, Y.; Kwon, I. K.; Jo, K.; Lee, H.; Jung, G. Y. Enhanced Light Absorption of Silicon Nanotube Arrays for Organic/Inorganic Hybrid Solar Cells. *Adv. Mater.* **2014**, *26* (21), 3445–3450.

(252) Song, T.; Xia, J.; Lee, J.-H.; Lee, D. H.; Kwon, M.-S.; Choi, J.-M.; Wu, J.; Doo, S. K.;

Chang, H.; Park, W. Il; Zang, D. S.; Kim, H.; Huang, Y.; Hwang, K.-C.; Rogers, J. A.; Paik, U. Arrays of Sealed Silicon Nanotubes As Anodes for Lithium Ion Batteries. *Nano Lett.* **2010**, *10* (5), 1710–1716.

(253) Park, M.-H.; Kim, M. G.; Joo, J.; Kim, K.; Kim, J.; Ahn, S.; Cui, Y.; Cho, J. Silicon Nanotube Battery Anodes. *Nano Lett.* **2009**, *9* (11), 3844–3847.

(254) Wang, M.; Ioccozia, J.; Sun, L.; Lin, C.; Lin, Z. Inorganic-Modified Semiconductor TiO 2 Nanotube Arrays for Photocatalysis. *Energy Environ. Sci.* **2014**, *7* (7), 2182–2202.

(255) Fan, R.; Wu, Y.; Li, D.; Yue, M.; Majumdar, A.; Yang, P. Fabrication of Silica Nanotube Arrays from Vertical Silicon Nanowire Templates. *J. Am. Chem. Soc.* **2003**, *125* (18), 5254–5255.

(256) La Rocca, R.; Messina, G. C.; Dipalo, M.; Shalabaeva, V.; De Angelis, F. Out-of-Plane Plasmonic Antennas for Raman Analysis in Living Cells. *Small* **2015**, *11* (36), 4632–4637.

(257) Messina, G. C.; Dipalo, M.; La Rocca, R.; Zilio, P.; Caprettini, V.; Proietti Zaccaria, R.; Toma, A.; Tantussi, F.; Berdondini, L.; De Angelis, F. Spatially, Temporally, and Quantitatively Controlled Delivery of Broad Range of Molecules into Selected Cells through Plasmonic Nanotubes. *Adv. Mater.* **2015**, *27* (44), 7145–7149.

(258) Chen, J.-K.; Chen, W.-T.; Cheng, C.-C.; Yu, C.-C.; Chu, J. P. Metallic Glass Nanotube Arrays: Preparation and Surface Characterizations. *Mater. Today* **2018**, *21* (2), 178–185.

(259) Li, J.; Liu, W.; Wang, J.; Rozen, I.; He, S.; Chen, C.; Kim, H. G.; Lee, H.-J.; Lee, H.-B.-R.; Kwon, S.-H.; Li, T.; Li, L.; Wang, J.; Mei, Y. Nanoconfined Atomic Layer Deposition of TiO 2 /Pt Nanotubes: Toward Ultrasmall Highly Efficient Catalytic Nanorockets. *Adv. Funct. Mater.* **2017**, *27* (24), 1700598.

(260) Heo, C.-J.; Kim, S.-H.; Jang, S. G.; Lee, S. Y.; Yang, S.-M. Gold "Nanograils" with Tunable Dipolar Multiple Plasmon Resonances. *Adv. Mater.* **2009**, *21* (17), 1726–1731.

(261) Zhang, J.; Li, Y.; Zhang, X.; Yang, B. Colloidal Self-Assembly Meets Nanofabrication: From Two-Dimensional Colloidal Crystals to Nanostructure Arrays. *Adv. Mater.* **2010**, *22* (38), 4249–4269.

(262) Davis, A. L.; Nijhout, H. F.; Johnsen, S. Diverse Nanostructures Underlie Thin Ultra-Black Scales in Butterflies. *Nat. Commun.* **2020**, *11* (1), 1294.

(263) De Angelis, F.; Malerba, M.; Patrini, M.; Miele, E.; Das, G.; Toma, A.; Zaccaria, R. P.; Di Fabrizio, E. 3D Hollow Nanostructures as Building Blocks for Multifunctional Plasmonics. *Nano Lett.* **2013**, *13* (8), 3553–3558.

(264) Mackus, A. J. M.; Bol, A. A.; Kessels, W. M. M. The Use of Atomic Layer Deposition in Advanced Nanopatterning. *Nanoscale* **2014**, *6* (19), 10941–10960.

(265) Dallorto, S.; Staaks, D.; Schwartzberg, A.; Yang, X.; Lee, K. Y.; Rangelow, I. W.; Cabrini, S.; Olynick, D. L. Atomic Layer Deposition for Spacer Defined Double Patterning of Sub-10 Nm Titanium Dioxide Features. *Nanotechnology* **2018**, *29* (40), 405302.

(266) Liu, C.-C.; Franke, E.; Mignot, Y.; Xie, R.; Yeung, C. W.; Zhang, J.; Chi, C.; Zhang, C.; Farrell, R.; Lai, K.; Tsai, H.; Felix, N.; Corliss, D. Directed Self-Assembly of Block Copolymers for 7 Nanometre FinFET Technology and Beyond. *Nat. Electron.* **2018**, *1* (10), 562–569.

(267) Moon, H.-S.; Kim, J. Y.; Jin, H. M.; Lee, W. J.; Choi, H. J.; Mun, J. H.; Choi, Y. J.; Cha, S. K.; Kwon, S. H.; Kim, S. O. Atomic Layer Deposition Assisted Pattern Multiplication of Block Copolymer Lithography for 5 Nm Scale Nanopatterning. *Adv. Funct. Mater.* **2014**, *24* (27), 4343–4348.

(268) Wan, Z.; Lee, H. J.; Kim, H. G.; Jo, G. C.; Park, W. I.; Ryu, S. W.; Lee, H.-B.-R.; Kwon, S.-H. Circular Double-Patterning Lithography Using a Block Copolymer Template and Atomic Layer Deposition. *Adv. Mater. Interfaces* **2018**, *5* (16), 1800054.

(269) Henry, M. D.; Walavalkar, S.; Homyk, A.; Scherer, A. Alumina Etch Masks for Fabrication of High-Aspect-Ratio Silicon Micropillars and Nanopillars. *Nanotechnology* **2009**, *20* (25), 255305.

(270) Williams, K. R.; Gupta, K.; Wasilik, M. Etch Rates for Micromachining Processing - Part II. *J. Microelectromechanical Syst.* **2003**, *12* (6), 761–778.

(271) Norasetthekul, S.; Park, P. Y.; Baik, K. H.; Lee, K. P.; Shin, J. H.; Jeong, B. S.; Shishodia, V.; Lambers, E. S.; Norton, D. P.; Pearton, S. J. Dry Etch Chemistries for TiO2 Thin Films. *Appl. Surf. Sci.* **2001**, *185* (1–2), 27–33.

(272) Shkondin, E.; Takayama, O.; Lindhard, J. M.; Larsen, P. V.; Mar, M. D.; Jensen, F.; Lavrinenko, A. V. Fabrication of High Aspect Ratio TiO 2 and Al 2 O 3 Nanogratings by Atomic Layer Deposition. *J. Vac. Sci. Technol. A Vacuum, Surfaces, Film.* **2016**, *34* (3), 031605.

(273) Chung, C.-K. Geometrical Pattern Effect on Silicon Deep Etching by an Inductively Coupled Plasma System. *J. Micromechanics Microengineering* **2004**, *14* (4), 656–662.

(274) Wu, B.; Kumar, A.; Pamarthy, S. High Aspect Ratio Silicon Etch: A Review. *J. Appl. Phys.* **2010**, *108* (5), 051101.

(275) Ashkin, A.; Dziedzic, J. M.; Bjorkholm, J. E.; Chu, S. Observation of a Single-Beam Gradient Force Optical Trap for Dielectric Particles. *Opt. Angular Momentum* **1986**, *11* (5), 288.

(276) Neuman, K. C.; Block, S. M. Optical Trapping. *Rev. Sci. Instrum.* **2004**, *75* (9), 2787–2809.

(277) Saleh, A. A. E.; Dionne, J. A. Toward Efficient Optical Trapping of Sub-10-Nm Particles with Coaxial Plasmonic Apertures. *Nano Lett.* **2012**, *12* (11), 5581–5586.

(278) Yoo, D.; Gurunatha, K. L.; Choi, H. K.; Mohr, D. A.; Ertsgaard, C. T.; Gordon, R.; Oh, S. H. Low-Power Optical Trapping of Nanoparticles and Proteins with Resonant Coaxial Nanoaperture Using 10 Nm Gap. *Nano Lett.* **2018**, *18* (6), 3637–3642.

(279) Miyazaki, H. T.; Kurokawa, Y. Squeezing Visible Light Waves into a 3-Nm-Thick and 55-

Nm-Long Plasmon Cavity. *Phys. Rev. Lett.* **2006**, *96* (9).

(280) Nagpal, P.; Lindquist, N. C.; Oh, S.-H.; Norris, D. J. Ultrasmooth Patterned Metals for Plasmonics and Metamaterials. *Science (80-.).* **2009**, *325* (5940), 594–597.

(281) Zhu, J.; Yu, Z.; Burkhard, G. F.; Hsu, C.-M.; Connor, S. T.; Xu, Y.; Wang, Q.; McGehee, M.; Fan, S.; Cui, Y. Optical Absorption Enhancement in Amorphous Silicon Nanowire and Nanocone Arrays. *Nano Lett.* **2009**, *9* (1), 279–282.

(282) Boden, S. A.; Bagnall, D. M. Tunable Reflection Minima of Nanostructured Antireflective Surfaces. *Appl. Phys. Lett.* **2008**, *93* (13), 133108.

(283) Garnett, E.; Yang, P. Light Trapping in Silicon Nanowire Solar Cells. *Nano Lett.* **2010**, *10* (3), 1082–1087.

(284) Huang, Y.-F.; Chattopadhyay, S.; Jen, Y.-J.; Peng, C.-Y.; Liu, T.-A.; Hsu, Y.-K.; Pan, C.-L.; Lo, H.-C.; Hsu, C.-H.; Chang, Y.-H.; Lee, C.-S.; Chen, K.-H.; Chen, L.-C. Improved Broadband and Quasi-Omnidirectional Anti-Reflection Properties with Biomimetic Silicon Nanostructures. *Nat. Nanotechnol.* **2007**, *2* (12), 770–774.

(285) Huang, Y. F.; Chattopadhyay, S.; Jen, Y. J.; Peng, C. Y.; Liu, T. A.; Hsu, Y. K.; Pan, C. L.; Lo, H. C.; Hsu, C. H.; Chang, Y. H.; Lee, C. S.; Chen, K. H.; Chen, L. C. Improved Broadband and Quasi-Omnidirectional Anti-Reflection Properties with Biomimetic Silicon Nanostructures. *Nat. Nanotechnol.* **2007**, *2* (12), 770–774.

(286) Yang, J.; Luo, F.; Kao, T. S.; Li, X.; Ho, G. W.; Teng, J.; Luo, X.; Hong, M. Design and Fabrication of Broadband Ultralow Reflectivity Black Si Surfaces by Laser Micro/Nanoprocessing. *Light Sci. Appl.* **2014**, *3* (7), e185–e185.

(287) Fan, Z.; Kapadia, R.; Leu, P. W.; Zhang, X.; Chueh, Y. L.; Takei, K.; Yu, K.; Jamshidi, A.; Rathore, A. A.; Ruebusch, D. J.; Wu, M.; Javey, A. Ordered Arrays of Dual-Diameter Nanopillars for Maximized Optical Absorption. *Nano Lett.* **2010**, *10* (10), 3823–3827.

(288) Choi, S.-J.; Yoo, P. J.; Baek, S. J.; Kim, T. W.; Lee, H. H. An Ultraviolet-Curable Mold for Sub-100-Nm Lithography. *J. Am. Chem. Soc.* **2004**, *126* (25), 7744–7745.

(289) Wang, L.; McCarthy, T. J. Covalently Attached Liquids: Instant Omniphobic Surfaces with Unprecedented Repellency. *Angew. Chemie Int. Ed.* **2016**, *55* (1), 244–248.

(290) Liu, V.; Fan, S. S4 : A Free Electromagnetic Solver for Layered Periodic Structures. *Comput. Phys. Commun.* **2012**, *183* (10), 2233–2244.

(291) Green, M. A. Self-Consistent Optical Parameters of Intrinsic Silicon at 300K Including Temperature Coefficients. *Sol. Energy Mater. Sol. Cells* **2008**, *92* (11), 1305–1310.

(292) Sun, T.; Feng, L.; Gao, X.; Jiang, L. Bioinspired Surfaces with Special Wettability. *Acc. Chem. Res.* **2005**, *38* (8), 644–652.

(293) Blossey, R. Self-Cleaning Surfaces - Virtual Realities. *Nat. Mater.* **2003**, *2* (5), 301–306.

(294) Lafuma, A.; Quéré, D. Superhydrophobic States. *Nat. Mater.* **2003**, *2* (7), 457–460.

(295) Peppou-Chapman, S.; Hong, J. K.; Waterhouse, A.; Neto, C. Life and Death of Liquid-Infused Surfaces: A Review on the Choice, Analysis and Fate of the Infused Liquid Layer. *Chem. Soc. Rev.* **2020**, *49* (11), 3688–3715.

(296) De Gennes, Pierre-Gilles, Françoise Brochard-Wyart, D. Q. *Capillarity and Wetting Phenomena: Drops, Bubbles, Pearls, Waves.*; **2013**.

(297) Kim, P.; Kreder, M. J.; Alvarenga, J.; Aizenberg, J. Hierarchical or Not? Effect of the Length Scale and Hierarchy of the Surface Roughness on Omniphobicity of Lubricant-Infused Substrates. *Nano Lett.* **2013**, *13* (4), 1793–1799.

(298) Vogel, N.; Belisle, R. A.; Hatton, B.; Wong, T.-S.; Aizenberg, J. Transparency and Damage Tolerance of Patternable Omniphobic Lubricated Surfaces Based on Inverse Colloidal Monolayers. *Nat. Commun.* **2013**, *4* (1), 2176.

(299) Wong, W. S. Y.; Hegner, K. I.; Donadei, V.; Hauer, L.; Naga, A.; Vollmer, D. Capillary Balancing: Designing Frost-Resistant Lubricant-Infused Surfaces. *Nano Lett.* **2020**, *20* (12), 8508–8515.

(300) Lee, J.; Jiang, Y.; Hizal, F.; Ban, G. H.; Jun, S.; Choi, C. H. Durable Omniphobicity of Oil-Impregnated Anodic Aluminum Oxide Nanostructured Surfaces. *J. Colloid Interface Sci.* **2019**, *553*, 734–745.

(301) Cui, J.; Zhu, H.; Tu, Z.; Niu, D.; Liu, G.; Bei, Y.; Zhu, Q. Effect of the Texture Geometry on the Slippery Behavior of Liquid-Infused Nanoporous Surfaces. *J. Mater. Sci.* **2019**, *54* (3), 2729–2739.

(302) Chen, X.; Wen, G.; Guo, Z. What Are the Design Principles, from the Choice of Lubricants and Structures to the Preparation Method, for a Stable Slippery Lubricant-Infused Porous Surface? *Mater. Horizons* **2020**, *7* (7), 1697–1726.

(303) Sett, S.; Yan, X.; Barac, G.; Bolton, L. W.; Miljkovic, N. Lubricant-Infused Surfaces for Low-Surface-Tension Fluids: Promise versus Reality. *ACS Appl. Mater. Interfaces* **2017**, *9* (41), 36400–36408.

(304) Al-Sharafi, A.; Yilbas, B. S.; Hassan, G. Droplet on Oil Impregnated Surface: Temperature and Velocity Fields. *Int. J. Therm. Sci.* **2019**, *146* (August), 106054.

(305) Lee, J.; Jiang, Y.; Hizal, F.; Ban, G.-H.; Jun, S.; Choi, C.-H. Durable Omniphobicity of Oil-Impregnated Anodic Aluminum Oxide Nanostructured Surfaces. *J. Colloid Interface Sci.* **2019**, *553*, 734–745.

(306) Weisensee, P. B.; Wang, Y.; Qian, H.; Schultz, D.; King, W. P.; Miljkovic, N. Condensate Droplet Size Distribution on Lubricant-Infused Surfaces. *Int. J. Heat Mass Transf.* **2017**, *109*, 187–199.

(307) Ma, C.; Nikiforov, A.; De Geyter, N.; Dai, X.; Morent, R.; Ostrikov, K. (Ken). Future Antiviral Polymers by Plasma Processing. *Prog. Polym. Sci.* **2021**, *118*, 101410.

Appendix

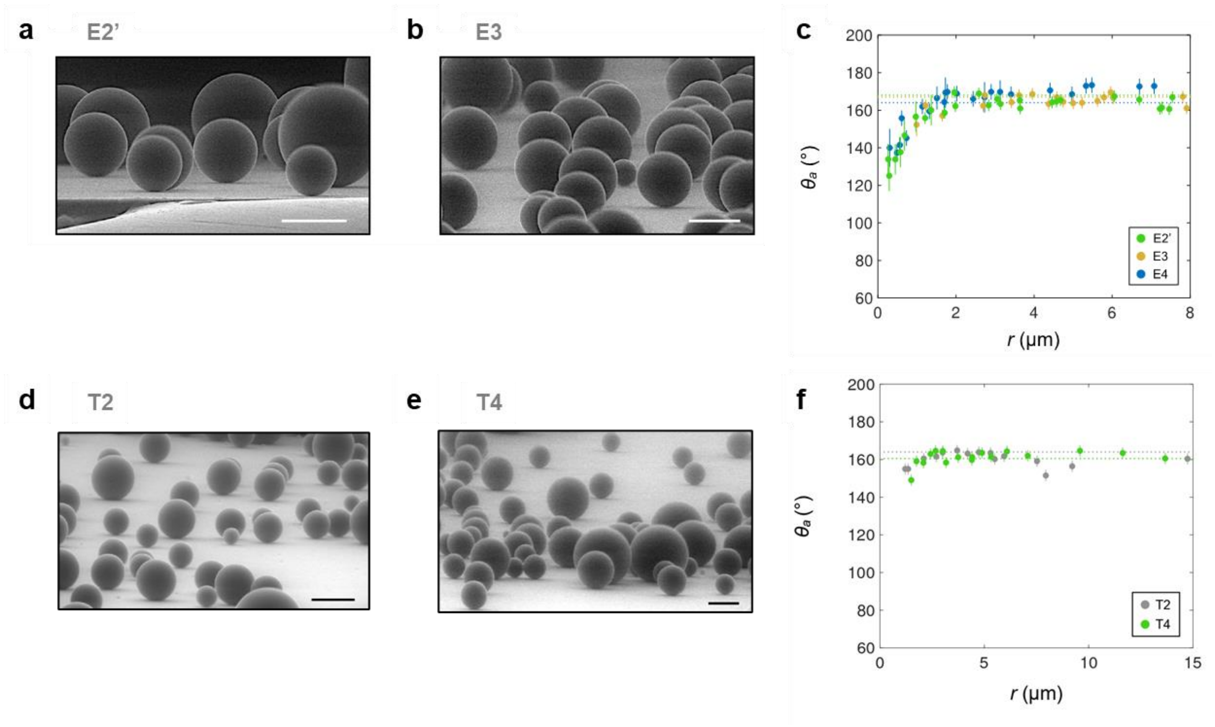

Figure S 1| ESEM images of water condensing on samples and plots of the corresponding contact angles of condensing microdroplets. **a,** sample E2'; **b,** sample E3; **d,** sample T2; **e,** sample T4. Scale bars indicate 10 µm. **c,** Advancing contact angle θ_a measured by ESEM imaging as a function of the droplet radius r for materials E2' (green dots), E3 (yellow dots) and E4 (blue dots). In all cases, the contact angle increases and saturates with r. For all three samples, data collapse on the same curve at small radii ($r < 2$ µm). At larger radii, data approach the contact angles of millimetric water drops drawn with dotted lines: $\theta_a = 168° \pm 3°$, $167° \pm 3°$ and $164° \pm 3°$ for E2', E3 and E4, respectively. **f,** Advancing contact angle θ_a as a function of the drop radius r for samples T2 and T4. θ_a increases towards the value measured on millimetric drops (dashed lines): $\theta_a = 164 \pm 1°$ and $160.5 \pm 1°$ for T2 and T4, respectively.

Supplementary Figures adapted from: Adapted from: P. Lecointre, S. K. Laney, M. Michalska, T. Li, *et al.*, Unique and robust dew repelllency of nanocones, **Nature Communications**, 2021, 12, 3458

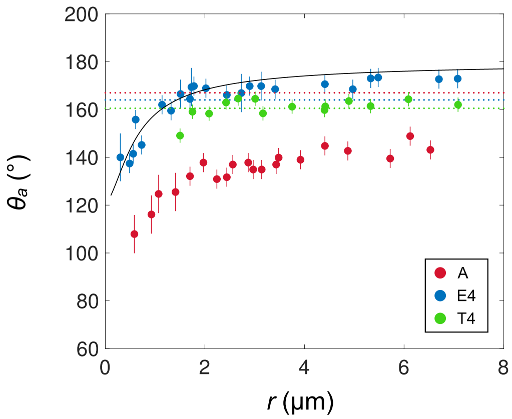

Figure S 2 | Contact angle of condensing microdroplets on nanostructures. Advancing contact angle θ_a measured by ESEM imaging as a function of the droplet radius *r* for materials A (nanocylinders, red dots), T4 (truncated nanocones, green dots) and E4 (nanocones, blue dots). In all cases, θ_a increases and saturates with *r*, but angles are systematically higher by about 20° and 30° on T4 and E4 than on A. Angles on A increase from 110° ± 5° to 140° ± 3° as *r* varies from 0.6 µm to 6 µm, on T4 from 150° ± 2° to 163° ± 2° as *r* varies from 2 µm to 7 µm, and on E4 from 140° ± 7° to 171° ± 3° as *r* varies from 0.3 µm to 7 µm. The solid line is the model for nanocones described in the text and in the SI (eqs. S1 and S2). We also report with dotted lines the contact angles obtained for millimetric water drops on A, T4 and E4, θ_a = 167° ± 3°, 160° ± 2° and 164° ± 3°, respectively. Interestingly, these angles are much larger for A and slightly smaller for T4 and E4 than the saturation value at microscale.

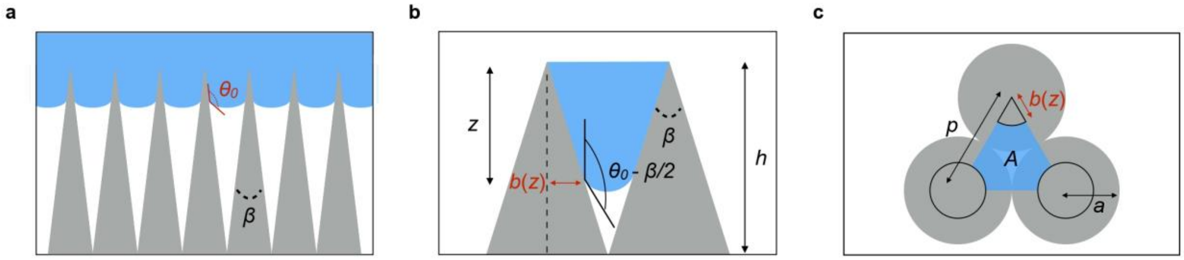

Figure S 3 | a, Cassie state for a drop resting on a dense array of cones. **b,** Side view of liquid inside the cones. The contact line sinks at a depth *z* and it makes an angle $\theta_0 - \beta/2$ with the vertical, denoting β as the cone angle and θ_0 as the Young contact angle. The radius of the cone at the contact line is denoted as *b*(*z*). **c,** Top view of an elementary triangular cell delimited by three cones. The liquid occupies an area *A*.

Supplementary Figures adapted from: Adapted from: P. Lecointre, S. K. Laney, M. Michalska, T. Li, *et al.*, Unique and robust dew repelllency of nanocones, **Nature Communications**, 2021, 12, 3458

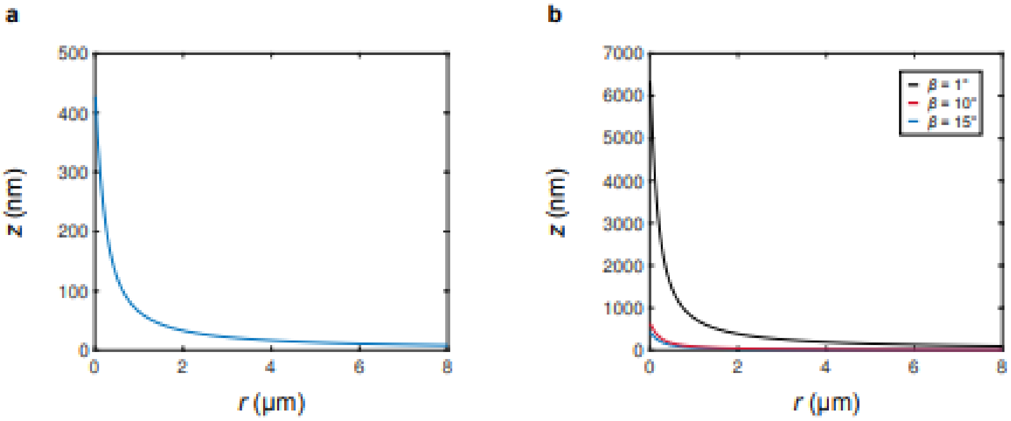

Figure S 4 | a. Sinking depth z for a drop of radius r in a Cassie state on an array of hydrophobic cones. The solid line is *Eq. 35* plotted for the parameters of sample E4 (p = 110 nm and h = 420 nm). The depth z decreases hyperbolically with the drop radius r. **b.** Sinking depth z for a drop of radius r for three values of cone angle β and using eq. (S1): β = 1° (black line), 10° (red line) and 15° (blue line). Sharper cones induce water penetration.

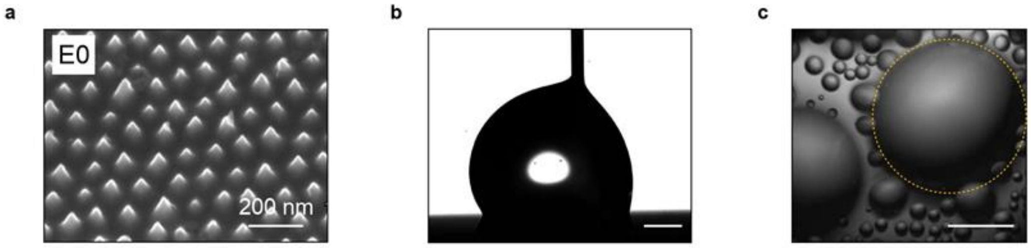

Figure S 5 | a, SEM images of the nanocones E0 with pitch p = 110 nm and reduced height h = 101 nm. They are arranged on a hexagonal array and coated in a hydrophobic layer. **b,** A water droplet on E0 exhibits simply a hydrophobic angle, in stark contrast with the other samples of family E. Water impregnates the texture and falls in the Wenzel state, owing to the large apex angle, $\beta = 57° \pm 2°$, smaller than the critical angle $\beta_c = 60°$ for cavity penetration. The scale bar indicates 500 μm**. c,** Breath figure on sample E0 under optical microscope after 25 min. The surface is largely covered by water and droplets are deformed (highlighted by the dotted circle). No jump is observed during 30 min. The scale bar indicates 100 μm.

Supplementary Figures adapted from: Adapted from: P. Lecointre, S. K. Laney, M. Michalska, T. Li, *et al.*, Unique and robust dew repelllency of nanocones, **Nature Communications**, 2021, 12, 3458

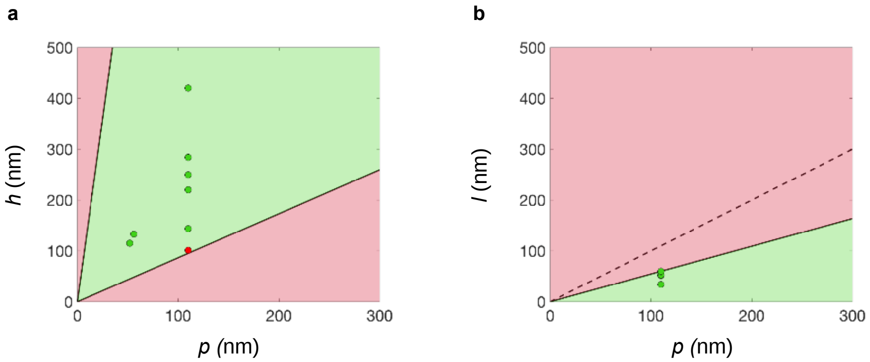

Figure S 6 | a, Phase diagram of antifogging on sharp nanocones. The two control parameters are the cone height *h* and the pitch *p*. The two limits are $h = p/2 \tan(\beta/2)$, where β is 4° and 60°. Observations (green and red symbols for jumping and non-jumping, respectively) with the 8 samples (extruded and homothetic families) are found to all agree with the model. **b,** Phase diagram of antifogging on truncated nanocones. The two control parameters are the cone top diameter *l* and the pitch *p*. The dotted line delimitates the limit $l = p$. The solid line shows the equation $p = (\boldsymbol{\pi/2\sqrt{3}\varphi_s})^{1/2}\, l$, where $\boldsymbol{\varphi_s}$ is the critical solid fraction (see eq. S2) for which the drop contact angle is equal to 150°. This line delimitates the frontier between antifogging (green) or not (red). Observations made at fixed *p* with four truncated cones (T family) all agree with the model.

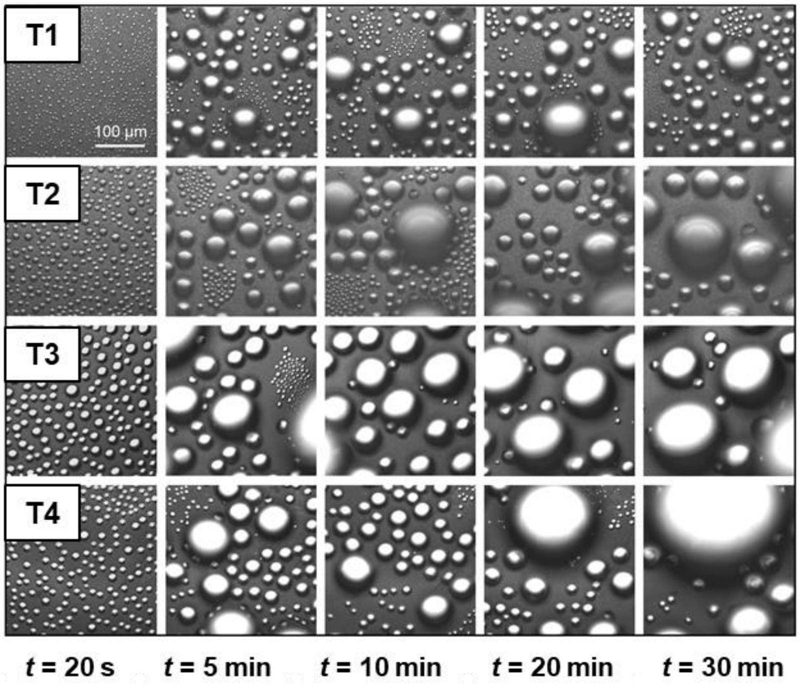

Supplementary Figures adapted from: Adapted from: P. Lecointre, S. K. Laney, M. Michalska, T. Li, *et al.*, Unique and robust dew repelllency of nanocones, **Nature Communications**, 2021, 12, 3458

Figure S 7 | Breath figures on the truncated family T (samples T1-T2-T3-T4) under optical microscope after 20 s, 5 min, 10 min, 20 min and 30 min. The room temperature is T = 21 ± 1°C, relative humidity RH = 52 ± 2% and sample temperature is T_S = 4 ± 1°C, which corresponds to S = 1.6 ± 0.2. A certain hierarchy seems to occur between the four samples, the more truncated, the more the sample is covered with water and sample T1 appears to be the most antifogging among the four samples.

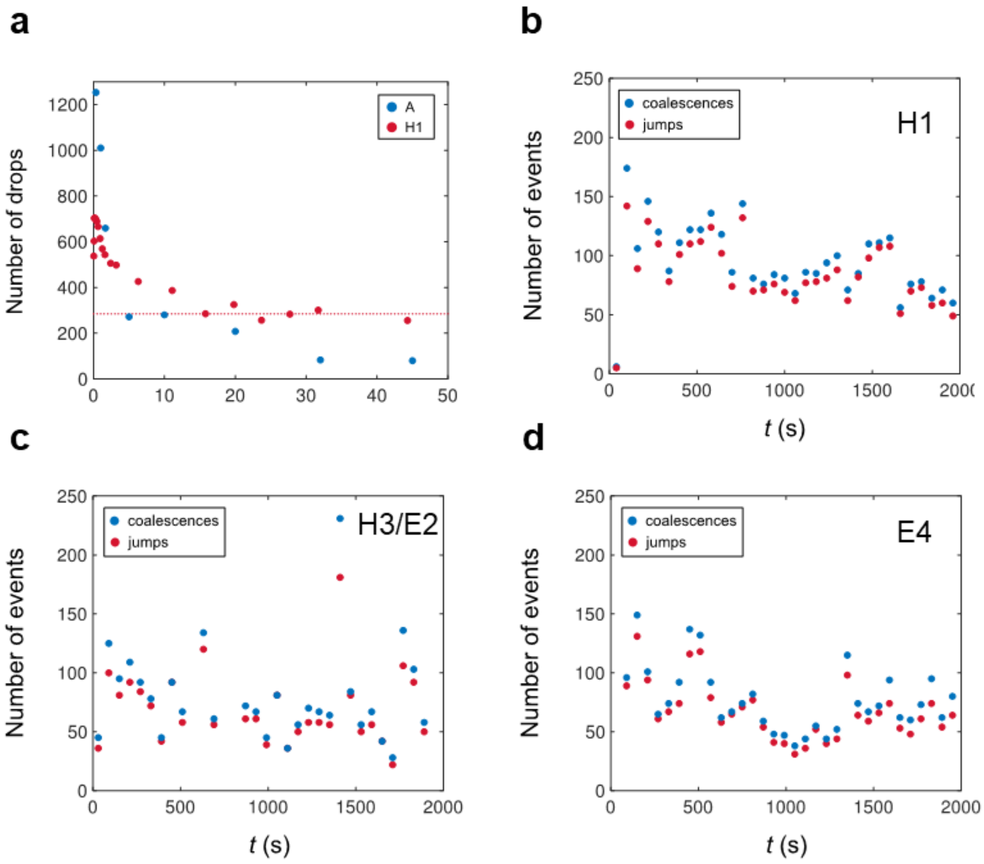

Figure S 8 | a, Absolute number of drops on sample H1 (red dots) and A (blue dots) as a function of time. For H1, the number first rises, then decreases until plateauing after 15 min; in contrast, it keeps decreasing on A. The red dotted line is a guide for the eye to mark the plateau obtained on sample H1. **b-d,** Absolute number of coalescences and jumps as a function of time *t* for materials decorated with nanocones. Each data point is obtained after measuring these numbers over 1 minute. For all samples, we successively observe an increase, a decrease and a stationary regime after ~500 s. More importantly, the two events strongly correlate, regardless of the amplitude of the observed fluctuations. **a,** Data on sample H1. **b,** Data on sample H3/E2. **c,** Data on sample E4.

Supplementary Figures adapted from: Adapted from: P. Lecointre, S. K. Laney, M. Michalska, T. Li, *et al.*, Unique and robust dew repelllency of nanocones, **Nature Communications**, 2021, 12, 3458

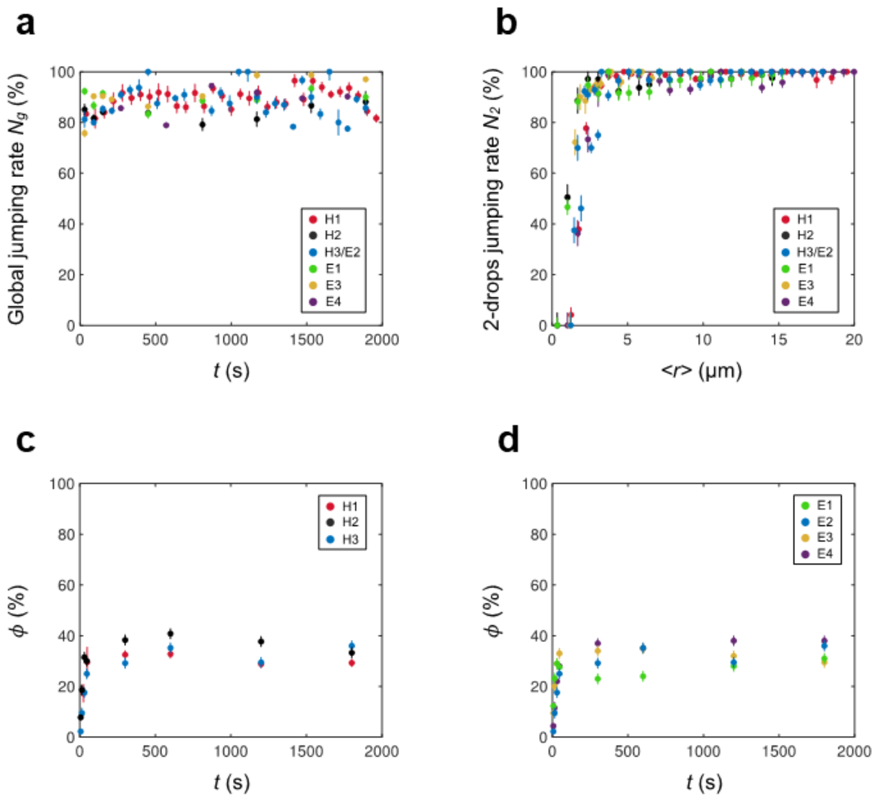

Figure S 9 | a, Global jumping rate N_g as a function of time t for all samples H and E. Each data point is obtained by averaging the proportion of jumps over one minute after considering all types of coalescences. N_g is roughly constant over time and it is ~90% for the three materials. **b,** Jumping rate N_2 for symmetric binary coalescences, where the drop radii do not differ by more than 20%. N_2 is plotted as a function of the average drop size $<r>$ for families H and E. In all cases, the jumping rate plateaus at 99 ± 1% above a critical radius $r_c \approx 1.5 \pm 0.4$ µm. **c,** Area fraction ϕ covered by liquid as a function of time t for samples H1-H3. **d,** Area fraction ϕ covered by liquid as a function of time t for samples E1-E4. In both cases, data are similar and no hierarchy can be established between the materials.

Supplementary Figures adapted from: Adapted from: P. Lecointre, S. K. Laney, M. Michalska, T. Li, *et al.*, Unique and robust dew repelllency of nanocones, **Nature Communications**, 2021, 12, 3458

***r* (µm)**	**[3.4 - 6.1[**		**[6.1 - 8.8[**		**[8.8 - 11.5[**		**[11.5 - 14.2[**		**[14.2 - 16.9[**		**[16.9 - 19.6[**		**[19.6 - 22.3[**		**[22.3 - 25[**	
	N jumps	*N* coal	*N* jumps	*N* coal	*N* jumps	*N* coal	*N* jumps	*N* coal	*N* jumps	*N* coal	*N* jumps	*N* coal	*N* jumps	*N* coal	*N* jumps	*N* coal
***n* = 3**	0	103	0	74	3	61	18	46	14	34	3	16	1	4	1	2
	0 %		0 %		5 %		39 %		41 %		19 %		25 %		50 %	
***n* = 4**	2	58	11	97	15	57	14	36	19	31	4	11	3	4	0	0
	3 %		11 %		26 %		39 %		61 %		36 %		75 %		N/A	
***n* = 5**	2	40	7	39	8	22	8	23	11	17	7	12	1	1	0	0
	2 %		18 %		36 %		35 %		65 %		58 %		100 %		N/A	

Table S 1 | Characteristics of the jumping rates N_n on sample T1. For each range of drop radii, we provide the number of coalescences and jumps for n = 3, 4 and 5 (where n is the number of drops involved in a multiple drop coalescence).

***r* (µm)**	**[3.4 - 6.1[**		**[6.1 - 8.8[**		**[8.8 - 11.5[**		**[11.5 - 14.2[**		**[14.2 - 16.9[**		**[16.9 - 19.6[**		**[19.6 - 22.3[**		**[22.3 - 25[**		**[25 - 27.7[**		**[27.7 - 30.4[**	
	N jumps	*N* coal	*N* jumps	*N* coal	*N* jumps	*N* coal	*N* jumps	*N* coal	*N* jumps	*N* coal	*N* jumps	*N* coal	*N* jumps	*N* coal	*N* jumps	*N* coal	*N* jumps	*N* coal	*N* jumps	*N* coal
***n* = 3**	0	110	0	51	0	46	0	34	0	43	0	26	0	20	1	6	0	11	1	4
	0 %		0 %		0 %		0 %		0 %		0 %		0 %		17 %		0 %		25 %	
***n* = 4**	0	62	0	39	0	22	1	36	4	15	4	13	2	9	2	5	4	8	0	0
	0 %		0 %		0 %		3 %		27 %		31 %		22 %		40 %		50 %		N/A	
***n* = 5**	0	40	0	21	0	16	0	9	1	9	2	7	3	7	1	2	2	5	2	3
	0 %		0 %		0 %		0 %		11 %		29 %		43 %		50 %		40 %		67 %	

Table S 2 | Characteristics of the jumping rates N_n on sample T4. For each range of drop radii, we provide the number of coalescences and jumps for n = 3, 4 and 5 (where n is the number of drops involved in a multiple drop coalescence).

Supplementary Figures adapted from: Adapted from: P. Lecointre, S. K. Laney, M. Michalska, T. Li, *et al.*, Unique and robust dew repelllency of nanocones, **Nature Communications**, 2021, 12, 3458

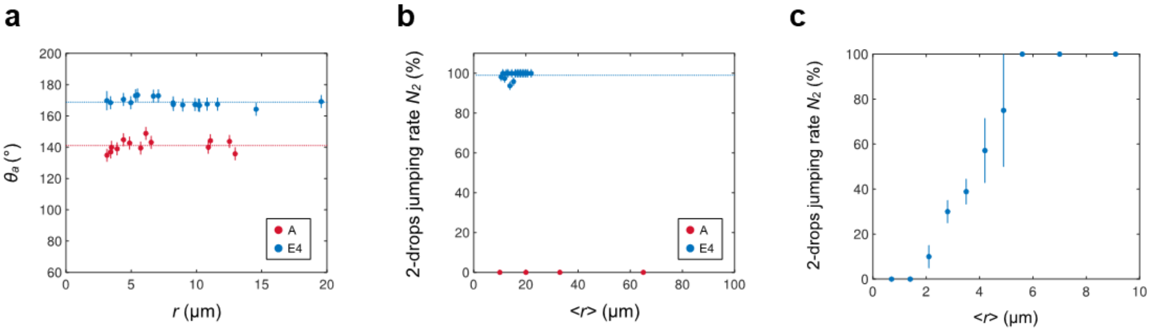

Figure S 10 | a, Advancing contact angle θ_a measured by ESEM as a function of the droplet radius *r* for samples A (nanopillars, red dots) and E4 (nanocones, blue dots), for *r* ranging from 3 to 20 µm. In both cases, the contact angle plateaus with *r* (dotted lines), at $\theta_a = 141° \pm 6°$ for A and 169° ± 6° for E4, respectively. **b,** Jumping rate N_2 for symmetric binary coalescences as a function of the average drop size <*r*> for nanopillars A and nanocones E4. The radius of jumping droplets does not exceed 25 µm on sample E4 because of the high antifogging efficiency. In contrast, it can reach 65 µm on A with no jumping, independently of <*r*>. **c,** Jumping rate N_2 for symmetric binary coalescences as a function of the average drop size <*r*>, for condensation on nanoneedles (height of 600 nm, interpillar distance of 300 nm, aspect ratio of 6). Contrasting with observations on short nanopillars, drops can jump if their radius is larger than typically 5 µm.

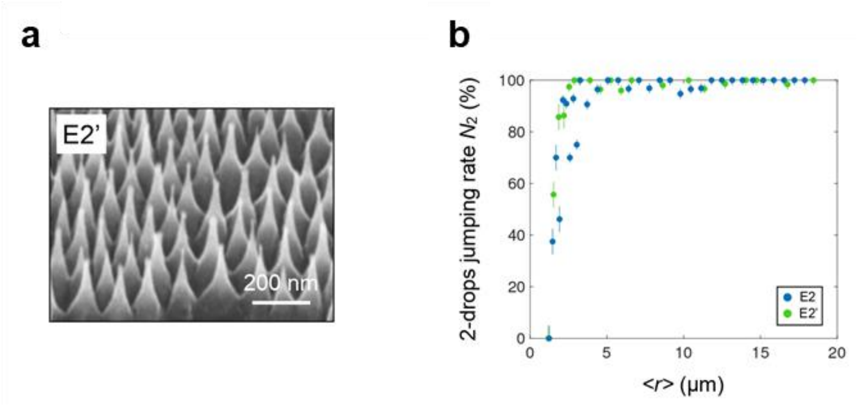

Figure S 11 | a, Scanning electron micrographs of the nanocones E2'. The cones have a height *h* = 220 nm and pitch *p* = 110 nm and they are disposed on a dense hexagonal array and covered by a hydrophobic layer. In contrast with its counterparts from the E family, cones are here convex with a varying cone angle. **b,** Jumping rate N_2 for binary, symmetric coalescences, as a function of droplet size for samples E2 and E2'. All data collapse on a single curve with a critical radius of jump $r_c \approx 1.6 \pm 0.3$ µm and 1.5 ± 0.3 µm, for E2 and E2' respectively, and a plateau value of 99 ± 1%. This curve is very similar to those obtained in Figure 57c,d.

Supplementary Figures adapted from: Adapted from: P. Lecointre, S. K. Laney, M. Michalska, T. Li, *et al.*, Unique and robust dew repelllency of nanocones, **Nature Communications**, 2021, 12, 3458

Supplementary Figures adapted from: Adapted from: P. Lecointre, S. K. Laney, M. Michalska, T. Li, *et al.*, Unique and robust dew repelllency of nanocones, **Nature Communications**, 2021, 12, 3458